Membrane interaction of amyloid–beta (1–42) peptide induces membrane remodeling and benefits the conversion of non–toxic Aβ species into cytotoxic aggregate

DISSERTATION

zur Erlangung des akademischen Grades
doctor rerum naturalium
(Dr. rer. nat.)

im Fach Biologie
eingereicht an der
Lebenswissenschaftlichen Fakultät
der Humboldt-Universität zu Berlin

von
M.Sc. Biophysikerin Sha Jin

Präsidentin der Humboldt-Universität zu Berlin
Prof. Dr.-Ing. habil. Dr. Sabine Kunst

Dekan der Lebenswissenschaftlichen Fakultät
Prof. Dr. Richard Lucius

Vorsitzender	Prof. Dr. Thomas Sommer
Gutachter	Prof. Dr. Erich Wanker
	Prof. Dr. Jan Bieschke
	Prof. Dr. Andreas Herrmann
Weiteres Mitglied	Prof. Thomas J. Buckhout, Ph.D

Tag der mündlichen Prüfung: 25.08.2016

For grandpa

Abstract

The accumulation of Amyloid beta peptide 1–42 ($A\beta_{1-42}$) in extracellular plaques is one of the pathological hallmarks of Alzheimer's disease (AD). Several studies have suggested that a cellular reuptake of $A\beta_{1-42}$ may be a crucial step in its cytotoxicity, but mechanisms of Aβ–membrane interaction and subsequent cellular uptake are not yet understood. Aβ may be present in an aggregated form prior to cellular uptake. Alternatively, monomeric peptide may enter the endocytotic pathway and conditions in the endocytotic compartments may induce the aggregation process. The first aim of the present study is therefore to answer the question whether aggregate formation is a prerequisite or a consequence of Aβ–membrane interaction and of Aβ endocytosis. We visualized aggregate formation of fluorescently labeled $A\beta_{1-42}$ by Förster resonance energy transfer (FRET) and tracked its internalization by human neuroblastoma cells. Both aggregated and monomeric $A\beta_{1-42}$ entered the cells, however, monomer uptake faced a concentration threshold and occurred only at concentrations and time scales that allowed β–sheet–rich aggregates to form. By uncoupling membrane binding from internalization, we found that $A\beta_{1-42}$ monomers as well as small aggregate species bound rapidly to the plasma membrane and formed β–sheet–rich aggregates. These structures were subsequently taken up and accumulated in endocytic vesicles. This process correlated with inhibition of cellular metabolism activities. Our data therefore imply that the formation of β–sheet–rich aggregates at the cell membrane is a prerequisite for $A\beta_{1-42}$ uptake and cytotoxicity. The second aim of the study is to investigate the Aβ–membrane interaction in vitro by using giant unilamellar vesicles (GUVs) and giant plasma membrane vesicles (GPMVs) as model membrane systems. We found that both Aβ isoforms, $A\beta_{1-42}$ and $A\beta_{1-40}$, interacted with the liquid disordered (Ld) phase of model membranes. Early aggregation intermediates of Aβ, which did not yet bind to the amyloiddophilic dye Thioflavin T (ThT), induced negative membrane (lipidbilayer) curvature. The ability of Aβ to induce membrane deformation suggests that Aβ may facilitate its own endocytosis. It also hints at a possible physiological function of non–toxic Aβ aggregate species.

Keywords: aggregation; membrane interaction; endocytosis; cytotoxicity; membrane curvature.

Zusammenfassung

Das Amyloid–beta Peptid (Aβ) ist der Hauptbestandteil der extrazellulären Plaques bei der Alzheimerschen Krankheit (AD). Die Aufnahme von Aβ aus dem extrazellulären in den intrazellulären Raum, die wahrscheinlich durch Endozytose erfolgt, könnte eine entscheidende Rolle bei der zytotoxischen Aktivitätvon Aβ spielen. Das Ziel der vorliegenden Arbeit ist es, die Mechanismen der Wechselwirkungen des Aβ Peptids, insbesondere von $Aβ_{1–42}$, mit der Plasmamembran und der nachfolgenden zellulären Aufnahme aufzuklären. Die Aggregation, die zelluläre Aufnahme und die Zytotoxizität von $Aβ_{1–42}$ wurden durch Verwendung von fluoreszenzmarkierten $Aβ_{1–42}$ in einem Neuroblastomzellkulturmodell untersucht. Sowohl bei Inkubation mit Monomeren als auch mit Aggregaten wurde in den Zellen fluoreszenzmarkiertes $Aβ_{1–42}$ detektiert. Dabei binden $Aβ_{1–42}$ Monomere und kleine Aggregate zunächst an die Zellmembran. Allerdings erfolgt keine direkte Aufnahme von Monomeren in die Zelle. Erst nach Ausbildung von Aggregaten mit geordneter Sekundärstruktur wurde $Aβ_{1–42}$ in den endozytotischen Vesikel mittels konfokaler Mikroskopie detektiert. Dieser vorangehende Aggregationsprozess von an der Zellmembran gebundenem $Aβ_{1–42}$ wurde durch Förster–Resonanzenergietransfer (FRET) nachgewiesen. Voraussetzung für den an der Membran ablaufenden Aggregationsprozess ist, dass die Monomere oberhalb einer kritischen Konzentration anwesend sind, um nach ausreichender Inkubationszeit eine Bildung von β–Faltblatt–Strukturen und entsprechenden Aggregaten zu ermöglichen. $Aβ_{1–42}$ Aggregate, die sich durch eine β–Faltblatt–Strukturenauszeichneten, benötigten keine kritische Schwellenkonzentration für die endozytotische Aufnahme. D.h., eine vorangegangene Bildung entsprechender Aggregate, deren β–Faltblatt–Struktur durch das Fluorophor ThioflavinT und/ oder ThioflavinS (ThT, ThS) nachgewiesen werden konnte, beschleunigt die zelluläre Aufnahme von $Aβ_{1–42}$. Eng mit der Aufnahme von $Aβ_{1–42}$ Aggregaten war die Veränderung des zellulären Metabolismus verbunden. Um die Wechselwirkung zwischen Aβ und der Membrannäher zu charakterisieren, wurden Modellmembransystemen einschl. riesigen Membranvesikeln (*giant unilamellar vesicles*(*GUVs*) und *giantplasmamembranevesicles*(*GPMVs*)) genutzt. Dabei wurde beobachtet, dass sowohl $Aβ_{1–42}$ als auch $Aβ_{1–40}$ Einstülpungen in der Membran induzieren können. Kleine Aggregate beider Isoformen, die noch keine β–Faltblatt–Struktur aufweisen, interagierten bevorzugt mit der ungeordneten Lipidphase (*liquid disordered, Ld*) und induzierten dabeieine negative Membrankrümmung. Diese Beobachtungen legen den

Schluss nahe, dass möglicherweise das Aβ Peptid selbst den endozytotischen Prozess unterstützt oder diesen sogar einleiten könnte. Dies könnte auch auf eine mögliche physiologische Funktion von Aβ Aggregaten, die nicht toxisch sind, hindeuten.

Schlagwörter: Aggregation; Membran–Wechselwirkung; Endozytose; Zytotoxizität; Membrankrümmung.

Acknowledgements

This work was carried out from Mai 2012 until Mai 2015 in the laboratory of Prof. Dr. Erich E. Wanker in the Department of Proteomics and Molecular Mechanisms of Neurodegenerative Diseases at the Max Delbrück Center for Molecular Medicine (MDC), and in the laboratory of Prof. Dr. Andreas Herrmann in the Department of Molekulare Biophysik at the Institut für Biologie of the Humboldt-Universität zu Berlin.

At first, I would like to thank Dr. Jan Bieschke for giving me the opportunity to do this great project, for his continuous support and his trust in allowing me to work independently. He made it possible that I got the opportunity to use the freeze–fracture electron microscopy at the Washington University in St. Louis. I am also thankful to him for correcting grammar and for carefully reading on revisions of this dissertation.

Many thanks to Prof. Dr. Erich E. Wanker for giving me the opportunity to work at the MDC and for the discussions in lab seminars.

I need to give a huge amount of appreciation for my co–supervisor, Prof. Dr. Andreas Herrmann, who gave me the freedom to realize my own idea, and at the same time his guidance to keep me marching forward and stay focused. Without his mentorship, encouragement and editing assistance, I would not have finished this work.

I am especially grateful to Dr. Jörg Nikolaus who introduced model membrane systems and helped me with all the questions of lipids. Thanks to Ivan Haralampiev for helping with GUVs and spinning disc confocal microscopy.

I would like to acknowledge Dr. Thomas Korte, Dr. Zoltan Cseresnyes and Dr. Anca Margineanu for help with fluorescence microscopy.

Thanks to PD Dr. Rainer König, PD Dr. Frank Westermann and Prof. Dr. Manfred Schwab for the gift of the SH–EP cell line. Thanks to Prof. Dr. Jochen Meier, Dr. Benjamin Förstera and Dr. Aline Winkelmann for the gift of the primary hippocampal neurons.

I sincerely thank Dr. Thomas Wiglenda and Dr. Anup Arumughan for scientific discussions.

Special thanks go to Alexandra Redel, Gerlinde Grelle, Christian Hänig and Erika Pisch for all the help and support during the whole time.

I am very grateful for all the support from the lab members of the HU Berlin, many others of my colleagues at the MDC as well as the colleagues of the Washington University in St. Louis.

Thanks to my family, my friends and my sweetheart DingDingTang for giving me a very happy and very free life! You are always there for me. I love all of you!

I would like to express my gratitude to DFG, this research would not have been possible without the financial assistance of DFG.

Contents

Abbreviations

AD	Alzheimer's disease
APP	amyloid precursor protein
Aß$_{1–40}$	amyloid beta 1–40 peptide
Aß$_{1–42}$	amyloid beta 1–42 peptide
BACE	β–site APP–cleaving enzyme
BSA	fetal bovine serum
BT	Bleed–Through
C6–NBD–PC	1–palmitoyl–2–[6–[(7–nitro–2–1,3–benzoxadiazol–4–yl)amino]hexanoyl]–sn–glycero–3–phosphocholine
CCVs	clathrin–coated vesicles
CD	circular dichroism
Chol	cholesterol
CLIC	clathrin– and dynaminindependent carrier
CL–MPR	cation–independent mannose–6–phosphate receptor
CME	clathrin–mediated endocytosis
C–terminal	carboxy–terminal
D	diffusion coefficient
DMEM	Dulbecco's Modified Eagle medium
DMSO	dimethyl sulfoxide
DOL	degree of labeling
DOPC	dioleoyl phosphatidylcholine
DOPE	dioleyl phosphatidylethanolamine
DTT	dithiothreitol
EEA	early edosome antigen
EM	electron microscopy
ERC	endocytic recycling compartment
FBS	fetal bovine serum
FRET	Förster resonance energy transfer
GEEC	glycosyl phosphatidylinositol–anchored protein enriched early endosomal compartments
GPMV	giant plasma membrane vesicles
GTPase	guanosine triphosphatase
GUV	giant unilamellar vesicles

HFIP	1,1,1,3,3,3–hexafluoro–2–propanol
IF	immunofluorescence staining
LAMP2	lysosome–associated membrane protein 2
Ld	liquid–disordered
LDL	low–density lipoprotein
LDLR	low–density–lipoprotein receptor
Lo	liquid–ordered
LUV	large unilamellar vesicle
MLV	multilamellar vesicle
MTT	3–(4,5–dimethylthiazol–2–yl)–2,5–diphenyltetrazolium bromide
MW	molecular weight
N.A.	Numerical Aperture
NaOH	sodium hydroxide
N–terminal	amino–terminus
p.a.	postaggregation
PBS	phosphate–buffered saline
PC	phosphatidylcholine
PFA	paraformaldehyde
PL	phospholipid
PS1 (PS2)	presenilin 1 (or 2)
RT	room temperature
sc–$A\beta_{1–42}$	scrambled– amyloid beta 1–42 peptide
SEC	size–exclusion chromatography
SSM	n–stearoyl–D–sphingomyelin
SUV	small unilamellar vesicle
TCEP	tris(2–carboxyethyl)phosphine
TGN	trans–Golgi network
ThS	thioflavin S
ThT	thioflavin T
UV	ultraviolet

1 Introduction

1.1 Overview of neurodegenerative diseases

Neurodegeneration relates to the pathological condition primarily affecting neurons, that results in a progressive loss of neuronal structure, function and neuronal death (Martin 1999; Przedborski et al. 2003; Dickson 2010). The loss of specific populations of neurons affects various functional systems, like pyramidal and extrapyramidal motor system or the higher order association and limbic cortices (Dickson 2011). The neuronal loss and damage of neurons in the function area of brain can lead to many different clinical symptoms, such as dementia, reduced motor control and psychological abnormalities.

Table 1–1: Molecular classification of neurodegenerative disorders. Adapted from Martin (Martin 1999).

Disease	Predominant affected brain regions	Mainly neuropathologic features	Proteins affected
Alzheimer's disease	Cerebral cortex	Senile plaques, neurofibrillary tangles, neuronal and synaptic loss	Plaques: β–amyloid, presenilin 1 and 2, α_1–antichymotrypsin, apolipoprotein E, α_2–macroglobulin, ubiquitin Neurofibrillary tangles: hyperphosphorylated tau, ubiquitin
Parkinson's disease	Basal ganglia	Neuronal loss in substantia nigra, Lewy bodies in pigmented neurons	α–Synuclein, ubiquitin parkin
Huntington's disease	Basal ganglia	Neuronal loss in neostriatum and subsequently in cerebral cortex	Huntingtin
Spinocerebellar ataxia	Brain stem and cerebellum	Neuronal loss in cerebellum and brain stem	Ataxin, α_1–Voltage–dependent calcium channel
Amyotrophic lateral sclerosis	Motor system	Loss of upper and lower motor neurons	Ubiquitin, neurofilaments, superoxide dismutase type 1

Traditionally classification of the neurodegenerative disorders was according to the clinical syndromes and the anatomical distribution of neuropathology, e.g. Alzheimer's disease (AD), Parkinson's disease, Huntington's disease, Spinocerebellar ataxia and Amyotrophic lateral sclerosis as listed in **Table 1–1** (Martin 1999; Dickson 2011).

The developments of molecular genetics, biochemical immunocytochemical and biophysical techniques (Burke et al. 2013), allowed to characterize the neurodegenerative disorders by the proteins, that accumulate within cells or in the extracellular space. Protein deposits within the affected tissues are a characteristic feature of many neurodegenerative diseases (**Table 1–1**).

The causes of neurodegenerative disease can be genetic mutations (Bertram & Tanzi 2005); medical conditions like alcoholism (Nixon 2006; Morris et al. 2010), tumors (Wang et al. 2013; Rice et al. 2003); viral infections (Zhou et al. 2013) like the infection of herpes simplex virus (Ito et al. 2000; Mégret et al. 2007) or influenza virus (White et al. 2014; Jang et al. 2009; Mori & Kimura 2001; Sulkava et al. 1981). However, in many cases of Alzheimer's and Parkinson's disease patients, the cause remains unknown.

1.2 Alzheimer's disease

AD is the most common fatal neurodegenerative disorder over 65 years of age (Glenner 1983; LaFerla et al. 2007; Babusikova et al. 2011; Brookmeyer et al. 1998) and belongs to the top 10 leading causes of death in USA (Alzheimer's Association 2015; National Center for Health Statistics 2015).

AD was first described by the German psychiatrist and neuropathologist Alois Alzheimer. In 1906, he reported a case of a 51 years old patient named Auguste Deter, who suffered from senile dementia and died five years later, at the age of 56 (Alzheimer 1907).

The major characteristic symptoms of AD are cognitive failures, impairment of memory and dramatic changes in behavior, with symptoms like loss of memory, problems with language, personality and mood changes (LaFerla et al. 2007; Babusikova et al. 2011). The understanding of cause and pathophysiology of AD is still very limited. An effective early diagnosis , therapy or prevention of AD are not available (Babusikova et al. 2011).

1.2.1 Characteristic microscopic findings of AD

Examining the preparations of the brain of the patient by using microscopy, Alzheimer found plaques that could be stained with Iodine (**Figure 1–1**) (Alzheimer 1907; Perl 2010). Emil

Kraepelin described this disease in his book ‘Psychiatrie’ and named it Alzheimer‘s disease (AD) (Alzheimer 1907). Structures that could be stained in such a way had been described by Rudolf Virchow as ‘starch–like’ or amyloid (Virchow 1853). The modern biophysical definition of amyloid focuses on their unique protein folding structure, in which intermolecular β–pleated sheets form a twisted fibrillar superstructure that can be detected by X–ray diffraction (Dobson 2003; Dobson 2004).

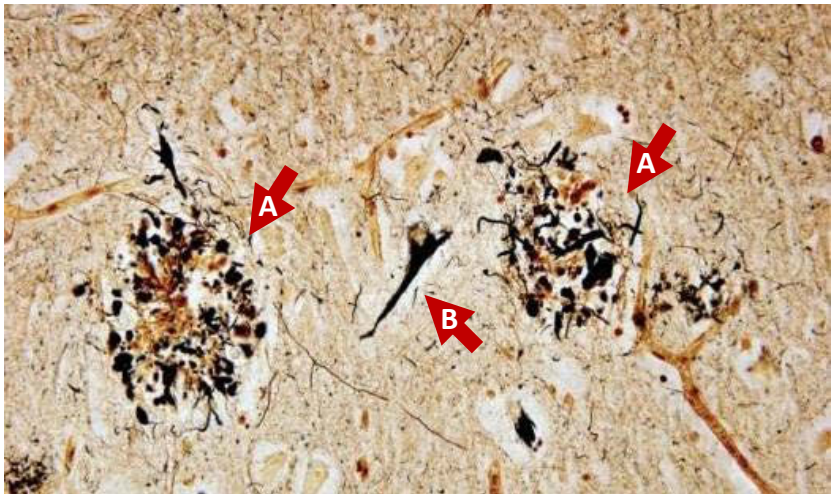

Figure 1–1: Photomicrograph of the temporal cortex of a patient with Alzheimer's disease (AD). Two senile (neuritic) plaques (arrow A) with a neurofibrillary tangle (arrow B) between them are shown, modified Bielschowsky stain; original magnification, 400x. Figure adapted from Perl et al. (Perl 2010).

1.2.2 Amyloid and tau hypothesis

The causes for most cases of AD are still unknown. However, 5–10% of AD patients with early–onset disease (< 65 years) suffer from familiar AD, caused by several mutations that were identified either in the amyloid precursor protein (APP), or inpresenilin 1 and presenilin 2, which are involved in the processing of APP as discussed in 1.3 (Campion et al. 1995; Levy–Lahad et al. 1995; Mullan et al. 1992; Rogaev et al. 1995; Babusikova et al. 2011).

The devastating neuropathology of AD is tightly linked to two polypeptides: the Amyloid beta peptide (Aβ), which deposits extracellularly in the cortical plaques (G G Glenner & Wong 1984; George G. Glenner & Wong 1984), and the tau protein, which deposits intracellularly in neurofibrillary tangles (Lee et al. 1991; Grundke–Iqbal et al. 1986).

1.3 APP processing and Aβ generation

The amyloid precursor protein (APP) is a transmembrane glycoprotein (O'Brien & Wong 2011). Its physiological function is still unclear (Babusikova et al. 2011). The amino–terminal (N–terminal) end of APP may be localized toward to the extracellular space or may be localized in the lumen of intracellular vesicles (Babusikova et al. 2011; Neve et al. 2000). The carboxy–terminal (C–terminal) end of APP is the cytoplasmic domain (Babusikova et al. 2011).

Aβ is generated at cholesterol–rich regions of neuronal membranes by proteolytic cleavage of the APP via groups of enzymes or enzyme complexes termed α–, β– and γ–secretases (**Figure 1–2**) (Jarrett et al. 1993; Shoji et al. 1992; Simons et al. 1998; LaFerla et al. 2007).

Three enzymes of the ADAM family with α–secretase activity have been identified: ADAM9, ADAM10 and ADAM17 (LaFerla et al. 2007; Allinson et al. 2003). The β–secretase, a type I integral membrane protein, is a β–site APP–cleaving enzyme 1 (BACE1) (Hussain et al. 1999; Sinha et al. 1999; Vassar et al. 1999; LaFerla et al. 2007). The γ–secretase is a enzymes complex, consisting of presenilin 1 and 2 (PS1 and PS2), nicastrin, anterior pharynx defective and presenilin enhancer 2 (Francis et al. 2002; Levitan et al. 2001; Steiner et al. 2002; Wolfe et al. 1999; Yu et al. 2000; LaFerla et al. 2007).

There are two pathways of the cleavage and processing of APP: a non–amyloidogenic pathway and an amyloidogenic pathway (**Figure 1–2**) (LaFerla et al. 2007):

- In the non–amyloidogenic pathway (**Figure 1–2**), APP is cleaved by the α–secretase at a position 83 amino acids from the C– terminus, producing a large N–terminal ectodomain (sAPPα), which is secreted into the extracellular medium (Kojro & Fahrenholz 2005; LaFerla et al. 2007). The product, a 83–amino–acid C–terminal fragment (C83), will still remain in the membrane (Haass et al. 1993; LaFerla et al. 2007). In this pathway, the cleavage of APP by the α–secretase occurs within the Aβ region, which may prevent formation of full–length Aβ (LaFerla et al. 2007). C83 fragment could also be cleavaged by the γ–secretase, a short peptide p3 and APP Intracellular Domain (AICD) would be then produces (Haass et al. 2012).
- In the amyloidogenic pathway (**Figure 1–2** and **Figure 1–3** a) , Aβ peptide is produced by endoproteolysis of APP by β– and γ–secretases and is secreted into the extracellular space (LaFerla et al. 2007). APP is at first cleaved by the β–secretase at a position located 99 amino acids from the C terminus; and then the membrane domain, 99–amino–acid C–terminal (C99), with newly generated N terminus of Aβ is cleaved by γ–secretase into fragments of 43 –36 aa length with in the membrane (LaFerla et al. 2007), which is then processed further to yield peptides of 37–43 aa.

While Aβ release by γ–secretase cutting, AICD, the rest part of C99, is released into cytosol (Haass et al. 2012).

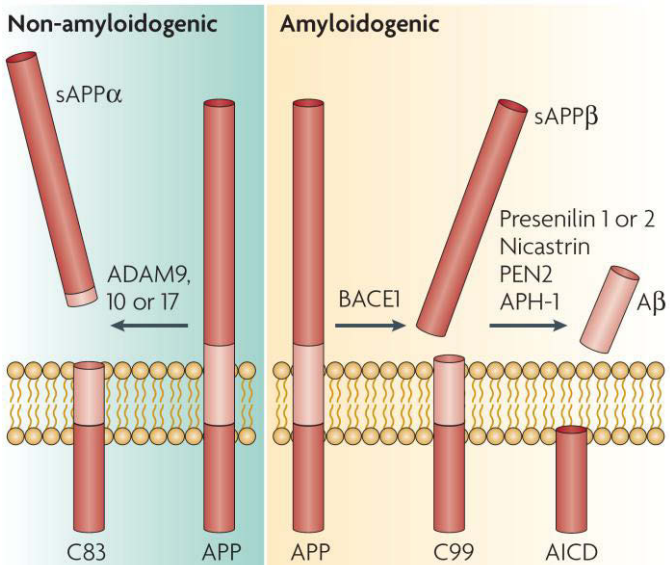

Figure 1–2: Two pathway of amyloid precursor protein (APP) proteolysis. Most APP is processed through the non–amyloidogenic pathway, which precludes Aβ formation. Figure adapted from LaFerla et al. (LaFerla et al. 2007).

Most of the produced Aβ peptide is 40 residues in length ($Aβ_{1–40}$), whereas a small proportion (approximately 10%) is the 42 residue variant ($Aβ_{1–42}$, **Figure 1–3** a and b) (LaFerla et al. 2007; Ahmed et al. 2010). Two additional hydrophobic residues, Ile–41 and Ala–42, at the C–terminus, let $Aβ_{1–42}$ is more hydrophobic than $Aβ_{1–40}$, that may lead $Aβ_{1–42}$ more prone to form fibril (Jarrett et al. 1993). Under the same aggregation conditions, such as the concentration of Aβ peptide, the compositions of buff solution, temperature and the frequency of mechanic shaking, $Aβ_{1–42}$ aggregates more quickly than $Aβ_{1–40}$ *in vitro* (Hasegawa et al. 1999; Ball et al. 2013; Jarrett et al. 1993).

Both types of Aβ form small soluble aggregates (**Figure 1–3** c), insoluble fibrils (**Figure 1–3** d) and plaques in the extracellular space of the brain in AD patients (Masters et al. 1985; George G. Glenner & Wong 1984). $Aβ_{1–42}$ is the predominant isoform found in cerebral plaques (Younkin 1998; LaFerla et al. 2007), causes more extensive damage to cultured neuronal cells than $Aβ_{1–40}$ (Iwatsubo et al. 1996; Suzuki et al. 1994; Gravina et al. 1995; Roher et al. 1993; Dahlgren et al. 2002; Ball et al. 2013). Those observations suggest that the addition of the two C–terminal residues has a significant effect on the physiological and biophysical behavior of the two type of Aβ isoforms (Ball et al. 2013).

The experiments of present study will therefore largely focus on the $Aβ_{1–42}$ behaviors of cultured cells and of model membrane systems.

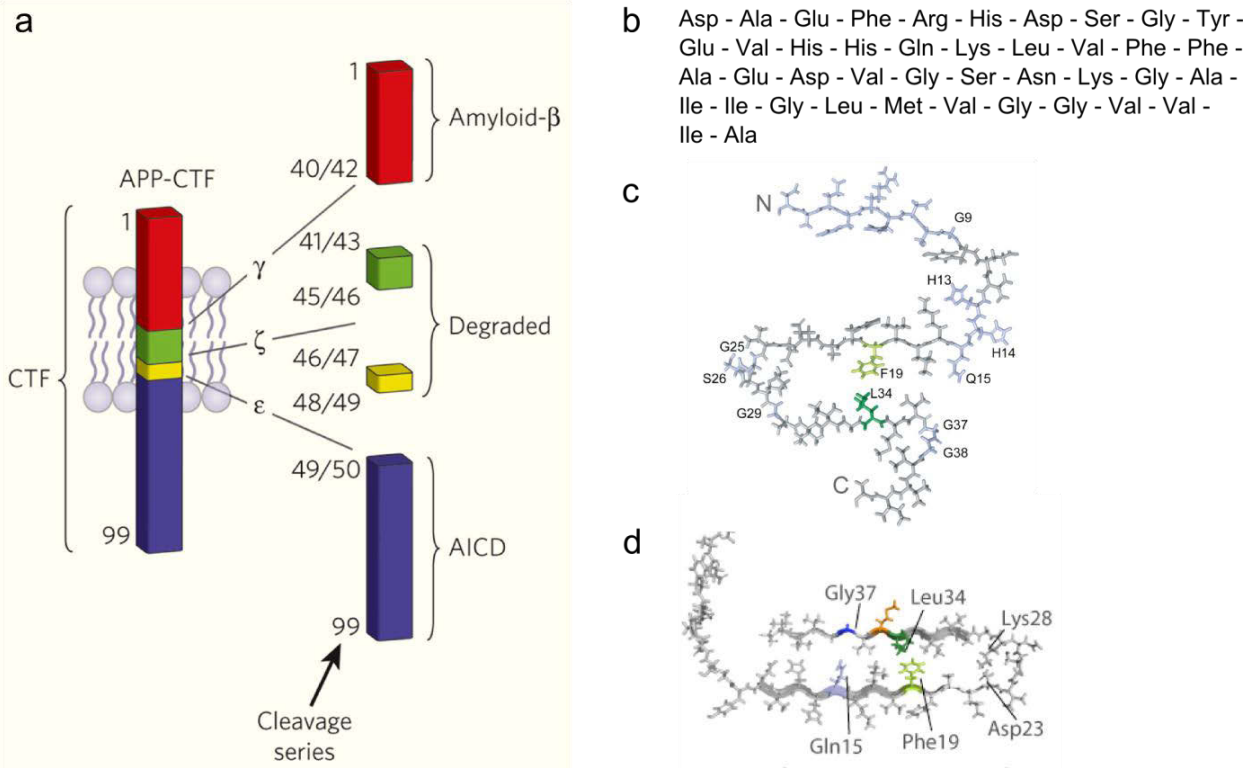

Figure 1–3: Aβ peptide structures. (a) The γ–secretase cleaves membrane domain (APP–CTF) of APP into different peptide length. Figure adapted from George–Hyslop & Schmitt–Ulms (George–hyslop & Schmitt–ulms 2010). **(b)** Sequence of human $A\beta_{1–40}$ and $A\beta_{1–42}$. **(c–d)** Models of monomeric $A\beta_{1–42}$ structure based on solid–state and solution NMR spectroscopy. **(c)** $A\beta_{1–42}$ monomer in small aggregates within lag–phase (ThT negative). **(d)** $A\beta_{1–42}$ monomer within fibril contained a β–turn—β fold between residues 11–40. Figures b–d adapted from Ahmed et al. (Ahmed et al. 2010).

1.4 Formation of Aβ aggregates

1.4.1 Protein folding and aggregation

To perform their biological function, most proteins need to fold into three dimensional structures that determine their activities (Anfinsen 1973). The conformational stability of a protein is generally defined as the free energy change (ΔG^0)of the equilibrium between the folded/native and the unfolded/denatured state (Mirsky & Pauling 1936). A schematic energy landscape for protein folding, i.e. the intramolecular interaction, and protein aggregation, i.e. the intermolecular interactions, is shown in **Figure 1–4** (Hartl & Hayer–Hartl 2009). In amyloid–forming polypeptides, the natively folded protein is not the lowest energy state. It is only meta–stable with respect to the amyloid fibril conformation. A substantial energy barrier prevents easy interconversion between both states.

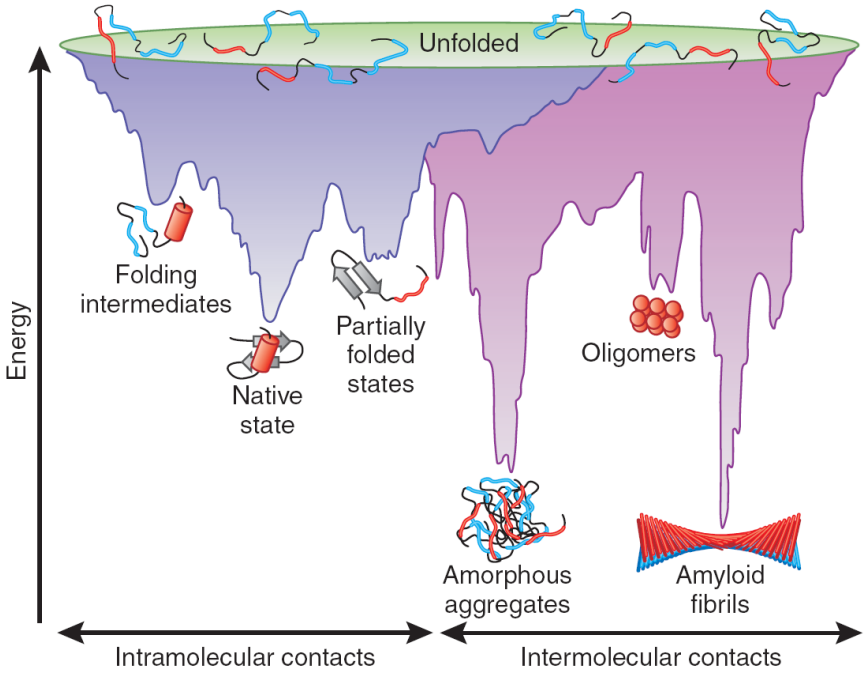

Figure 1–4: Schematic energy landscape of protein folding and aggregation. The surface simulates the the energy landscape of folding of a small protein, and the energy levels of possible conformational states. The unfolded state is the starting point for folding into a native structure, in order to minimize its free energy. The intermolecular protein (lilac) associations cause the energy minimum of those higher order species, such as fibril, deeper and sharper than native state (blue). Figure adapted from Hartl and Hayer–Hartl (Hartl & Hayer–Hartl 2009).

1.4.2 Aβ aggregation – polymerization model

The aggregation of amyloid peptide has been hypothesized to follow a nucleated polymerization mechanism (Burke et al. 2013; Lomakin et al. 1996; Murphy 2002; Chiti & Dobson 2006). The formation of aggregates is assumed to occur in two phases, first the nucleation phase or lag phase, which is a thermodynamically unfavored event; and second the elongation phase or growth phase (**Figure 1–5**) (Kumar & Walter 2011).

1.4.2.1 Lag phase

The formation of amyloid aggregates is a sequential addition of the monomers to a growing multimer (**Figure 1–5**). The thermodynamics of this process depend on the size of the multimer. It is unfavourable for the formations of dimmers and small oligomers. The monomer may be incorporated more easily, in regard to the reaction energy, when the multimer is larger than a critical size. This critical size (n monomer units) defines the nucleus, which has highest–energy on the polymerization pathway (Bieschke et al. 2006; Frank Ferrone 1999; Goldstein & Stryer 1986; Powers & Powers 2008; Powers et al. 1986).

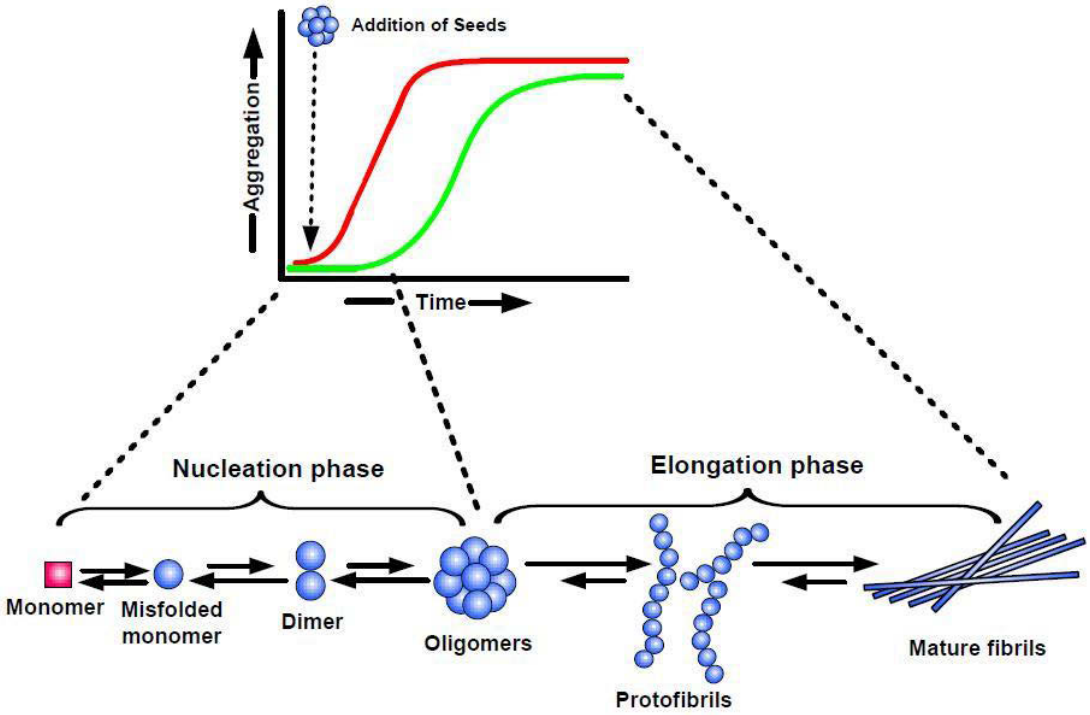

Figure 1–5: Model of amyloid aggregation. The formation of amyloid aggregates/fibrils was hypothesized in a nucleation and an elongation phase. Typical kinetic of monomer aggregation is a sigmoidal curve with a slow lag phase and a rapid growth phase (green curve). Aggregation kinetic with preformed seeds (nucleus) display a very short lag phase (red curve). Figure adapted from Kumar and Walter (Kumar & Walter 2011).

In the Asakura and Oosawa model (Asakura & Oosawa 1954; Asakura & Oosawa 1958), reactions of a classical nucleated polymerization are characterized by:

- a critical concentration (Kc), below which aggregates and/or fibrils cannot form; at peptide concentrations above Kc, aggregates grow until the monomer concentration decreases to Kc;
- a lag phase before aggregates/fibrils form which can be eliminated by the addition of preformed aggregates (seeds or nuclei);
- the rate limiting step is the formation of seeds/nuclei to promote aggregation, i.e. aggregate formation rate depend strongly on monomer concentration, which increases with the size of the nucleus.

T_{50}, a time at which the formation of aggregates/fibril approachs to 50% of steady state (the saturation phase), is used to present this concentration–dependent manner of Aβ aggregation kinetics. Common logarithm of t_{50} can be calculated as:

$$\log(t_{50}) = \text{constant} - \left(\frac{n+1}{2}\right)\log[X]_{tot} \qquad [1]$$

where $[X]_{tot}$ is the total concentration of amyloid peptide, n is the number of subunits in the nucleus.

Log–log plots of t_{50} versus $[X]_{tot}$ are often used in studies of amyloid fibril formation reactions to determine if the reaction follows the simple nucleation model (Arvintes et al. 1993; Bieschke et al. 2006; Frankenfield et al. 2005; Hurshman et al. 2004; Powers & Powers 2008; Serio et al. 2000; Sokolowski et al. 2003; Cohen et al. 2013).

1.4.2.2 Elongation phase

In the elongation phase, i.e. growth phase, the nuclei form speedily by adding of monomers, grow to reach the steady state. The larger polymers/fibrils will be then formed (**Figure 1–5**).

In addition to the classical nucleated polymerization model, the formation of a higher order structure is suggested through a secondary nucleation pathway (**Figure 1–6**), that results from fibril fragmentation or it is a fibril surface catalyzed aggregation process (Meisl et al. 2014; Cohen et al. 2013).

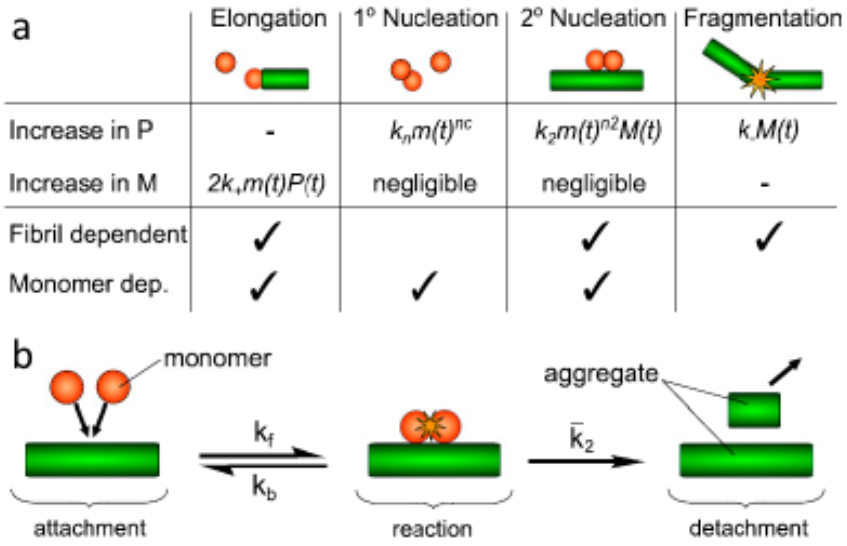

Figure 1–6: Schematic representations of the microscopic steps in aggregation. (a) Overview of different aggregation processes, comparing their dependences on the concentration of monomers (m) and fibril, and their contribution to the number (P) and mass concentrations (M) of fibrils; with k_+, the rate constants for elongation at fibril ends, k_n, primary nucleation in solution of order n_c. k_2, secondary nucleation on the fibril surface of order n_2, and k_-, fibril fragmentation. **(b)** Reaction scheme for secondary nucleation. Monomers accumulate to an aggregate; monomers aggregate to an aggregate; the detachment step of aggregate fragments. Figure adapted from Meisl et al (Meisl et al. 2014).

1.4.3 Structural classification of Aβ aggregates

Aβ aggregates accumulate extracellularly in specific regions of the brain of AD patients (Selkoe 2002). Because of the aggregation and the different preparation methods, Aβ has been observed in a variety of forms in vitro, such as disordered monomers, dimers, small oligomers, ring–like oligomers, protofibrils or twisted fibrils (Meinhardt & Fändrich 2009).

The Aβ aggregates sizes range from dimers up to very large aggregates, for which molecular weights of more than a million Da have been reported *in vitro* (Morales–Penningston et al. 2010; Glabe 2008; Harper et al. 1997; Walsh et al. 1999; Garzon–Rodriguez et al. 1997; Soreghan et al. 1994; Hilbich et al. 1991; Burdick et al. 1992).

Oligomers of A□ were suggested to be the primary toxic species in AD (Glabe 2008; Lue et al. 1999; McLean et al. 1999). These spherical particles of 3–10 nm are formed at an early phase of aggregation and disappear as mature fibrils are formed (Anguiano et al. 2002; Lashuel et al. 2002; Glabe 2008; Harper et al. 1997). They are therefore intermediates in the pathway of fibril formation (Glabe 2008). However, there is no standard definition for “oligomer” with respect to size and structure.

Under different conditions of preparation, soluble Aβ oligomers may show a rich variety in sizes, morphologies, such as amorphous aggregates, micelles, protofibrils, prefibrillar aggregates, globulomers, amylospheroids, toxic soluble Aβ, paranuclei and annular protofibrils, showing different levels of cytotoxicity (Walsh et al. 1997; Burdick et al. 1992; Soreghan et al. 1994; Harper et al. 1997; Glabe 2008; Lashuel et al. 2002; Lomakin et al. 1997; Lambert et al. 1998; Bucciantini et al. 2002; Lesné et al. 2006; Barghorn et al. 2005; Yamamoto et al. 2007; Hoshi et al. 2003; Bitan et al. 2003). The size of the oligomers could be differentiated by sedimentation, size exclusion chromatography and gel electrophoresis (Glabe 2008).

It is not easy to get a homogeneous Aβ oligomer preparaation with only one defined structure. The preparation is mostly heterogeneous, which may contain Aβ oligomers without β–sheets, with parallel β–sheets and/ or with antiparallel β–sheets (Glabe 2008; Ahmed et al. 2010). Small oligomers/aggregates are mobile and have a higher rate of diffusion (Glabe 2008), which may enable them to spread between cells. Due to their small size, the number of reaction ends for the monomer addition per unit mass of peptide is higher than for large fibrils (Glabe 2008). If the growth of β–sheets is important for pathogenesis, small oligomers/aggregates with β–sheet structure would have high toxicity (Glabe 2008).

1.5 Interaction of Aβ and its aggregation on membrane surfaces

Several studies have suggested that the interaction of misfolded proteins with liquid interfaces and surface plays a crucial role for protein–misfolding diseases, such as Alzheimer's disease, Parkinson's disease and Huntington's disease (Burke et al. 2013). Lipid bilayer properties may modulate the protein conformations and influence their aggregation state (Burke et al. 2013).

Based on its amphiphilic character, Aβ may have the ability to interact with membranes, and even insert into the lipid bilayer (Williams & Serpell 2011; Lansbury & Lashuel 2006; Burke et al. 2013). Additionally, Aβ is cleaved from APP and contains a part of the transmembrane domain of APP, suggesting that Aβ may be able to modulate the lipid bilayer function (Burke et al. 2013).

Many observations indicate that the binding of Aβ to membrane could depend on the presence of specific lipid components, i.e, cholesterol (Burke et al. 2013; Yip et al. 2001; Reiss et al. 2004; Yu & Zheng 2012), sphingolipids (Burke et al. 2013; Van Echten–Deckert & Walter 2012), gangliosides (Burke et al. 2013; McLaurin & Chakrabartty 1996), and neutral or charged phospholipids (Burke et al. 2013; McLaurin & Chakrabartty 1997; Sabaté et al. 2005; Sabaté & Estelrich 2005; Sabaté et al. 2012).

It has been hypothesized that aggregation of Aβ in or near membrane leads to disruption of membrane structure, change of the membrane curvature or creation of membrane pores (**Figure 1–7**) (McLaurin & Chakrabartty 1997; McLaurin & Chakrabartty 1996; Mirzabekov et al. 1996; Gorbenko & Kinnunen 2006; Burke et al. 2013).

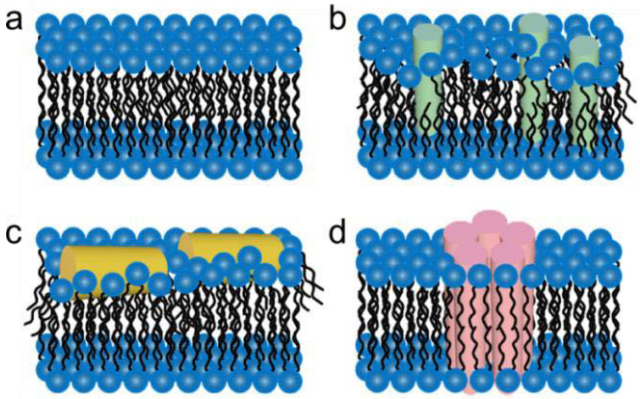

Figure 1–7: Schematic representations of potential mechanisms of amyloid/lipid association. (a) A schematic representation of the lipid bilayer. **(b)** Insertion of amyloid peptides into the lipid bilayer. **(c)** Lateral association of amphiphilic α–helices lipid–binding domains of amyloid peptide. **(d)** Transmembrane pore formation by amyloid peptide. Figures adapted from Burke et al. (Burke et al. 2013).

1.6 Internalization of Aβ

The plaques in the brain of AD patients also contain numerous proteins other than $A\beta_{1-42}$, which are normally only found in the intracellular space, such as lysosomal proteases or molecular chaperones (Friedrich et al. 2010). One hypothesis to explain this observation is that extracellular Aβ could be taken up by certain cells at low physiologically relevant concentrations of Aβ **(Figure 1–8 a**), and then concentrated into endosomes and lysosome (Hu et al. 2009). Concentrated Aβ in endocytic vesicles with low pH would find optimal conditions for a rapid aggregation (Hu et al. 2009).

The intraneuronal accumulation of Aβ is also observed in transgenic mice model and human patients, suggesting that intracellular accumulation may contribute to disease progression (LaFerla et al. 2007).

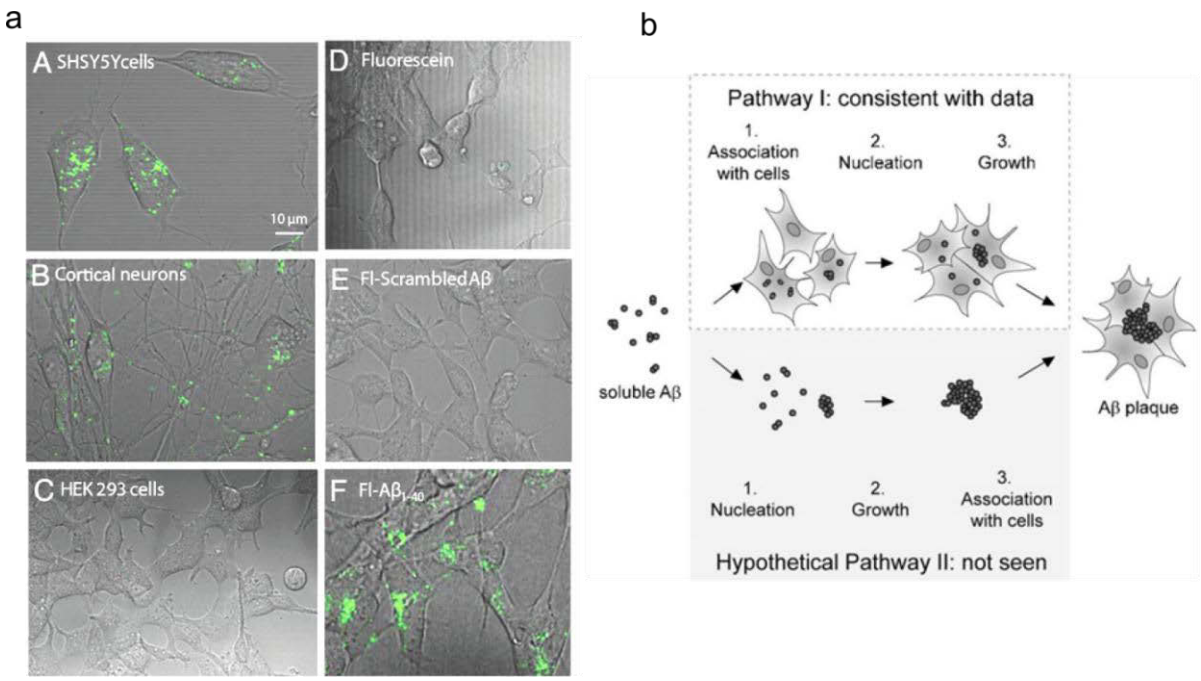

Figure 1–8: $A\beta_{1-42}$ cellular uptake and hypothetical pathway. (a) Cell uptake of FITC–$A\beta_{1-42}$. SHSY5Y cells (a–A), primary murine cortical neurons (a–B) and HEK293 cells (a–C) were treated with 250 nM FITC–$A\beta_{1-42}$ for 24 h, imaged by confocal/phase–contrast microscopy. Vesicular uptake of FITC–$A\beta_{1-42}$ was observed only in the neurons and SHSY5Y cells. No uptake could be observed in SHSY5Y cells by treating with 250 nM fluorescein (a–D) or FITC–scrambled–$A\beta_{1-42}$ (a–E) for 24 h. A similar uptake as FITC–$A\beta_{1-42}$ could be observed by treating with FITC–$A\beta_{1-40}$ (a–F). Figures adapted from Hu et al (Hu et al. 2009). Scale bar, 10 µm. **(b)** Schematic representation of the mechanism of intracellular amyloid plaque formation. Pathway I, consistent with data by Friedrich et al, the formation of large intracellular aggregates is followed by the uptake of small and (white background). Hypothetical pathway II, the formation of large aggregates are extracellularly, they will be then taken up by the cells (gray background). Figure adapted from Friedrich et al (Friedrich et al. 2010).

Friedrich et al have speculated that, after association of soluble Aβ with the cells, the amyloid plaques would be formed intracellularly (Friedrich et al. 2010). However, this is not the only possible pathway of Aβ internalization. In an alternative model, monomeric Aβ could aggregate extracellularly on the plasma membrane into oligomers, which are then endocytosed (**Figure 1–8 b**).

The present study aims to answer the question, where the intracellular Aβ aggregates originate, and whether Aβ aggregation occurs in the extracellular space, on the membrane or in the endocytotic pathway. It will explore in detail the relation between Aβ aggregation, membrane interaction, endocytosis and toxicity.

1.7 The plasma membrane

The most basic function of biological membranes is to be a physically barrier, to separate the intracellular components from the extracellular matrix and to regulate exchange between the two spaces (Chan & Boxer 2007).

Cellular membranes are formed by a large number of different lipid species and membrane proteins, including integral and peripheral membrane proteins, in various conformational states and topology, such as the number of transmembrane domains and their orientations in the membrane (van Meer et al. 2008). Singer and Nicolson described a two dimensional cell membrane, called fluid mosaic model, which proteins molecules distributed among a large number of phospholipid molecules (**Figure 1–9 a**) (Singer & Nicolson 1972). Modern research found that multiple factors increase the complexity of the plasma membrane, such as the ratio between membrane proteins and lipid molecules, limited lateral diffusion or the function of channel proteins.

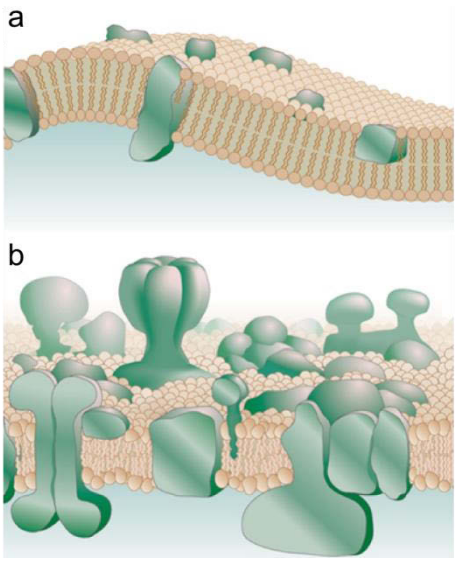

Figure 1–9: General models for membrane structure. **(a)** The Singer–Nicholson "fluid mosaic model" (Singer & Nicolson 1972). **(b)** An amended and updated version based on original model by Singer and Nicholson. Figures adapted from Engelmann (Engelman 2005).

The fluidity of membrane is influenced by the lipid compositions of the membranes. Some lipids facilitate membrane deformations, such as budding, tubulation, fission and fusion, and allow aggregation of particular proteins in membranes (van Meer et al. 2008). Lipids can display rotational and lateral movements within the membrane (Mouritsen 2005). The lipid compositions as a percentage of the total phospholipid (PL) of different membranes in mammals cells and yeast are shown in **Figure 1–10** (van Meer et al. 2008). Among them, phosphatidylcholine (PC) is always relatively dominant in all cell organelle membranes.

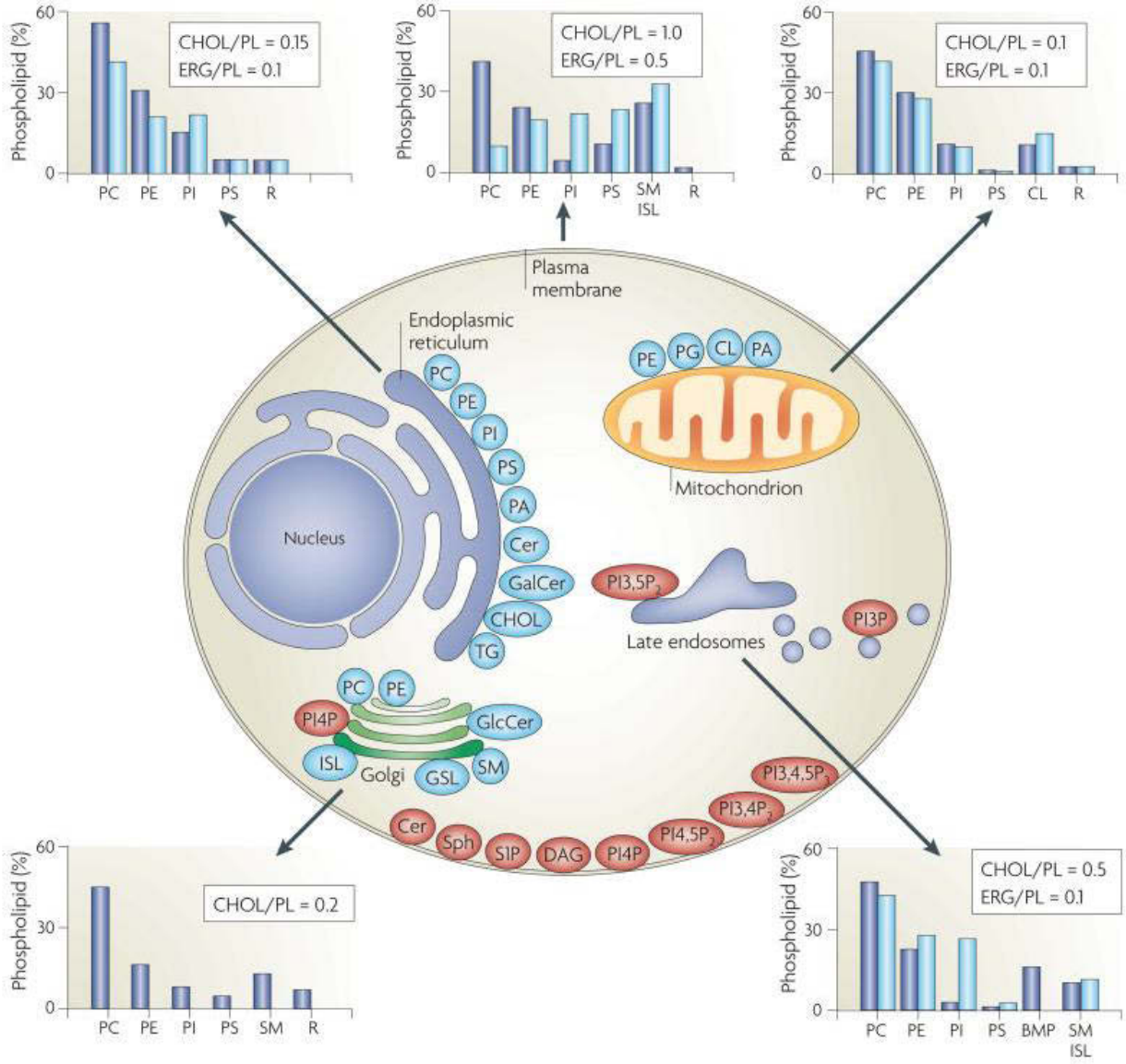

Figure 1–10: **Lipid synthesis and steady–state composition of cell membranes.** The lipid composition of different membranes varies throughout the cell in mammals (blue) and yeast (light blue). In mammal cells, phosphatidylcholine (PC) is the major phospholipids of all the membranes, followed by phosphatidylethanolamine (PE) and sphingomyelin (SM) in plasma membrane, in membranes of late endosomes and in the endoplasmic reticulum (ER). Figure adapted from van Meer et al. (van Meer et al. 2008)

1.8 Model membrane systems

To study particular lipid–lipid and protein–lipid interactions of complex natural membranes, different model systems have been developed (Chan & Boxer 2007; Stöckl & Herrmann 2010). The simplified model membrane systems retain the bilayer structure, with defined individual lipid or protein components (Chan & Boxer 2007). The organization of these components and heir dynamics can be visualized (Chan & Boxer 2007). These systems can be grouped into two different classes by the topology of the membrane (Stöckl & Herrmann 2010):

- Planar model systems: the membrane forms planar structures in lipid monolayers or supported bilayers.
- Vesicular model systems: the membrane forms a curved vesicular structure. Multilamellar vesicles are enveloped by more than one phospholipid bilayer, and unilamellar vesicles consist of a single bilayer.

The unilamellar vesicles can be divided by their sizes in (Stöckl & Herrmann 2010):

- Small unilamellar vesicles (SUVs) have diameters < 100 nm.
- Lange unilamellar vesicles (LUVs) are around 100 nm – 200 nm. LUV may resemble intracellular vesicles like lysosomes or other trafficking vesicles.
- Giant unilamellar vesicles (GUVs) have diameters up to several tens of micrometers.

Due to their size, shape changes of GUVs can be directly visualized by optical microscopy (Staneva et al. 2004; Papadopulos et al. 2007; Farge & Devaux 1992; Stöckl & Herrmann 2010). A direct observation of membrane permeabilization is possible as well (Ambroggio et al. 2005; Stöckl & Herrmann 2010).

GUVs made from appropriate lipid mixtures show separation into liquid disordered (Ld) and liquid ordered (Lo) phases (Stöckl & Herrmann 2010). These domains can be visualized by labeling with fluorescent compounds that either partition into the different lipid phases or change physical properties like fluorescence lifetime or polarization depending on the different domains (Veatch & Keller 2003; Veatch & Keller 2005; Owen et al. 2006; Margineanu et al. 2007; Korlach et al. 1999; Dietrich et al. 2001; de Almeida et al. 2007; Baumgart, Hunt, et al. 2007; Bagatolli 2006; Stöckl & Herrmann 2010; Stöckl, Plazzo, et al. 2008; Stöckl, Fischer, et al. 2008).

1.9 Giant plasma membrane vesicles

Giant plasma membrane vesicle (GPMV), average diameter up to 10 nm, is type of vesicular model membrane system, that is isolated from the plasma membranes of cultured cells (Baumgart, Hammond, et al. 2007). The examinations of GPMVs shown, that GPMVs are purely plasma membrane vesicles without any intracellular organelles, assembled cytoskeleton or nuclear material (Scott et al. 1979; Sezgin, Kaiser, et al. 2012). The compositions of GPMVs, such as the pinning of plasma membrane domains by cytoskeleton, membrane–associated proteins or membrane rugosities induced by protein–protein interactions (Baumgart, Hammond, et al. 2007), could be characterized by electron microscopy (EM). Compared to GUVs (**Table 1–2**), their biological nature makes GPMVs more physiological membrane models.

Table 1–2: Comparing properties of GUVs and GPMVs. The generalized polarization (GP) value is calculated from maximum emissions intensities at 440 nm and at 490 nm (Parasassi et al. 1990; Kaiser et al. 2009), $GP = \frac{I_{440} - I_{490}}{I_{440} + I_{490}}$ [2]. GUV standard raft mixture with dioleoylphosphatidylcholine (DOPC) :sphingomyelin (SSM) : cholesterol (chol) at 2:2:1. D: diffusion coefficient. Table adapted from Sezgin et al. (Sezgin, Kaiser, et al. 2012).

Characteristic	GUV	GPMV
Complexity	Simple lipid composition; few, if any, proteins reconstituted.	Physiological lipid complexity, contains native proteins.
Order difference between phases	Large (>1.0 GP units) (Kaiser et al. 2009)	Small (~0.2 GP units) (Kaiser et al. 2009)
Protein partitioning	Most peptides/proteins enrich in disordered phase (Kahya et al. 2005; Shogomori et al. 2005; Bacia, Schuette, et al. 2004).	GPI–anchored and some palmitoylated proteins are raft phase preferring (Levental et al. 2010; Sengupta et al. 2008; Baumgart, Hammond, et al. 2007).
Lipid analog partitioning	Most lipid analogs are disordered phase preferring (Baumgart, Hunt, et al. 2007).	Many lipid analogs retain partitioning characteristics of native lipids (Sezgin, Levental, et al. 2012).
Diffusivity difference between phases	$\frac{D_{Ld}}{D_{Lo}} \cong 10$ (Bacia, Scherfeld, et al. 2004).	$\frac{D_{Ld}}{D_{Lo}} \cong 3$ (Levental et al. 2009).
Microscopic phase separation temperature	Up to 35–38°C (Veatch & Keller 2003).	Preparation–dependent; below 20°C (Levental et al. 2011).

In pharmaceutics, GPMVs have been used as models to study the interactions of pharmaceutical compound and biological membrane in vitro, to test membrane permeability or therapeutic effect. (Säälik et al. 2011; Dubavik et al. 2012; Sezgin, Kaiser, et al. 2012).

In the 1970s, "clusters of lipids" in membranes were first described (Israelachvili et al. 1980; Karnovsky et al. 1982; Stier & Sackmann 1973). Those membrane microdomains with organized lipid mixtures were later named rafts. Recently, GPMVs becomes a popular tool to study lipid rafts and to observe the phase separation of membranes. This model membrane system carries its own complexity of protein and lipid composition from cellular plasma membrane. The biological nature of GPMVs might allow a relatively uniform small scale partitioning of the Ld phase into Lo phase, i.e. lipid rafts. Thus, in GPMVs the phase separations can only be observed in at low temperatures, that would not be simply like in GUVs (Baumgart et al. 2003; Baumgart, Hammond, et al. 2007).

In the present study, GPMVs were isolated from the SH–EP cells, which were also used for study of Aβ cellular uptake.

1.10 Endocytosis

The formation and inward movement of plasma membrane vesicles is called endocytosis (Vassilieva & Nusrat 2008; Marsh & McMahon 1999; Higgins & McMahon 2002). Endocytosis plays a decisive role in the cell survival and stimulates numerous cell functions, including antigen presentation, nutrient acquisition, clearance of apoptotic cells, pathogen entry, receptor regulation, hypertension, and synaptic transmission (Marsh & McMahon 1999).

Extracellular materials can be absorbed via different pathways into the cells (**Figure 1–11**) (Mayor & Pagano 2007).

There are three main endocytic pathways: phagocytosis for solid particles, macropinocytosis for fluid and the clathrin or caveolin mediated endocytosis for small entities, such as proteins. Small molecules and proteins, can be internalized by receptor mediated endocytosis via several mechanisms, which occur on the membranes of the whole cell body (Marsh & McMahon 1999).

Formation of membrane vesicles is a complex process that is dependent on the nature of the vesicle protein coat and the cargo (Vassilieva & Nusrat 2008). The complexities of endocytosis require many intermediate steps. After the formation of endocytic vesicle on the plasma membrane, lots of cellular compartments are involved in followed fusion process of endocytic vesicles (Vassilieva & Nusrat 2008; Ivanov 2008).

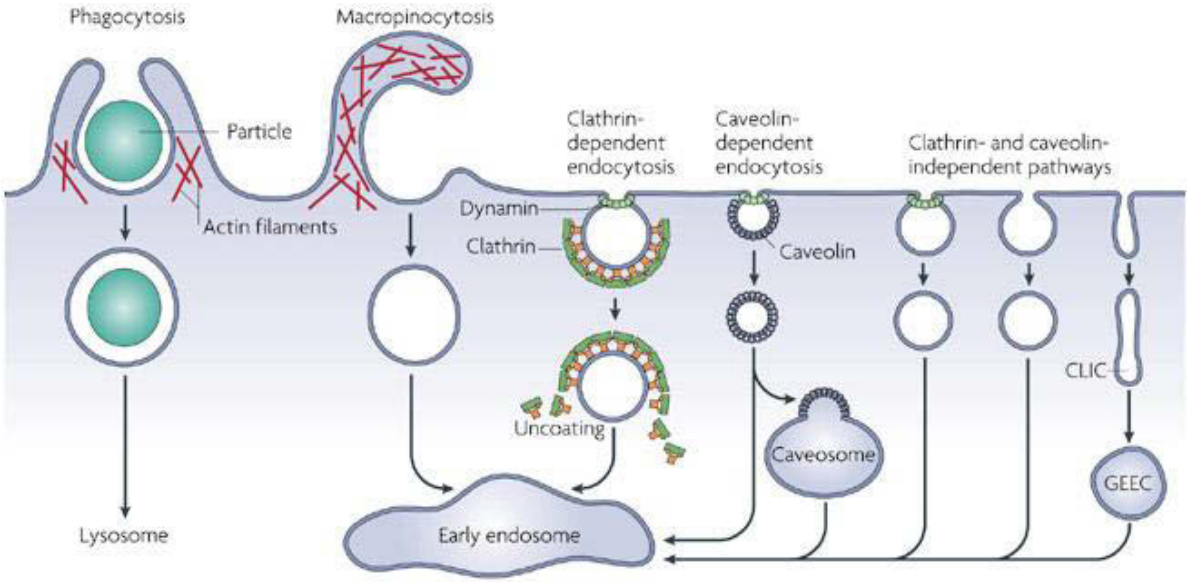

Figure 1–11: Pathways of entry into cells. Large and solid particles via phagocytosis; extracellular fluid via macropinocytosis; and the receptor–mediated endocytosis, such as clathrin or caveolin dependent endocytosis. CLIC, clathrin– and dynaminindependent carriers; GEEC, glycosyl phosphatidylinositol–anchored protein enriched early endosomal compartments. Figure adapted from Mayor and Pagano (Mayor & Pagano 2007).

The receptor mediated endocytosis can be categorized as clathrin–dependent or clathrinindependent (Vassilieva & Nusrat 2008). Their endocytotic mechanisms are presented below.

1.10.1 Clathrin–mediated endocytosis

Clathrin–mediated endocytosis is described a formation invagination, namely clathrin–coated vesicles (CCVs), by the plasma membrane to absorb the molecules from extracellular milieu (Vassilieva & Nusrat 2008; Marsh & McMahon 1999). **Figure 1–12** shows a schematic of clathrin assembly and release, and clathrin coated pit formation (Higgins & McMahon 2002).

Studies showed that, the assembly of a CCV may take about 1 min in cultured cells, and up to thousands those CCV can form per minute (Gaidarov et al. 1999; Marsh & Helenius 1980; Marsh & McMahon 1999). This pathway usually mediates by membrane receptors, such as transferrin receptors, epidermal growth factor (EGFR), and low–density lipoproteins (LDLR) (Vassilieva & Nusrat 2008).

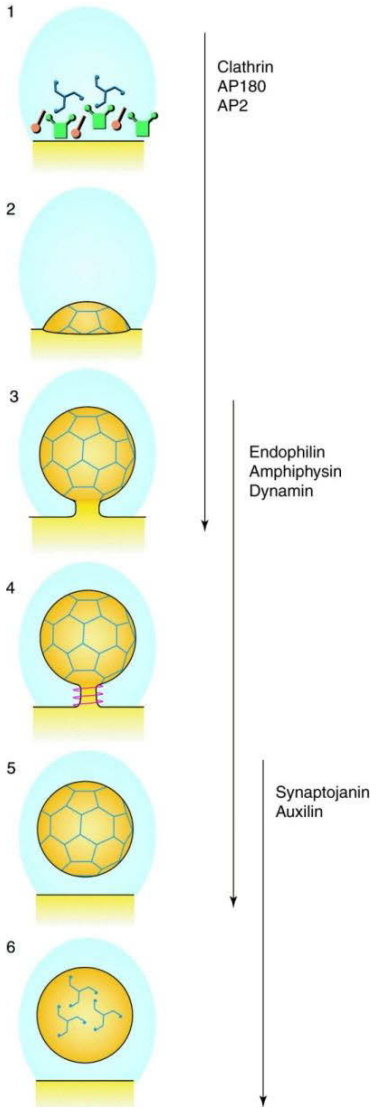

Figure 1–12: Clathrin–mediated endocytosis. (1) Clathrin (blue), AP180(red) (Ford et al. 2001) and AP2 adaptor complex (green) assemble on the surface of the cytoplasmic side of membrane. **(2)** Pits formation. **(3)** Formation of pits neck (Stowell et al. 1999) through endophilin (Farsad et al. 2001), amphiphysin (Takei et al. 1999) and dynamin (Sweitzer & Hinshaw 1998). **(4)** GTP–dependent scission caused by dynamin and amphiphysin leading to **(5)** Vesicle release (Marks et al. 2001; Sweitzer & Hinshaw 1998; Stowell et al. 1999). **(6)** Release of clathrin lattice with the participation of synaptojanin (Cremona et al. 1999) and auxilin (Greener et al. 2001). The uncoated vesicle will fuse with an acceptor membrane and releases its cargo. Figures adapted from Higgins and McMahon (Higgins & McMahon 2002).

1.10.2 Caveolar–mediated endocytosis

Caveolar–mediated endocytosis, also called clathrin–independent endocytosis, is raft–dependent plasma membrane invagination process. Cholesterol, sphingolipids and cholesterol–binding proteins accumulate in those invaginations (**Figure 1–11**) (Parton 2003; Parton & Simons 2007; Cohen et al. 2004; Hommelgaard et al. 2005; Parton & del Pozo 2013; Vassilieva & Nusrat 2008). Particles are internalized by caveolar–mediated endocytosis into an endosomal compartment called a caveosome (Pelkmans et al. 2001; Vassilieva & Nusrat 2008). Caveosomes contain caveolins but they do not accumulate transferrin, EEA1 or other markers of clathrin–mediated endocytosis and have neutral pH (Stan 2005; Vassilieva & Nusrat 2008). Comparing with the clathrin cycle, such as in the synapse, caveolar–mediated endocytosis may slower and be not tightly regulated (Marks & McMahon 1998; De Camilli 1995; Cremona & De Camilli 1997; Marsh & McMahon 1999).

For both clathrin–dependent and –independent endocytosis, dynamin, is involved in the scission of invaginations from plasma membrane (Vassilieva & Nusrat 2008; Mayor & Pagano

2007). Dynamin is a fission guanosine triphosphatase (GTPase) (Mayor & Pagano 2007). It self–assembles around liposomes which can disperse the liposomes into small vesicles (Hinshaw 2000; Vassilieva & Nusrat 2008). The regulation of fission of plasma membrane vesicles through dynamin activity was observed in living cells (Vassilieva & Nusrat 2008).

1.10.3 Macropinocytosis

Macropinocytosis (**Figure 1–11**) was observed and first filmed by Warren Lewis (Warren H. Lewis 1936). He described a non–specific process to internalize the fluid and membrane into macropinosomes. This endocytotic process is growth factor–induced and actin–dependent (Mercer & Helenius 2009; Lim & Gleeson 2011). Macropinocytosis plays an important role in cell motility and antigen presentation, and can be modified by infectious pathogens, such as protozoa, bacteria, viruses and prions, while entering the host cells (Mercer & Helenius 2009; Lim & Gleeson 2011).

Macropinocytosis of tau protein was reported by Holmes et al. The authors suggested that it may be a key step in aggregate propagation in tauopathies and synucleinopathies (Holmes et al. 2013; Holmes et al. 2014).

1.10.4 Receptor–mediated endocytosis of transferrin

Transferrin is an iron–binding plasma glycoprotein (Crichton & Charloteaux–Wauters 1987). When loaded with iron, transferrin protein can bind to a transferrin receptor (TfR) at neural pH (~ 7.2), and can be internalized by receptor–mediated endocytosis through clathrin–coated pits (Frazier et al. 1982; Karin & Mintz 1981; Nunez et al. 1977; van Bockxmeer & Morgan 1979; Ward et al. 1982). A decrease of the endosomal pH (~ 5.5) induces the release of iron from transferrin–TfR complex. Once iron is released, TfR and ligand will return to the cell surface (**Figure 1–13**) (Harding et al. 1983; Maxfield & McGraw 2004; Hsu et al. 2012). Therefore, fluorescent transferrin conjugates and TfR are broadly used as marker for tracking endocytic pathways (Iacopetta et al. 1983; Harding et al. 1983; Jandl & Katz 1963; Laurell & Ingelman 1947)

The uptake of transferrin depends on both temperature and energy (Sullivan et al. 1976; Harding et al. 1983). Low temperature and/or ATP depletion can inhibit transferrin uptake. Transferrin has been oberserved that only bind to the plasma membrane at 4°C, but would not be taken up at this temperature. By a further incubating the cells at 37°C, transferrin is then taken up into a trypsin–resistant space (Harding et al. 1983). However, their binding and uptake are substantially less (2.5 fold) and slower than under the normal condition, i.e.

constant at 37°C (Harding et al. 1983). The possible reason could be that the structure of TfR is disrupted by attacking of trypsin at 4°C. Although TfR regenerate with subsequent incubation at 37°C, the number of TfRs and their uptake are reduced (Harding et al. 1983).

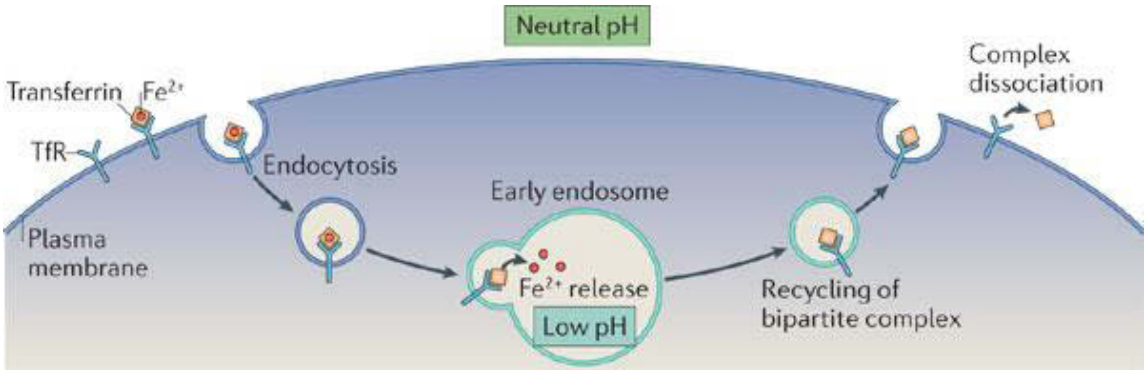

Figure 1–13: Schema of endocytic recycling pathways of transferrin. Iron loaded transferrin binds to transferrin receptor (TfR) at the cell surface at neutral pH. Iron and transferring–TfR complex is endocytosed via clathrin–coated pits. After releasing the iron (early endosome, pH about 5.5), transferrin and TfR return to the cell surface. Figure adapted from Hsu et al. (Hsu et al. 2012).

1.11 Thioflavin dyes

Thioflavin dyes, thioflavin T (ThT, **Figure 1–14**) and thioflavin S (ThS), are benzothiazole dyes. They are widely used to visualize β–sheet–rich amyloid structures under pathophysiological conditions both in vitro and in vivo (Kelényi 1967; Vassar & Culling 1959; LeVine 1993). In very recently study, the cationic ThT was also used to study the oscillations in membrane potential (Prindle et al. 2015).

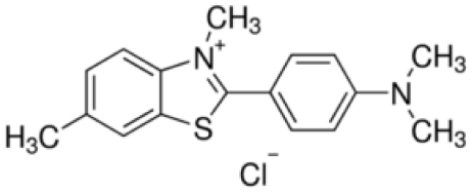

Figure 1–14: Structure of thioflavin T (ThT). Figure adapted from LeVine. (LeVine 1993).

ThT is positively charged in a solution with pH 5–9 (LeVine 1993; Prindle et al. 2015), binds rapidly to β–sheet structures of amyloid aggregates, which results a red shift in both excitation maximum (Ex. max) to 450 nm and emission maximum (Em. max) to 482 nm, compared to the free dye with Ex. max at 385 nm and Em. max at 445 nm (LeVine 1993).

There are two main hypotheses for the binding mechanism between ThT and amyloid. The channel model suggests that ThT recognizes the surfaces of cross–β structures (Biancalana &

Koide 2010); and the self–association models suggests that ThT molecules forms micelles in aqueous solutions resulting in hydrophobic interactions between ThT micelles and amyloid (Biancalana & Koide 2010; Khurana et al. 2005). ThT expresses stable fluorescence in solution with neutral pH or above 7 (LeVine 1993). The intensity and stability of fluorescence are reduced by lowering pH (Khurana et al. 2005; LeVine 1993). Khurana et al. suggested that the formation of ThT micelles depends on the concentration and charge of ThT and the disruption of ThT micelles at low pH leads to the reduction of the binding to amyloid and ThT fluorescence (Khurana et al. 2005).

Unlike ThT, ThS is negatively charged at solution pH 5–9 (LeVine 1993), is a mixture of at least 6 sulfonated compounds (LeVine 1993; Wei et al. 2005), displays an enhanced Em.max with red shift at 482 nm and unchanged Ex. max at 385 nm occurring β–sheet binding (LeVine 1993). Its binding and fluorescence are less sensitive to pH (LeVine 1993). Thus ThS is more suitable for staining inside the endocytic vesicles or under acidic conditions.

Additionally, in the praxis, I observed that ThS seems to be better at passing through the membranes without accumulating on the membrane and binding selectively to Aβ aggregate with high affinity, but not to Aβ monomers.

Based on their different binding characteristics, ThT was used for the aggregation assay in vitro and ThS for the microscopy of cultured cells in the present study.

1.12 MTT assay

3–(4,5–Dimethylthiazol–2–yl)–2,5–diphenyltetrazolium bromide (MTT) is a tetrazolium dye. MTT is reduced from a yellow tetrazole to purple formazan by NAD(P)H–dependent oxidoreductase enzymes (Berridge et al. 2005; Mosmann 1983). Therefore, the MTT assay is broadly used to measure the activity of cellular metabolism, cytotoxicity, cell viability and cytostatic activity (Mosmann 1983). The most part of NAD(P)H metabolismdepends on oxidoreductase enzymes, so that the reduction of MTT is an adequate marker of the cellular metabolic activity due to NAD(P)H flux (Berridge & Tan 1993; Berridge et al. 2005). The insoluble purple formazan product can be dissolved by adding a solubilization solution, and then the absorbance of the colored solution can be measured at 500–600 nm wavelengths by a spectrophotometer (**Figure 1–15**).

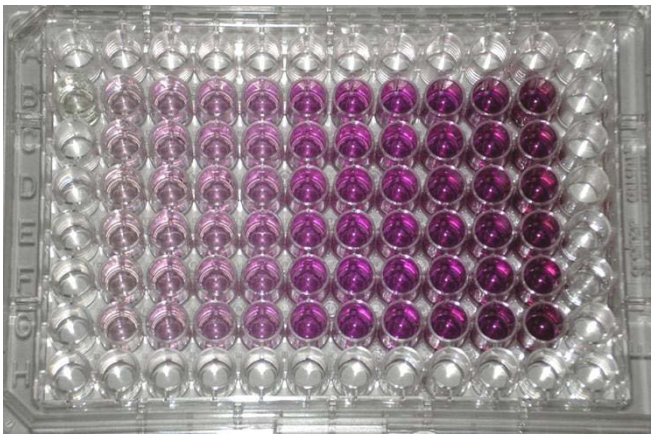

Figure 1–15: A microtiter plate after an MTT assay. Increasing amounts of cells resulted in increased purple colouring. Figure adapted from *http://en.wikipedia.org/wiki/MTT_assay*.

1.13 Förster resonance energy transfer

Fluorescence involves the absorption of light energy by a fluorophore molecule and emission of that energy at a longer (lower energy) wavelength (Remedios 2001). Förster resonance energy transfer (FRET) is a physical process by which energy is transferred nonradiatively from an excited molecular fluorophore (the donor) to another fluorophore (the acceptor) by means of intermolecular long–range dipole–dipole coupling (Förster 1948).

FRET becomes a powerful and sensitive tool, to visualize spatial distribution of single molecule in vitro and inside the cells (Swift & Trinkle–Mulcahy 2004) and to investigate the proximity of two molecules as well as related biological phenomena (dos Remedios et al., 1987).

Besides the fluorescence emission, there are many other competing pathways can decrease the energy level of an excited fluorophore, FRET is one of them. Their rate constants include (Remedios 2001):

- the fundamental photon emissive rate (K_F) of fluorescence;
- the rate of loss as heat by internal conversion (K_{IC});
- the rate of transfer to a quencher (K_Q);
- the rate of photodestruction or photobleaching (K_{PB});
- the rate of triplet state formation through intersystem crossing (K_{ISC});
- the rate of resonance energy transfer (K_{FRET}).

Donor fluorescence lifetime (τ) is therefore given by:

$$\frac{1}{\tau} = \kappa_{FRET} + \kappa_{OP} \qquad [3]$$

where K_{OP} is the rate constant for all other processes (Remedios 2001). From this relationship, an increase in K_{FRET} will decrease the donor lifetime (τ) (Remedios 2001). K_{OP} describe the total energy loss occurred a parallel processes beside the resonance energy transfer that should be considered and introduced into the calculation of the donor fluorescence lifetime (Remedios 2001). Only under very ideal circumstances, the acceptor of a donor–acceptor pair can gain all the energy loss of the donor (Remedios 2001).

The relationship between vibrational energy states, the fluorescent state and resonance energy transfer can be demonstrated in the Jablonski diagram (**Figure 1–16**) (Lakowicz 2006; Remedios 2001).

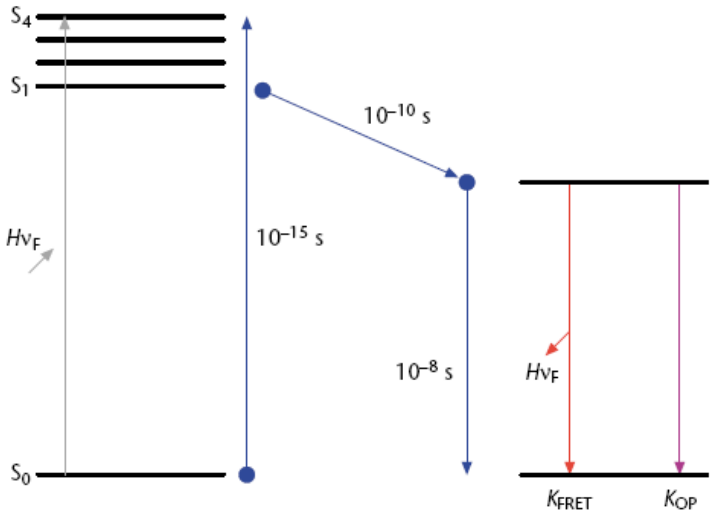

Figure 1–16: **Modified Jablonski diagram indicating the donor energy levels at ground state (S0) and in the excited state (S1–4).** A radiationless transfer of energy from the donor to an acceptor will reduce the intensity of the donor fluorescence. K_{FRET}: Rate of resonance energy transfer; K_{OP}: rate constant. Diagram adapted from Remedios (Remedios 2001).

The Förster equation defines the essential elements needed to calculate donor–acceptor distance R:

$$E = \frac{1}{\left(1 + \frac{R^6}{R_0^6}\right)} \qquad [4]$$

$$R_0^6 = 8.79 \times 10^{23} \kappa^2 n^{-4} \Phi_d J_{da} \qquad [5]$$

FRET is a physically energy transfer process, which depends on distances between donor and acceptor molecules. A typically theoretically distances for highly efficient FRET is within the Förster radius, which is defined as the distance at which half the excitation energy of the donor is transferred to the acceptor (typically 3–6 nm), and measures approximately 10–100 Å (Sekar & Periasamy 2003).

2 Aim of the thesis

One of the pathological hallmarks of Alzheimer's disease (AD) is deposits of the protein fragment β–amyloid in the form extracellular plaques (George G. Glenner & Wong 1984). Amyloid–beta peptides (Aβ) between 38–43 amino acids in length are formed by proteolytic cleavage of a membrane protein, the amyloid precursor protein (APP). Aβ is released as a monomer and tends to form aggregates spontaneously. The oligomeric species of $A\beta_{1-42}$ are tightly linked to AD pathogenesis and are presumed to be the cause of neuronal damage(Walsh et al. 2002). Many studies have suggested that the reuptake of extracellular $A\beta_{1-42}$ and subsequent formation of intracellular aggregates might be one pathway that leads to neuronal damage and neurotoxicity (Friedrich et al. 2010; Hu et al. 2009). However, questions remain as to where aggregates form, how the state of aggregation of $A\beta_{1-42}$ relates to its internalization, and why oligomeric species are far more toxic than monomers and large fibrils. Clearly the aggregation and internalization of $A\beta_{1-42}$ and the connections between these processes may be vital in understanding the ultimate toxic effects of this peptide.

My thesis project aims to understand the structural and mechanistic details of $A\beta_{1-42}$ internalization. We examined the relationship between the aggregation state of extracellular $A\beta_{1-42}$ and the efficiency of its internalization, to determine whether the formation of aggregates is a prerequisite to or the consequence of its neuronal uptake; used fluorescently labeled $A\beta_{1-42}$ to visualize the aggregation state of peptides and track their neuronal uptake in a human neuroblastoma (SH–EP) cell model.

The second aim of my thesis is to characterize Aβ – membrane interaction in detail. One of the key reactions in these processes is the binding and aggregation of $A\beta_{1-42}$ on the plasma membrane. Therefore, we observed interactions of $A\beta_{1-42}$ with lipid bilayers by using different types of giant unilamellar vesicles (GUVs) as simplified model system and the giant plasma membrane vesicles (GPMVs) isolating from the plasma membrane of neuroblastoma cells by confocal microscopy. By using two species of $A\beta_{1-42}$ monomers that were each labeled with a different fluorophore, we could track Aβ self–association by Förster resonance energy transfer (FRET).

3 Materials and methods

3.1 Materials

Cells	
Primary hippocampal neuron	AG Jochen Meier, MDC–Berlin, Germany
SH–EP cells line	R. König, F Westermann and M. Schwab, German Cancer Research Center (DKFZ), Heidelberg, Germany.

Peptides	
Amyloid beta 1–40 peptide	R. Volkmer, Institute for Medical Immunology, Charité, Berlin, Germany.
Amyloid beta 1–42 peptide	
Amyloid beta 1–42 peptide with a single N–terminal cysteine residue	
Scrambled– Amyloid beta 1–42	Millipore, AG916

Lipids	
Dioleoyl–phosphatidylserine (DOPS)	Avanti Polar Lipids Inc., 840035
1,2–dioleoyl–*sn*–glycero–3–phosphocholine (DOPC)	Avanti Polar Lipids Inc., 850375
1–palmitoyl–2–[6–[(7–nitro–2–1,3–benzoxadiazol–4–yl)amino]hexanoyl]–sn–glycero–3–phosphocholine (C6–NBD–PC)	Avanti Polar Lipids Inc., 810130
1,2–dioleoyl–*sn*–glycero–3–phosphoethanolamine (DOPE)	Avanti Polar Lipids Inc., 850725
N–stearoyl–D–*erythro*–sphingosylphosphorylcholine (SSM)	Avanti Polar Lipids Inc., 860586
Cholesterol	Sigma–Aldrich, C8667

Antibodies	
Anti–58K Golgi protein antibody	Abcam, ab27043
Anti–caveolin–1 antibody	Santa Cruz, sc–894
Anti–clathrin heavy chain antibody	Abcam, ab21679
Anti–EEA1 (C45B10) antibody	Cell Signaling, 3288
Anti–LAMP2 antibody	Abcam, ab13524
Anti–mouse IgG Peroxidase antibody	Sigma–Aldrich, A9044
Anti–β–amyloid mouse monoclonal antibody 6E10	Covance, SIG–39320

Fluorescent labels

Cell Stain	
Hoechst 33342	Invitrogen, 639181

Dyes	
Calcein	Sigma–Aldrich, C0875
ChemiGlow	Alpha Innotech Corporation
Merocyanine 540	Sigma–Aldrich, 323756
Thioflavin S	Sigma–Aldrich, T1892
Thioflavin T	Merck, 49005

Protein Conjugates	
Transferrin From Human Serum, Alexa Fluor® 488 Conjugate	Invitrogen, T–13342
Transferrin From Human Serum, Alexa Fluor® 647 Conjugate	Invitrogen, T–23366
Anti–mouse lgG antibody, cy5	Abcam, ab6563
Anti–rabbit lgG antibody, cy5	Abcam, ab6564

Reactive Fluorophores	
Alexa Fluor 488 C5 maleimide	Life Technologies, A–10254
Alexa Fluor 488 NHS Ester	Life Technologies, A–20000
Alexa Fluor 633 C5 maleimide	Life Technologies, A–20234
Alexa Fluor 633 NHS Ester	Life Technologies, A–20005
Alexa Fluor 647 C2 maleimide	Life Technologies, A–20347
Atto 488 maleimide	Atto tec, AD 488–41
Atto 565 maleimide	Atto tec, AD 565–41
Atto 633 maleimide	Atto tec, AD 633–41
Atto–488 NHS–Ester	Atto tec, AD 488–31
Atto–565 NHS–Ester	Atto tec, AD 565–31
Atto–633 NHS–Ester	Atto tec, AD 633–31
Cy5 maleimide	GE, PA15131

Chemicals and kits

1,1,1,3,3,3–hexafluoro–2–propanol (HFIP)	Fluka, 1441290V
Bovine serum albumin (BSA)	Sigma, A8531
Dimethyl sulfoxide (DMSO)	Sigma, 078K06961
Dithiothreitol	Sigma, D0632
Dulbecco's Modified Eagle Medium (DMEM)	ThermoFisher, 11880–028
Ethanol	Roth, 5054.4
Fetal Bovine Serum (FBS)	Invitrogen, 10099133
Formaldehyde solution	Sigma, F8775
Glucose	Sigma, G8270
L–Glutamine	Invitrogen, 25030
Penicillin–Streptomycin, Liquid, 10000 units / ml of Pen, 10000 µg / ml of Strep	ThermoFisher, 015140
Tris(2–carboxyethyl)phosphine hydrochloride (TCEP)	Sigma, 75259–1G
Trypsin 0.05 %/EDTA 0.02 % in PBS without Ca2+ and Mg2+	Pan–biotech, P10–023100
Tween–20	Serva, 100260
CellTiter 96® Non–Radioactive Cell Proliferation Assay [3–(4,5–dimethylthiazol–2–yl)–2,5–diphenyltetrazolium bromide (MTT) assay]	Promega Corporation, G4000

Instruments

96–well black tissue culture treated	BD Falcon, 353219
Cell culture dish 35mm, poly–lysine–coated glass bottom	MatTek Corporation, P35GC–1.5–14–C
Cell culture flask	BD Falcon
FESP cantilevers for AFM, 75 kHz	Bruker, A079/19
Gel filtration, Superdex 75 PC 3.2/30	GE, 17–0771–01
Membrane filter, 0.22 µm	Millipore, UFC30GV00
Membrane filter, 200 nm polycarbonate	Nuclepore, Whatman Schleicher & Schuell
Membrane filter, 30 kD	Millipore, UFC503024
Mica	Ted Pella

Atomic Force Microscopy, Nano wizard II	JPK, Berlin
CD spectrometer, Model J–720	Jasco
Centrifuge	Eppendorf
Gel Filtration, SMART System	GE
Image reader LAS–3000	Fujifilm
Lyophyllization	Savant Speed Vac
NanoDrop 8000 Photometer	Peqlab,
Plate reader, Infinit E M200	Tecan, Austria
Sonication (water bath)	Bandelin Sonorex TK 52
Thermomixer shaker	Eppendorf

Confocal microscope, FV–1000MPE	Olympus
Confocal microscope, Olympus IX83 microscope with Yokogawa CSU–W1 Confocal Spinning Disc unit	Olympus
Confocal microscope TSC SP2 & SP5, with Leica HyD hybrid detector for SP5	Leica
Evolve 512 EMCCD Camera for Spinning Disc	Photometrics
Fluorescence microscopy, automated, ArrayScan VTI HCS Reader (Cellomics)	Thermo Scientific

Mediums and buffers

Blocking buffer	3 % (w/v) BSA in PBS
Cell culture medium	DMEM, 10 % (v/v) fetal bovine serum, 4 mM L–Glutamine, 110 mg/L sodium pyruvate, 100 units/ml penicillin, 100 units/ml streptomycin, 4.5 g/L D–glucose
Dulbecco's phosphate–buffered (PBS)	ThermoFisher, Gibco, 14190. 200 mg/L KCl, 200 mg/L KH_2PO_4, 8 g/L NaCl, 2.16 g/L Na2HPO_4–7H_2O
Freezing medium	10 % DMSO, 90 % fetal bovine serum
Glucose buffer / GUVs microscopy buffer	280 mM glucose, 5.8 mM NaH2PO4, 5.8 mM Na2HPO4, osmolality 300 mOsm/kg, pH 7.2
GPMV buffer / vesiculation chemicals	10 mM hepes, 150 mM NaCl, 2 mM $CaCl_2$, pH 7.4
Sucrose buffer	250 mM sucrose, 15 mM NaN_3, Osmolarity 280 mOsm/kg, pH 7.2

3.2 Methods

3.2.1 Preparation and fluorescent labeling of Amyloid beta peptide

3.2.1.1 Aβ peptide peptide stock solutions

Synthetic human Amyloid beta 1–40 peptide ($A\beta_{1-40}$), Amyloid beta 1–42 peptide ($A\beta_{1-42}$) and $A\beta_{1-42}$ with a single N–terminal cysteine residue (Institute for Medical Immunology, Charité, Berlin, Germany) were dissolved in hexafluoro–2–propanol (HFIP) to a final concentration of 5 mg/ml, were sonicated in a water bath for 15 min, and were incubated at room temperature (RT) overnight. Aliquots of 100 µl were flash frozen by liquid nitrogen, HFIP was removed by lyophilization (Savant SpeedVac, Thermo), and the aliquots of peptides were stored at –20 °C until use.

3.2.1.2 Monomerization of unlabeled Aβ peptide

To prepare unlabeled monomer, lyophilized $A\beta_{1-42}$ was dissolved in 10 mM Sodium hydroxide (NaOH, pH 12), sonicated for 30 min in ice–cold water bath, passed through a 0.22 µm and a 30 kD filter (Millipore). The monomers was kept on ice and used immediately or within 1 h.

The concentration of labeled $A\beta_{1-42}$ monomers were calculated by Beer–Lambert law at 280 nm using an extinction coefficient of 1280 $M^{-1}cm^{-1}$.

3.2.1.3 Fluorescence labeling and purification

The fluorescent dyes were dissolved in dimethyl sulfoxide (DMSO) of 10 mg/ ml, and stored at –20 °C until use.

$A\beta_{1-42}$ (200 µM) with a single N–terminal cysteine residue was labeled by Atto 488 maleimide ($A\beta_{1-42}^{488}$), Atto 565 maleimide ($A\beta_{1-42}^{565}$) or Atto 633 maleimide ($A\beta_{1-42}^{633}$, Atto–tec) at a 1:1.5 molar ratio in NaOH (10 mM, pH 12) containing 0.05 mM tris(2–carboxyethyl)phosphine hydrochloride (TCEP). The mixture has pH at 7.5, and would be incubated at 4 °C overnight.

$A\beta_{1-42}^{565}$ and free Atto565 maleimide were separated by size–exclusion chromatography (SEC, SMART gel filtration system, GE) using Superdex 75 PC 3.2/30 column (GE). Superdex 75 PC 3.2/30, a prepacked Precision Column (2.4 ml), has a separation range for molecules with molecular weights between 3 000 and 70 000 and pH stability working range of 3–12. Sample of 50 µl was loaded, run in 10 mM NaOH buffer (pH 12) with a flow rate at 40 µl/min at RT. The eluents were collected in 100 µl fraction, were examined by ultraviolet (UV)

absorption to determine the concentration of eluted Aβ, protein at 214 nm and 280 nm, Atto 488 at 488 nm, Atto 565 at 565 nm and Atto 633 at 600 nm.

For the preparation of Atto 565 labeled scrambled–$A\beta_{1-42}$ (sc–$A\beta_{1-42}$[565], Millipore), sc–$A\beta_{1-42}$ was dissolved in 10 mM NaOH and labeled with Atto 565–NHS. The labeling process and the separation of sc–$A\beta_{1-42}$[565] and free dyes were the same as described above.

Degree of labeling was determined from absorption at 280 nm and at the excitation maximum of the fluorophores, and correcting for absorbance of the fluorophores at 280 nm,

$$DOL = \frac{A_{\max} / \varepsilon_{\max}}{A_{prot} / \varepsilon_{prot}} = \frac{A_{\max} / \varepsilon_{prot}}{(A_{280} - \mathrm{A}_{\max} \times \mathrm{CF}_{280}) / \varepsilon_{\max}} \qquad [6]$$

where A is absorption; ε_{max} is the extinction coefficient at absorption maximum of fluorescent dye; ε_{prot} is the extinction coefficient at λmax of labeled protein; CF_{280} is correction factor, which is given by the product description.

The concentrations of labeled $A\beta_{1-42}$ monomers and protofibrils were calculated through area ratio of SEC at 565 nm by integration.

3.2.2 Preparation and labeling of lipid membrane vesicles

3.2.2.1 Preparation of large unilamellar vesicles (LUVs)

Large unilamellar vesicles (LUVs) were preparted from multilamellar vesicles (MLVs). To develop the MLVs, lipids were dissolved in chloroform with or without 1 mol% of the fluorescent lipid analogue, and were dried under nitrogen in a glass tube to form a thin lipid film. The lipid film was dissolved in 1 ml PBS to a final lipid concentration of 1 mM, and was vortexed well to generate MLVs. Following five freeze–thaw cycles, MLVs were extruded ten times through a 200 nm polycarbonate membrane filter (Nuclepore, Whatman Schleicher & Schuell, Dassel, Germany). Large unilamellar vesicles (LUVs) were stored at 4°C and used within one week after preparation.

3.2.2.2 Preparation of giant unilamellar vesicles (GUVs)

Giant unilamellar vesicles (GUVs) were prepared using the electroformation method as described by Stöckl et al (Stöckl et al. 2010). In brief, lipids with or without 1 % of lipid analogue were dissolved in 50 µl chloroform to a total lipid concentration of 100 nM. The titanium chambers (**Figure 3–1**) were preheated to 50 – 60°C by hotplate. Lipid solution was spotted onto two slides. The slides were further heated on the hotplate to evaporate the chloroform, and to keep a homogenous distributed lipid films on the slides. Chambers were

assembled with parafilm (**Figure 3–1**), and were placed under vacuum (< 10 mbar) for 1 h, to remove the rest of the chloroform. Lipid coated titanium chambers were filled with 1 ml sucrose buffer (osmolality of 280 mOsm/kg), were supplied an alternating electric field of 10 Hz rising from 0.02 – 1.1 V in the first 48 min and hold for 3 h, then increased the voltage of 1.3 V frequency of 4 Hz for 30 min to detach GUVs. GUVs were stored at RT, were used within one week.

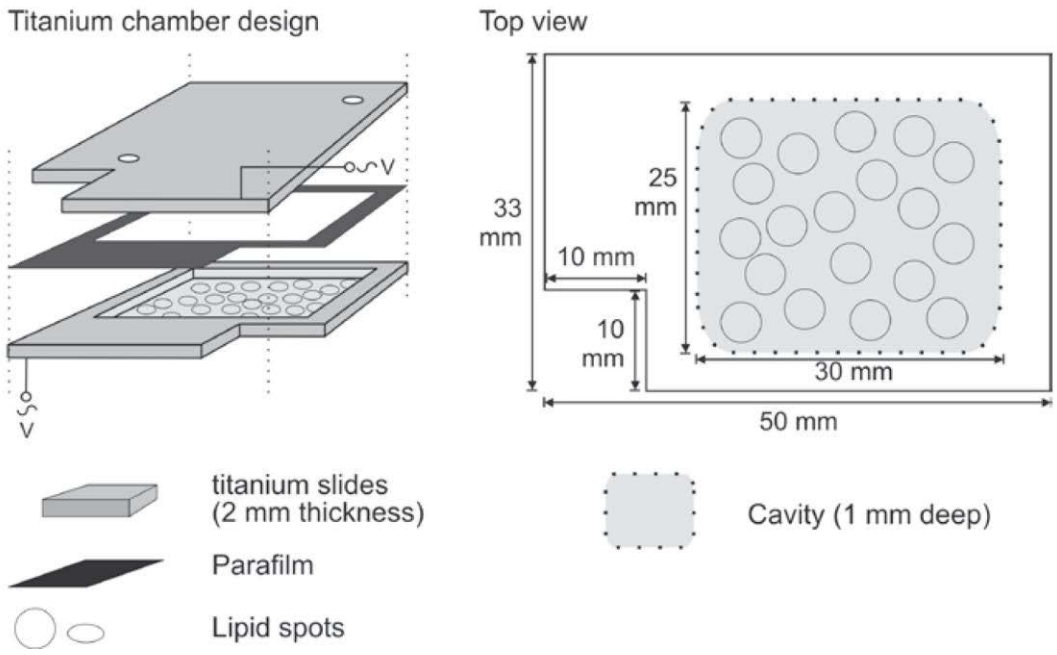

Figure 3–1: Schema of titanium chamber slides for giant unilamellar vesicles preparation. Figure adapted from Stöckl et al. (Stöckl et al. 2010).

3.2.2.3 Preparation of giant plasma membrane vesicles (GPMVs)

Cell–free giant plasma membrane vesicles (GPMVs) formation and isolation followed a procedure modified from the protocol by Sezgin *et al* (**Figure 3–2a)** (E Sezgin et al. 2012). SH–EP cells were grown in a 75–cm^2 cell culture flask to 90 – 100% confluency. Cells were washed twice with GPMV buffer (10 mM Hepes; 0.15 M NaCl; 2 mM $CaCl_2$; pH 7.4), and then added 1.5 ml of GPMV buffer containing vesiculation agents (25 mM Paraformaldehyde (PFA); 2 mM Dithiothreitol (DTT)). The cells were then incubated at 37°C for 1 h. The GPMVs rich supernatant was removed from 75–cm^2 cell culture flask into an Eppendorf tube, and was stored at 4 °C for 2 h to concentrate the GPMVs via gravity. If necessary, GPMVs could be labeled by fluorescent dye. GPMVs were incubated with fluorescent dye, such as merocyanine 540 (0.02 mg/ml), at 4°C for 1h, before they were imaged by microscopy (**Figure 3–2** b). GPMVs were stored at 4 °C and were measured within two days.

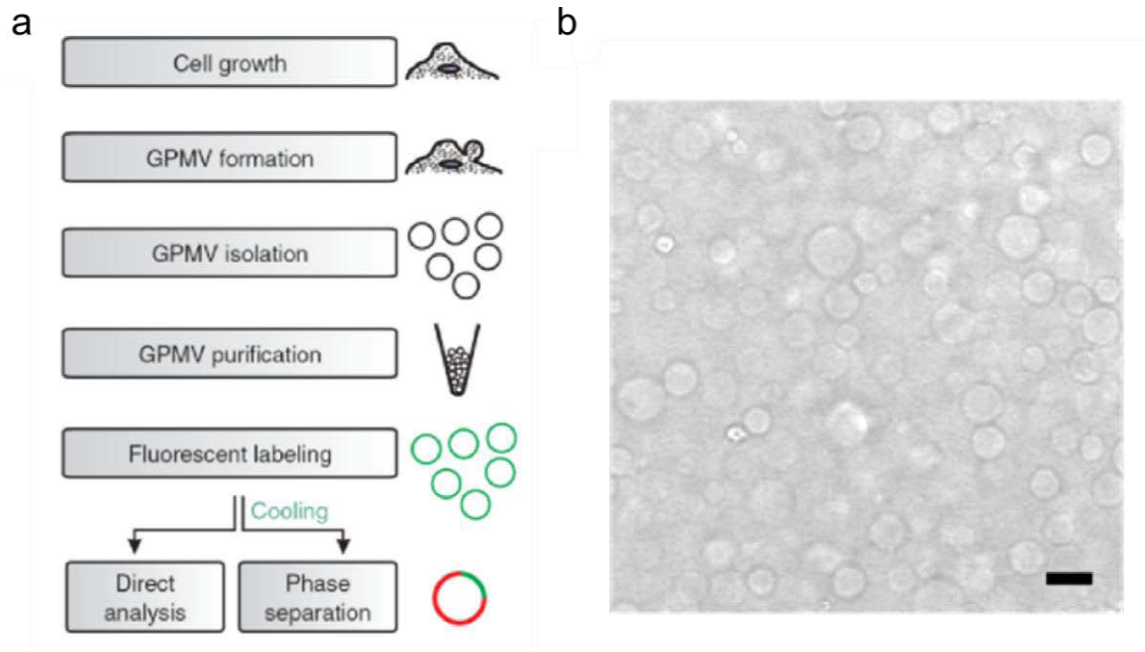

Figure 3–2: Preparation of giant plasma membrane vesicles (GPMVs) (a) Flow of isolation of GPMVs from the cells. GPMVs form and separate from the plasma membrane after incubating the cells with vesiculation chemicals. Isolated GPMVs can be then labeled: green circles represent fluorescently labeled vesicles; red and green areas represent phase–separated GPMVs. Figure adapted from Sezgin et al. (Sezgin, Kaiser, et al. 2012). **(b)** DIC image of our GPMVs harvesting, were recorded by confocal microscopy. Scale bar 10 µm.

3.2.3 Monitor aggregation kinetics of $A\beta_{1-42}$ by thioflavin T

$A\beta_{1-42}$ monomer aggregation assay was performed in PBS containing 20 µM thioflavin T (ThT) in a plate reader (Infinit E M200, Tecan) at 25°C or 37 °C. ThT fluorescence (excitation wavelength of 440 nm and emission wavelength of 485 nm) was measured through the bottom of the 96–well plate every 5 min after 5 s shaking. Every experiment was carried out in separated 3 wells of each concentration. The results are presented as mean values.

3.2.4 Circular dichroism spectroscopy

$A\beta_{1-42}$ samples of 15 µM in PBS were measured in a 1–mm path length cuvette. Circular dichroism (CD) spectra were recorded between 200 – 260 nm with a step size of 1 nm by using a CD spectrometer (Model J–720, Jasco).

3.2.5 Atomic Force Microscopy

Mica was glued on a glass slide with superglue. The surface layer of mica was removed by adhesive tape. Samples of 10 µl were loaded onto the freshly cleaved mica disk for 5 min, washed three times with freshly filtered deionized water (3 x 100 µl) and dried overnight. All the images were taken using intermittent contact mode on a Nanowizard II/Zeiss Axiovert setup (JPK) and FESP tips (Bruker).

3.2.6 Cell culture

SH–EP (German Cancer Research Center, Heidelberg) cells were maintained in culture medium in 75 cm^2 cell culture flasks at 37 °C and 5% CO_2. Before monolayers reached 80 – 90 % confluency, the cells were subcultured: washed twice with PBS; incubated with 1 ml trypsin solution at 37 °C for 5 min; added 9 ml culture medium to stop the trypsinization; and ca. 10^5 cells were seeded into a new 75 cm^2 cell culture flasks. For the different experiments, cells were seeded into 96–well plates or 35 mm cell culture dishes.

For storage, the cells were detached from culture flask, were pelleted for 3 min at 2500 g, were resuspended in freezing medium, kept at –80 °C for 1 d and stored in liquid nitrogen.

For thawing cells, cryotube of frozen cells from liquid nitrogen were incubated in water bath at 37 °C. The cells suspension (1 ml) were added into 5 ml culture medium, were pelleted for 1 min at 2500 g, were resuspended in culture medium, were transferred into a cell culture flask, and were incubated in the incubator (37 °C, 5% CO_2)as usual.

Primary hippocampal neurons from rat embryos were a gift of J. Meier, MDC Berlin and were prepared and cultured as previously described (Winkelmann et al. 2015).

3.2.7 Cellular uptake of $A\beta_{1-42}$

The cells were cultured in 96–well black tissue culture treated plates (BD Falcon) or 35 mm poly–lysine–coated glass bottom dishes (MatTek Corporation) to reach ca. 80% confluency. After washing twice with PBS (100 µl / well for 96–well plate or 1.5 ml for dish), the cells were treated by $A\beta_{1-42}$ or labeled $A\beta_{1-42}$ at various concentrations, temperatures and times, as indicated in each experiment. The cells were then washed twice with PBS, were further incubated in culture medium for live cell imaging, or were fixed with 3.7% PFA in PBS for 10 min. The fixed cells were incubated in PBS for microscopy.

3.2.8 MTT assay

The cells were cultured in 96–well plates, grown up to about 80% confluency and treated with different aggregates species of Aβ at various concentrations as indicated in each experiment. Each experiment was carried out in 2 separate 96–well plates. One plate was prepared for determination of cell number by high–content screening (HCS) microscopic. The second plate was used for 3–(4,5–dimethylthiazol–2–yl)–2,5–diphenyltetrazolium bromide (MTT) assay (Promega Cell Proliferation Assay kit). Each concentration of Aβ was repeated in 12 separate wells per plate. After treatment with Aβ, the cells were washed twice with PBS, were incubated with 15 µl MTT solution (12 mM) in 100 µl fresh culture medium per well at 37 °C for 4 h. The reaction was stopped by adding solubilization solution (100 µl / well, Bio-Rad). The cells were further incubated at 37 °C for 2 h. The absorbance of MTT was recorded at 570 nm by using a plate reader.

3.2.9 Thioflavin S staining

Thioflavin S (ThS) was dissolved in 50% ethanol to 1 mg/ml, was stored at 4°C.

Fixed or live cells were washed twice with PBS, were incubated with Thioflavin S (ThS) of 10 µg / ml in PBS or cell culture medium, at RT or living cells required temperatures, 4°C or 37°C, for 10 min. After that the cells were washed with PBS 2–5 times, were incubated in PBS for fixed cells or in cell culture medium for live cells until microscopy.

3.2.10 Secondary immunofluorescence staining (IF)

To examine if the dye fluorescence of $A\beta_{1-42}{}^{565}$ accurately reports the formation of intracellular $A\beta_{1-42}$ aggregates and their cellular locations, the cells were costained with anti–β–amyloid mouse monoclonal antibody (6E10, Covance) or endocytic markersby immunofluorescence staining after treatment with $A\beta_{1-42}{}^{565}$ aggregate.

The fixed cells were permeabilized with 0.5 % Triton X–100 at RT for 5 min, washed twice with PBS. Then cells were incubated with blocking buffer (3 % BSA in PBS) at RT for 1 h, then with primary and secondary antibody in blocking buffer in the dark at RT for 1 h, respectively. The cells were washed with PBS twice between each step. Cell nuclei were stained with Hoechst 33342 or DAPI. The dishes were stored in the dark until being viewed by using a confocal microscopy.

The primary antibodies and their dilutions used for presented project are listed in **Table 3–1**. Cy5–labeled anti–mouse and –rabbit antibodies were used as secondary antibodies, were diluted at 1:2000 in blocking buffer.

Table 3–1: Primary antibodies for IF.

	Antibodies	Working dilution
Aβ	Anti–β–amyloid mouse monoclonal antibody 6E10	1:1000
Caveolin marker	Anti–caveolin–1 antibody	1:500
Clatherin	Anti–clathrin heavy chain antibody	1:500
Early endosome marker	Anti–EEA1 (C45B10) antibody	1:500
Golgi marker	Anti–58K Golgi protein antibody	1:1000
Lysosome marker, LAMP2	Anti–LAMP2 antibody	1:500

3.2.11 Fluorescence microscopy

3.2.11.1 Confocal microscopy

All confocal microscopic experiments were performed in 35 mm culture dishes. The images were recorded by confocal laser scanning microscopy (Leica TSC SP2 and SP5, SP5 with Leica HyD hybrid detector; Olympus FV–1000MPE) with 60x or 63x/ 1.4–0.6 oil–immersion objective, 40x/1.35 or 60x/1.2 water immersion objective, or spinning disc confocal microscopy (Olympus IX83 microscope with Yokogawa CSU–W1 Confocal Spinning Disc unit and Evolve 512 EMCCD Camera) with 60x/1.2 water objective. The climate chamber for microscopy was set to 25 °C for fixed cells and 37 °C for living cells. Confocal fluorescence images were obtained by sequential excitation, if more than two fluorophores were monitored. Wavelength settings are given as **Table 3–2**. Additionally, differential interference contrast (DIC) pictures were recorded simultaneously in each case.

The visualization of GUVs was followed by the protocol by Stöckl *et al* (Stöckl et al. 2010). GUVs, Aβ and microscopy buffer were mixed at a ratio of 1:1:1 and at final osmolarity of 250 mOsm/kg.

Table 3–2: Wavelength settings.

Fluorophores	Excitation / nm	Emission / nm or filters
Alexa488	488	490 – 540
Alexa647	633 or 640	650 – 700; ET 700/75 nm
Atto488	488	500 – 550; ET 525/50 nm
Atto565	543 or 561	550 or 580 – 610; ET600/50 nm
Atto633	633 or 640	650 – 700; ET 700/75 nm
Calcein	488	490 – 540; ET470/25 nm
Cy5	633 or 640	650 – 700
DAPI	405	440 – 470
Hoechst 33342	405	440 – 470; ET460/50 nm
Merocyanine 540	543	560 – 600; U–MWG2
NBD	488	500 – 550
Thioflavin S	405	420 – 470; ET460/50 nm

3.2.11.2 Live cell microscopy

Experiments of live cell imaging were performed in 35 mm dishes by using confocal / spinning disc confocal microscopy. The temperature of incubation chamber on microscope was set on 37°C, and 5% CO_2 was filled into the incubation chamber.

3.2.11.3 High–content screening and analysis

For HCS microscopy experiments, the cells were cultured in 96–well plates. The fixed cells were incubated with Hoechst 33342 (1 µg/ml in PBS) at RT for 10 min to visualize the nuclei.

The images were acquired automatically on ArrayScan VTI HCS Reader (Thermo Scientific) with a 10x objective. Autofocus was set on Hoechst 33342 channel. For the compartmental analysis, ArrayScan VTI software was used to identify nuclei by Hoechst 33342 fluorescence, to fit cell dimensions and to identify $A\beta_{1–42}$ aggregates through Atto 565 fluorescence. Nine images were recorded per well for each channel. Readout measurements included nuclear number area and intensity; aggregates intensity, number and size; and sizes of the cells. Total intensity of spots and mean intensity/count/area of spots per well were calculated from nine images, and were normalized to cell numbers.

Figure 3–3 shows one of the compartmental analysis, identified nuclei by Hoechst 33342 fluorescence (white) were used to fit cell dimensions, blue line of nuclei and red line of cell, and identify $A\beta_{1–42}$ aggregates by labeling fluorescence (yellow spot).

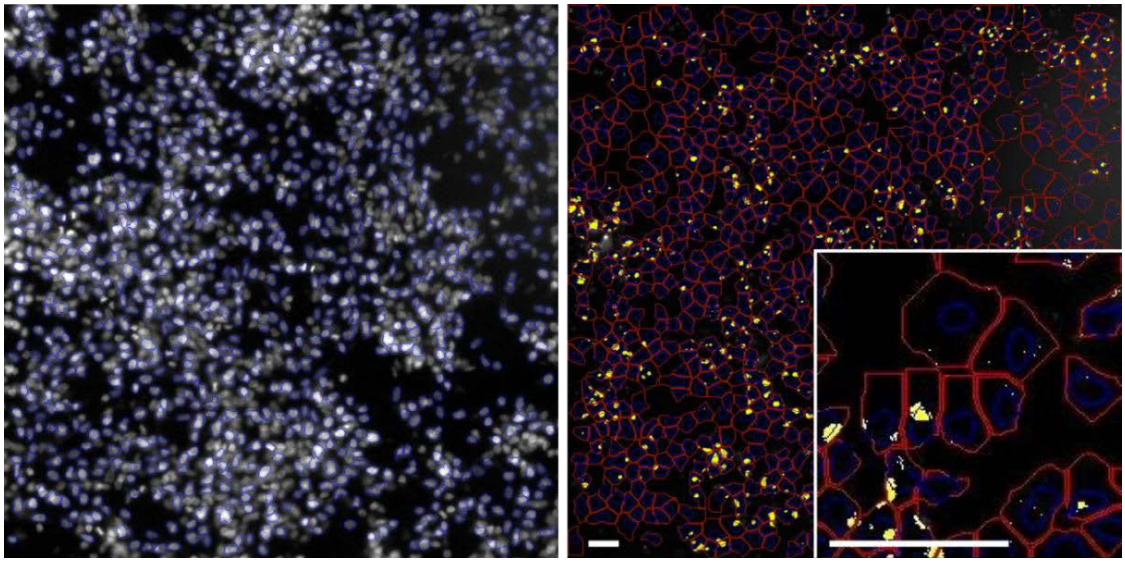

Figure 3–3: High–content screening (HCS) microscopic images of SH–EP cells with $A\beta_{1-42}^{565}$ aggregates. Left: cell nuclei were stained with Hoechst 33342 (white), identified by the image analysis software (blue contour lines). Right: the software identification of $A\beta_{1-42}$ aggregates (yellow), nuclei (blue contour lines) and the cell bodies (red contour lines). Scale bar 100 µm.

3.2.12 Förster resonance energy transfer (FRET)

Spectroscopy–Based Förster resonance energy transfer (FRET) measurement was performed in 96–well plate, was recorded through the bottom of the 96–well plate in a plate reader (Infinit E M200, Tecan) at 25°C.

The FRET efficiency is calculated by:

$$E = 1 - \frac{I_D^{'}}{I_D} \qquad [7]$$

where $I_D^{'}$ and I_D are the donor fluorescence intensities with and without acceptor, respectively.

The images for sensitized emission FRET analysis were recorded by confocal microscopy described as above. Corrected FRET images were calculated from FRET, donor, and acceptor pixel intensities using the Fiji distribution and the PixFRET plugin (Feige et al. 2005).

Briefly, for FRET analysis three group cells were prepared: sample contained only donor; sample contained only acceptor; sample contained donor and acceptor. Each sample was imaged with following settings: the first one excitation of the donor and detection of the

donor; the second one excitation of the acceptor and detection of the acceptor; the third one excitation of the donor and detection of the acceptor.

For the Atto 488 – Atto 633 FRET pair, the fluorescence was measured with excitation wavelengths of 488 nm for Atto 488 (donor only sample), 633 nm for Atto 633 (acceptor only sample) and 488 nm for $A\beta_{1-42}^{488}$ – to – $A\beta_{1-42}^{633}$ FRET (FRET sample), and emission wavelengths 500–600 nm (donor only sample), 650–800 nm (acceptor only sample) and 650–800 nm (FRET sample), respectively.

Bleed–Through (BT) values were calculated from the images of the donor or acceptor only sample by using Donor or Acceptor Model of PixFRET program. Intensity–independent donor and acceptor BT were determined by:

$$BT_{donor} = \frac{I_{FRET}}{I_{donor}} \quad [8]$$

$$BT_{acceptor} = \frac{I_{FRET}}{I_{acceptor}} \quad [9]$$

which were fitted with a linear model.

The corrected FRET intensity for each pixel is given by:

$$I_{FRET} = I^{0}_{FRET} - BT_{donor} \times I_{donor} - BT_{acceptor} \times I_{acceptor} \quad [10]$$

where I_{FRET} is the raw fluorescence intensity of the FRET channel, I_{donor} and $I_{acceptor}$ are the fluorescence intensities of the donor and accepto, respectively. I_{FRET} is normalized (nFRET) as a function of the square root of the product of donor and acceptor intensities:

$$nFRET = \frac{I_{FRET}}{\sqrt{I_{donor} \times I_{acceptor}}} \times 100 \quad [11]$$

3.2.13 Fluorescence recovery after photobleaching

Fluorescence recovery after photobleaching (FRAP) measurements were carried out on a Olympus microscope using the built–in setting for photobleaching. The experiments were performed in 35 mm dishes as described above.

For FRAP of calcein, laser intensity at 488 nm was increased until calcein fluorescence had been completely bleached. FRAP was then performed in the focus plane of GUV membrane area of about 7 µm × 1 µm. After the photobleaching, the microscope programm was switch back to normal setting for observing the recovery of fluorescence. The bleached area was then scanned continuously with low laser intensity in normal modus as usual.

4 Results

4.1 Membrane interaction of non–toxic $A\beta_{1-42}$ benefits the conversion of cytotoxic aggregate

One of the pathological hallmarks of Alzheimer's disease (AD) is the presence of extracellular plaques composed mainly of 42aa Amyloid beta peptide ($A\beta_{1-42}$) (George G. Glenner & Wong 1984). The small hydrophobic $A\beta_{1-42}$ peptide, which is generated by proteolytic cleavage of the amyloid precursor protein (APP), is released as a monomer from the plasma membrane into extracellular space, and tends to aggregate spontaneously into oligomeric, protofibrillar and fibrillar assemblies (Simons et al. 1998; Shoji et al. 1992; Jarrett et al. 1993). Oligomeric species of $A\beta_{1-42}$ are tightly linked to AD pathogenesis and are presumed to be the cause of neuronal damage (Walsh et al. 2002). Several studies have suggested that the reuptake of extracellular $A\beta_{1-42}$ into neurons may lead to the formation of intracellular aggregates, resulting in neuronal damage and neurotoxicity (Ida et al. 1996; Hu et al. 2009; Friedrich et al. 2010). Endocytosis of misfolded proteins has also been observed in cell models of the tau protein, α–synuclein and huntingtin (Frost et al. 2009; Brundin et al. 2010), and recent evidence suggests that it may be the initial step in the replication of the misfolded protein by prion mechanisms (Brundin et al. 2010; Sanders et al. 2014; Prusiner 1998; Bieschke et al. 2004; Frost & Diamond 2010). Several possible endocytotic pathways, such as macropinocytosis and receptor mediated endocytosis, have been discussed for Aβ and other misfolded protein aggregates (Yu et al. 2014; Lai & McLaurin 2010; Holmes et al. 2013; Treusch et al. 2011; Kanekiyo et al. 2013). However, our understanding of the connection between aggregation and cytotoxicity is still limited. It has not been conclusively determined how and when the $A\beta_{1-42}$ peptide becomes toxic, whether Aβ aggregates prior to internalization or during the internalization process and, if so, in which intracellular compartments the aggregates form. Elucidating the connection between aggregation and internalization of $A\beta_{1-42}$ peptide may be thus vital in understanding its toxicity.

Here, we examine the relationship between the aggregation state of extracellular $A\beta_{1-42}$ and the efficiency of its internalization. We aimed to determine whether the formation of aggregates and particularlyβ–sheet–rich structures , as reported by thioflavin dyes (LeVine 1993), is a prerequisite for its neuronal uptake.

4.1.1 Preparation and characterization of fluorescently labeled $A\beta_{1-42}$

In order to track the peptide and to observe aggregation of monomeric $A\beta_{1-42}$ in the cultured cells, fluorescently labeled $A\beta_{1-42}$ peptides were generated. $A\beta_{1-42}$ with a single N–terminal cysteine residue is linked thiol–reactive fluorophores (maleimide–activated derivative), such as Atto565–maleimide ($A\beta_{1-42}{}^{565}$), Alexa488–maleimide ($A\beta_{1-42}{}^{488}$), or Alexa633–maleimide ($A\beta_{1-42}{}^{633}$), via sulfhydryl–reactive crosslinking (as described in method section 3.2.1.3).

Labeled $A\beta_{1-42}$ and free dyes were separated by size exclusion chromatography (SEC). $A\beta_{1-42}$ eluted in two populations, which were identified as monomers (at 1.39 ml) and protofibrils (at 0.86 ml), respectively (**Figure 4–1** a). Unlabeled monomeric $A\beta_{1-42}$ and aggregation–incompetent labeled scrambled–$A\beta_{1-42}{}^{565}$ (sc–$A\beta_{1-42}{}^{565}$) were used as controls for the peak location of monomers on SEC. Unlabeled monomeric $A\beta_{1-42}{}^{565}$ was located from 1.3 ml to 1.5 ml and has a peak at 1.31 ml (**Figure 4–1** b);sc–$A\beta_{1-42}$ was from 1.3 ml to 1.5 ml, peak at 1.38 ml (**Figure 4–1** c), both of which eluted similar to $A\beta_{1-42}{}^{565}$ monomer fraction.

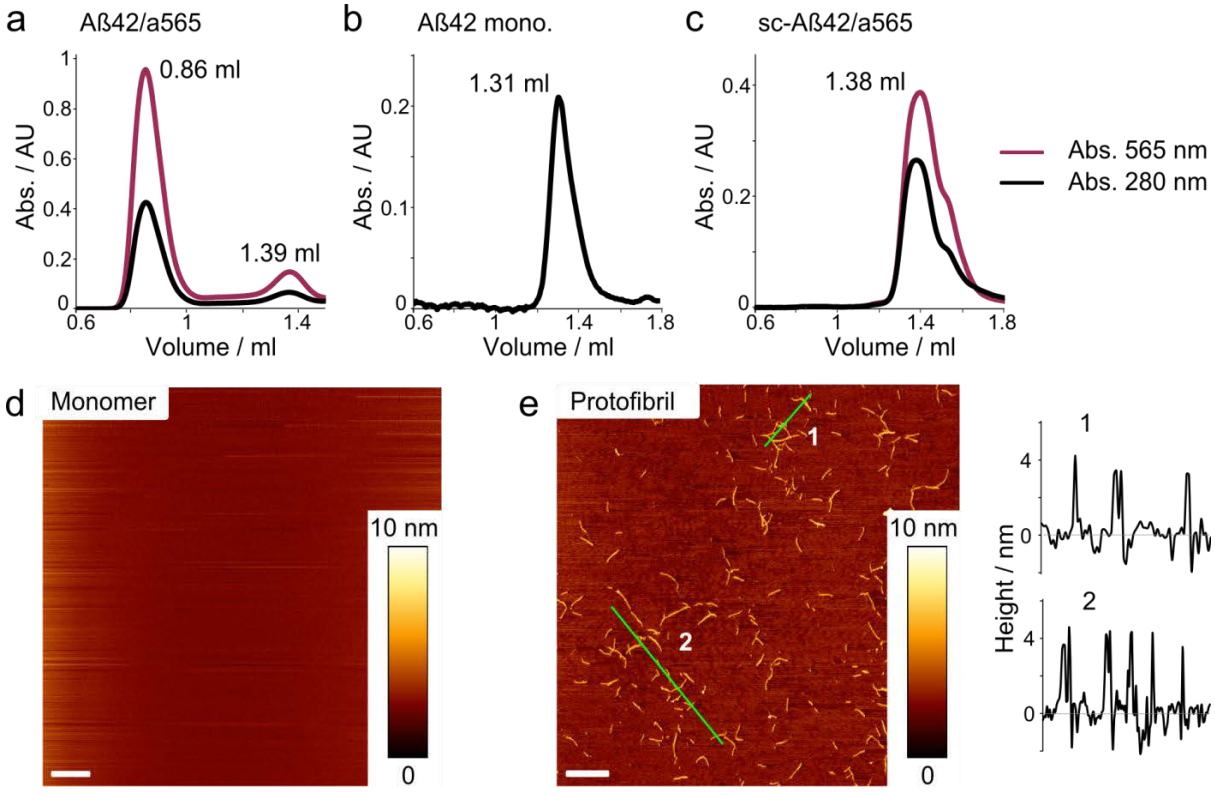

Figure 4–1: Separation of $A\beta_{1-42}$ by size–exclusion chromatography (SEC) and detection by atomic force microscopy (AFM). (a–c) Peptides and labels were detected by absorption at 280 nM and 565 nm, respectively. **(a)** Atto565 labeled $A\beta_{1-42}$ ($A\beta_{1-42}{}^{565}$) eluted in a two populations, protofibril at 0.86 ml and monomer at 1.39 ml. Unlabeled monomeric $A\beta_{1-42}$ **(b)** and Atto565 labeled scrambled–$A\beta_{1-42}$ (sc– $A\beta_{1-42}$, **c**), have very similar SEC elution profiles as $A\beta_{1-42}{}^{565}$ monomer. **(d)** No monomers or aggregates were detected by AFM in the $A\beta_{1-42}{}^{565}$ monomer fraction collected from SEC (1.39 ml). **(e)** $A\beta_{1-42}{}^{565}$ protofibrils with an average height of about 4 nm could be detected in the high molecular weight fraction of SEC (0.86 ml) by AFM. Scale bars, 1 µm.

Those monomers could not be detected by atomic force microscopy (AFM, **Figure 4–1** d). In contrast, AFM identified the PF fraction of $A\beta_{1-42}^{565}$ to be protofibrils, which had an average height in 4 nm (**Figure 4–1** e).

The concentration of labeled $A\beta_{1-42}$ monomers and protofibrils, i.e. the productions from SEC, were calculated through area ratio of SEC at 565 nm by integration. The concentrations of unlabeled $A\beta_{1-42}$ monomers were calculated by Beer–Lambert law at 280 nm.

When incubated with thioflavin T (ThT), the protofibrils (35 µM monomer equivalent) bound the dye immediately and ThT fluorescence changed little over the course of an hour, while ThT fluorescence of the monomeric Aβ (35 µM) displayed sigmoid kinetics typical of nucleated polymerization (**Figure 4–2**). To avoid the influence of label to ThT fluorescence, unlabeled protofibrils were used in this experiment. Those unlabeled protofibrils were prepared by following the same protocol as for labeled $A\beta_{1-42}$. When preparing unlabeled protofibrils, the same volume DMSO, in which the fluorophores were dissolved, was added but without fluorophores.

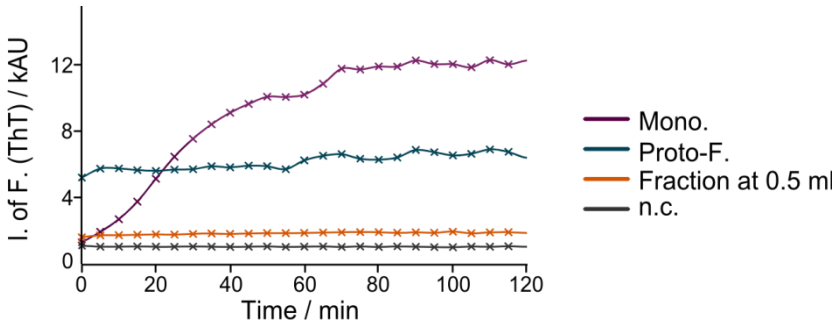

Figure 4–2: Thioflavin T (ThT) binding assay of $A\beta_{1-42}$ elutions from SEC. Unlabeled monomeric $A\beta_{1-42}$ (35 µM, Mono.), $A\beta_{1-42}$ protofibrils (35 µM monomer equivalent, Proto-F.) and an elution fraction at 0.5 ml on SEC (20 µl) were incubated in PBS in presence of ThT (20 µM). ThT fluorescence of monomers displayed typical sigmoid kinetics. Protofibrils bound ThT immediately and stayed constant in fluorescence.

To examine whether the fluorescence label influences $A\beta_{1-42}$ monomer aggregation kinetics, we compared fibril formation kinetics and fibril morphologies of labeled and unlabeled $A\beta_{1-42}$. Unlabeled monomeric $A\beta_{1-42}$ was mixed with 10% $A\beta_{1-42}^{565}$ (total $A\beta_{1-42}$ concentration of 15 µM) and incubated in PBS at 25 °C. Aggregation kinetics were monitored by binding of ThT *in vitro* (**Figure 4–3** a) (LeVine 1999). ThT aggregation curves were normalized to the maximum intensity of ThT fluorescence of plateaus. The addition of 10 % $A\beta_{1-42}^{565}$ monomer slowed the formation of the higher orderedβ–sheet–rich structures only slightly.

After 2 d further incubation, fibrils from both samples have twisted structures and in heights of about 5 nm, as observed by AFM (**Figure 4–3** b and c). However, the amount of small

globular aggregates in mixed sample (c c), which do not have fibril structures, is more than those in the sample of pure unlabeled $A\beta_{1-42}$ (**Figure 4–3** b). The mixing of $A\beta_{1-42}^{565}$ seems to cause a delay of aggregation rate in the conversion of globular aggregates to well formed mature fibrils, but the morphologies and structures of aggregate and fibril did not show significant change.

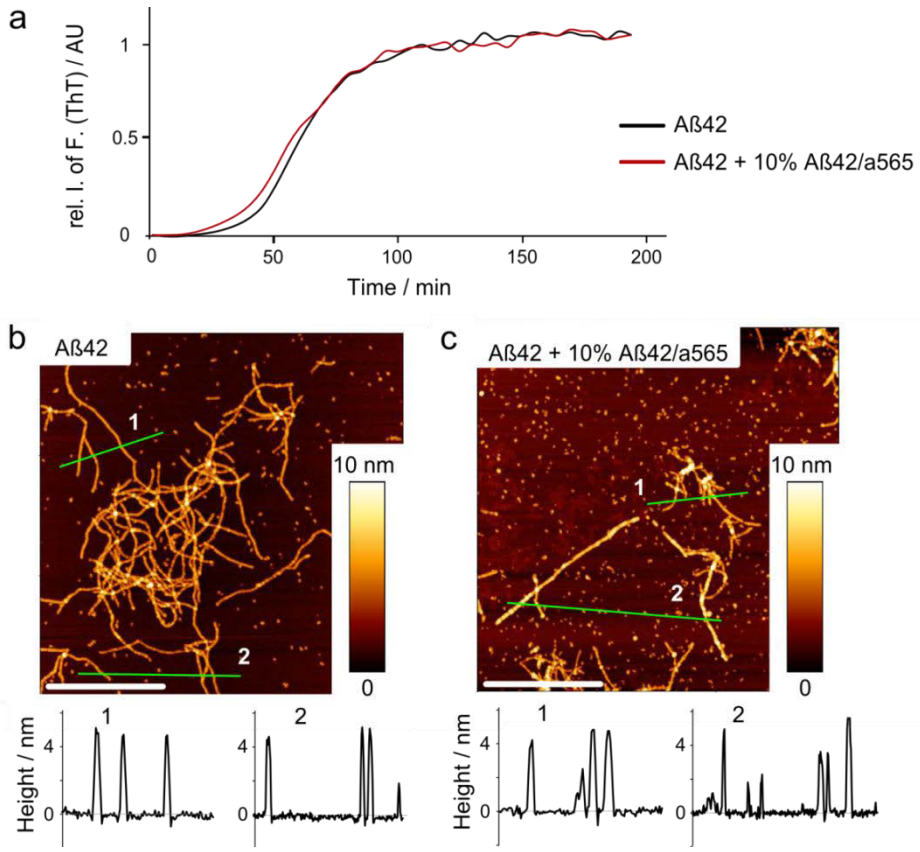

Figure 4–3: Aggregates formation of $A\beta_{1-42}$ monomers with labeling. (a) Monomeric $A\beta_{1-42}$ was mixed with 10 % $A\beta_{1-42}^{565}$ monomers (total $A\beta_{1-42}$ concentration of 15 µM) and incubated in PBS with intermittent shaking (5s every 5 min). Aggregation was monitored by ThT fluorescence. The curves were normalized to the maximum intensity of fluorescence of plateaus. All results are represented as mean values of 3 replicate wells. **(b & c)** Unlabeled monomeric $A\beta_{1-42}$ was mixed without **(b)** or with 10% $A\beta_{1-42}^{565}$ **(c)**, incubated in PBS for 2 d. Similar fibril structures with twisted structures and height of about 5 nm were detected in both samples by AFM. Scale bars, 1 µm. Figure b and c adapted from Sha Jin, Master Thesis "*Cellular uptake of amyloid–ß aggregates*".

To test whether labeled $A\beta_{1-42}$ co–aggregate with unlabeled $A\beta_{1-42}$, two types of labeled $A\beta_{1-42}$, $A\beta_{1-42}^{565}$ and $A\beta_{1-42}^{633}$, were used. Monomeric $A\beta_{1-42}^{565}$ (1 µM), monomeric $A\beta_{1-42}^{633}$ (4 µM) and unlabeled $A\beta_{1-42}$ monomer of different concentrations (0 to 20 µM) were incubated in PBS at pH 7 at 25 °C for 3d. Additionally, donor only sample contained $A\beta_{1-42}^{565}$ (1 µM) and $A\beta_{1-42}$ (4 µM), and acceptor only sample contained $A\beta_{1-42}$ (1 µM) and $A\beta_{1-42}^{633}$ (4 µM), were prepared under the same conditions as controls. $A\beta_{1-42}^{565}$–to– $A\beta_{1-42}^{633}$ FRET was

then measured by a fluorescence plate reader at excitation at 520 nm. Fluorescence emission spectrum was detected from 550 to 700 nm.

Comparing with the samples containing only donor ($A\beta_{1-42}^{565}$, red curve) or acceptor ($A\beta_{1-42}^{633}$, dark blue curve) fluorophores, FRET samples, which contain both donor and acceptor fluorophores, have a decreased fluorescence intensity of emission maximum (Em. max) at 592 nm, at which is the emission maximum of donor fluorophore (**Figure 4–4** a).

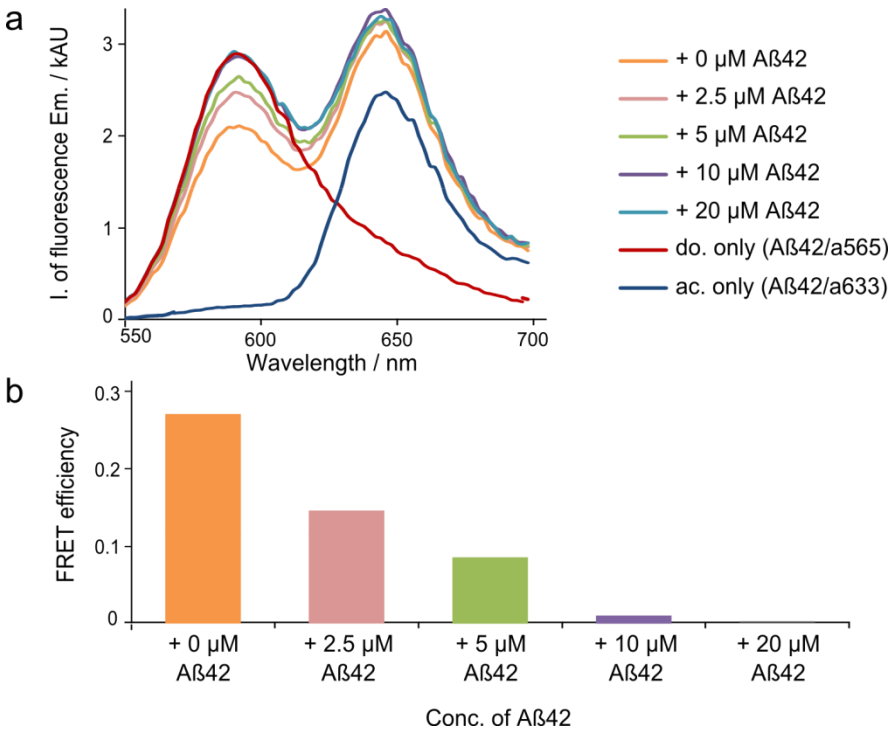

Figure 4–4: Co–aggregation of unlabeled and labeled $A\beta_{1-42}$ monomers. (a) To prepare co–aggregates from labeled and unlabel monomers, monomeric $A\beta_{1-42}^{565}$ (1 µM), monomeric $A\beta_{1-42}^{633}$ (4 µM) and unlabeled $A\beta_{1-42}$ monomer of different concentrations (0 to 20 µM) were incubated in PBS at pH 7 at 25 °C for 3d. Donor only sample ($A\beta_{1-42}^{565}$ of 1 µM and $A\beta_{1-42}$ of 4 µM), and acceptor only sample ($A\beta_{1-42}$ of 1 µM and $A\beta_{1-42}^{633}$ of 4 µM) were as controls. $A\beta_{1-42}^{565}$–to– $A\beta_{1-42}^{565}$ FRET was measured by a fluorescence plate reader at excitation at 520 nm. **(b)** FRET efficiency, which is strongly influenced by concentration of added unlabeled $A\beta_{1-42}$, was gived by $E = 1 - I_D' / I_D$. I_D' and I_D are the donor ($A\beta_{1-42}^{565}$) fluorescence intensities at 592 nm with and without acceptor ($A\beta_{1-42}^{633}$).

The degrees of fluorescence intensities decreasing at Em. max show a strong dependence on the concentrations of mixed unlabeled $A\beta_{1-42}$ monomers, the higher the concentration of unlabeled $A\beta_{1-42}$, the less the decrease of the donor fluorescence intensities.

The FRET efficiency were calculated as:

$$E = 1 - \frac{I_D'}{I_D} \quad [12]$$

where $I_D^{'}$ and I_D are the donor ($A\beta_{1-42}^{565}$) fluorescence intensities at 592 nm with and without acceptor ($A\beta_{1-42}^{633}$), respectively. The decreased FRET efficiencies by increasing the concentration of unlabeled $A\beta_{1-42}$ indicate there are coaggregation and no segregation between labeled and unlabeled $A\beta_{1-42}$ (**Figure 4–4** b).

To be noted, the acceptor fluorophore (atto633) alone has a very strong emission at 655 (±10) nm when exciting at 520 nm, it may the cause that fluorescence intensity of the acceptor showed only weak changes at this spectrum area (655 nm) when mixing with unlabeled $A\beta_{1-42}$.

Nevertheless, this FRET experiment demonstrated that labeled and unlabeled $A\beta_{1-42}$ form co–aggregates. $A\beta_{1-42}^{565}$ and $A\beta_{1-42}^{633}$ forms co–aggregates, resulting in a reduction of donor fluorescence. Adding excess unlabeled $A\beta_{1-42}$ results in a rescue of the donor fluorescence signal, indicating that FRET between the two labeled species is reduced.

In the present study, labeled $A\beta_{1-42}$ preparations were used in cellular uptake experiments. To determine whether $A\beta_{1-42}$ monomers can be take up by the cells and to investigate whether the state of aggregation influences cellular uptake, protofibrils (**Figure 4–1** e) and well–formed mature fibrils (**Figure 4–3** c) were used to compare their respective cellular uptake with that of monomers.

For kinetic analysis, based on the aggregation kinetic in vitro and AFM data, the mixtures of 90% unlabeled $A\beta_{1-42}$ and 10% $A\beta_{1-42}^{565}$ was used, so that the internalized $A\beta_{1-42}$ can be detected via fluorescence, and at the same time their aggregation kinetics are not too much affected by the fluorescent tag (**Figure 4–3** a).

Internalized $A\beta_{1-42}$ in cultured human neuroblastoma (SH–EP) cells was imaged by confocal microscopy, or quantified using high–content screening microscopy (HCS).

4.1.2 Cellular uptake of $A\beta_{1-42}$ depends on its aggregation state

First, we examined which form and under which conditions $A\beta_{1-42}$ can be taken up by the cells. SH–EP cells were incubated with monomeric $A\beta_{1-42}^{565}$ or aggregates, which were the protofibrils in this case, contained β–sheet–rich structures at 37 °C for 24 h. The monomer and protofibril fractions, which were isolated by SEC after the labeling process (**Figure 4–1** a), were used. A fluorescently labeled aggregation–incompetent scrambled peptide, $sc–A\beta_{1-42}^{565}$, was used as control. A soluble membrane–impermeable fluorescent dye, calcein (20 µM), was added to the extracellular medium, to mark the uptake of extracellular medium during vesicular trafficking from the plasma membrane into the cells in endocytic vesicles. Fixed cells were imaged by confocal microscopy (**Figure 4–5** a–e).

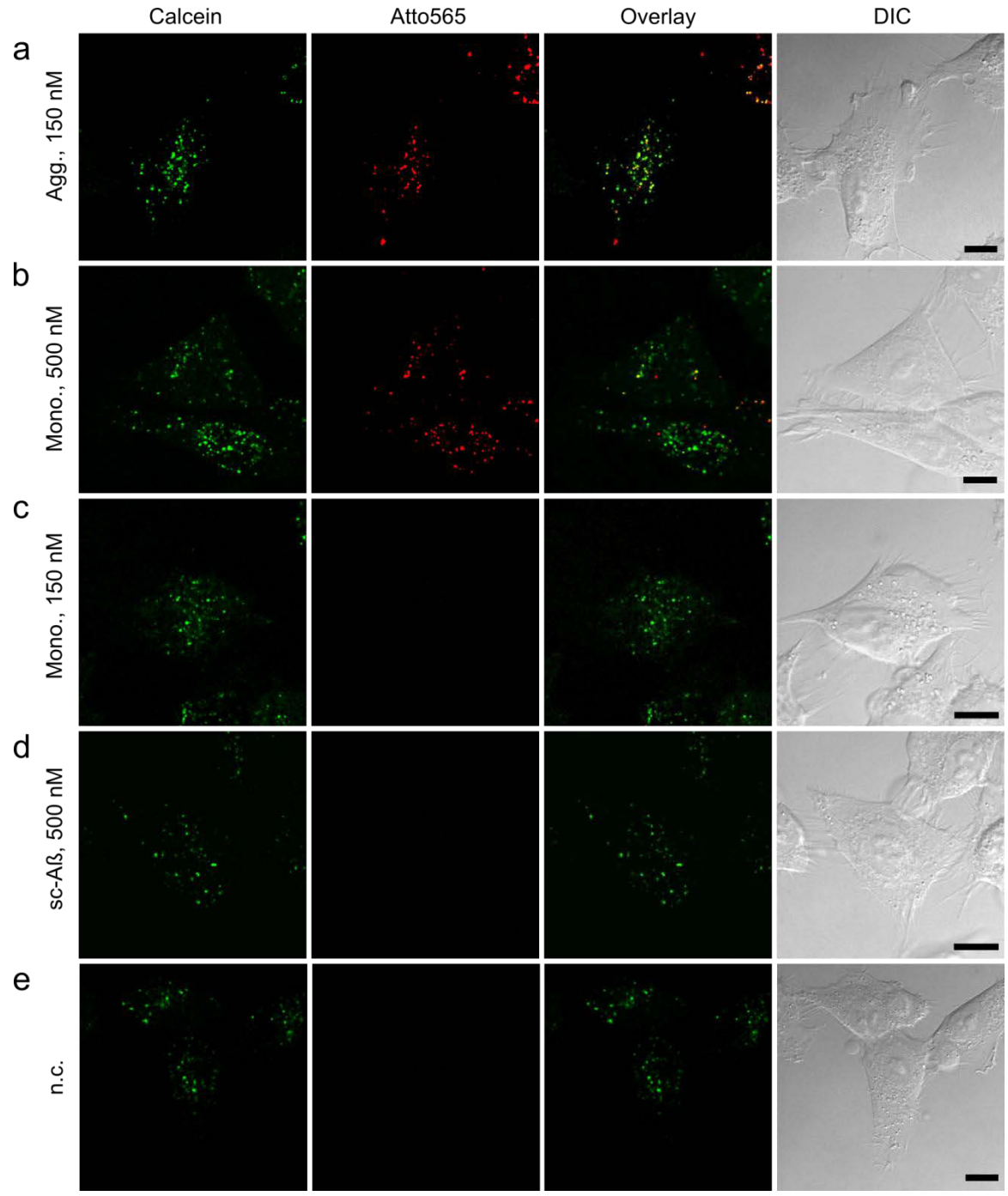

Figure 4–5: Internalization of $A\beta_{1-42}$ depends on aggregation states. (a–d) Human neuroblastoma (SH–EP) cells were incubated with purified monomer or aggregates (protofibrils) of $A\beta_{1-42}^{565}$ (red) at 37 °C for 24 h, were imaged by confocal microscopy. Calcein (20 µM, green) was added to indicate the trafficking vesikels. **(a)** $A\beta_{1-42}^{565}$ aggregates (Agg.) of 150nM, **(b)** monomeric $A\beta_{1-42}^{565}$ (mono.) of 500nM, **(c)** monomeric $A\beta_{1-42}$ of 150 nM, **(d)** scrambled–$A\beta_{1-42}^{565}$ (sc–Aβ)of 500 nM and **(e)** negative control (n.c.). Cellular uptake of $A\beta_{1-42}^{565}$ was only observed by treating with aggregates or with monomers at 500 nM. Co–localization of internalized $A\beta_{1-42}^{565}$ with calcein suggested that internalized $A\beta_{1-42}^{565}$ was located in endocytic vesicles. Scale bars, 10 µm.

Intracellular $A\beta 1_{-42}^{565}$ aggregates could be detected after treatment with aggregates (150 nM, monomer equivalent, concentration in medium, **Figure 4–5** a) or with monomers at a higher concentration (500 nM, concentration in medium, **Figure 4–5** b). Treatment with low

concentrations of monomeric $A\beta_{1-42}^{565}$ (150 nM, concentration in medium, **Figure 4–5** c) or with aggregation–incompetent sc–$A\beta_{1-42}^{565}$ at higher concentration (500 nM, concentration in medium, **Figure 4–5** d), did not lead to detectable $A\beta_{1-42}^{565}$ inclusions inside the cells, and showed background signals in Atto 565 channel similar to untreated cells (**Figure 4–5** d). These observations suggest that $A\beta_{1-42}$ uptake may depend on a particular state of aggregation, and that an effective uptake of monomer may require forming an ordered structure, i.e. in an aggregated state. Colocalization of internalized $A\beta_{1-42}^{565}$ with calcein suggested that internalized $A\beta_{1-42}^{565}$ was located in endocytic vesicle.

Compared with the uptake of monomeric $A\beta_{1-42}^{565}$ and of aggregation–incompetent sc–$A\beta_{1-42}^{565}$ at relatively high peptide concentration (500 nM), $A\beta_{1-42}^{565}$ monomer could be observed (**Figure 4–5** b) and there is no detectable sc–$A\beta_{1-42}^{565}$ in the cells (**Figure 4–5** d). The lack of uptake of sc–$A\beta_{1-42}^{565}$ verified that internalization was specific for the Aβ sequence and not a result of the fluorescent label.

Intensities of the 565 nm channel from **Figure 4–5** a–e were analyzed. Average fluorescence intensities per pixel were calculated from the endocytic vesicles marked by calcein, areas in the cytosol without vesicles or in the extracellular areas, respectively (**Figure 4–6**).

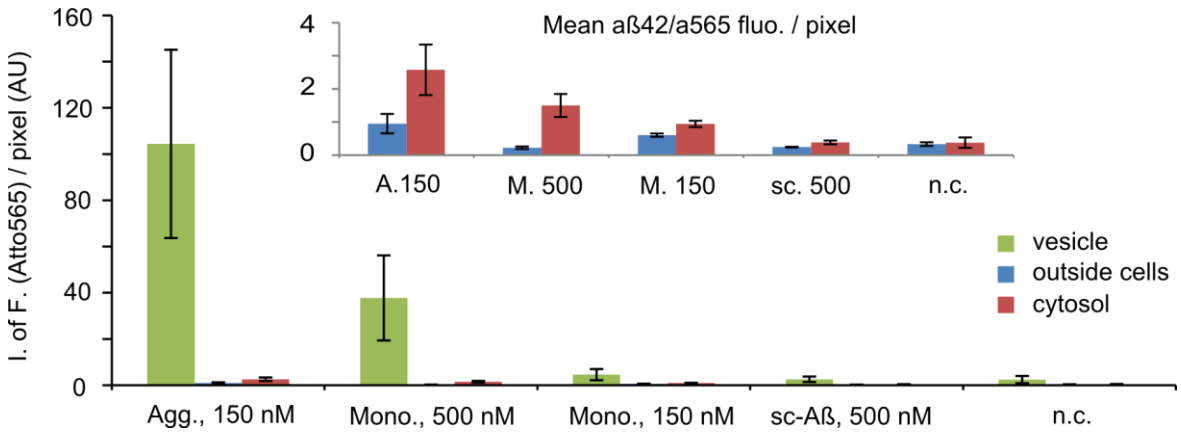

Figure 4–6: Quantitative analysis of $A\beta_{1-42}^{565}$ fluorescence. Average fluorescence intensities per pixel inside endocytotic vesicles, in the cytosol and in the extracellular space were calculated from the 565 nm channel of confocal images in Figs. 2A–E. Bar graphs represent average values of ± standard deviations (SD) from image areas corresponding to endocytotic vesicles marked by calcein (n=10), or from areas in the cytosol without vesicles (n=3) or in the extracellular space (n=3), respectively. Only cells treated with aggregated $A\beta_{1-42}^{565}$ (150 nM; A.150) or monomeric $A\beta_{1-42}^{565}$ (500 nM; M. 500) displayed fluorescence above the background of untreated cells (n.c.), whereas those treated with $A\beta_{1-42}^{565}$ monomers at 150 nM (M. 150) and scrambled $A\beta_{1-42}^{565}$ (500 nM; sc. 500) did not. Inset: Cells treated under conditions that resulted in uptake of $A\beta_{1-42}^{565}$ aggregates displayed a threefold increase in cytosolic $A\beta_{1-42}^{565}$ signal compared to the extracellular space. $A\beta_{1-42}^{565}$ fluorescence in the cytosol is ~ 30–fold lower than inside the vesicles.

Quantitative analysis of $A\beta_{1-42}^{565}$ fluorescence intensities in the endocytic vesicles and in the cytosol revealed that a low level cytosolic $A\beta_{1-42}^{565}$ signal could be detected after treatment with aggregates (150 nM) or high concentration (500 nM) monomeric $A\beta_{1-42}$ but not at low monomer concentrations (150 nM). The $A\beta_{1-42}^{565}$ signal in the surrounding cytosol was about 30–fold lower than in the vesicles.

Additionally, to test whether $A\beta_{1-42}$ is equally internalized into primary neurons, primary rat hippocampal neurons were treated with $A\beta_{1-42}^{565}$. The phagocytic active glial cells were eliminated during preparation process. Primary neurons were incubated with $A\beta_{1-42}^{565}$ monomer of 150 nM or of 500 nM at 37°C. Calcein (20 µM) was added to show the endocytic vesicles. The cells were fixed after 24 h incubating with $A\beta_{1-42}^{565}$ and were imaged by confocal microscopy. The uptake of $A\beta_{1-42}^{565}$ by primary hippocampal neurons was observed when monomeric $A\beta_{1-42}^{565}$ at 500 nM (**Figure 4–7** a), but not at 150 nM (**Figure 4–7** b), which were very similar as observed in the cultured SH–EP cells. The colocalizations with calcein indicate internalized $A\beta_{1-42}^{565}$ was located in endocytic vesicles.

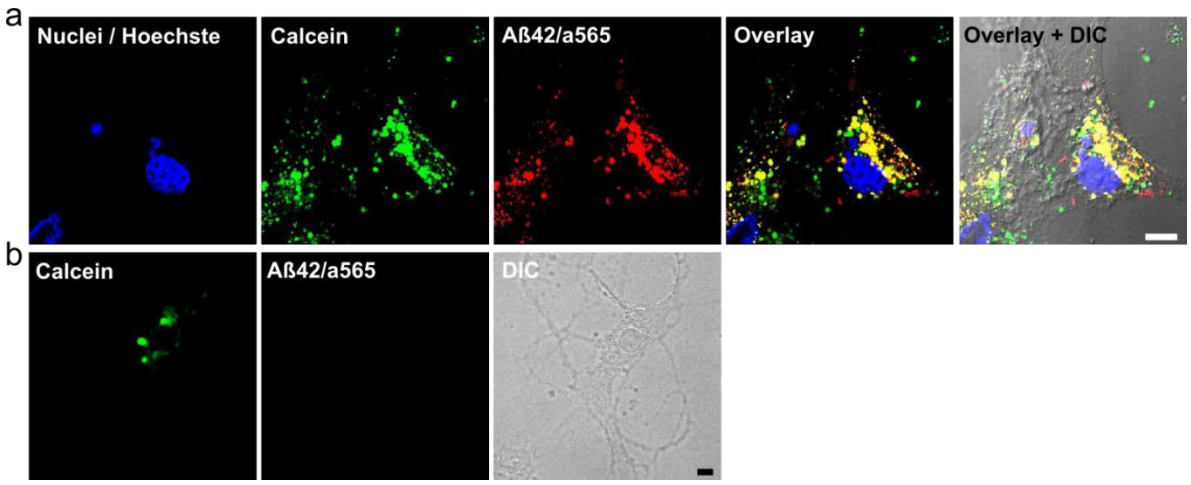

Figure 4–7: Internalization of $A\beta_{1-42}$ primary hippocampal neurons. Primary hippocampal neurons were treated with $A\beta_{1-42}^{565}$ monomer at 500 nM **(a)** or 150 nM **(b)** and calcein (20 µM) at 37 °C for 24 h. Fixed cells were imaged by confocal microscopy. Scale bars, 10 µm.

These results suggest that $A\beta_{1-42}$ uptake depends on a particular state of aggregation, and that the monomeric $A\beta_{1-42}$ concentration in the cell culture medium has to reach a critical concentration for a successful uptake. A possible explanation may be that the threshold concentration of monomeric $A\beta_{1-42}$ uptake would correspond to the critical concentration for $A\beta_{1-42}$ aggregation. The freshly formed aggregate would be then taken up. This hypothesis will be discussed in section 4.1.5.

4.1.3 Calcein as fluid–phase marker for $A\beta_{1-42}$ endocytosis

Calcein is a soluble membrane–impermeable fluorescent dye. A colocalization of internalized $A\beta_{1-42}^{565}$ with calcein (**Figure 4–5** a and b) suggests $A\beta_{1-42}^{565}$ would be endocytosed via a vesicular trafficking into endocytic vesicles. To test whether calcein indeed distinguishd the locations of $A\beta_{1-42}$ inside the cells, i.e. in the endocytic vesicles, or on the cell surface. SH–EP cells were treated with calcein (20 µM) and $A\beta_{1-42}$ mixture (500 nM, equivalent monomer concentration), which contained small aggregates and well–formed mature fibrils as described in **Figure 4–3** c. After incubation at 37°C for 24 h, fixed cells were imaged by confocal microscopy (**Figure 4–8**).

Two different morphology patterns of $A\beta_{1-42}^{565}$ staining were observed. The point–like $A\beta_{1-42}^{565}$ was close to nuclei and colocalized with calcein, suggesting they are in endocytic vesicles inside the cells. The second group of $A\beta_{1-42}^{565}$ aggregates show relatively large size and irregular form, which located probably on the cell surface, did no show colocalization with calcein.

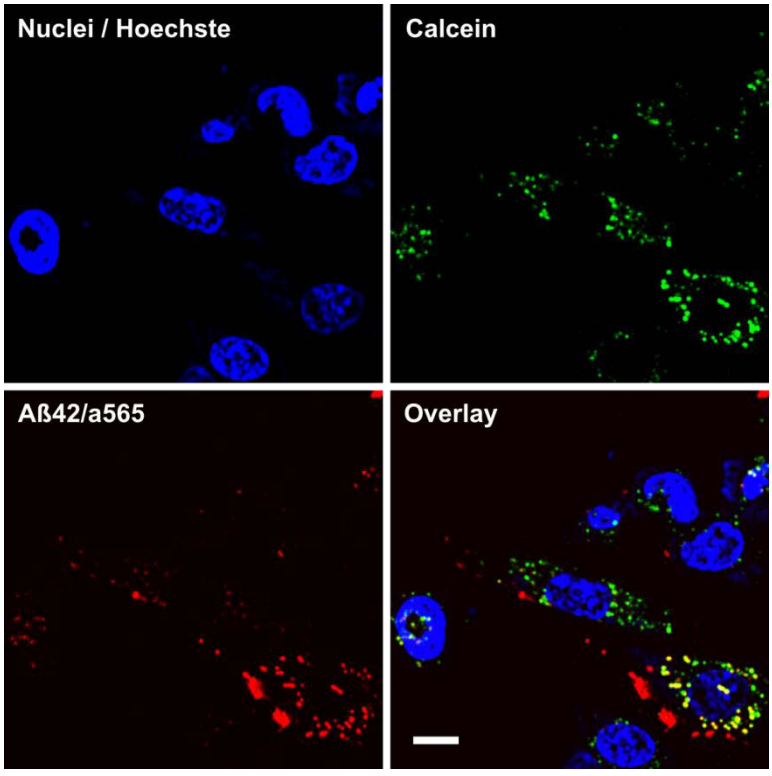

Figure 4–8: Internalization of $A\beta_{1-42}$ small aggregates vs. large fibrils. SH–EP cells were incubated with a mixture of small aggregates and well–formed fibrillar $A\beta_{1-42}$ (500 nM, equivalent monomer concentration), containing 10% $A\beta_{1-42}^{565}$, at 37 °C for 24 h, were imaged by confocal microscopy. Calcein (20 µM) were added together with $A\beta_{1-42}$ to the cells, to distinguish internalized $A\beta_{1-42}$ (co–localized with calcein) and surface bound $A\beta_{1-42}$ (without co–localization with calcein). Scale bar, 10 µm.

4.1.4 Costaining of the internalized $A\beta_{1-42}$ with anti–β–amyloid antibody.

To validate that the intracellular Atto 565 fluorescence indeed corresponds to internalized $A\beta_{1-42}$, SH–EP cells were incubated with $A\beta_{1-42}$ aggregates (identical experiment as shown in **Figure 4–8**, total $A\beta_{1-42}$ concentration at 500 µM, equivalent monomer concentration) or with Atto 565 dye only (500 nM) at 37 °C for 24 h. The fixed cells were then costained with anti–β–amyloid mouse antibody 6E10 by immunofluorescence staining (IF) and were visualized by cy5 conjugated anti–mouse secondary antibody.

The colocalization between fluorescence and 6E10/cy5 confirmed the presence of the Aβ peptide (**Figure 4–9** a), i.e. Atto 565fluorescence of labeled $A\beta_{1-42}{}^{565}$ represents $A\beta_{1-42}$. This demonstrated that the fluorescent labels of $A\beta_{1-42}$ can be used to track $A\beta_{1-42}$ uptake and aggregates formation.

Lack of the primary antibody, 6E10, to against $A\beta_{1-42}{}^{565}$, no the fluorescence signal of Cy5 conjugated secondary antibody could be detected (**Figure 4–9** b), indicating no binding of Cy5 conjugated secondary antibody to Atto 565 dye or to $A\beta_{1-42}{}^{565}$ molecules. 6E10/Cy5 recognized specifically $A\beta_{1-42}{}^{565}$ sequence (**Figure 4–9** a).

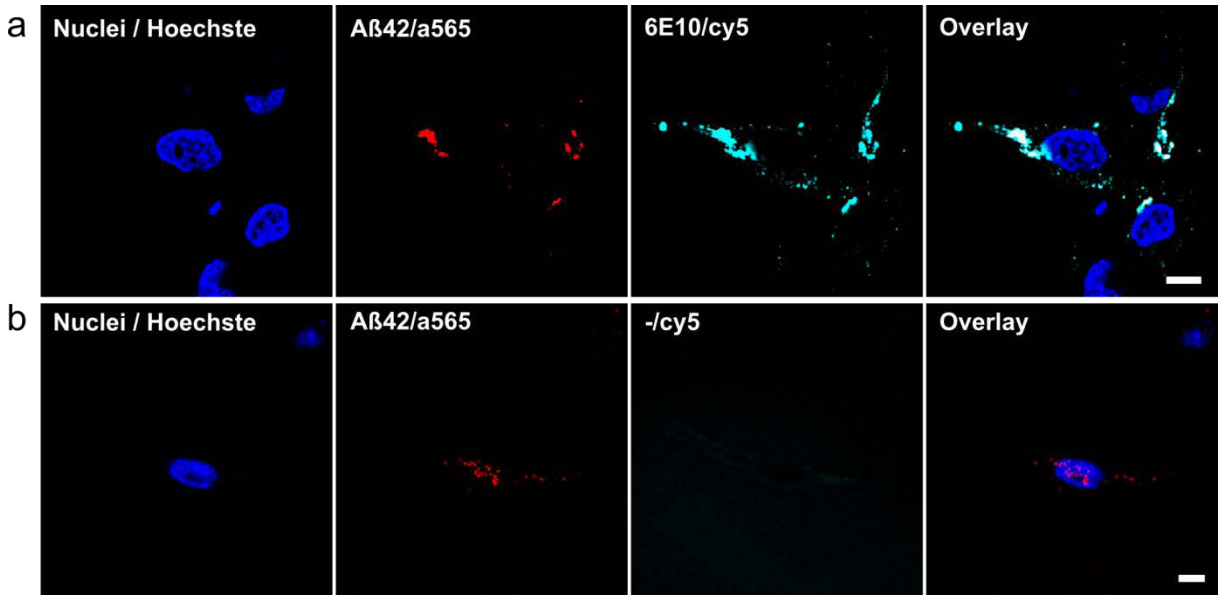

Figure 4–9: Costaining of the internalized $A\beta_{1-42}$ with anti–β–amyloid antibody. SH–EP cells were incubated with $A\beta_{1-42}{}^{565}$ aggregates (500 nM, equivalent monomer concentration) **(a and b)**, or Atto 565 dye **(c)** at 37 °C for 24 h. **(a)** Fixed cells were stained by anti–Aβ antibody (6E10) using immunofluorescence staining (IF), visualized by cy5 conjugated secondary antibody (cyan), and imaged by confocal microscopy. Cell nuclei were stained with Hoechst 33342 (blue). Internalized $A\beta_{1-42}{}^{565}$ were costained and co–localized with 6E10/cy5. **(b)** No secondary antibody binding observed without primary antibody (6E10) to $A\beta_{1-42}{}^{565}$. Scale bars, 10 µm.

By incubating SH–EP cells only with Atto 565 dye and staining with 6E10/Cy5, no Atto 565 fluorescence could be detected, indicating that Atto 565 dye alone could not be taken up by SH–EP cells. Uniformly distributed Cy5 fluorescence in very small dots–form, which was from IF staining, was observed, that correspond probably to the endogenous amyloid precursor protein APP (**Figure 4–10**). However, internalized $A\beta_{1-42}^{565}$ can be distinguished from those background signals through their distribution and morphology.

These control experiments confirmed that $A\beta_{1-42}$ could be represented by using fluorescence label and be tracked via fluorescence in the cultured cells.

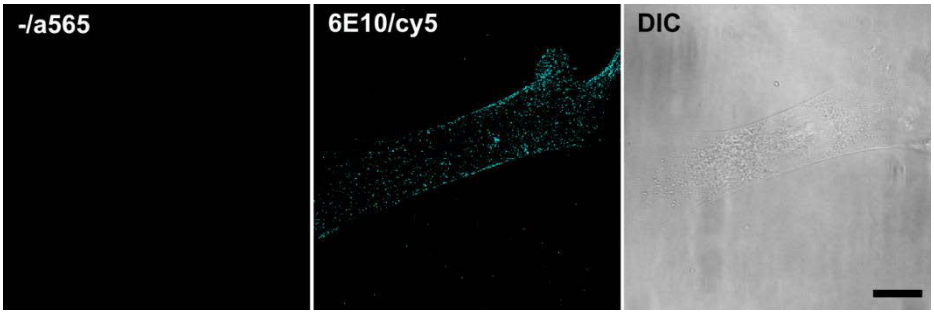

Figure 4–10: Uptake of Atto 565 dye as control experiment. SH–EP cells were Atto 565 dye (500 nM) at 37 °C for 24 h. Uptake of Atto 565 dye cannot be observed by SH–EP cells, 6E10/cy5 could not recognize any dye molecules. Scale bar, 10 µm.

4.1.5 Uptake of monomer requires a minimum concentration

In the case of monomeric $A\beta_{1-42}$ uptake, the intracellular $A\beta_{1-42}$ would only be detected by treating the cells with $A\beta_{1-42}$ monomer at 500 nM (**Figure 4–5** b), but not at 150 nM (**Figure 4–5** c). An effective uptake of monomers seems to depend on concentration of $A\beta_{1-42}$.

To test this hypothesis we titrated the cells either with $A\beta_{1-42}$ monomer or small aggregates at varying concentrations and quantified intracellular $A\beta_{1-42}$ aggregates as a function of $A\beta_{1-42}$ concentration by fluorescence of labeled $A\beta_{1-42}$ using HCS microscopy.

First, we tracked the amount of internalized Aβ aggregates as a function of time and found maximal intracellular $A\beta_{1-42}$ signal after treatment with $A\beta_{1-42}$ for about 1d (**Figure 4–11**). SH–EP cells were incubated with purified $A\beta_{1-42}^{488}$ monomers of 200 nM at 37 °C from 1 h to 49 h. Intracellular $A\beta_{1-42}^{565}$ in fixed cells was analyzed by HCS microscopy. Maximal intracellular $A\beta_{1-42}$ fluorescence was reached after 27 h. We thus used 1d incubation for subsequent uptake experiments.

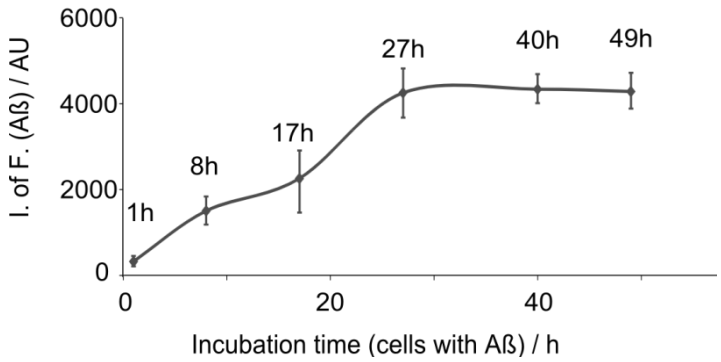

Figure 4–11: The time–dependence manner of internalized $A\beta_{1-42}$. SH–EP cells were incubated with purified $A\beta_{1-42}{}^{488}$ monomer (200 nM) at 37 °C from 1 h to 49 h. Intracellular $A\beta_{1-42}{}^{488}$ in fixed cells was analyzed by high–content screening (HCS) microscopy. Maximal intracellular $A\beta_{1-42}$ was reached after 27 h. All results are represented as mean values ± SD of 6 replicate wells.

SH–EP cells were then treated with $A\beta_{1-42}$ monomers and aggregates, protofibrils from SEC (**Figure 4–1** e) were used as aggregates, at 15 – 1500 nM (equivalent monomer concentration) incubated at 37°C for 24 h. For monomeric $A\beta_{1-42,}$ the total amount of intracellular aggregated $A\beta_{1-42}$ as well as the number of aggregates and their total areas were proportional to $A\beta_{1-42}$ monomer concentrations in the medium. No intracellular $A\beta_{1-42}$ aggregates were observed below a threshold concentration of about 300 nM (**Figure 4–12** a and b). In contrast, no such threshold concentration existed for the internalization of preformed $A\beta_{1-42}{}^{565}$ aggregates (**Figure 4–12** c and d). Neither form of $A\beta_{1-42}$, monomer or small aggregates, has significant effect on the number of cells (**Figure 4–12** a and c).

In all experiments, the concentrations of aggregates are reported as the equivalent concentration of the $A\beta_{1-42}$ monomer. It means the total number of aggregates in the medium is much smaller than the number of monomers. However, the amount of internalized $A\beta_{1-42}{}^{565}$ in the cells that were treated by aggregates is 3–5 times higher than in monomer treated cells. One possible explanation of the low number of cellular aggregates after monomer uptake could be detection bias of our method. The weak signal of a single fluorophore is not easy to detect by HCS microscopy and the aggregate detection algorithm requires a certain fluorescence threshold, which biases against the detection of monomers and very small aggregates. Nevertheless, it would be also very probable that uptake of performed $A\beta_{1-42}$ aggregates is much more efficient than monomer. They can already be taken up by cells at very low concentration, based on their well–formed structures.

The observed threshold concentration for monomer uptake is similar to the critical concentration (Usui et al. 2009) that was reported for the aggregation of $A\beta_{1-42}$ monomers, which suggests that aggregation may be a prerequisite for uptake. If so, it would be important to determine the location of aggregates formation and which type of aggregate species is efficiently taken up by the cells. In the next chapters will compare the cellular uptake of $A\beta_{1-42}$ at different stages of its aggregation process.

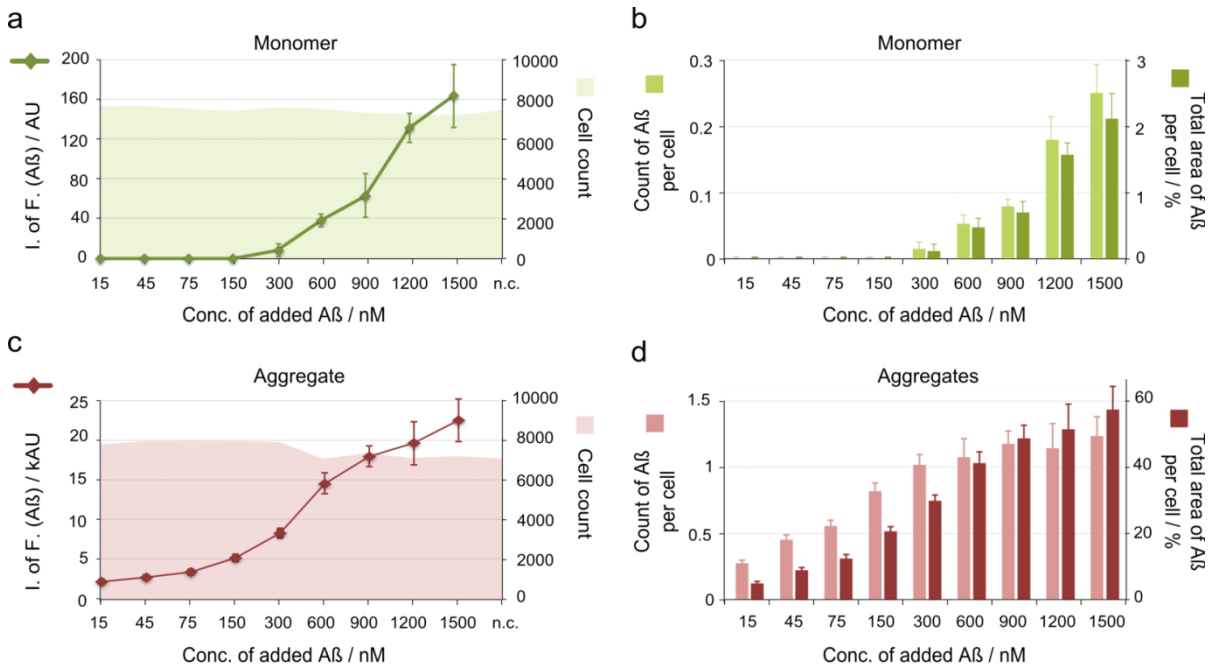

Figure 4–12: The concentration–dependence manner of $A\beta_{1-42}$ uptake. SH–EP cells were incubated with purified $A\beta_{1-42}^{565}$ monomer **(a & b)** or aggregates **(c & d)** at 37 °C for 24 h. Intracellular $A\beta_{1-42}^{565}$ in fixed cells was analyzed by HCS microscopy. Total fluorescence intensities of $A\beta_{1-42}^{565}$, cell counts per well, the counts of $A\beta_{1-42}^{565}$ aggregates per cell and their total area were plotted as a function of $A\beta_{1-42}^{565}$ concentration in the cell culture medium. All results are represented as mean values ± SD of 6 replicate wells. Figure adapted from Sha Jin, Master Thesis "*Cellular uptake of amyloid–ß aggregates*".

4.1.6 Aggregation on plasma membrane precedes uptake of $A\beta_{1-42}$ by a clathrin independent pathway

To investigate the location at which the aggregates form that are the requested for uptake and to better track the dynamics of monomer uptake, we repeated the uptake experiment under conditions that allowed us to temporarily separate Aβ membrane interaction from its uptake into the cell.

The cells were cooled to 4°C, which slows down both $A\beta_{1-42}$ aggregation and cell metabolism. By lowering the temperature, Aβ aggregation kinetic is slower than at room temperature (RT) or at 37°C, the fluidity of membrane is decreased and the cell metabolisms is slowed (Alberts 2008; Lodish et al. 2008; Uzman et al. 2000). Additionally, clathrin–mediated endocytosis is inhibited at 4°C as indicated by blocking the uptake of transferrin (Harding et al. 1983), which provides also an opportunity to investigate the pathway of Aβ cellular uptake.

The general experimental process is shown in **Figure 4–13**. The cells were cooled to 4°C for 15 min, and then were treated with Aβ at 4°C for 45 min. In this step, Aβ would be loaded to the cells. The cells were then washed with ice–cold PBS to remove unbound $A\beta_{1-42}$. Depending on the goal of experiments, the cells were imaged directly, or were further

restored at 37°C in fresh media for the uptake of $A\beta_{1-42}$. The uptake of labeled $A\beta_{1-42}$ was read out by confocal microscopy or HCS microscopy.

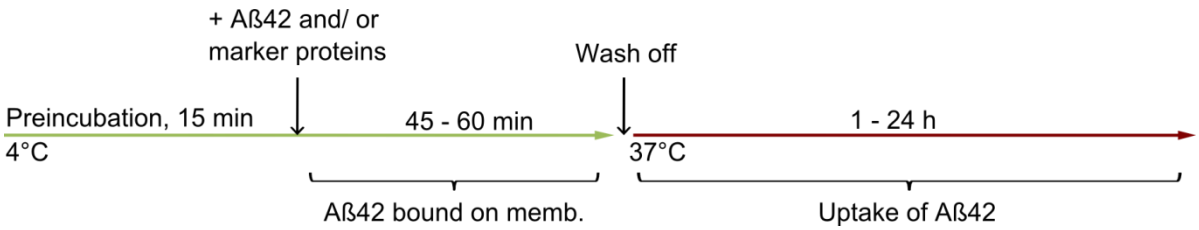

Figure 4–13: Scheme of experimental flow. The cells were incubated with monomeric $A\beta_{1-42}$at 4°C for loading of $A\beta_{1-42}$, then cells were either imaged directly, or were washed offto remove unbound $A\beta_{1-42}$ and were further incubated in fresh medium at 37 °C. Intracellular $A\beta_{1-42}$was quantified by confocal microscopy or HCSmicroscopy.

4.1.6.1 $A\beta_{1-42}$ uptake at 4°C

The clathrin–mediated endocytosis is blocked at 4°C (Harding et al. 1983), and the fluidity of membrane is limited by reducing the temperature (Uzman et al. 2000; Lodish et al. 2008). We, therefore, first of all tested whether cooling to 4°C leads to a cellular change that prevents $A\beta_{1-42}$ uptake. Transferrin was used to report the inhibition of clathrin–mediated endocytosis pathway. Following incubation with monomeric and preaggregated $A\beta_{1-42}{}^{565}$ (150 nM, respectively) calcein (20 µM) and transferrin (10 ng / ml) at 4 °C for 45 min, fixed SH–EP cells were imaged by confocal microscopy (**Figure 4–14**). The transferrin was located exclusively in the cell membrane, demonstrating that clathrin–mediated endocytosis was efficiently inhibited.

Under these conditions $A\beta_{1-42}$ was only observed on the plasma membrane and was not internalized in the cells treated with $A\beta_{1-42}$ monomers (**Figure 4–14** a). However, the membrane associated $A\beta_{1-42}$, which localized exclusively on the membrane at the time point of the cell fixation, did not colocalize with Transferrin. It suggested that the inhibition of monomer uptake may not due to the blocking of clathrin–dependent pathway. The down regulation of temperature was also unfavourable for $A\beta_{1-42}$ aggregation. In this case, monomeric $A\beta_{1-42}$ may still in monomeric or very early aggregation state, which probabely may not be able to be taken up.

The uptake of preaggregated $A\beta_{1-42}$ species was reduced but not totally inhibited under these conditions (**Figure 4–14** b). Due to transferrin still located on the plasma membrane, internalized $A\beta_{1-42}$ found in endocytic vesicles did not colocalize with them.

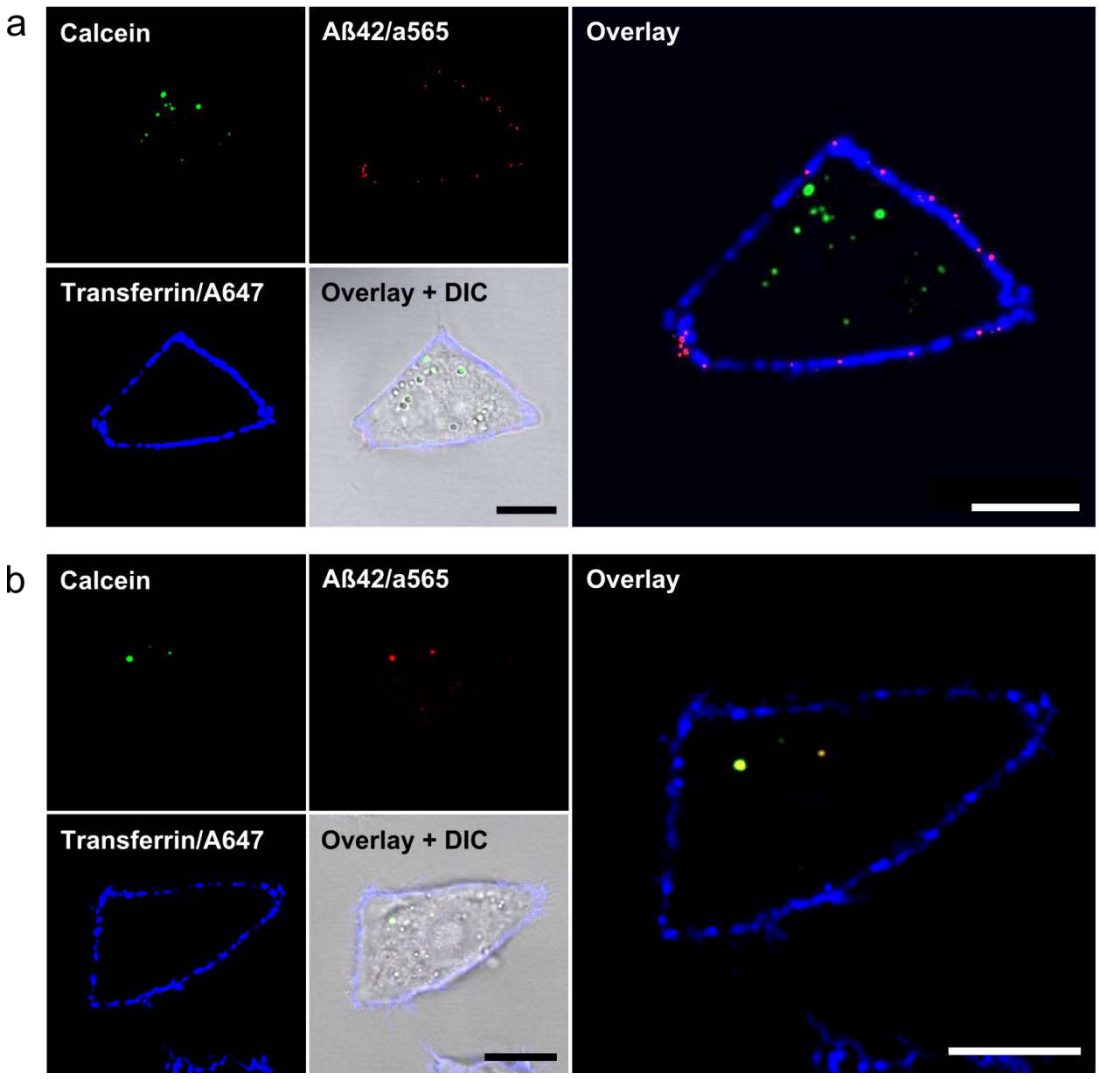

Figure 4–14: $A\beta_{1-42}$ uptake at 4°C. SH–EP cells were incubated with monomeric **(a)** or preaggregated **(b)** $A\beta_{1-42}^{565}$ (red) of 150 nM, calcein (20 µM, green) and transferrin (10 ng / ml, blue) for 45 min at 4 °C, and were imaged by confocal microscopy. Transferrin and $A\beta_{1-42}^{565}$ monomer were observed in the plasma membrane. $A\beta_{1-42}^{565}$ aggregate could be detected inside the cells. Scale bars, 10 µm.

These data suggest that uptake of preaggregated $A\beta_{1-42}$ may be independent of clathrin–mediated endocytosis, and an efficient uptake of $A\beta_{1-42}$ may depend on their aggregation status.

A quantitative analysis of the amount of internalized $A\beta_{1-42}^{565}$ aggregates at 4°C and at 37°C was carried out in 96–well plates by using HCS microscopy. SH–EP cells were incubated with preaggregated $A\beta_{1-42}^{565}$ (as used in **Figure 4–14** b) of 150 nM at 4°C and 37°C for 45 min, respectively (**Figure 4–15**). At 37°C, the total amount of more internalized $A\beta_{1-42}^{565}$ was about 5 times than at 4°C. At the same time, no significant changes of cell counts were seen different temperatures.

Our data suggested, while clathrin–mediated endocytosis may be the prominent mechanism by which both monomeric and oligomeric $A\beta_{1-42}$ enters the cell, there is a secondary

pathway by which $A\beta_{1-42}$ oligomers can cross the cell membrane that is still functional under conditions when receptor mediated endocytosis of transferrin is blocked.

A more detailed analysis of the $A\beta_{1-42}$ uptake pathway is found in section 4.1.9.

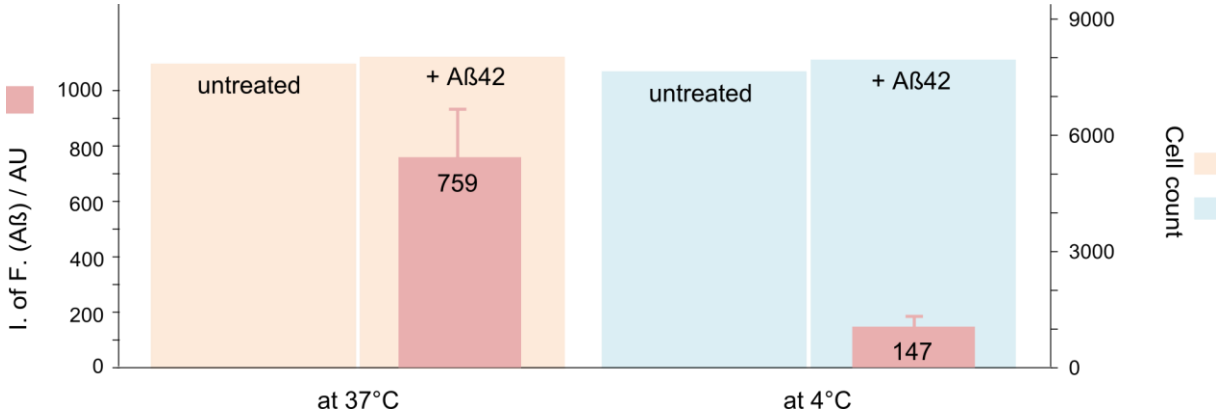

Figure 4–15: $A\beta_{1-42}$ uptake at 37°C vs. at 4°C. SH–EP cells were incubated with preaggregated $A\beta_{1-42}^{565}$ (150 nM) in 96–well plate at 37°C and at 4°C, respectively. Internalized $A\beta_{1-42}^{565}$ was analyzed by using HCS microscopy. Internalized $A\beta_{1-42}^{565}$ was decreased at 4°C. The cell counts kept stable. All results are represented as mean values ± SD of 6 replicate wells.

4.1.6.2 Uptake of aggregates formed on plasma membranes

Figure 4–14 a shows that $A\beta_{1-42}$, in monomeric form or in a state that cannot be taken up, is capable to associate with the cell membrane, even under conditions that prevented its endocytosis. This observation raises the question whether monomeric $A\beta_{1-42}$ is able to aggregate on the cell membrane. To answer this question, the formation of $A\beta_{1-42}$ aggregates on the cell membrane was quantified by using Förster resonance energy transfer (FRET) between two fluorophores of labeled $A\beta_{1-42}$ monomers.

SH–EP cells were incubated with two types of fluorescently labeled monomeric $A\beta_{1-42}$, $A\beta_{1-42}^{488}$ and $A\beta_{1-42}^{633}$. After pre–incubation at 4 °C for 15 min, SH–EP cells were treated with monomeric $A\beta_{1-42}^{488}$ and $A\beta_{1-42}^{633}$ at 4°C for 45 min. Total $A\beta_{1-42}$ concentration was 500 nM with $A\beta_{1-42}^{488}$ to $A\beta_{1-42}^{633}$ ratio in 3:7. Confocal imaging showed that both $A\beta_{1-42}^{488}$ and $A\beta_{1-42}^{633}$ accumulated on the plasma membrane. $A\beta_{1-42}^{488}$ and $A\beta_{1-42}^{633}$ not only colocalized but also displayed a FRET signal, indicating direct interaction between the two–labeled $A\beta_{1-42}$ species (**Figure 4–16** a). These data demonstrate that at least a fraction of the monomeric $A\beta_{1-42}$ peptides rapidly coaggregated on the plasma membrane.

Next, we investigated whether the cell takes up these membrane–bound $A\beta_{1-42}$ aggregates, rather than Aβ species that may be present extracellularly in solution.

Under conditions like in **Figure 4–16** a (4°C, 60 min incubation time with the cells), monomeric $A\beta_{1-42}^{565}$ was located only on the plasma membrane even at a monomer

concentration of 1 µM (**Figure 4–16** b). No uptake of $A\beta_{1-42}^{565}$ could be observed. Uptake of calcein (20 µM) exhibited that the cell still had some endocytotic activity under these conditions.

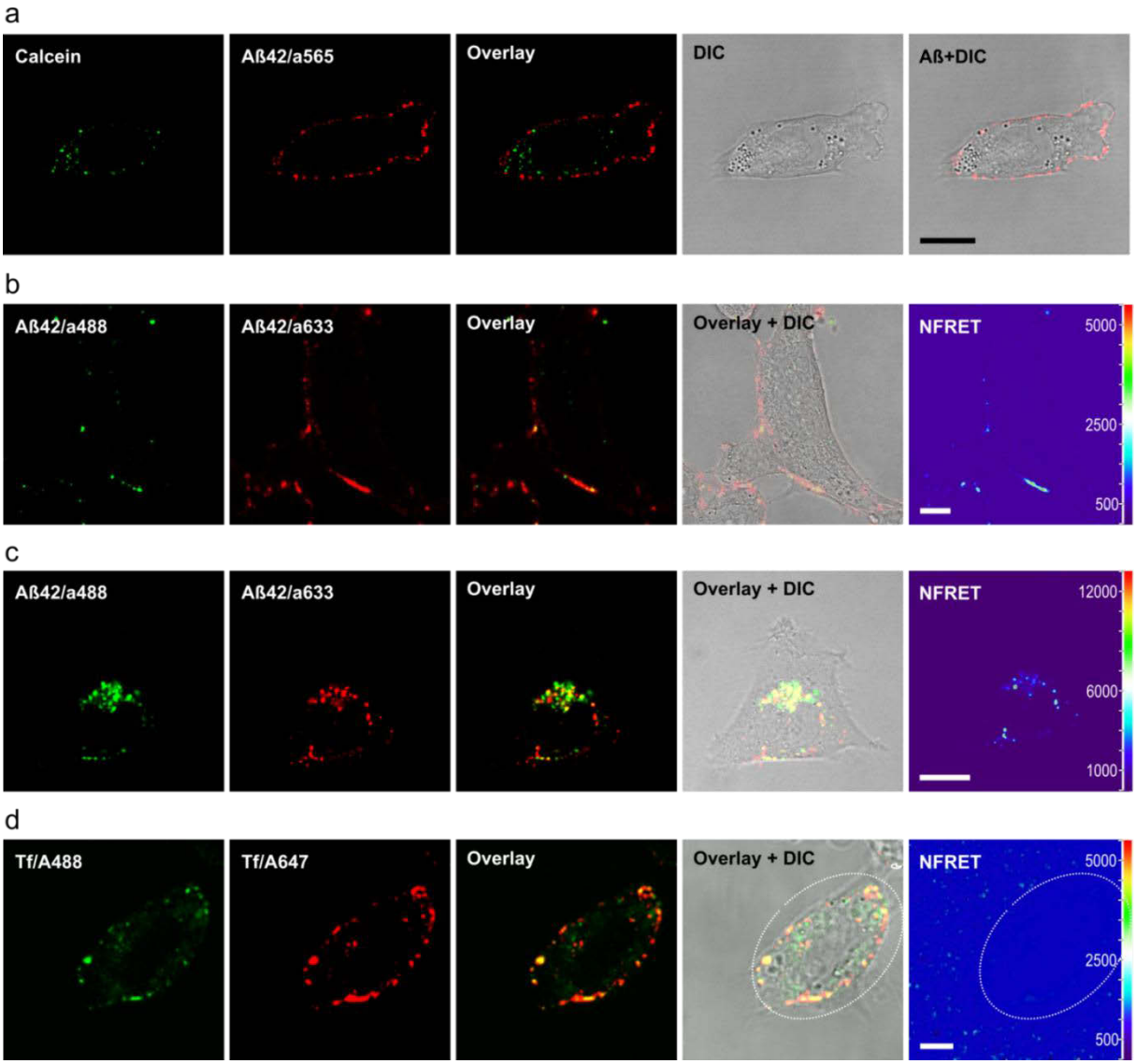

Figure 4–16: Aggregation of $A\beta_{1-42}$ occurs on the plasma membrane. (a) $A\beta_{1-42}$ – to – $A\beta_{1-42}$ Förster resonance energy transfer (FRET) on the plasma membrane. SH–EP cells were incubated with monomeric $A\beta_{1-42}$ (500 nM total $A\beta_{1-42}$) at 4 °C for 45 min, were imaged by confocal microscopy. $A\beta_{1-42}^{488}$ – to – $A\beta_{1-42}^{633}$ FRET indicated aggregates species bound to the plasma membrane. **(b)** After incubating with monomeric $A\beta_{1-42}^{565}$ (1 µM) and calcein (20 mM) at 4 °C for 60 min, $A\beta_{1-42}$ was located only on the plasma membrane, no uptake could be observed. Calcein indicates the cells are still active. **(c)** SH–EP cells were treated successively with monomeric $A\beta_{1-42}^{488}$ and $A\beta_{1-42}^{633}$ (each 500 nM in the medium) at 4°C for 30 min, were then incubated in fresh medium at 37 °C for 3 h. Co–localization of $A\beta_{1-42}^{488}$ and $A\beta_{1-42}^{633}$ indicates that internalized $A\beta_{1-42}$ was in aggregated form. **(d)** SH–EP cells were incubated with transferrin/Alexa488 (Tf/A488, 5 ng/ml) and transferrin/Alexa647 (Tf/A647, 10 ng/ml) conjungates at 4 °C for 45 min. No FRET occurred between two co–localized transferrin conjungates. White outlines in DIC and FRET images mark cells areas. Scale bars, 10 µm.

In the next step, SH–EP cells were treated successively with monomeric $A\beta_{1-42}^{488}$ and $A\beta_{1-42}^{633}$, each at 500 nM concentration. First, SH–EP cells were incubated with monomeric $A\beta_{1-42}^{488}$ at 4°C for 30 min. Unbound $A\beta_{1-42}^{488}$ was removed by washing the cells with ice–cold PBS. The cells were treated with the second labeled $A\beta_{1-42}$, $A\beta_{1-42}^{633}$, at 4°C for another 30 min. After that, the cells were washed again to remove unbound $A\beta_{1-42}^{633}$, were incubated in fresh medium at 37 °C for 3 h to permit internalization of $A\beta_{1-42}$, and were imaged by confocal microscopy (**Figure 4–16** c). Most of internalized $A\beta_{1-42}$ colocalized with each other, suggesting coaggregations of both labeled $A\beta_{1-42}$ species. The Positive NFRET signals between both labeled $A\beta_{1-42}$ species inside the cell confirmed that they form coaggregates.

Based on the observation that by incubating <60 min, either at 500 nM or 1 µM $A\beta_{1-42}$ associated only with the plasma membrane (**Figure 4–16** a & b), we conclude that $A\beta_{1-42}^{488}$ coaggregated with $A\beta_{1-42}^{633}$ while located on the plasma membrane, either on the membrane surface or in a compartment that is localized on the membrane. The membrane bound aggregates were then taken up by endocytosis after the cells were returned to 37°C.

To verify that the FRET signal is specific to coaggregation of $A\beta_{1-42}$ and is not an artefact of the label or calculation method of FRET, we used transferrin (Tf) as a negative control.

After incubating SH–EP cells with two types of fluorescent transferrin conjugates, Tf/Alexa488 (5 µg/ml) and Tf/Alexa647 (10 µg/ml), at 4°C for 45 min, colocalization of both Tf were observed, but no FRET between them (**Figure 4–16** d). Sensitized emission FRET analysis were based on confocal microscopy images, and calculated using the same method used in **Figure 4–16** a and c (Feige et al. 2005).

These data strongly suggest that the FRET between $A\beta_{1-42}$ molecules results from a specific aggregation process.

For a more comprehensive analysis of the membrane assisted aggregation and subsequent uptake of $A\beta_{1-42}$ monomers, the cells were treated with monomeric $A\beta_{1-42}^{565}$ at various concentrations (0 – 1600 nM) in 96–well plates at 4 °C for 45 min. Following a wash off process with ice–cold PBS to remove unbound $A\beta_{1-42}$, the cells were further incubated in fresh medium. Subsequently, the temperature was raised to 37°C to permit internalization of $A\beta_{1-42}$ and the cells were incubated for 24 h. Intracellular $A\beta_{1-42}^{565}$ was quantified by HCS microscopy (**Figure 4–17**). Intracellular $A\beta_{1-42}^{565}$ aggregate signals could be detected at $A\beta_{1-42}^{565}$ monomer concentrations above 200 nM, similar to the threshold concentration (~ 300 nM) we previously observed for monomer uptake at 37°C (**Figure 4–12**). These data demonstrate that $A\beta_{1-42}$ binds to the plasma membrane and forms aggregates prior to cellular uptake, that the cell membrane assists the $A\beta_{1-42}$ aggregation, and that monomer uptake requires a critical concentration of membrane–bound $A\beta_{1-42}$.

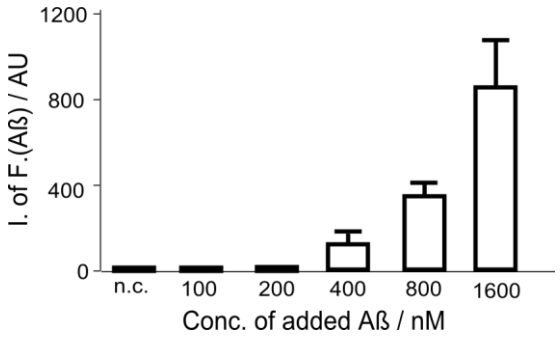

Figure 4–17: The concentration–dependence manner of $A\beta_{1–42}$ uptake at 4°C. SH–EP cells were treated with monomeric $A\beta 1_{–42}^{565}$ (0 – 1600 nM) at 4°C for 45 min and then in fresh medium at 37°C for 24 h. Intracellular $A\beta_{1–42}^{565}$ was quantified by HCS microscopy. All results are represented as mean values ± SD of 6 replicate wells.

Conceivably, small $A\beta_{1–42}$ aggregates that are competent for uptake, could be forming in solution and then bind to the plasma membrane. However, a comparison of conditions and time scales of $A\beta_{1–42}$ aggregation in solution with those of the membrane binding experiment makes this hypothesis less likely. Incubation of cells with $A\beta_{1–42}$ monomer for 45 min at 500 nM was sufficient to initiate uptake. In this time frame, ThT positive $A\beta_{1–42}$ species did not form in solution under the same conditions (**Figure 4–18**). At monomer concentrations of 1500 nM, which is the approximate concentration used for uptake (**Figure 4–17**), the conversion intoβ–sheet–rich structures took more than 3 h.

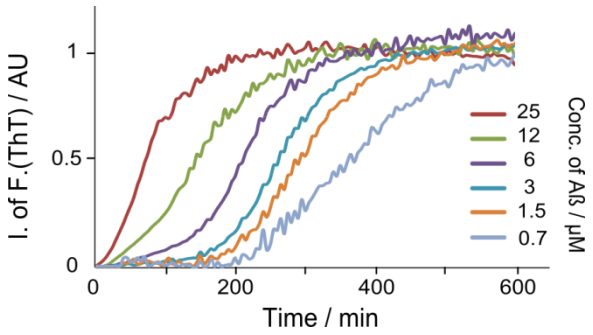

Figure 4–18: The concentration–dependence manner of monomeric $A\beta_{1–42}$ aggregation kinetics in vitro. Normalized $A\beta_{1–42}$ (0.7–25 µM) aggregation kinetics were monitored by ThT (20 µM) fluorescence. All results are represented as mean values of 3 replicate wells. Figure adapted from Sha Jin, Master Thesis "*Cellular uptake of amyloid–ß aggregates*".

Taken together, our results suggest that an efficient uptake required aggregated structures were formed on the plasma membrane. Binding of $A\beta_{1–42}$ to the plasma membrane occurred within the lag phase of ThT aggregation kinetics, well before the formation of β–sheet–rich aggregates. However, the experiment cannot exclude the possibility that $A\beta_{1–42}$ formed small, pre–β–sheet oligomers in solution, which then bound to the plasma membrane.

After the observation that monomers and/or small aggregates were already capable associated to the plasma membrane, we then examined the $A\beta_{1–42}$ aggregates inside the cells, whether they containedβ–sheet–rich structures or not.

The interaction of $A\beta_{1–42}$ with model membranes will be analyzed detailedly in section 4.2 of this thesis.

4.1.7 Internalized $A\beta_{1-42}$ aggregate containβ–sheet–rich structures

Our previous experiments found: i) monomeric $A\beta_{1-42}$ is internalized at concentrations above ~200 nM; ii) $A\beta_{1-42}$ aggregates on the plasma membrane, and iii) aggregates contained β–sheet structure were taken up very efficiently, all suggesting a possible conversion of monomeric $A\beta_{1-42}$ into β–sheet structure during uptake. To identify the secondary structure of internalized $A\beta_{1-42}$ in the cultured cells, we stained them by Thioflavin S (ThS) after their uptake.

ThS is widely used dye to identify amyloid structure in tissue or in the cultured cells. Like Thioflavin T, ThS display an enhanced Em.max with red shift at 482 nm occurring β–sheet binding (LeVine 1993). Binding and fluorescence of ThS to β–sheet structure is less pH sensitivity than ThT (LeVine 1993).

To resolve whether this conversion occurs, we performed a competitive uptake experiment between monomer at sub–critical concentration ($A\beta_{1-42}^{565}$, 150 nM), which was co–incubated with β–sheet aggregates ($A\beta_{1-42}^{633}$, 900 nM). Both species were labeled with different fluorophores to track in which compartment both monomers and aggregates were found. In addition,β–sheet–rich structures s were recognized by ThS.

SH–EP cells were preincubated at 4°C for 15 min, were treated with $A\beta_{1-42}^{565}$ monomer of 150 nM at 4°C for 20 min. Monomeric $A\beta_{1-42}^{565}$ was removed via washing with ice–cold cell culture medium, and then were treated with $A\beta_{1-42}^{633}$ aggregates of 900 nM at 4°C for 20 min. Following remove of unbound $A\beta_{1-42}$ peptide, the cells were incubated with ThS of 0.5% (w/v) at 4°C for 10 min. After that, the cells were further incubated in fresh cell culture medium with calcein (20 μM) at 37 °C for 1 h. After removing the calcein rich medium, the cells were incubated in calcein free medium at 37 °C, and live cell imaging were taken by spinning disk confocal microscopy at 37°C with 5 % CO_2 (**Figure 4–19**).

$A\beta_{1-42}^{565}$ was observed in both state, ThS positive (**Figure 4–19** circle 1) and ThS negative (**Figure 4–19** circle 2 and 3). In **Figure 4–19** circle 1 and 2 show two aggregates that contained both $A\beta_{1-42}^{565}$ and $A\beta_{1-42}^{633}$. However, only the ThS positive aggregates colocalized with calcein (**Figure 4–19** circle 1). In contrast, ThS negative structures did not colocalize with calcein and were thus not inside the endocytic vesicles (**Figure 4–19** circle 2). Similarly, $A\beta_{1-42}^{565}$ structures that had not coaggregated with $A\beta_{1-42}^{633}$ aggregates did not bind ThS and did not co localize with calcein (**Figure 4–19** circle 3).

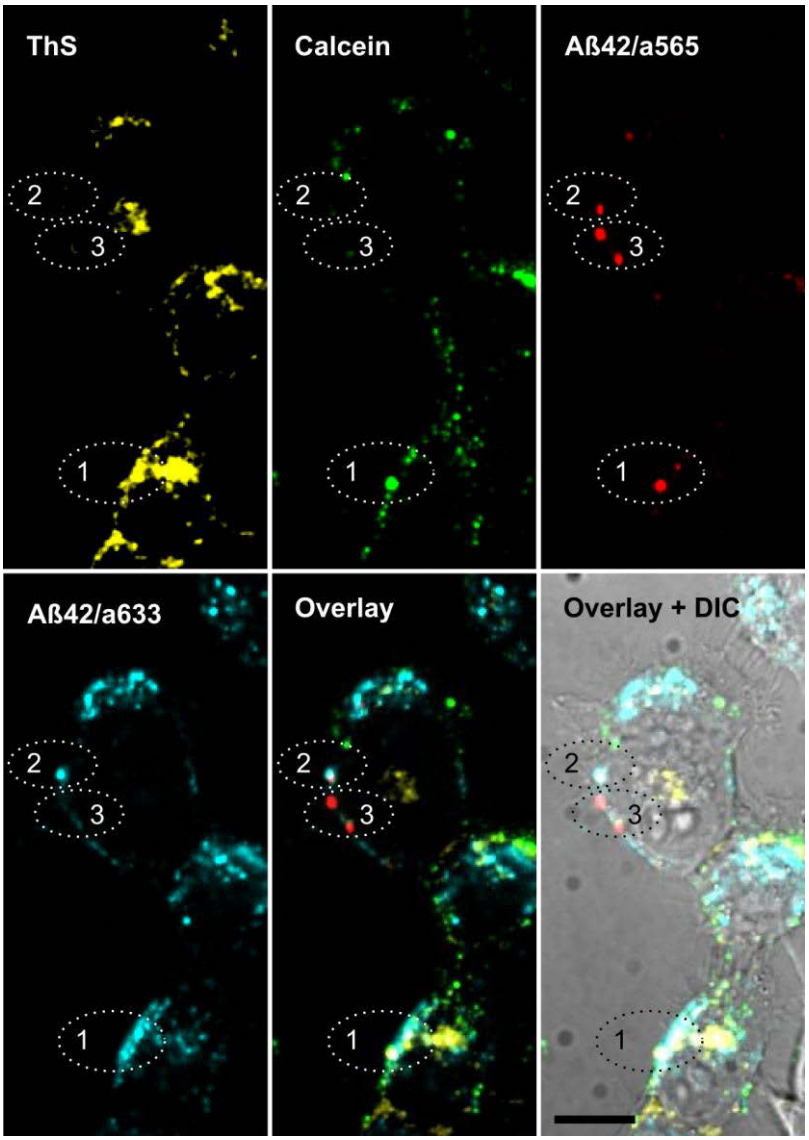

Figure 4–19: Thioflavin S (ThS) staining of internalized $A\beta_{1-42}$ on living cells. SH–EP cells were treated with $A\beta_{1-42}^{565}$ monomer (150 nM, red) and $A\beta_{1-42}^{633}$ aggregates (900 nM, cyan), at 4°C for 20 min each; were stained with Thioflavin S (ThS, 0.5% w/v, yellow) at 4°C for 10 min; were incubated with calcein (20µM, green) at 37 °C for 1 h; were imaged by spinning disk confocal microscopy. Internalized aggregates that contained β–sheet structures showed positive ThS staining and positive calcein signals (circle 1). ThS negative $A\beta_{1-42}^{565}$, co–aggregated with $A\beta_{1-42}^{633}$ (circle 2) or by itself (circle 3), was not taken up into endocytic vesicles and did not co–localize with calcein. Scale bar, 10 µm.

This means that ThS and calcein fluorescence signals were linked and that under these conditions only β–sheet aggregates located in endocytic vesicles. Sub–threshold concentrations of $A\beta_{1-42}$ monomers were capable of binding to the plasma membrane. These observations strongly suggest that $A\beta_{1-42}$ converted into aggregates on the membrane prior to uptake, coaggregation into β–sheet–rich structures was needed for their efficient uptake.

Our previous data indicate that $A\beta_{1-42}$ species with pre–β–sheet structure bound to the plasma membrane. Those β–sheet structures, which probably be formed directly on the plasma membrane, may play an important role for an efficient and successfully uptake of $A\beta_{1-42}$ by neuroblastoma cells in culture.

4.1.8 Efficient uptake correlates with formation of β–sheet–rich structures

To verify our hypothesis that formation of β–sheet structure is prerequisite of uptake and to determine which aggregate species could be taken up efficiently, we combined in vitro aggregation kinetics and cellular uptake experiments. $A\beta_{1-42}$ amyloid formation is monitored in vitro to collect $A\beta_{1-42}$ species at different stages of aggregation. Then their uptake is monitored through fluorescence of labeled $A\beta_{1-42}$.

Monomeric $A\beta_{1-42}$ (15 µM, with 10 % $A\beta_{1-42}{}^{565}$) aggregation kinetics was monitored by ThT fluorescence (**Figure 4–20** a, red curve). Samples at four time points, which corresponded to different phases of peptide aggregation: initiation (t0), lag phase (t1), growth phase (t2), and plateau phase (t3) were collected. The samples were characterized by circular dichroism spectroscopy (CD, **Figure 4–20** b). Within the lag phase (t0 and t1), $A\beta_{1-42}$ partially lost its disordered state. It adopted a β–sheet structure during the growth phase (t2 and t3) of ThT kinetics.

To determine which of these aggregation states are efficiently taken up, the SH–EP cells were incubated with these aggregates (t0 – t3) at 37 °C at a 150 nM equivalent monomer concentration. This is a concentration below the threshold concentration, at which $A\beta_{1-42}{}^{565}$ monomers could not be internalized but preformed aggregates could be (**Figure 4–5** a and c; **Figure 4–12** a and c). After 24 h incubation, intracellular $A\beta_{1-42}$ aggregates were quantified by HCS microscopy (**Figure 4–20** c). Intracellular $A\beta_{1-42}{}^{565}$ aggregates were detected in cells that had been treated with growth (t2) and the steady–state phase (t3) aggregates. In contrast, no uptake of $A\beta_{1-42}$ peptides was observed with samples from the initiation (t0) and lag phase (t1) of the polymerization reaction.

These data suggest that $A\beta_{1-42}$ aggregates at time points t2 and t3 that had β–sheet–rich structures are efficiently internalized, while unstructured monomers (t0) or small oligomers (t1) without β–sheet structure are not.

The efficient uptake of β–sheet–rich oligomers / aggregates might also explain why oligomeric $A\beta_{1-42}$ species have many times been observed to have higher cytotoxicity (Haass & Selkoe 2007; Walsh et al. 2002).

Our previous data show that neither form, monomer or small aggregates, had a strong effect on the count of living cells (**Figure 4–12** a and c), i.e. internalized $A\beta_{1-42}{}^{565}$ did not cause cell death. We therefore analyzed cell metabolic activities after treating with $A\beta_{1-42}$ by 3–(4,5–dimethylthiazol–2–yl)–2,5–diphenyltetrazolium bromide (MTT) reduction as a measure of cytotoxicity.

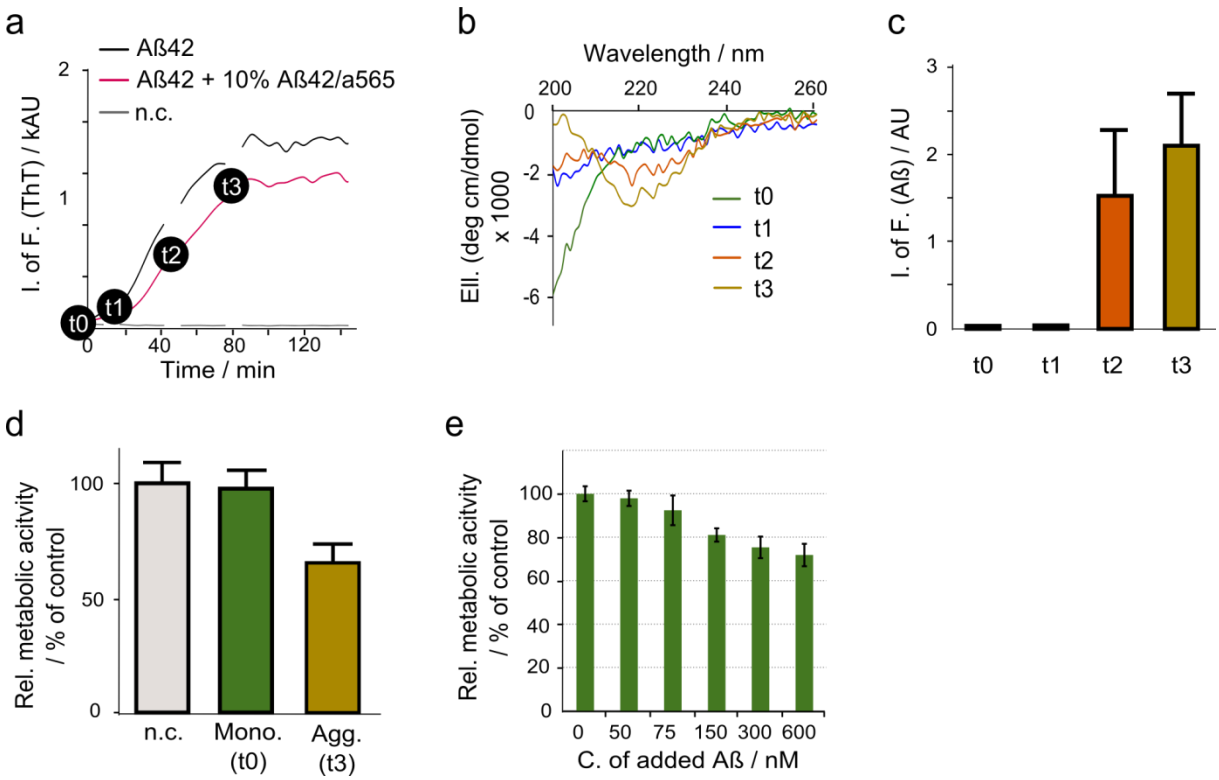

Figure 4–20: β–Sheet structure promotes $A\beta_{1-42}$ uptake. (a) Aggregation kinetics of monomeric $A\beta_{1-42}$ (15 µM) with 10 % $A\beta_{1-42}^{565}$ in PBS were monitored by ThT fluorescence. Aggregates were collected from the aggregation assay at four time points (t0 – t3). **(b)** Secondary structures of $A\beta_{1-42}$ from t0 – t3 were measured by circular dichroism spectroscopy. **(c)** $A\beta_{1-42}$ (t0–t3) were diluted to a final concentration of 150 nM, were added to SH–EP cells for 24 h incubation time at 37°C. Internalized $A\beta_{1-42}^{565}$ of fixed cells was quantified by HCS. **(d & e)** SH–EP cells were treated with $A\beta_{1-42}$ for 1 d at 37 °C, their metabolic activities were measured by MTT assay. The cells were incubated with $A\beta_{1-42}$ monomers (t0, 150 nM), aggregates (t3, 150 nM) or without $A\beta_{1-42}$ (n.c) **(d)**; or with monomeric $A\beta_{1-42}$ at 0–600 nM **(e)**. All results are represented as mean values ± SD of 3 replicate wells for ThT kinetics (a), of 6 replicate wells for uptake (c) and of 12 replicate wells for the MTT assay (d and e).

SH–EP cells were treated with unlabeled $A\beta_{1-42}$ preparations collected at time point t0 and t3 from ThT kinetics (**Figure 4–20** a, black curve). MTT assays were carried out after 24 h incubation at 37°C. $A\beta_{1-42}$ aggregates formed during the growth phase (t3) were significantly more toxic than monomers (t0), and inhibited metabolic activity (**Figure 4–20** d). $A\beta_{1-42}$ monomers became cytotoxic only at concentrations above 150 nM (**Figure 4–20** e), a point at which they also underwent internalization (**Figure 4–12** a). MTT assay was carried out after treating SH–EP cells with $A\beta_{1-42}$ monomer at a concentration range of 0–600 nM at 37°C for 24h. Thus, their toxicity was correlated to their more efficient uptake.

It should be noted that because of the dilution, the structure of aggregates at 150 nM in medium and at the time of uptake might be not the same as seen in the CD spectrum, which was measured at 15 µM (**Figure 4–20** b). Nevertheless, below 300 nM only $A\beta_{1-42}$ that contained β–sheet–rich structures (t2, t3) was internalized, while unstructured monomers

(t0) or small aggregates (t1) without β–sheet structure were not. This suggests that it was indeed the β–sheet aggregates that were taken up, rather than a different $A\beta_{1–42}$ species.

These data support the hypothesis that the formation of an ordered structure, β–sheet–rich structures, may be a prerequisite for efficient uptake and subsequent cytotoxicity of $A\beta_{1–42}$ aggregates in neuronal model cells. The plasma membrane may serve as a platform in formation of toxic aggregates.

4.1.9 Examination of intracellular location of internalized $A\beta_{1–42}$

The observations that internalized $A\beta_{1–42}$ aggregates located in endocytic vesicles raised the question by which endocytic pathway β–sheet–rich aggregates are internalized.

In previous experiments (in section 4.1.6.1), we had observed that uptake of $A\beta_{1–42}$ may be independent of clathrin–mediated endocytosis (CME, **Figure 4–14**). In those experiments, CME pathway was blocked by lowering the temperature to 4°C (Harding et al. 1983), and used transferrin as specific reporter to show the inhibition of CME pathway.

We also analyzed the internalization of $A\beta_{1–42}$ aggregates at 37°C under conditions, which permitted CME, and tested whether internalized $A\beta_{1–42}$ colocalized with CME or other endocytic marker.

SH–EP cells were treated with $A\beta_{1–42}{}^{565}$ β–sheet aggregates (150 nM, equivalent monomer concentration) at 37°C. Fixed cells were costained with endocytic markers by IF staining: clathrin for clathrin–mediated endocytosis; caveolin for receptor–independent endocytosis; early endosome antigen 1 (EEA1); Lysosome–associated membrane protein 2 (LAMP2). Primary antibodies were visualized by cy5 conjugated secondary antibody. Nuclei were stained with Hoechst 33342 (**Figure 4–21**). No colocalization with clathrin (**Figure 4–21** a) and LAMP2 (**Figure 4–21** b) was observed, supporting that $A\beta_{1–42}$ was not internalized via CME. Rather, internalized $A\beta_{1–42}{}^{565}$ colocalized with caveolin (**Figure 4–21** c) and EEA1 (**Figure 4–21** d), confirming that $A\beta_{1–42}{}^{565}$ was localized in endocytic vesicles and were taken up in a CME–independent pathway.

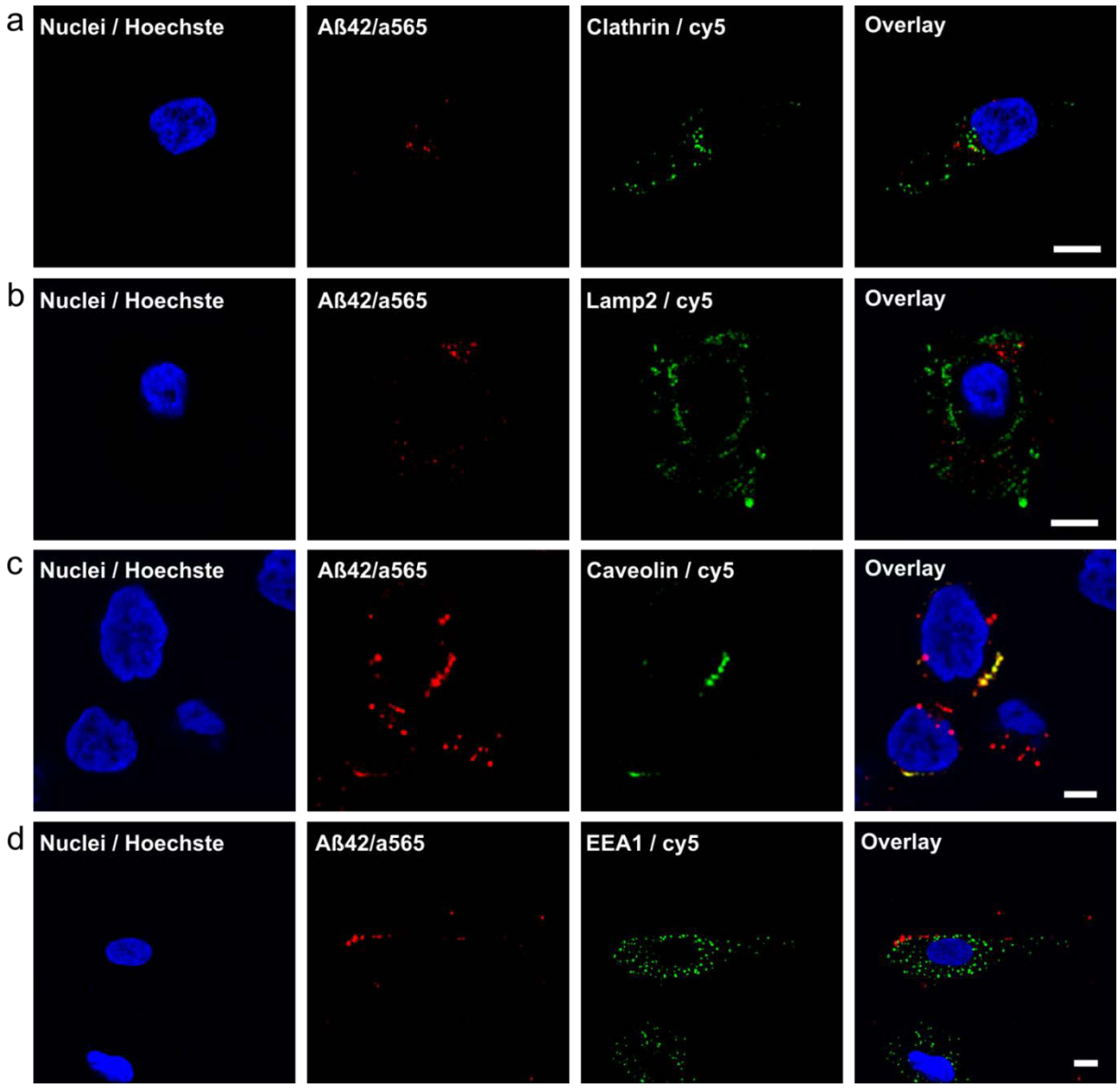

Figure 4–21: Costaining of the internalized $A\beta_{1-42}$ with markers of endocytosis. SH–EP cells were treated with $A\beta_{1-42}^{565}$ aggregates (150 nM, red) at 37°C. Colocalization of internalized $A\beta_{1-42}^{565}$ detected by clathrin **(a)**, LAMP2 **(b)**, caveolin **(c)**, EEA1 **(d)** by immunofluorescence staining. The primary antibodies of endocytic marker proteins were visualized by cy5 conjugated secondary antibody (green), and were imaged by confocal microscopy. Nuclei were stained with Hoechst 33342 (blue). Part of internalized $A\beta_{1-42}^{565}$ was colocalized with caveolin and EEA1, not with clathrin and LAMP2. Scale bars, 10 µm.

In a further control experiment, the CME pathway was selectively blocked by potassium depletion (Ivanov 2008; Larkin et al. 1983). The effect of K^+ depletion on $A\beta_{1-42}$ uptake was compared with the internalization of transferrin.

SH–EP cells were incubated with a hypotonic medium for 5 min, and then were incubated in isotonic medium with or without K^+. In both of cases, with or without K^+, $A\beta_{1-42}^{565}$ β–sheet aggregates of 150 nM (equivalent monomer concentration) or transferrin Alexa Fluor 647–conjugates (Tf/A647, 10 ng/ml) were added. Following the incubation at 37 °C for 1h,

intracellular $A\beta_{1-42}^{565}$ or Tf/A647 of fixed cells were analysed by HCS microscopy (**Figure 4–22**).

Internalization of $A\beta_{1-42}^{565}$ was not reduced by blocking CME pathway. Surprisingly, K^+ depletion actually stimulated $A\beta_{1-42}$ uptake. The increased amount of internalized $A\beta_{1-42}^{565}$ by incubating with K^+ depleted media might be caused by a reorganization of the cortical actin cytoskeleton (Altankov & Grinnell 1993; Rajasekaran et al. 2001; Ivanov 2008). In contrast, Tf/A647 uptake was inhibited by blocking CME via K^+ depletion. These results support our hypothesis that CME pathway does not play the primary role in the uptake of β–sheet–rich $A\beta_{1-42}$ aggregates.

Taking together, we conclude that the cellular uptake of β–sheet $A\beta_{1-42}$ aggregates was achieved via a clathrin independent pathway. Alternatively, internalized $A\beta_{1-42}$ may have progressed into late endosomal compartments at the time of fixation, that may lead to only part of internalized $A\beta_{1-42}$ colocalize with EEA1 (**Figure 4–21** d). The exact mechanism and the precise uptake pathway of $A\beta_{1-42}$ monomers via membrane–assisted aggregation should be discussed in future studies.

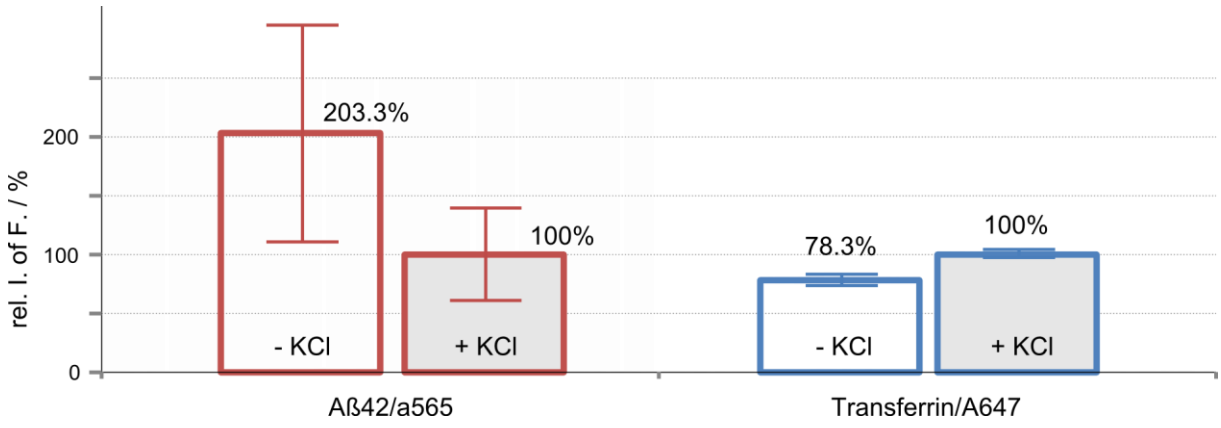

Figure 4–22: Blocking clathrin–mediated endocytosis (CME) pathway by potassium depletion. SH–EP cells were incubated with $Aß_{1-42}^{565}$ aggregates (150 nM) or transferrin Alexa Fluor 647–conjugates (Tf/A647, 10 ng/ml) at 37°C for 1h in K^+ depleted (–KCl) or not depleted (+KCl) medium. Intensities of fluorescence in cells incubated in –KCl media were normalized of those in +KCl media. Uptake of Tf/A647 was reduced by blocking CME, whereas uptake of $A\beta_{1-42}^{565}$ was increased. All results are represented as mean values ± SD of 6 replicate wells.

4.1.10 Inhibition of $A\beta_{1-42}$ protofibril uptake by using chemical compound

In studying the cellular uptake of monomeric $A\beta_{1-42}$, we found their aggregation into β–sheet–rich structures had strongly promoted their internalization.

In this section, we changed our view from monomers to well–formed protofibrils, and investigated whether a structure change by treatment with a chemical compound would affect their uptake.

A small hydrophobic molecule, named AMC (unpublished, provided from AG Wanker, MDC–Berlin) was used, which may disturb the structure and change the solubility of $A\beta_{1-42}$ protofibril. We tested, whether cellular uptake of protofibrils would consequent change after their treatments by AMC.

The $A\beta_{1-42}^{565}$ protofibrils that used were isolated by SEC, had high molecular weight, and were relative homogenous (**Figure 4–1**). This protofibrillar $A\beta_{1-42}^{565}$ could be internalized directly and more efficiently than monomeric form by SH–EP cells (**Figure 4–5** a).

To test the effect of the durg on $A\beta_{1-42}$ uptake, $A\beta_{1-42}^{565}$ protofibrils of 15 µM (equivalent monomer concentration) were pretreated with AMC in buffer (DMSO) in a dose–dependent manner, at 3 – 1.5 – 0.75 – 0 µM, at 37 °C for 1 d, respectively, before the uptake experiments. The molar ratios of $A\beta_{1-42}$ to AMC were in 5 – 10 – 20 – 0. In this group, both $A\beta_{1-42}^{565}$ protofibrils and AMC had relatively high concentrations. In a second group, the concentrations of $A\beta_{1-42}^{565}$ protofibril and AMC were lowered. But, their molar ratios were maintained at the same level as in the first group. $A\beta_{1-42}^{565}$ protofibrils and AMC were mixed and incubated in cell culture media with $A\beta_{1-42}^{565}$ at 150 nM (equivalent monomer concentration), 100 times lower than the concentration of the first group. Correspondingly, AMC had a concentration range at 30 – 15 – 7.5 – 0 nM. The mixtures were incubated at 37 °C for 1 d, just as the samples in first group.

After 1 d incubation, $A\beta_{1-42}^{565}$ protofibrils and AMC mixtures were added to SH–EP cells for uptake experiments. The samples of the first group that contained $A\beta_{1-42}^{565}$ protofibrils and AMC in higher concentrations were diluted in cell culture media and then were added to the cells, so that the final concentration of $A\beta_{1-42}^{565}$ protofibrils in the cell culture media was at 150 nM, and AMC were at 30 – 15 – 7.5 – 0 nM. Thus $A\beta_{1-42}^{565}$ protofibrils and of AMC have the same concentration as in the second group. The $A\beta_{1-42}^{565}$ protofibrils and AMC mixtures of second group were added directly to the cells, i.e. $A\beta_{1-42}^{565}$ protofibrils of 150 nM and AMC at 30 – 15 – 7.5 – 0 nM. Additionally, in a third group as comparison experiments, $A\beta_{1-42}^{565}$ protofibrils (final concentration 150 nM in cell culture media, equivalent monomer concentration) and AMC (final concentration 30 – 15 – 7.5 – 0 nM in cell culture media) were added to the cell, namely $A\beta_{1-42}$ and AMC had the same concentrations and molar ratios as in the second group, but without pretreatment.

Internalized $A\beta_{1-42}^{565}$ of fixed cells was quantified by HCS microscopy after incubation at 37°C for 24h incubation time (**Figure 4–23** a). The pretreatment of $A\beta_{1-42}^{565}$ protofibrils with AMC strongly reduced the uptake of Aβ in a dose dependent manner. This was especially true in the first group, the pretreatment of $A\beta_{1-42}^{565}$ protofibrils in buffer, when $A\beta_{1-42}$ and AMC both had relatively high concentrations. Treatment with AMC showed no significant influence on the cell count (**Figure 4–23** b).

However, our understanding on the mechanism of AMC is still very limited. One of the possible reaction mechanisms might be that, AMC may bind to hydrophobic regions of $A\beta_{1-42}$ protofibrils thanks to its hydrophobic properties. This may cause a change of the solubility and / or surface–hydrophobicity of $A\beta_{1-42}$ protofibrils, leading to a fragmentation of protofibrils and / or change the binding interface of the plasma membrane and $A\beta_{1-42}$. Alternatively, altered structure of $A\beta_{1-42}$ protofibrils via AMC binding may benefit its intracellular degradation. Therefore, a further study of AMC effect mechanism on $A\beta_{1-42}$ is not only to be looking for a possible drug for AD, it can also promote our understandings about the toxicity and pathogenesis related structures of $A\beta_{1-42}$.

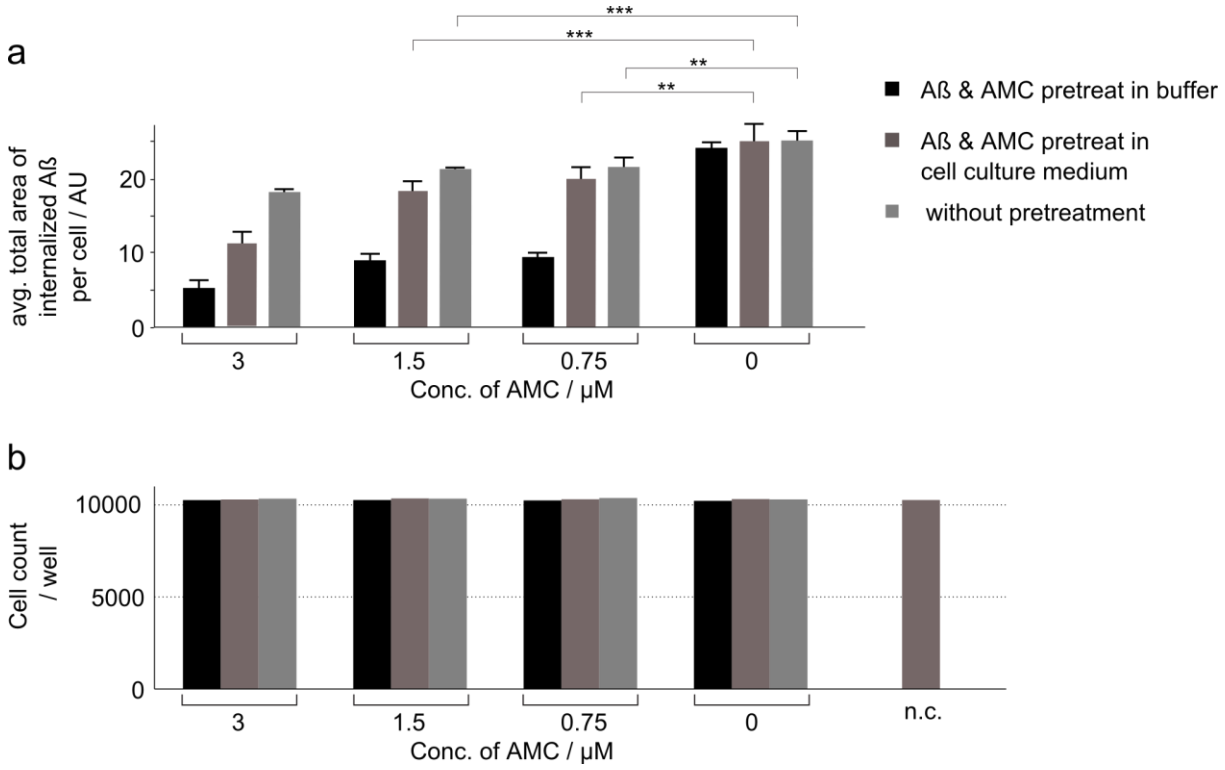

Figure 4–23: Inhibition of $A\beta_{1-42}$ protofibril uptake by AMC. (a) Preincubation of $A\beta_{1-42}^{565}$ protofibril with AMC lead to a reduction of cellular uptake of $A\beta_{1-42}^{565}$. **(b)** Average Cell count per well. All results are represented as mean values ± SD of 6 replicate wells. All pairwise comparisons were used t–test, *** $P < 0.0002$, ** $P < 0.002$.

4.1.11 Summary

Taken together, our data allow us to map the first steps in $A\beta_{1–42}$ internalization starting from the monomeric peptide. First, Aβ monomers or very early disordered oligomers bind rapidly to the plasma membrane. Their binding partner could be either the lipid bilayer itself or plasma membrane proteins. Numerous studies have demonstrated interaction of Aβ with lipid bilayers, which will be scrutinized in section 4.2. On the plasma membrane, $A\beta_{1–42}$ peptide aggregate into β–sheet–rich structures either on the membrane surface itself or in a compartment that is very close to the membrane, from which they are taken up into endocytic vesicles. The highly efficient uptake of β–sheet–rich structures, suggests that aggregation into, or co–aggregation with β–sheet aggregates occurs.

In the case of $A\beta_{1–42}$ monomers uptake, the peptide concentration has to be sufficient to initiate the first two steps of the process, resulting in a threshold for internalization at the saturation concentration, or critical concentration, for $A\beta_{1–42}$ aggregation (Usui et al. 2009). In contrast, no concentration threshold exists for the internalization of preformed $A\beta_{1–42}$ aggregates with β–sheet structure. They are internalized more efficiently and at much lower concentrations than the monomer.

This has several implications for the possible mechanism of $A\beta_{1–42}$ toxicity. In our experiments metabolic inhibition was directly correlated with the formation and/or uptake of β–sheet–rich aggregates. Aggregated species have been found to play a central role in Aβ toxicity, not all of which are large β–sheet–rich structures (Walsh et al. 2002). It is tempting to speculate that small oligomers may have a higher affinity to the plasma membrane than the monomeric peptide, facilitating the conversion to β–sheet–rich structures and subsequent internalization. Our results demonstrate that, unlike monomers, pre–existing Aβ aggregates are internalized at low nanomolar concentrations, which corresponds to previously observed binding of Aβ oligomers to neuronal plasma membranes at nanomolar concentration (Johnson et al. 2013; Johnson et al. 2011).

Our experiments did not provide evidence that uptake of aggregated proceeds via clathrin–mediated endocytosis. $A\beta_{1–42}$ aggregates may be taken up via receptor independent endocytosis, as had been observed previously (Omtri et al. 2012). Other pathways for the internalization of amyloidogenic proteins have been discussed. Synthetic peptide aggregates of sizes < 500 nm were taken up into HEK cells by non–specific endocytosis whereas larger aggregates were internalized by a mechanism similar to phagocytosis (Couceiro et al. 2015). Tau aggregates can be internalized via micropinocytosis, mediated by glycoaminoglycans (Holmes et al. 2014). It is possible that Aβ aggregates enter the cell by the same pathway.

Secondly, we found that Aβ aggregates can form in a concentration–dependent manner through self–assembly of monomers on the plasma membrane. It has long been known that lipid interaction promotes $A\beta_{1–40}$ transition to β–sheet structure (Terzi et al. 1995) and our

data support the interpretation that this process is central to Aβ uptake and toxicity. Our data suggest the binding of $A\beta_{1-42}$ monomers to the lipid bilayer or to membrane proteins may be the first step in the formation of cytotoxic Aβ aggregates *de novo*. Factors that increase partitioning of Aβ to the plasma membrane will likely promote the formation of β–sheet–rich aggregates on the membrane. These include lipid peroxidation products, such as seco–cholesterol and 4–hydroxy–nonenal that facilitate Aβ membrane binding and aggregation (Bieschke et al. 2005; Siegel et al. 2007; Murray et al. 2007), divalent metal ions promoting Aβ membrane interaction (Curtain et al. 2003), and interaction with membrane proteins (Lai & McLaurin 2010). Our data support a central role of endocytosis in Aβ cytotoxicity (Yu et al. 2014) and provide strong evidence that aggregation precedes endocytosis, a question that had previously not been conclusively resolved (Friedrich et al. 2010; Hu et al. 2009). This experimental evidence may improve our understanding of AD pathology and may inform more focused therapeutic approaches targeting membrane binding and self–assembly of the Aβ peptide.

4.2 Interaction of $A\beta_{1-42}$ with model membrane system

In the previous chapter (4.1) we discussed relationship of the toxicity of misfolded $A\beta_{1-42}$ aggregates and their cellular uptake, and provided evidence for the possible location of cytotoxic aggregates formation. Non–toxic $A\beta_{1-42}$ species, including monomers and small aggregates, associate rapidly to the plasma membrane, where they convert into cytotoxic aggregates. The cellular metabolism is inhibited by internalisation those aggregates that contained β–sheet–rich structures. These observations raise the question how the plasma membrane can serve as a platform for aggregation. A possible hypothetical mechanism is that $A\beta_{1-42}$ peptide accumulates on the plasma membrane, increasing its local concentration, which may lead to a rapid aggregation. However, the plasma membrane is a very complicated system consisting of numerous types of lipid in different phases, a great number of integral and peripheral membrane proteins. $A\beta_{1-42}$ might bind to lipids, proteins or protein receptors of the plasma membrane.

Based on our observations that $A\beta_{1-42}$ associated to the plasma membrane rapidly with highly affinity; and many other studies demonstrating the interaction of $A\beta_{1-42}$ with lipids and membranes (Wood et al. 2003), the following chapter will focus on the mechanism of $A\beta_{1-42}$–lipids interaction, specifically which $A\beta_{1-42}$ aggregate species interact with lipid bilayers, with which lipid compositions and phases $A\beta_{1-42}$ is interacting.

For this end, giant unilamellar vesicles (GUVs) and giant plasma membrane vesicles (GPMVs) were used to study the interaction of $A\beta_{1-42}$ with lipid bilayers. Models membrane systems, such as large unilamellar vesicles (LUVs) and GUVs, of definable lipid compositions were

broadly used for investigating interactions of Aβ or another misfolded protein, e.g. α–Synuclein, with membrane lipids (Morita et al. 2010; Wood et al. 2003; Morita et al. 2014; Stöckl, Fischer, et al. 2008). GUVs were prepared in varying lipid compositions, either as single phase vesicles or with liquid disordered (ld) and liquid ordered (lo) domains. GPMVs were isolated from the plasma membrane of neuroblastoma cells, the SH–EP cells, which were model cell line of our cellular uptake and cytotoxicity studies in chapter 4.1. As a consequence of their sizes $A\beta_{1-42}$–lipids interactions on the membranes of GUVs and GPMVs can be directly visualized via fluorescently label by using confocal microscopy.

Surprisingly, we observed that $A\beta_{1-42}$ did not only bind to lipid bilayer (GUVs) and isolated plasma membranes (GPMVs), but were also capable of remodelling membrane curvature, inducing small vesicle–like invaginations in the membrane bilayer.

4.2.1 $A\beta_{1-42}$ aggregation kinetics in GUVs buffer system

Monomeric $A\beta_{1-42}$ peptides are known to form aggregates rapidly and spontaneously. Their aggregation kinetics are influenced strongly by changing the aggregation conditions, such as ionic strength and pH value of the buffers. It is essential to determine the influence of GUVs buffer composition on the aggregation kinetics of $A\beta_{1-42}$ and to examine whether the $A\beta_{1-42}$–membranes interaction varied as a function of the peptide's aggregation state, before discussing the interaction of different aggregation states of $A\beta_{1-42}$ with model membranes. For GUVs preparations, sucrose (swelling buffer) and glucose (microscopy buffer) were used at high molarity, which may also affect aggregation kinetics of $A\beta_{1-42}$. We first monitored the aggregation kinetics of $A\beta_{1-42}$ monomer in sucrose and glucose buffers by using ThT fluorescence, and comparing them with kinetics in PBS.

Monomerized $A\beta_{1-42}$ (15 µM) was incubated in glucose buffer (280 mM), in sucrose buffer (280 mM), in mixture of sucrose and glucose (280 nM each, in 1:1 v/v) or in PBS, respectively. Na_2HPO_4 (5.8 mM) and NaH_2PO_4 (5.8 mM) were added to all the types of buffer systems to keep their pH values constantly at 7.4. Aggregation kinetics were carried out in a plate reader with shaking at 25°C and were monitored by ThT fluorescence (**Figure 4–24**).

The kinetic curves have similar amplitudes of ThT fluorescence intensities at the steady state in glucose, sucrose and glucose/sucrose mix buffers, decreasing only slightly in PBS. However, the length of lag phases varies greatly. In glucose buffer, the lag phase was very short. $A\beta_{1-42}$ aggregation was accelerated in glucose buffer compared to PBS and sucrose buffer. In contrast, the aggregation kinetics were slowed down in sucrose buffer. The lengths of the lag phase were measured to be about 15 min for the glucose and about 50 min for the sucrose buffers, respectively. Aggregation kinetics in the 50% glucose plus 50% sucrose mix that

corresponded to the conditions encountered by $A\beta_{1-42}$ when mixed with GUVs preparations was identical to those in glucose buffer.

From these data, we conclude that the time interval between 15 min and 50 min is crucial for lag phase of $A\beta_{1-42}$ aggregation. Membrane interaction assays will therefore concentrate on processes in this time interval.

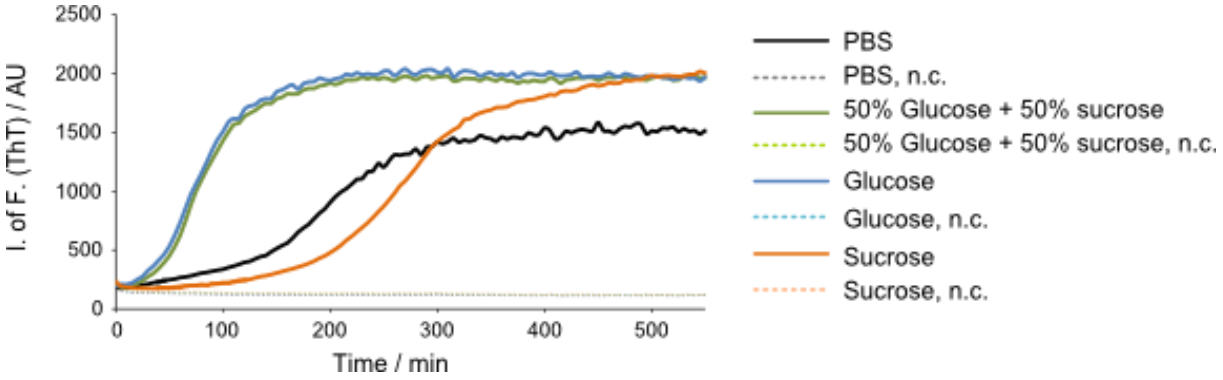

Figure 4–24: ThT aggregation kinetic in PBS, glucose and sucrose buffer. $A\beta_{1-42}$ monomer of 15 µM was incubated with ThT (20 µM) in different buffers at 25°C. The lengths of the lag phases are 15 min for the glucose and for glucose / sucrose mix; 20 min for PBS; and about 50 min for the sucrose buffers. n.c., negative control, without $A\beta_{1-42}$ in solution. All results are represented as mean values of 3 replicate wells.

4.2.2 $A\beta_{1-42}$ aggregation kinetics in presence of lipid

According to possible influences of $A\beta_{1-42}$–membrane interaction itself to $A\beta_{1-42}$ monomer aggregation kinetics, we examined $A\beta_{1-42}$ aggregation kinetics in presence of lipids in the buffer systems and under experimental conditions we used. For these experiments, large unilamellar vesicles (LUV) were used rather than GUV. Compared to GUVs, LUVs could provide larger lipid–water interface at the same lipid concentration as GUVs, they are more stable than GUVs, which would not survive the shaking during the aggregation assays.

LUVs were prepared from pure synthetic dioleoyl phosphatidylcholine (DOPC) by using a 200 nm membrane filter (as described in methods 3.2.2.1). Monomerized $A\beta_{1-42}$ (15 µM) was incubated with DOPC LUVs in a lipid monomer concentration range of 0 – 750 µM in PBS. The molar ratios of lipid to $A\beta_{1-42}$ were in the range of 0 – 50 (equivalent monomer concentration). Aggregation kinetics were monitored by ThT fluorescence intensity at 25 °C using a fluorescence plate reader.

The kinetics displayed similar time courses, increasing the concentrations of lipid delayed weakly delayed the aggregation kinetics (**Figure 4–25** a).

For quantitative analysis of the aggregation kinetics with different concentration, the times to reach 50% maximal amplitude (t_{50}) of kinetic traces were measured (Hurshman et al. 2004). The values of t_{50} were plotted in function of lipid concentrations on a logarithmic scale to test if the effect of lipid on aggregation of $A\beta_{1-42}$ could be modelled by simple monomer binding (**Figure 4–25** b).

Then logarithms (to the base e) of t_{50} ($\ln(t_{50})$) versus lipid concentration (lnC) were plotted, to test whether the presence of the lipid membrane changed the reaction order of aggregation(**Figure 4–25** c) (Hurshman et al. 2004). A slope of 0.07, which was calculated by linear regression of the data, suggests that in this case DOPC lipid had no influence on reaction order and thus on the mechanism of $A\beta_{1-42}$ aggregation and very little effect on the lag phase time of its aggregation.

In a complementary assay the concentration dependence of $A\beta_{1-42}$ aggregation kinetics were measured in the presence of DOPC lipid. Monomerized $A\beta_{1-42}$ in a concentration range of 2 – 20 µM (equivalent monomer concentration) was incubated with DOPC LUVs at a constant concentration of 150 µM (by lipid monomer concentration), i.e. with the molar ratios of lipid to $A\beta_{1-42}$ from 7.5 to 75. Fluorescence intensities of ThT were normalized to the amplitude at the onset of plateau phase (**Figure 4–25** d).

$\ln(t_{50})$ vs lnC ($A\beta_{1-42}$ concentrations) plot shows $A\beta_{1-42}$ aggregation kinetic depends on its own concentration (**Figure 4–25** e and f). The aggregations were accelerated by increasing the concentration of $A\beta_{1-42}$ monomer with a slope of –0.8. The concentration dependence of the lengths of lag phases in these kinetics data are similar to the data in the absence of lipid (**Figure 4–18**). The slope of –0.8 indicates that aggregation kinetics are dominated by secondary nucleation (Cohen et al. 2013), but its efficiency may be slightly reduced in the presence of lipids.

Combining the data of those experiments, the concentration of $A\beta_{1-42}$ monomer as variables at constant lipid concentration (**Figure 4–25** a–c), and the concentration of lipid as variables at constant $A\beta_{1-42}$ monomer concentration (**Figure 4–25** d–f), we conclude that: i) the aggregation kinetics of $A\beta_{1-42}$ in the presence of DOPC lipids show a dependence on concentration of $A\beta_{1-42}$, as had been observed previously without the lipids (**Figure 4–18**). Both cases are dominated by secondary nucleation; ii) the aggregations have a very weak dependence on lipid concentration in lipid to $A\beta_{1-42}$ molar ratios from 0 – 50, which suggests that the DOPC lipid membrane interacts with $A\beta_{1-42}$ in its monomeric or oligomeric state but does not change the rate limiting step of aggregation under these experimental conditions. This interpretation corresponds to the model that the rate limiting step is secondary nucleation by fibrils, either by fragmentation or by secondary nucleation on the fibril surface (Cohen et al. 2013).

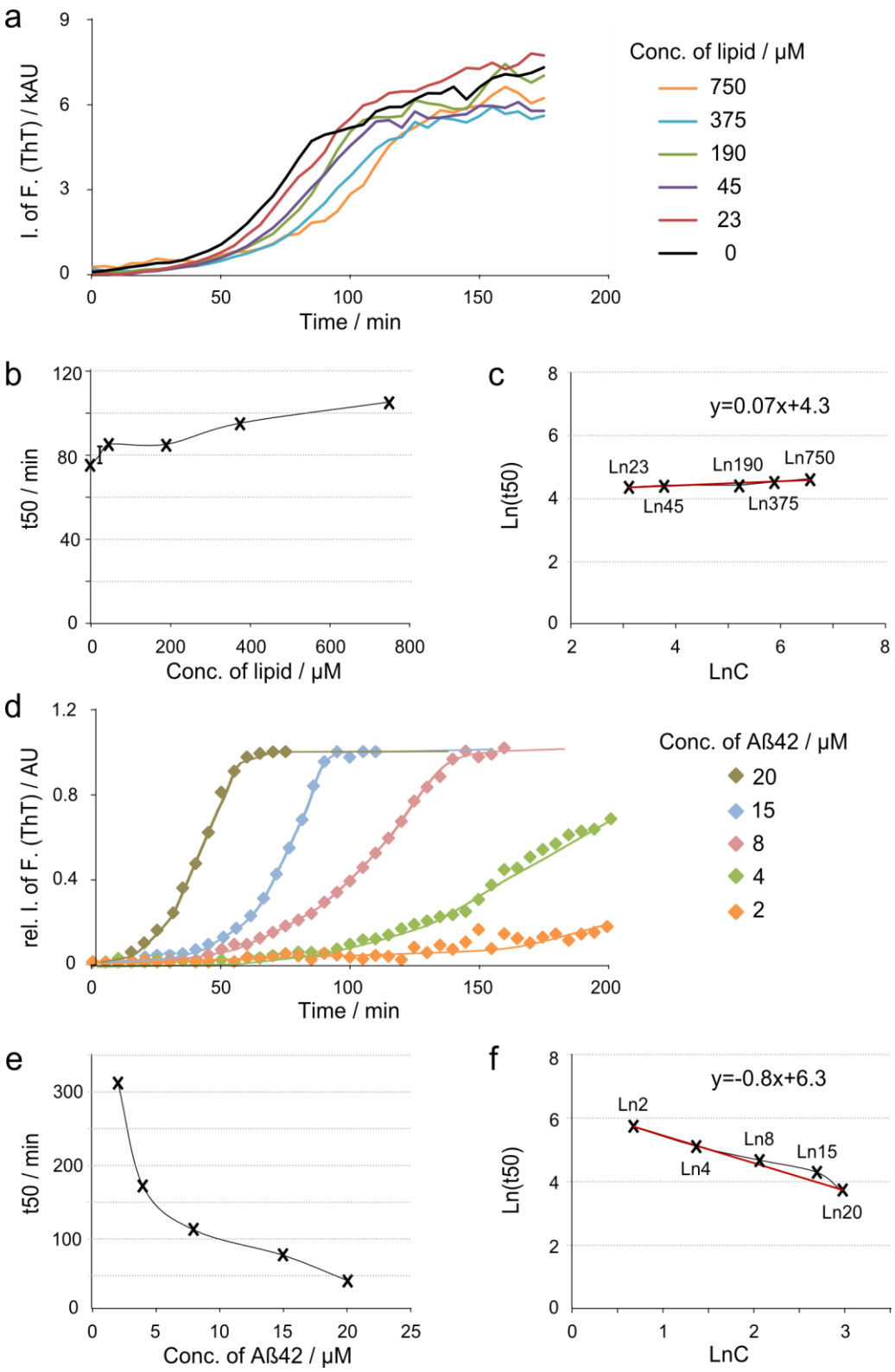

Figure 4–25: Aggregation kinetic of $A\beta_{1-42}$ monomer with DOPC large unilamellar vesicles (LUVs). (a) Aggregation kinetic of monomeric $A\beta_{1-42}$ (15 µM) with DOPC concentrations at 0 – 750 µM were monitored by ThT fluorescence intensity. **(b)** Half–maximal fluorescence times (t_{50}) were plotted in the function of the lipid concentration (lnC). **(c)** $Ln(t_{50})$ vs lnC (lipid concentration) plot, a slope of 0.07 was calculated by linear regression (red line). Change of DOPC concentration shows no significantly influence on aggregation kinetic. **(d)** The ThT aggregation kinetics shows a concentration dependent manner of monomeric $A\beta_{1-42}$ (2 – 20 µM) with constant DOPC concentration (150 µM). **(e)** t_{50} were plotted in the function of $A\beta_{1-42}$ concentrations. **(f)** $Ln(t_{50})$ vs lnC ($A\beta_{1-42}$ concentration) plot, with a slope of 0.8 calculated by linear regression (red line). ThT kinetics were accelerated by increasing $A\beta_{1-42}$ concentration. All results are represented as mean values of 3 replicate wells.

The same general features of $A\beta_{1-42}$ aggregation kinetics were observed in buffer systems we used: lag phase, growth phase and plateau phase. At 10 µM $A\beta_{1-42}$ concentration, these correspond to 0–15 min, 15–90 min, and >90 min, respectively. Therefore, the studies of $A\beta_{1-42}$ –membrane interaction would focus on these time intervals.

Our study of Aβ–membrane relationship was then carried out in the range of $A\beta_{1-42}$–lipid molar ratios between 0 – 50 (equivalent monomer concentration).

Notably, the aggregation assays of $A\beta_{1-42}$ in this section did not specifically probe aggregation in the membrane, but rather in both membrane and in bulk solution. The aggregation state in the membrane may be different from that of the peptide in solution, which may strongly affect aggregation kinetics under conditions when primary nucleation is rate limiting. However, this was not the case under the experimental conditions used in our $A\beta_{1-42}$ –membrane interaction assays.

4.2.3 $A\beta_{1-42}$–lipid bilayer interaction

Our observation showed that small $A\beta_{1-42}$ aggregates in disordered state are capable to bind rapidly to the plasma membrane (chapter 4.1.6). Based on the amphipathic character of $A\beta_{1-42}$, a possible interaction partner could be the membrane lipids.

To investigate the behavior of $A\beta_{1-42}$ toward lipid bilayer and to specify with which lipid phase $A\beta_{1-42}$ interacted, GUVs of definite lipid compositions were used. Phosphatidylcholine (PC) is the most abundant lipid in the membranes of mammalian cells, therefore we first probed the interaction of $A\beta_{1-42}$ with GUVs consisting 100 % DOPC, in which the lipid molecules adopt pure ld phase. GUVs consisting pure lo phase (raft GUVs) were prepared from DOPC, sphingomyelin (SSM) and cholesterol (Chol) in 1:1:8 molar ratios (Stöckl & Herrmann 2010). Both typs of GUVs were generated by electroformation as described in methods 3.2.2.2.

To directly visualize of $A\beta_{1-42}$ on the membrane by confocal microscopy, $A\beta_{1-42}$ was labeled with fluorescence dye Atto565 and was monomerized by high pH treatment and gel filtration as described in methods 3.2.1.3.

GUVs were incubated with monomeric $A\beta_{1-42}^{565}$ at a concentration of 10 µM at RT for 30 min (**Figure 4–26** a and c). Then $A\beta_{1-42}^{565}$ in the outside of GUVs were diluted to 100 nM by adding buffer (**Figure 4–26** b and d). The osmolarity of the buffer inside GUVs was 280 mOsm/kg and outside was 200 mOsm/kg.

An accumulation of $A\beta_{1-42}^{565}$ on the membrane of DOPC GUVs was observed after the dilution of $A\beta_{1-42}^{565}$ in outside, indicating a high affinity of $A\beta_{1-42}^{565}$ to membrane of DOPC

GUVs (**Figure 4–26** b). Additionally, a number of invaginations, could also be observed on the membrane (**Figure 4–26** a).

Comparing with DOPC GUVs, neither accumulation of $A\beta_{1-42}^{565}$ nor invagination could be observed in raft GUVs (**Figure 4–26** c and d, DOPC:SSM:Chol=1:1:8). DIC image verifies the presence of raft GUVs after dilution of $A\beta_{1-42}^{565}$.

Labeled sc–$A\beta_{1-42}$ peptide (sc–$A\beta_{1-42}^{565}$) was used as control, when incubating DOPC GUVs with sc–$A\beta_{1-42}^{565}$ (10 µM before and 100 nM after the dilution) at RT for 30 min, the accumulation of sc–$A\beta_{1-42}^{565}$ and invaginaion induction on the membrane are both negative (**Figure 4–26** e and f). This verified that interaction with membrane of DOPC GUVs was specific for the Aβ sequence and not the result of the fluorescent label.

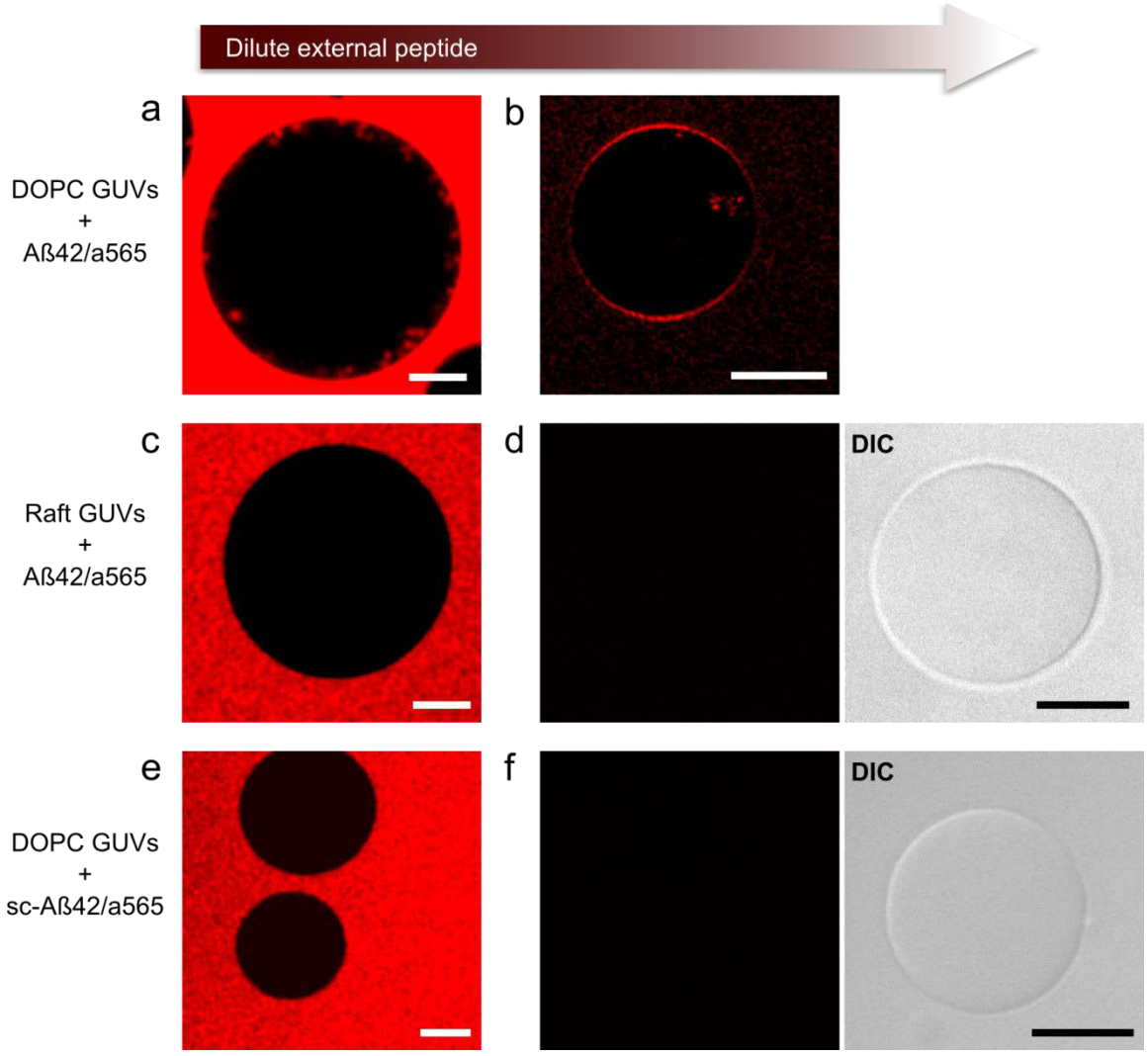

Figure 4–26: $A\beta_{1-42}$ & lipid bilayer interaction. $A\beta_{1-42}^{565}$ or sc–$A\beta_{1-42}^{565}$ of 10 µM were incubated with DOPC GUVs (100 % DOPC) or raft GUVs (DOPC:SSM:Chol=1:1:8) at RT for 30 min. Peptides in outside of GUVs were diluted. GUVs were imaged by confocal microscopy. Invaginations **(a)** and accumulation of $A\beta_{1-42}$ **(b)** were observed on membrane of DOPC GUVs, not on raft GUVs **(c & d)** or sc–$A\beta_{1-42}^{565}$ treated DOPC GUVs **(e & f)**. DIC images verify the presences of GUVs. Scale bars, 10 µm.

These results indicate $A\beta_{1-42}$ peptide accumulates specifically or preferred on the ld (DOPC GUVs) but not on lo phase (raft GUVs) of the GUVs membranes, and $A\beta_{1-42}$ –membrane interaction may lead to formation of invaginations. We next investigated whether $A\beta_{1-42}$ molecule and lipids of the GUVs membrane are close enough to each other to permit a Förster resonance energy transfer (FRET) between them. The questions, whether the invaginations are specifically induced by Aβ peptide and whether they depend on the aggregation state of Aβ and whether they occur within a specific membrane phase, will be discussed in later sections.

4.2.4 Interaction of $A\beta_{1-42}$ with DOPC GUVs

To demonstrate the interaction between Aβ and membrane lipids, we performed a FRET experiment between $A\beta_{1-42}$ molecules and lipids of the GUVs membrane, DOPC GUVs, containing 1% of the green fluorescent lipid analogue 1–palmitoyl–2–[6–[(7–nitro–2–1,3–benzoxadiazol–4–yl)amino]hexanoyl]–sn–glycero–3–phosphocholine (C6–NBD–PC, Ex.max at 460 nm and Em.max at 535 nm), were incubated with $A\beta_{1-42}{}^{633}$ monomers (4.5µM, Ex.max at 629 nm and Em.max at 657 nm) in a 96–well plate at RT for 15 min. Fluorescence emission spectra were measured at 25°C by using a fluorescence plate reader at excitation of 450 nm.

The FRET sample containing donor and acceptor displayed a decreased fluorescence intensity of donor emission and an increased fluorescence intensity of acceptor emission with a FRET efficiency approximate 0.4 (**Figure 4–27** a), providing strong evidence to $A\beta_{1-42}$–membrane binding. In contrast, the donor only sample emitted at its own typical spectrum with an Em.max at 540 nm. The acceptor only sample was not efficiently excited at 450 nm.

To verify that $A\beta_{1-42}$–lipid interaction event indeed happened on the membrane, GUVs were imaged by confocal microscopy (**Figure 4–27** b). Corrected FRET image was calculated from intensity–based images as described in methods section 3.2.12. Analysis by PixFRET showed a strong FRET signal on the membrane of GUV, demonstrating the interaction of $A\beta_{1-42}$ with PC molecules on the membrane.

The existence of the FRET signal also permits us to estimate the maximum distance between the $A\beta_{1-42}$ and the lipid to be smaller than 10 nm. This may be due to a direct interaction of the N–terminus with the membrane or may be caused by a compact conformation of the membrane bound $A\beta_{1-42}$ peptide.

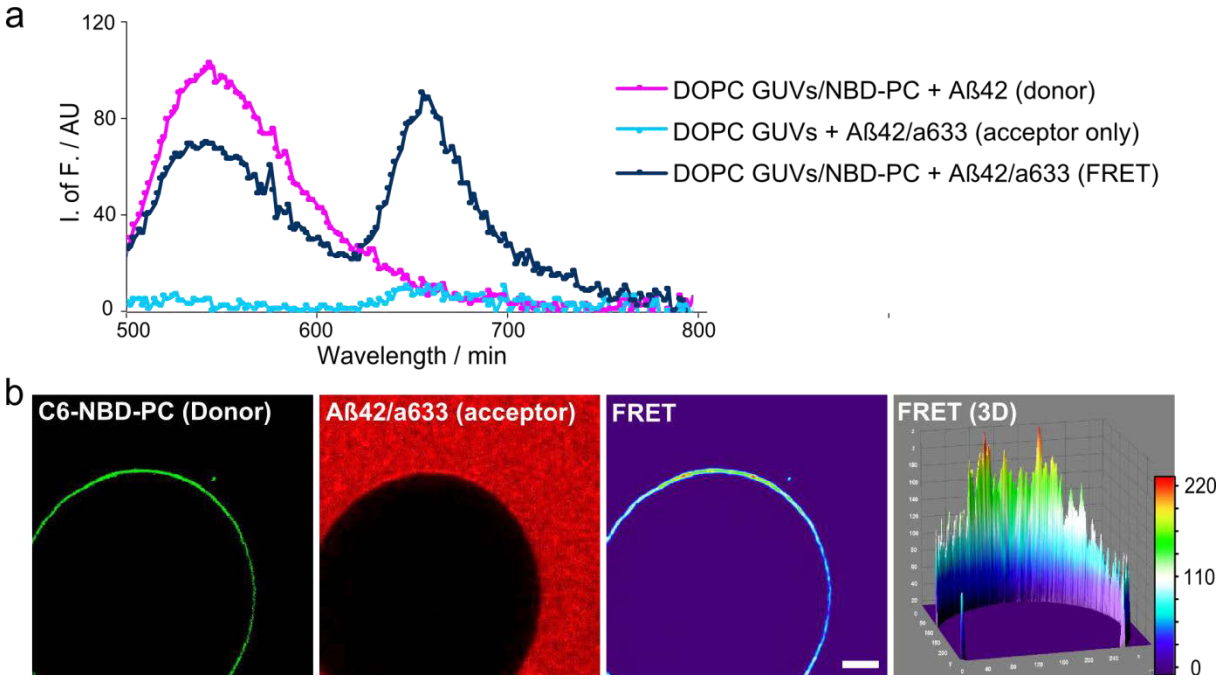

Figure 4–27: Interaction of $A\beta_{1-42}$ with DOPC GUVs. (a) DOPC/C6–NBD–PC (Ex.max=460 nm, Em.max=535 nm) GUVs with $A\beta_{1-42}$ monomer (4.5 µM) for donor only, DOPC GUVs with $A\beta_{1-42}{}^{633}$ monomer (4.5 µM, Ex.max=629 nm, Em.max=657 nm) for acceptor only, and DOPC/C6–NBD–PC with $A\beta_{1-42}{}^{633}$ monomer (4.5 µM, for FRET) were incubated at RT for 15 min, were measured by a fluorescence plate reader at excitation at 450 nm. A typical FRET spectrum, decreased donor emission and increased acceptor emission, with FRET efficiency ~0.4 was recorded. **(b)** A corrected FRET image of FRET sample was calculated by intensity–based images of confocal microscopy. Scale bar, 10 µm. Color scale, the relative FRET efficiency value of FRET images.

4.2.5 $A\beta_{1-42}$ induces invaginations in GUVs membrane

As indicated in section 4.2.4, invaginations were observed in the membrane of DOPC GUVs when studying the $A\beta_{1-42}$ –membrane interactions (**Figure 4–26** a), which could be possibly induced by the $A\beta_{1-42}$ peptide. In the control experiment, neither invagination nor accumulation of peptides could be observed on DOPC GUVs membrane when incubating with scrambled peptide sc–$A\beta_{1-42}{}^{565}$ (**Figure 4–26** e & f).

To confirm that those invaginations are specifically induced by $A\beta_{1-42}$ peptide rather than the fluorescent dye Atto565, DOPC GUVs were incubated with unlabeled monomeric $A\beta_{1-42}$ (10 µM) at RT for 15 min and were imaged by confocal microscopy.

A soluble but membrane–impermeable fluorescent dye, calcein (20 µM, green), was added to mark the buffer, to visualize the invaginations, and to demonstrate that the membrane bilayer remained intact. Invaginations were filled with the calcein dye.

To ensure that invaginations are not cause by random membrane fluctuations, the membrane was also kept at high tension during all the experiments. To do so, GUVs were maintained at a higher inside pressure than outside via an osmotic pressure difference. The

osmotic gradient was achieved through different sugar concentrations. The osmolarity inside the GUVs was 280 mOsm/kg and osmolarity of the outside buffer was 200 mOsm/kg.

Even under these conditions, i.e. GUVs membrane in a expansion state, small vesicle–shaped invaginations in a diameter of approximate 1 µm, were detected on the membrane of DOPC GUVs (**Figure 4–28** a).

In the absence of $A\beta_{1-42}$, invaginations could not be observed (**Figure 4–28** b). Likewise, no invaginations were observed on the membrane of DOPC GUVs when incubating with sc–$A\beta_{1-42}$ (10 µM) (**Figure 4–28** c).

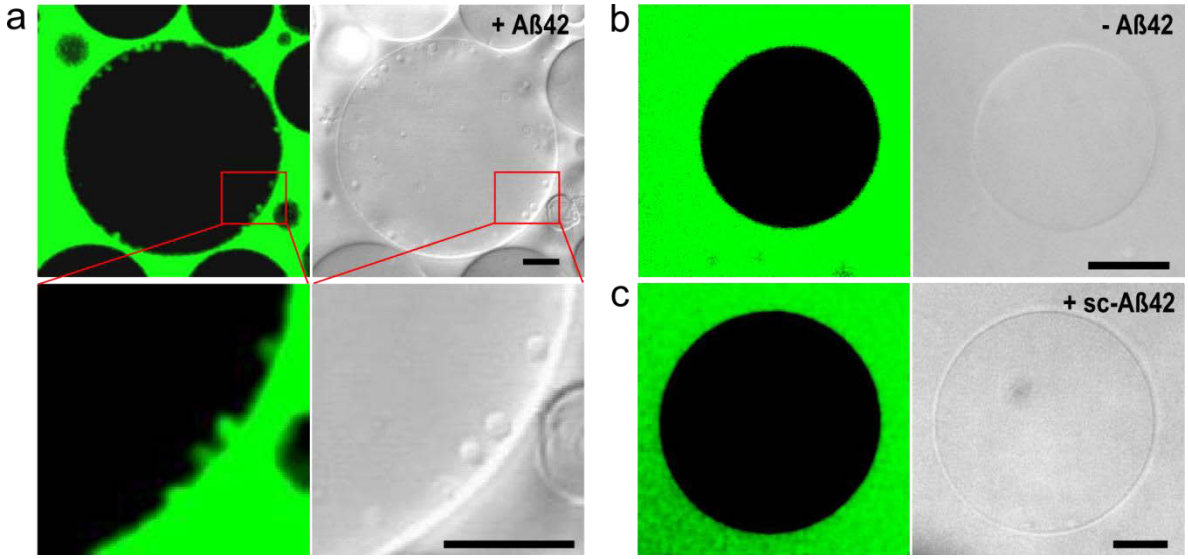

Figure 4–28: $A\beta_{1-42}$ induces invaginations in the membrane of DOPC GUVs. (a) Monomerized $A\beta_{1-42}$ (10 µM) was incubated with DOPC GUVs and calcein (20 µM, green) at RT for 15 min. The invaginations, diameter about 1 µm, were observed in the membrane of DOPC GUVs by confocal microscopy. No invagination was detected when incubating DOPC GUVs with calcein and buffer only **(b)** or with sc– $A\beta_{1-42}$ **(c)**. Scale bars, 10 µm.

These data show that the formation of membrane invaginations was specific to the Aβ peptide, suggesting that the modulation of membrane curvature is specific to the $A\beta_{1-42}$ peptide sequence and/or the ability of $A\beta_{1-42}$ to form aggregates.

We then tested if the formation of invaginations depended on lipid composition. $A\beta_{1-42}$ was incubated with GUVs generated from phospholipid mixtures, consisting of DOPC and uncharged lipid dioleyl–phosphatidylethanolamine (DOPE) in 1:1 molar ratio (PC/PE GUVs). The total concentrations of mixed lipids composition were identical to the DOPC concentration of pure DOPC GUVs. DOPC GUVs and PC/PE GUVs were incubated with $A\beta_{1-42}{}^{565}$ monomer (10 µM) in the presence of calcein (20 µM) at RT for about 15 min, and were imaged by confocal microscopy.

Invaginations, which were filled with the labeled $A\beta_{1-42}$ peptide and with calcein, were observed on the membrane of both types of GUVs, of PE/PC GUVs (**Figure 4–29** a) and of DOPC GUVs (**Figure 4–29** a). Those vesicular shaped invaginations with a diameter of approximate 1 µm are quite similar to those we previously found on the membrane of DOPC GUVs (**Figure 4–26** a and **Figure 4–28** a).

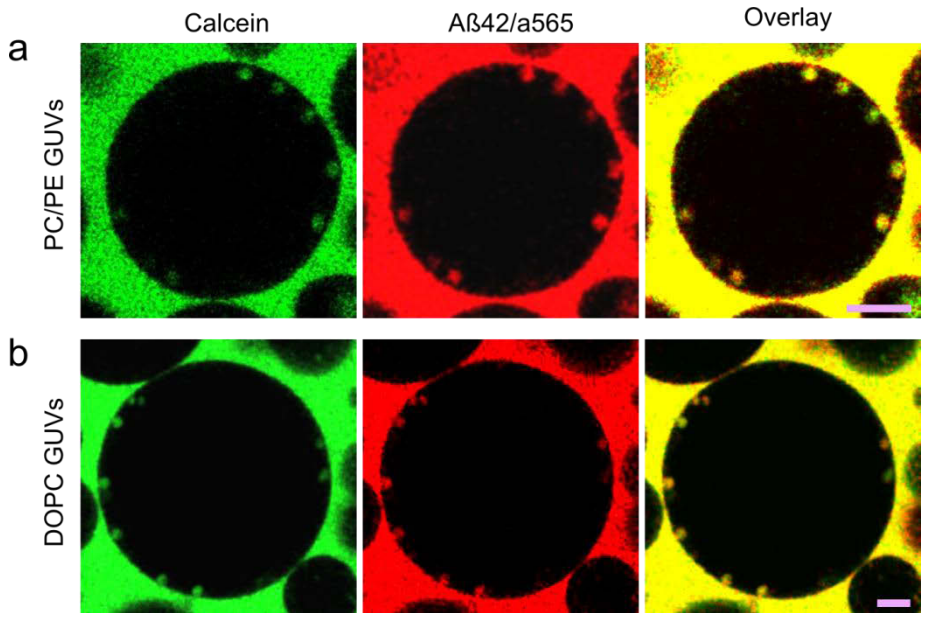

Figure 4–29: $A\beta_{1-42}$ induces invaginations in the membrane of PC/PE GUVs. PC/PE GUVs **(a)** DOPC/DOPE in 1:1 molar ratio**)** and DOPC GUVs **(b)** were incubated with $A\beta_{1-42}{}^{565}$ (10 µM, red) in the presence of calcein (20 µM, green) at RT for about 15 min. The invaginations, diameter about 1 µm, were detected in the membrane of both GUVs types. Scale bar: 10 µm.

Furthermore, to test whether the formation of invaginations is specific to the Aβ peptide, and whether other membrane active peptides could have the same effect in our model membrane system, we compared $A\beta_{1-42}$ and melittin, which is an active peptide in bee venom. Melittin is known to insert itself into the membrane and disrupts membrane integrity (Lee et al. 2013).

DOPC GUVs were imaged under the same conditions as in **Figure 4–28**. Membrane integrity of DOPC GUVs were assessed by calcein (20 µM) fluorescence and DIC imaging (**Figure 4–30** a). About 4 min after adding melittin (10 µM), calcein fluorescence was found inside the DOPC GUVs, indicating an increased membrane leakage induced by melittin. No invagination was observed (**Figure 4–30** b).

Taken together, our observations show that, $A\beta_{1-42}$ peptide is capable to induce membrane invaginations of DOPC or PE/PC GUVs membrane, occurring $A\beta_{1-42}$–membrane interactions. Those invaginations are induced specifically by $A\beta_{1-42}$ peptide, neither by fluorescence label nor calcein or sc–$A\beta_{1-42}$.

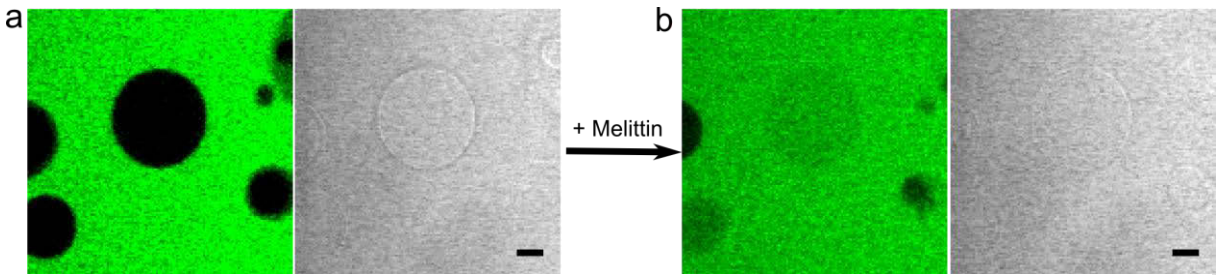

Figure 4–30: Melittin induced membrane leakage. (a) DOPC GUVs were visualized by calcein (20 µM, green) fluorescence and DIC imaging. **(b)** Melittin (10 µM) induced membrane leakage resulting in GUVs filled with calcein. Scale bar 10 µm.

4.2.6 Aβ induced invaginations specifically in Ld domains of GUVs membranes

We observed $A\beta_{1-42}$ preferentially accumulation and induction invagination in GUVs that prepared from pure ld phase, such as DOPC GUVs (**Figure 4–26** a & b, **Figure 4–28** a and **Figure 4–29** b) and PC/PE GUVs (**Figure 4–29** a), neither accumulation of $A\beta_{1-42}$ nor invagination was detected on the membrane from pure lo phase, which consisted DOPC:SSM: chol in 1:1:8 molar ratios (**Figure 4–26** c & d).

For a more direct comparison of different behaviors of $A\beta_{1-42}$ on ld and lo phases of membranes, a multiphase GUV was used to model partitioning of lipids into ld and lo domains. GUVs were formed from DOPC, SSM and cholesterol in 1:1:1 molar ratio (ld/lo GUVs), a mixture that separates into lo and ld domains. ld/lo GUVs contained 1 mol% of lipid analogue C6–NBD–PC, which partitions preferentially into the ld domain and can thus be used to visualize membrane phase partitioning (Stöckl & Herrmann 2010; Shaw et al. 2006).

Ld/lo GUVs were incubated with $A\beta_{1-42}{}^{565}$ (10 µM) at RT for 20 min and were imaged by confocal microscopy. Invaginations were found only in C6–NBD–PC stained phase, indicating they were exclusively in ld phase, whereas no invagination was detected in lo phase (**Figure 4–31**).

This result corresponds to our previous data using single phase GUVs, the invaginations were observed in GUVs with pure Ld phase not in GUVs with pure lo phase.

It should be noted that GUVs did not contain membrane proteins, so that the putative interaction of $A\beta_{1-42}$ with protein complexes in the raft domains was not probed in this model. We therefore probed the $A\beta_{1-42}$–membrane interaction by using native neuronal membranes.

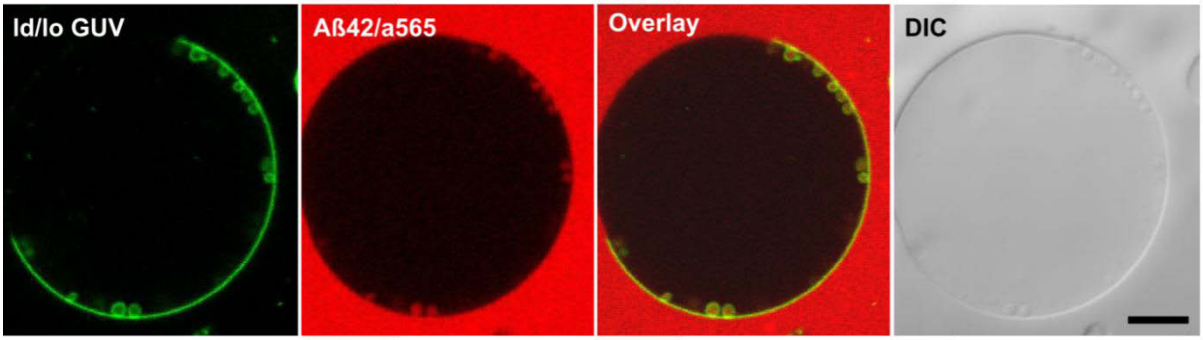

Figure 4–31: $A\beta_{1-42}$ induced invagination in ld domain. $A\beta_{1-42}^{565}$ (red) was incubated with multiphase GUVs, generating from DOPC/SSM/Chol (in 1:1:1 molar ratio) and containg 1% C6–NBD–PC (green) for the visualization of liquid disordered (ld) phase. After 20 min incubation, invaginations were found in ld phase. Scale bar, 10 µm.

4.2.7 $A\beta_{1-42}$ induced invagination in giant plasma membrane vesicles

$A\beta_{1-42}$ induced invaginations exclusively on the ld phase suggesting a distinct preference toward ld over lo domains on GUVs model system. This observation leads to the question, whether this phenomena is applicable to the neuronal membrane. We therefore studied $A\beta_{1-42}$ and membrane behavior on biological membrane systems, in which ld/lo domains coexist, by using giant plasma membrane vesicles (GPMVs). GPMVs are isolated from cells, containing the biological membrane compositions. They resemble more closely physiological plasma membranes, containing biological membrane lipids, raft–like microdomains and natural membrane proteins (Sezgin, Kaiser, et al. 2012; Baumgart, Hammond, et al. 2007).

GPMVs were isolated from cultured neuroblastoma (SH–EP) cells (**Figure 4–32** a), which had been used as the model cell line for cellular uptake experiments of $A\beta_{1-42}$, following the protocol by Sezgin et al (Sezgin, Kaiser, et al. 2012) as described in methods section (section 3.2.2.3).

GPMVs were incubated with monomerized $A\beta_{1-42}$ (10 µM) and calcein (20 µM) at RT for 15 min. Spherical invaginations, which had a diameter of approximate 1 µm and were morphologically very similar to those that were found on the GUVs membrane, were imaged in the membrane of GPMVs by confocal microscopy (**Figure 4–32** b), suggesting that $A\beta_{1-42}$ is able to induce the negative membrane curvature in isolated cell membranes as well as in model membrane systems.

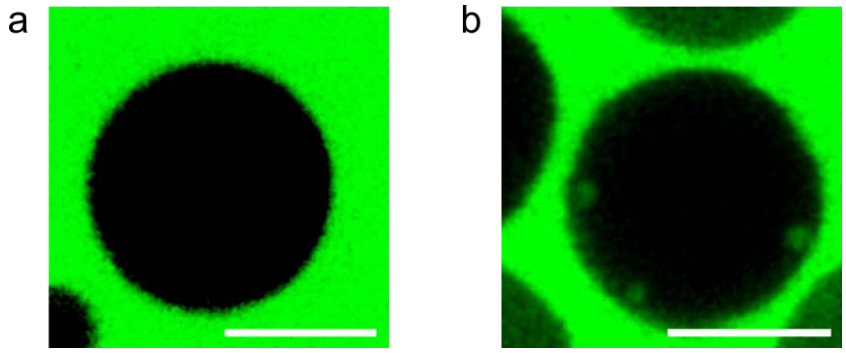

Figure 4–32: $A\beta_{1–42}$ induced invagination in giant plasma membrane vesicles (GPMVs). GPMVs were incubated with buffer **(a)** or $A\beta_{1–42}$ monomer of 10 µM **(b)** in presence of calcein (green, 20 µM) at RT for 15 min. Invaginations were observed in $A\beta_{1–42}$ treated GPMVs by confocal microscopy. Scale bars, 10 µm.

Compared with GUVs, the number of invaginations per liposome seems reduced. A possible reason may be the different ld/lo phases behavior and their sizes in GUVs and in GPMVs. Raft–like lo domains are disperse in GPMVs, whereas ld and lo domains of multiphase GUVs (ld/lo GUVs, from DOPC/SSM/Chol in 1:1:1 molar ratio, **Figure 4–31**) merge into a large homogenous phase at RT. In contrast, phase behavior of GPMVs shows more temperature–dependence. Ld/lo phase separation can be imaged only at lower temperature, at which phases coalesce into a larger macroscopic scale (Baumgart, Hammond, et al. 2007). **Figure 4–33** show a phase separation of GPMVs isolated from SH–EP cells. Lo domains were stained by merocyanine 540 in GPMV buffer, and imaged by confocal microscopy at 9 °C.

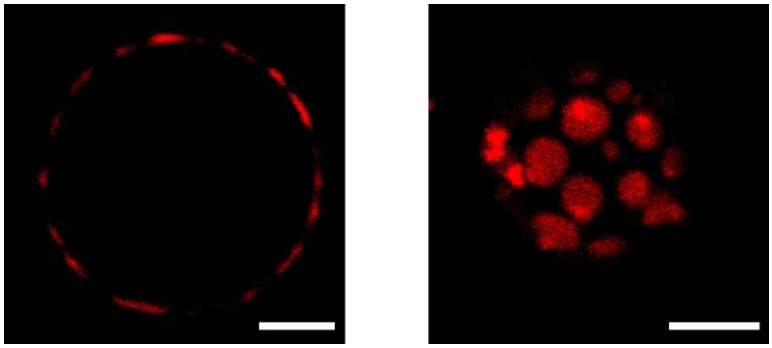

Figure 4–33: Phase separation of GPMVs. The membrane of GPMVs were stained by merocyanine 540. The phase separation of lo /ld phases, cross–section (left) and top view (right), were observed at 9 °C by confocal microscopy. Scale bars, 10 µm.

4.2.8 Invaginations remain connected to GUVs outer lumen

Vesicular endocytosis consists of several steps. The first step is the formation of the negative membrane curvature, namely the invagination, which is then in a second step pinched off the membrane to form a vesicle (Introduction 0 and **Figure 1–12**).

We had observed that $A\beta_{1-42}$ induced negative curvature in the membrane of DOPC GUVs. Next, we examined whether those invaginations are still connected to the outer buffer, or whether $A\beta_{1-42}$ is also capable to drive the scission of the invaginations from membrane. To do this, fluorescence recovery after photobleaching (FRAP) was used.

DOPC GUVs were incubated with $A\beta_{1-42}^{565}$ monomer (10 µM) and calcein (20 µM), and were imaged by confocal microscopy. Calcein fluorescence in one of the invaginations was bleached by a 488 nm laser beam; the fluorescence recovery of this invagination was then monitored over time (**Figure 4–34**). Fluorescence of $A\beta_{1-42}^{565}$ was used to identify the location of target vesicle during the FRAP process. A total recovery of calcein fluorescence was completed in about 4 min, indicating the invaginations were still connected to the outside solution. From these data we conclude that the invaginations are not pinched off from the membrane.

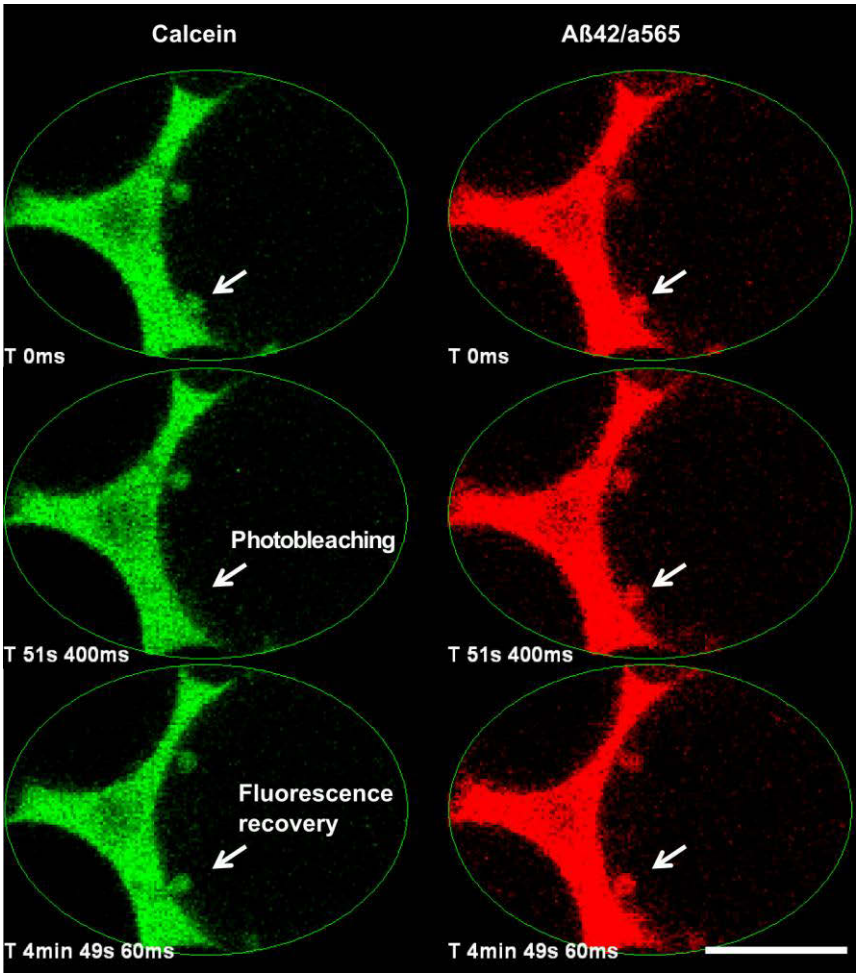

Figure 4–34: Fluorescence recovery after photobleaching (FRAP) of invagination.
Invaginations in the membrane of DOPC GUVs were induced after incubating with $A\beta_{1-42}^{565}$ monomer (10 µM, red). Calcein (20 µM, green) was added. Calcein fluorescence of the indicated invagination (white arrows) was bleached by 488nm laser beam, would be recovered in ca. 4 min, suggesting that invaginations connect to buffer. Fluorescence of $A\beta_{1-42}^{565}$ was used to indicate the vesicle existence during the FRAP. Scale bar, 10 µm.

4.2.9 ThT negative Aβ$_{1-42}$ aggregate species bind to lipid bilayer

Observations in the previous experiments showed that the generation of invaginations on the membrane of GUVs always required a certain time after adding Aβ$_{1-42}$ monomers. E.g. it took approximate 15 min incubation time to observe invaginations at a concentration of Aβ$_{1-42}$ monomer of 10 µM. This time lag was independent of the compositions of GUVs or GPMVs (**Figure 4–26** a & **Figure 4–28**a of DOPC GUVs, **Figure 4–29** of PC/PE GUVs, **Figure 4–31** of ld/lo GUVs and **Figure 4–32** b of GPMVs). Referring to the aggregation kinetics (described in chapter 4.2.2), this time span is in lag phase at an aggregation kinetic of 10 µM Aβ$_{1-42}$ monomer, during which aggregate species are in a ThT negative state (**Figure 4–25** c). We hypothesize, that the Aβ$_{1-42}$ aggregate species that induce invagination may be in an early aggregation state and their β–sheet–rich structures have not formed yet. Aβ$_{1-42}$–membrane binding may occur before the formation of β–sheet–rich structures, which may correspond to the formation of small Aβ aggregates directly in or on the membrane.

To test these hypotheses, we measured the time–dependent formation of invaginations in two experimental designs: i) DOPC GUVs were incubated directly with monomeric Aβ$_{1-42}$; ii) Aβ$_{1-42}$ aggregates were prepared by preincubating in buffer without DOPC GUVs, and DOPC GUVs were then incubated with those aggregates species.

To prepare the aggregates, monomeric Aβ$_{1-42}$ (20 µM) was incubated in the glucose buffer, which was used for GUVs microscopy (section 4.2.1), for four time internals corresponding to different phases of the aggregation kinetics: 0 (monomer), 15 (15 min–aggregate), 30 (30 min–aggregate), or 45 min (45 min–aggregate). These aggregates were then added to the GUVs solution at a final concentration of Aβ$_{1-42}$ of 10 µM (equivalent monomer concentration). Calcein (20 µM) was used to visualize the GUVs and the invaginations by confocal microscopy.

Figure 4–35 shows that, after treating the DOPC GUVs with monomeric Aβ$_{1-42}$ (10 µM), the earliest time point of invagination detection was 15 min after adding Aβ$_{1-42}$ monomers. This time matches the results of our previous experiments (**Figure 4–26** a, **Figure 4–28**a, **Figure 4–29**, **Figure 4–31** and **Figure 4–32** b).

By treating DOPC GUVs with preformed Aβ$_{1-42}$ aggregates, invaginations were only observed after addition of the 15 min–aggregates (**Figure 4–35**, indicated with red box). Unlike when incubating GUVs with monomeric Aβ$_{1-42}$, the invaginations could be detected immediately after adding 15 min–aggregates to DOPC GUVs. In contrast, no invaginations were observed after incubating DOPC GUVs with the other two aggregate species, 30 min–aggregates and 45 min–aggregates, which had been preincubated for 30 or 45 minutes in buffer and had therefore formed higher ordered structures than 15 min–aggregates. These observations strongly suggest that invaginations are induced as a result of Aβ$_{1-42}$ aggregation, and there is a population of early aggregate species that is crucial for inducing invagination. When

referring to the time scale of the ThT aggregation kinetic of $A\beta_{1-42}$ monomer (**Figure 4–25** a), the time required to induce the invaginations corresponds to the end of the lag phase.

We therefore assume that Aβ induced invagination coincides with the aggregates formed during the lag phase. This suggests that the $A\beta_{1-42}$ aggregates into a membrane active species before β–sheet–rich structures are formed; they are not the monomer nor the aggregates species with β–sheet structure that bind ThT.

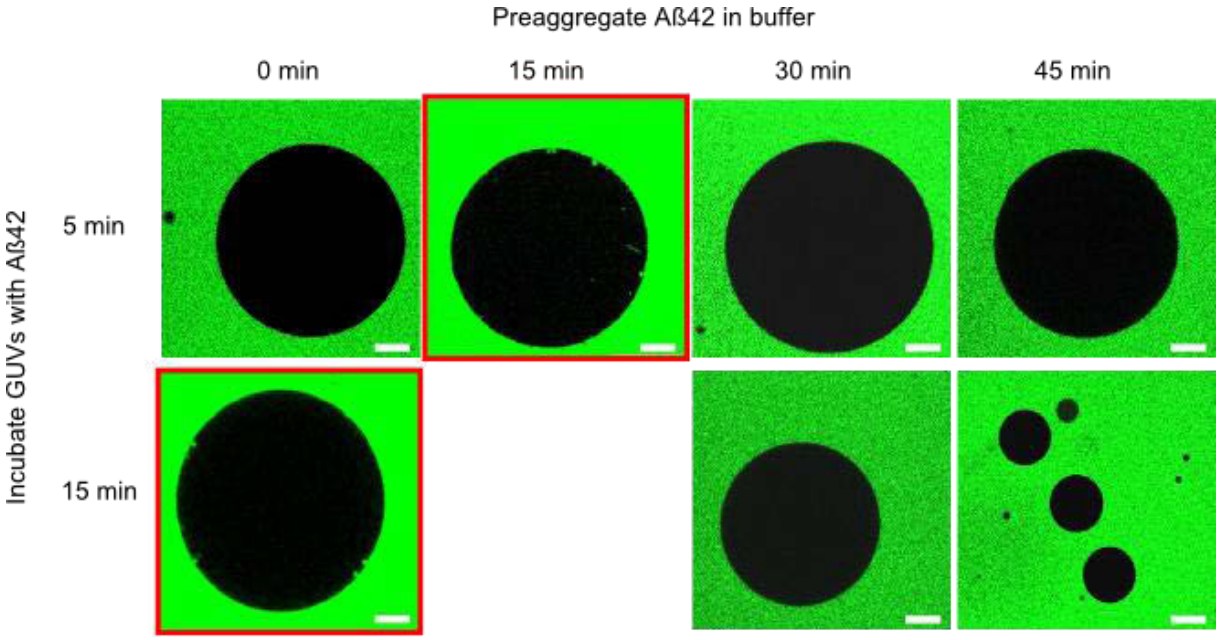

Figure 4–35: Early aggregated $A\beta_{1-42}$ induces invagination in the membrane of DOPC GUVs. DOPC GUVs were incubated with monomer or aggregates of $A\beta_{1-42}$ (10 µM), respectively. Calcein (20 µM) were added to visualize DOPC GUVs by confocal microscopy. Invaginations were only observed after 15 min incubation DOPC GUVs with monomer; or directly after adding $A\beta_{1-42}$ aggregates, which were preaggregated 15 min in buffer (both highlight in red boxes). No invagination was imaged by incubating with monomeric $A\beta_{1-42}$ shorter than 15 min or with aggregates that were preaggregated in buffer for more than 15 min. Scale bars, 10 µm.

To test the validity of our hypothesis, DOPC GUVs were incubated with monomeric $A\beta_{1-42}{}^{565}$ of 10 µM until detection of invaginations (~ 15 min), or only for a short time (~5 min), before the invagination were observed. Then $A\beta_{1-42}{}^{565}$ outside the DOPC GUVs was diluted to 100 nM by adding buffer.

When comparing these two time points, i.e. decreasing the concentration of $A\beta_{1-42}{}^{565}$ before or after the formation of invaginations, a clearly visible accumulation of $A\beta_{1-42}{}^{565}$ on the membrane of DOPC GUVs was only observed after the formation of invaginations (**Figure 4–36** a), not before (**Figure 4–36** b).

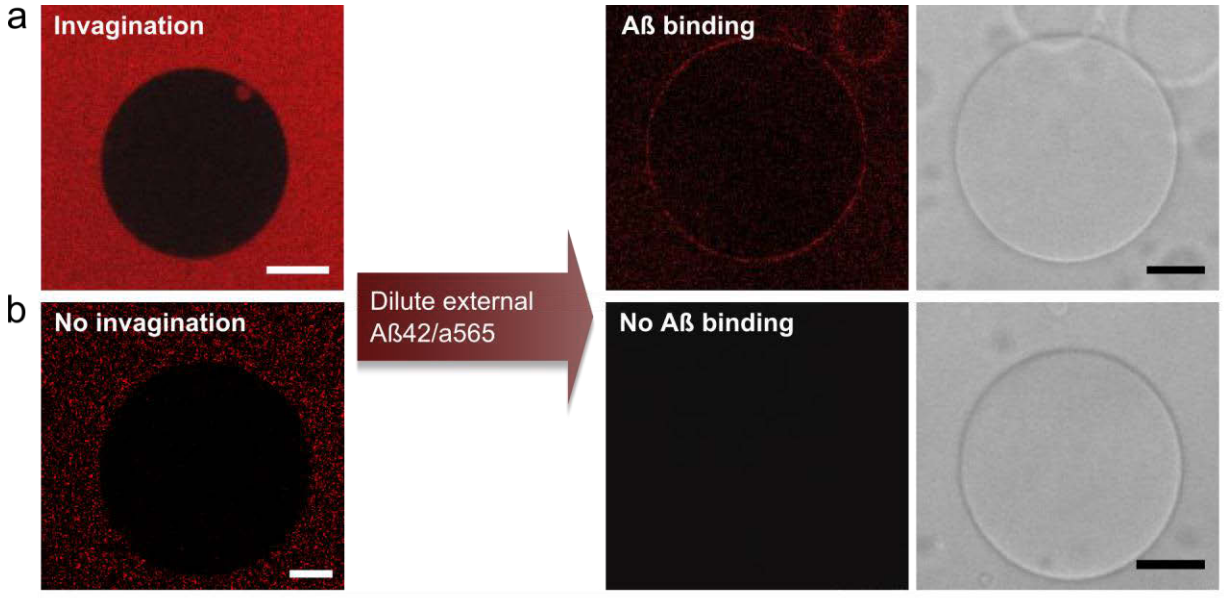

Figure 4–36: A stable binding of $A\beta_{1-42}$ to membrane of DOPC GUVs benefit formation of invaginations. DOPC GUVs were incubated with $A\beta_{1-42}^{565}$ monomer (10 µM). Then $A\beta_{1-42}^{565}$ was diluted to 100 mM after (a) or before (b) the invaginations been detected. Accumulation of $A\beta_{1-42}^{565}$ in membrane was only detected when the dilution of external $A\beta_{1-42}^{565}$ after invaginations had been formed. Scale bars, 10 µm.

Compared the time scale of membrane interaction with the time scale of the ThT aggregation kinetics (**Figure 4–25** a), after 15 min incubation at 10 µM concentration, the aggregated $A\beta_{1-42}$ species are still in within the lag phase before the formation of β–sheet structure. This observation suggests that $A\beta_{1-42}$ species that bind tightly to the membrane are still in a ThT negative state. Those small disordered and ThT negative aggregates are able to bind to the membrane of DOPC GUVs with high affinity, and are capable of inducing invaginations. In contrast, monomeric species seem not to have a stable binding to the membrane nor induce invaginations.

4.2.10 Summary

We observed that the plasma membrane can serve as a platform for the formation of toxic $A\beta_{1-42}$ aggregates (chapter 4.1). This observation suggested a very close association between $A\beta_{1-42}$–membrane interaction, $A\beta_{1-42}$ aggregation, neuronal uptake of $A\beta_{1-42}$ and cytotoxicity of $A\beta_{1-42}$ and prompted us to study the membrane interaction in model membrane systems.

To study the interaction of $A\beta_{1-42}$ with lipid bilayers, we used DOPC GUVs and PC/PE GUVs (from DOPC/DOPE in 1:1 molar ratio) for pure ld phase, raft GUVs (from DOPC/SSM/Chol in 1:1:8 molar ratio) for pure Lo phase, the ld/lo phase coexisted GUVs (from DOPC/SSM/Chol

in 1:1:1 molar ratio) and GPMVs, which were isolated from SH–EP cells containing physiological lipids and proteins.

We investigated the influence of lipid bilayer presence on aggregation kinetic of $A\beta_{1-42}$; studied the $A\beta_{1-42}$–membrane binding in both ld and lo phases; observed $A\beta_{1-42}$ binding resulted membranes transformation; and examined which aggregation state of $A\beta_{1-42}$ preferentially bind to lipid bilayers.

We found that a population of Aβ aggregate species, which had no β–sheet structures and formed during the lag phase of ThT aggregation kinetic, binds with high affinity to a ld phase as opposed to a lo phase in the GUVs membrane. The association of $A\beta_{1-42}$ to membrane results a negative curvature in ld phase of the DOPC GUVs, DOPE GUVs and GPMVs membrane, which then form vesicle–like invaginations.

4.3 Comparisons of $A\beta_{1-42}$ and $A\beta_{1-40}$ in membrane curvature modelling and in cytotoxicity

In the previous chapters, we focused on $A\beta_{1-42}$ peptide and found that, i) $A\beta_{1-42}$ monomers and/or small aggregates associate rapidly with the plasma membrane, where they form aggregates and are then taken up into neuronal cells in a process that correlated with cytotoxicity; ii) one population of $A\beta_{1-42}$ species from the late lag phase of ThT aggregation kinetics has high affinity with lipid bilayer of GUVs and GPMVs model membrane systems and induced negative curvature in the ld phase of the membrane bilayer. These data may suggest that membrane remodelling is coupled with cellular uptake and cytotoxicity. Alternatively, the membrane activity could be independent of Aβ toxicity and could have a yet unknown physiological role.

Aβ peptide with 40aa, i.e. $A\beta_{1-40}$, is the most common isoform in healthy and AD brain. In the healthy brain, the $A\beta_{1-40}$ to $A\beta_{1-42}$ ratio is approximately 10:1 (Simons et al. 1998; Shoji et al. 1992; Jarrett et al. 1993). $A\beta_{1-42}$ is only prevalent in amyloid deposits in the brain of AD patients. It is still unknown, what, if any, is the physiological function of $A\beta_{1-40}$ or $A\beta_{1-42}$; why $A\beta_{1-42}$ which has a lower synthesis rate and a lower concentration in healthy brains is dominantly desposited in AD brains; and what are the differences in cellular processing of $A\beta_{1-40}$ and $A\beta_{1-42}$.

Several studies have shown the uptake (Friedrich et al. 2010) and the membrane interaction of $A\beta_{1-40}$ (Ding et al. 2012). Here, we compared both isoforms of Aβ peptides, $A\beta_{1-42}$ and $A\beta_{1-40}$, to test whether Aβ induced membrane invagination is correlated to neuronal toxicity and to provide evidence towards a possible physiological role of Aβ induced invagination.

For this end, we used the two well–established model systems from the previous chapters, DOPC GUVs and cultured neuroblastoma cells (SH–EP cells), to examine $A\beta_{1-40}$ and $A\beta_{1-42}$ on their membrane interaction and on cell toxicity.

4.3.1 $A\beta_{1-40}$ vs. $A\beta_{1-42}$ in the aggregation kinetics

First, we compared the aggregation kinetics of $A\beta_{1-40}$ and $A\beta_{1-42}$. $A\beta_{1-40}$ and $A\beta_{1-42}$ were monomerized as described in the methods section (chapter 3.2.1.2). Monomerized $A\beta_{1-40}$ and $A\beta_{1-42}$ (15 µM each) were incubated with ThT (20 µM) in PBS at pH 7.4 in a 96–well plate. Intensities of ThT florescence were recorded at 37°C with shaking (5 s every 5 min) in a fluorescence plate reader (**Figure 4–37**).

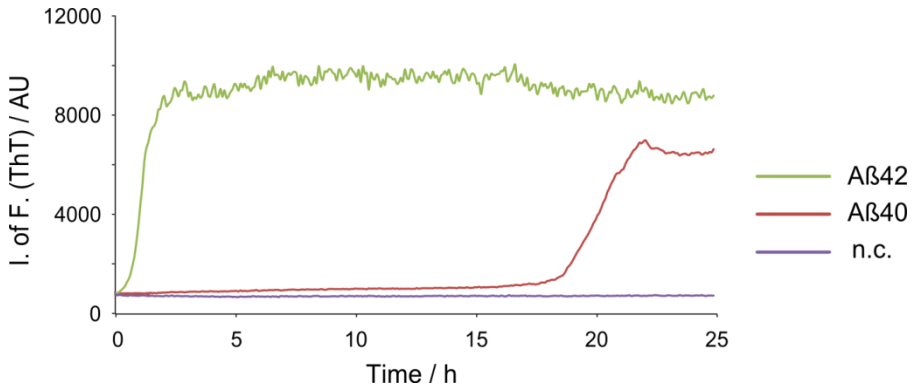

Figure 4–37: ThT Kinetic of Aß$_{1-40}$ and Aß$_{1-42}$. Monomerized $A\beta_{1-40}$ (red curve) or $A\beta_{1-42}$ (green curve) at 15 µM each was incubated in PBS at 37°C with intermittent shaking, respectively. ThT fluorescence was measured by a plate reader.

As expected, lag phase of $A\beta_{1-40}$ took ca. 18 h, which was much longer than for $A\beta_{1-42}$, and reached the steady state in approximate 22 h. In contrast, lag phase of $A\beta_{1-42}$ was less than 1 h. Both peptides had a similar intensity of ThT fluorescence at the end of the aggregation.

The difference in lag phase between both isoforms allowed us to better test whether the increased lag phase played a role in the Aβ–membrane interaction, to investigate whether $A\beta_{1-40}$ could also induce membrane invagination as $A\beta_{1-42}$ did, and to test whether a pre–ThT–aggregate species of Aβ induced membrane curvature or not.

4.3.2 $A\beta_{1-40}$ vs. $A\beta_{1-42}$ in membrane activity – induction of negative curvature

Our previous data show that, $A\beta_{1-42}$ aggregate from late lag phase of aggregation kinetic has high affinity to lipid bilayer, and is able to induce invaginations in the ld phase of GUVs and GPMVs membrane. The induction of negative curvature depends on the primary sequence of Aβ, i.e. no invaginations observed by sc–$A\beta_{1-42}$ (**Figure 4–28** b), and depends on the aggregation state (**Figure 4–35**).

Here, we examined whether $A\beta_{1-40}$ has the same abilities to induce invaginations in the same model membrane system as $A\beta_{1-42}$ does, and if so, in which aggregation state.

GUVs from 100% DOPC were generated by electroformation. DOPC GUVs were incubated with $A\beta_{1-40}$ under the same experimental conditions that were previously used for $A\beta_{1-42}$ (**Figure 4–35**). Preparation of $A\beta_{1-40}$ aggregates used the same protocol as used for $A\beta_{1-42}$ aggregates, monomerized $A\beta_{1-40}$ of 20 µM was incubated in the glucose buffer with shaking at 300 rpm at 37 °C. The aggregates of $A\beta_{1-40}$ were collected from different phases of aggregation, i.e. after 5 or 16 h incubation time. DOPC GUVs were then incubated with these $A\beta_{1-40}$ aggregates, which had a final concentration of 10 µM (equivalent monomer concentration) at RT. Calcein (20 µM) was addd for imaging DOPC GUVs by confocal microscopy (**Figure 4–38**).

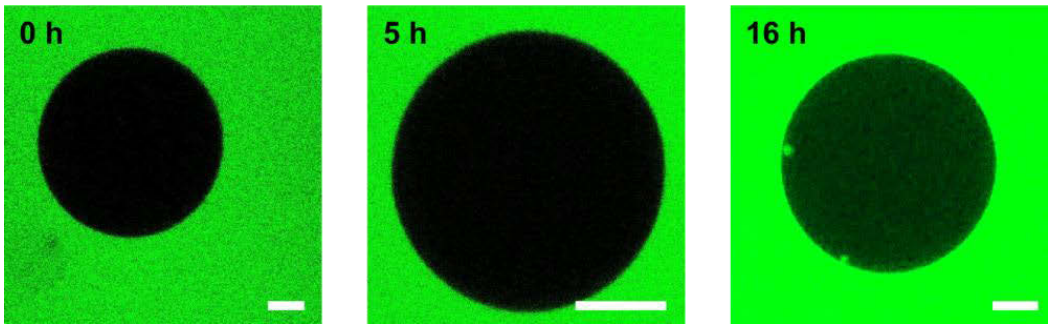

Figure 4–38: $A\beta_{1-40}$ aggregates induce the invaginations in the membrane of DOPC GUVs. Monomeric $A\beta_{1-40}$ (20 µM) were incubated in glucose buffer with shaking at 300 rpm at 37 °C for 5 or 16 h. DOPC GUVs were incubated in glucose buffer with calcein (20 µM) and $A\beta_{1-40}$ monomers (0 h) or aggregates (10µM, corresponding monomer concentration). Invaginations in approximate 1 µm diameter were observed in the membrane of DOPC GUVs when incubating with 16 h aggregates for 5 min by confocal microscopy. No invagination was observed when incubating with monomers (0 h) or 5 h aggregates. Scale bar, 10 µm.

We observed that $A\beta_{1-40}$ peptides have very similar membrane behaviors like $A\beta_{1-42}$. Invaginations in the membrane of DOPC GUVs could be imaged after a relative short time (~ 5 min) by incubating with the aggregates that collected after 16 h aggregation times

(**Figure 4–38**, 16 h), i.e. approximately from the end of lag phase (**Figure 4–37**). The shapes and the size (~ 1 µm diameter) of invaginations are very similarly to those been induced by $A\beta_{1-42}$.

When incubating with monomer or small aggregates, which were collected after 5 h aggregation times, i.e. from the middle of lag phase, no invaginations could be detected until 45 min incubation time (**Figure 4–38**, 0 h & 5 h), which is our standard time duration for GUVs microscopy.

The aggregation kinetics show that, $A\beta_{1-40}$ monomers require much longer incubation time than $A\beta_{1-42}$ to form the membrane active aggregate species under the same conditions, which corresponds to their different aggregation rates (**Figure 4–37**). Interestingly, the membrane active species of both isoforms, which induce invaginations in the membrane of DOPC GUVs, are in aggregated from, indicating the aggregation state is crucial to Aβ–membrane interaction. Those aggregates of both Aβ isoforms locate at similar phases of the aggregation process, which are the end of the lag phase or beginning of the exponential growth phase. This indicates that these aggregates might have similar activity on the membrane of DOPC GUVs, that may be resulted by their similar sizes and/ or their similar surface structures, such as surface charges and hydrophobicity.

It should be noted, in order to keep the membrane in a consistent state from the beginning of experiment to its end, and to prevent lipid phase transition occurred by local temperature increase via laser beam during microscopy, the maximum time of microscopy is limited in 45 min for all the experiments on GUVs (both $A\beta_{1-40}$ and $A\beta_{1-42}$) in this study. However, if the membrane can be kept in an ideal constant state, we could speculate that invaginations would be observed after incubating with $A\beta_{1-40}$ monomers for 16 h. A similar experiments design has been used for $A\beta_{1-42}$ (**Figure 4–35**).

4.3.3 $A\beta_{1-40}$ vs. $A\beta_{1-42}$ in the cytotoxicity

We found that, both $A\beta_{1-40}$ and $A\beta_{1-42}$, which were collected from late lag phases of the aggregation process, could induce invaginations in the membrane of DOPC GUVs, suggesting those aggregates from both isoforms may have similar membrane activities. In this aggregation state, both isoforms may have similar structures, which result similar behaviours to model membrane bilayer.

The study of Friedrich et al. has shown that $A\beta_{1-40}$ can be taken up by the cells (Friedrich et al. 2010). Here, we compared the cytotoxicity effect of $A\beta_{1-40}$ and $A\beta_{1-42}$ in SH–EP cells using MTT assay, to examination whether they effected differently on cellular metabolism activities.

In the previous chapter (chapter 4.1.8), we also found that the cytotoxicity of $A\beta_{1-42}$ was tightly linked to its cellular uptake. The metabolism activities of the cultured neuroblastoma (SH–EP) cells were inhibited once $A\beta_{1-42}$ was internalized by the cells (**Figure 4–20**). The internalizations of $A\beta_{1-42}$ can be achieved by treating with monomeric form when its concentration above 150 nM. When the concentrations of $A\beta_{1-42}$ were lower than 150 nM, an efficient uptake required a aggregated form simultaneously containing β–sheet structure (**Figure 4–5**, **Figure 4–12**).

To compare the cytotoxicity of $A\beta_{1-40}$ and of $A\beta_{1-42}$, SH–EP cells were therefore correspondingly treated with $A\beta_{1-40}$ monomer or aggregates species at 150 nM or 500 nM (equivalent monomer concentration), respectively. To prepare β–sheet–rich aggregate species, monomers were incubated in PBS for 24 h, to form mature fibrils in ThT positive state (**Figure 4–37**). In the control experiments, the SH–EP cells were treated with $A\beta_{1-42}$ under the same conditions like $A\beta_{1-40}$, i.e. with monomer at 150 nM or 500 nM and with $A\beta_{1-42}$ aggregates species from steady state phase at 150 nM or 500 nM, respectively. After 24 h incubation with Aβ peptides at 37°C, metabolic activity of SH–EP cells was evaluated by MTT assay (**Figure 4–39**).

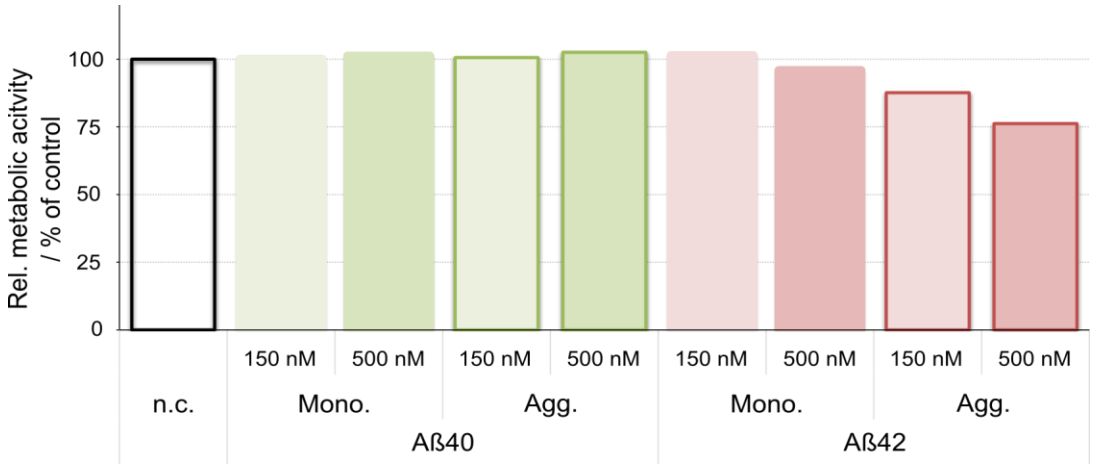

Figure 4–39: MTT assay of $A\beta_{1-40}$ and $A\beta_{1-42}$. SH–EP cells were incubated with $A\beta_{1-40}$ and $A\beta_{1-42}$ monomer or aggregates at 37°C for 24 h, respectively. Activities of cellular metabolism were then evaluated by MTT assay. Monomeric $A\beta_{1-42}$ at 500 nM, aggregated $A\beta_{1-42}$ at 150 nM and at 500 nM showed inhibition of cell metabolism activities. No inhibition was detected by treating with other Aβ species. All results are represented as mean values of wells of 6 replicate wells.

Untreated cells were used as negative control for 100% metabolic activity. None of the $A\beta_{1-40}$ species showed influence of cellular metabolic activity, regardless of their aggregation state. Both of $A\beta_{1-40}$ species, monomer and aggregates with β–sheet–rich structures from the steady state of the ThT aggregation kinetic, did not change MTT reduction regardless of their concentrations 150 nM or 500 nM. In contrast, as in our previous experiments had observed, monomeric $A\beta_{1-42}$ at low concentration (150 nM) displayed no inhibition effect on

the activity of cell metabolism, but monomers at higher concentration (500 nM) inhibited the metabolic activity. $A\beta_{1-42}$ aggregates at both concentrations, 150 nM and 500 nM, showed inhibition of cellular metabolism activitiy.

4.3.4 Summary

$A\beta_{1-40}$ and $A\beta_{1-42}$ are the two major isoforms from the processing of APP in the amyloidogenic pathway. We used ThT aggregation kinetic curves to assess the membrane activities and cytotoxicities of Aβ aggregate species from different phases of aggregation, and compared $A\beta_{1-40}$ and $A\beta_{1-42}$ in their membrane interaction and in cell viability within our established model systems.

We found that within the lag phase, when $A\beta_{1-40}$ and $A\beta_{1-42}$ are in a similar aggregation state, they behave quite similarly with respect to the lipid bilayer. In both isoforms, one population of the species from the end of the lag phase induce invaginations on DOPC GUVs membrane. However, $A\beta_{1-40}$ and $A\beta_{1-42}$ have markedly different effects on cellular metabolism. Regardless of aggregation state, monomer or aggregate with β–sheet–rich structures, and regardless of concentration, 150 nM or 500 nM, $A\beta_{1-40}$ shows no influence on cell metabolism activity, whereas $A\beta_{1-42}$ monomer at 500 nM, and aggregates at both concentrations (150 nM and 500 nM) were toxic.

These observations underline the pathological role of $A\beta_{1-42}$, such as cytotoxicity of $A\beta_{1-42}$ aggregates. The fact that both peptides have similar membrane activities may suggest that Aβ induced membrane remodelling not only plays a role in the pathological way. Rather, it hints at a possible physiological function of Aβ peptide membrane association and the induction of membrane negative curvature.

5 Discussion

Alzheimer's disease (AD) is a highly complex neurodegenerative disorder, in which Amyloid beta (Aβ) peptides are deposited extracellularly in the form of amyloid plaques. A variety of hypotheses exists in current research for the cause of AD and the mechanisms underlying pathogenesis, but so far these hypotheses cannot fully explain the complexity of the pathogenesis of AD.

Aβ peptides are produced both in the neurons of in AD patients and in healthy individuals. However, the understanding of why the cells produce this small and hydrophobic peptide, its physiological function, as well as the exact mechanism of pathogenesis of $A\beta_{1-42}$ are still very limited (Jarrett et al. 1993; Knowles et al. 2014).

The existing researches show that soluble oligomeric and/or small aggregated species are tightly linked to AD pathogenesis and are presumed to be the cause of neuronal damage (Walsh et al. 2002). However, there are still many questions, why $A\beta_{1-42}$, which has only two amino acids (aa) more than $A\beta_{1-40}$, is dominantly deposited in brain of AD patients; why the aggregated form of $A\beta_{1-42}$ is more toxic than the monomer; how and where those monomers become aggregates; and how this extracellular peptide induced neurotoxicity.

The first aim of present study is to address an important and fundamental phenomenon of $A\beta_{1-42}$ related toxicity, specifically how the monomeric $A\beta_{1-42}$ forms aggregates connected to the cytotoxicity, while the second part examines the interaction of $A\beta_{1-42}$ with model membranes.

5.1 Monomeric and aggregated $A\beta_{1-42}$ species

In the present study, monomeric Aβ and its aggregated forms from their early aggregation state are our main focus. Thus, it is very important to elucidate the quality of monomers, to prepare relatively pure and homogen monomers, and to define the aggregates before the studies of their behaviors.

Comparing with monomers and well formed mature fibrils, small aggregates including oligomers are believed to be central to amyloid toxicity (Haass & Selkoe 2007; Walsh et al. 2002). Therefore, an important question in the amyloid hypothesis is the aggregation state of Aβ peptide. However, the aggregation of Aβ peptide is influenced by many environmental

factors, such as concentration of Aβ peptide, pH value of the buffer system, the temperature, and other components (such as sugar) of the milieu. In practice, it is very difficult to determine the sizes, the aggregation states, the structures of Aβ and their possible conformations under physiological conditions at the same time (Burke et al. 2013).

In several studies, the solubility or the size of aggregates are broadly used to define the aggregation state of amyloids (Glabe 2008). Various forms of Aβ had been observed in vitro and in vivo, such as disordered monomers, dimers, small oligomers, ring–like oligomers, protofibrils or twisted fibrils (Meinhardt & Fändrich 2009). Different types of Aβ oligomers/ small aggregates, which are usually in spherical form, have been described, such as SDS–stable Aβ oligomers of 8 – 12 kD MW that were detected in cortex of AD patients (McLean et al. 1999); soluble oligomers of 56 kD detected in human AD brain (Kayed et al. 2003); SDS unstable oligomers of 20 kD that were ThT negative and cytotoxic (Ahmed et al. 2010); toxic Aβ–derived diffusible ligands (ADDLs, a type of soluble Aβ oligomers) (Krafft & Klein 2010); or cylindrin–like, out–of–register hexameric and cytotoxic oligomers (Laganowsky et al. 2012; Liu et al. 2012) etc.

The confusing variety of species that were characterized as Aβ oligomers hinders our precise understanding of their role in AD pathogenesis and cytotoxicity. In the present study, we therefore focused on two easily measured parameters: the presence of aggregates as measured by Förster energy transfer (FRET) and the secondary structure of Aβ aggregates as measured by circular dichroism and by the binding of the amyloidophilic dyes ThT and ThS. This study investigated whether the presence of β–sheet–rich structures of Aβ aggregates affects the behavior of Aβ in neuronal model cells and its membrane interaction, rather than attempting a detailed analysis of the aggregate size or molecular weight of the Aβ species involved.

To provide a clear starting point for our study, Aβ peptides were monomerized by passing through 30kD membrane filter, and fluorescently labeled $A\beta_{1-42}$ monomers and protofibrils were purified by SEC to prepare a relatively homogeneous monomers and protofibrils (**Figure 4–2** a, b, d and e). Small Aβ aggregates were then prepared in vitro (**Figure 4–20** a and b).

The small Aβ aggregates discussed in this study are classified in two populations: in the state before the formation of β–sheet structures, i.e. small aggregates without β–sheet structure, and in the state they just been formed, i.e. small aggregates with β–sheet structures. To identify and separate both types of aggregates, we used a classic tool – the ThT binding assay (LeVine 1993). Aggregation kinetic curve in vitro was used as a metric for the formation of β–sheet aggregates. During the aggregation process, different type of aggregated species co–existed, ThT binding assay is a very sensitive tool for grouping whether presence β–sheet structures of those aggregates. The majority of $A\beta_{1-42}$ contains β–

sheet structures shown by ThT binding assay and CD spectroscopy at the same time points (**Figure 4–20** a and b, t1 vs. t2).

In the present study, we aimed to investigate whether the presence of secondary structure effects on the behavior $A\beta_{1-42}$ towards the cells and the membranes. Picking species from different time points of the ThT aggregation curve allows us to define aggregate species and to compare the behavior of same aggregate population in various model systems, e.g. the behavior of $A\beta_{1-42}$ to cultured cells and to GUVs; or to observe those aggregates in same model systems.

5.2 Cellular internalization of $A\beta_{1-42}$

Aβ peptide is secreted into extracellular space and amyloid plaques locate typically outside the cells. However, several studies have suggested that the reuptake of extracellular $A\beta_{1-42}$ into neurons may lead to the formation of intracellular aggregates, resulting in neuronal damage and neurotoxicity (Ida et al. 1996; Hu et al. 2009; Friedrich et al. 2010). $A\beta_{1-42}$ forms aggregate spontaneous and rapid, at a relative high rate and relative low concentrations (Usui et al. 2009), and oligomers of $A\beta_{1-42}$ are observed to be central to amyloid toxicity (Haass & Selkoe 2007; Walsh et al. 2002). A detailed understanding of those processes and possible links between them should thus further our understanding in Aβ pathogenesis.

The first goal of the present study was to investigate how monomeric $A\beta_{1-42}$ becomes cytotoxic. Specifically, we investigated the location of $A\beta_{1-42}$ aggregation, tested how aggregated structure is connected to uptake, examined whether internalization of $A\beta_{1-42}$ is correlated to cytotoxicity, and investigated the pathway of $A\beta_{1-42}$ uptake.

We found that $A\beta_{1-42}$ monomers as well as small aggregate species bound rapidly to the plasma membrane and formed β–sheet–rich aggregates. These structures were subsequently taken up and accumulated in endocytic vesicles. This process correlated with metabolic inhibition. Our data therefore imply that the formation of β–sheet–rich aggregates at the cell membrane is a prerequisite for $A\beta_{1-42}$ uptake and cytotoxicity.

5.2.1 Uptake of $A\beta_{1-42}$ monomer and the location of the aggregate formation

5.2.1.1 Membrane binding and aggregation

Aβ peptides are generated by APP and released then in a monomeric form from the plasma membrane into extracellular space (LaFerla et al. 2007). One of the characteristic features of $A\beta_{1-42}$ is rapid formation of aggregates.

The studies by Johnson et al. have described that small $A\beta_{1-42}$ oligomers are capable of binding to the plasma membrane at nanomolar concentration in cultured neurons, and that $A\beta_{1-42}$ oligomers can grow on the plasma membrane (Johnson et al. 2011; Johnson et al. 2013). After adding monomeric Aβ (final monomer concentration 1 nM in cell culture medium), the Aβ bound in oligomeric form to membrane, and grew over the next 48 h.

Another study by Bateman and Chakrabartty have showed that, membrane associated monomeric Aβ aggregates on the cell surface. The interaction of Aβ with cells mediated their aggregation (Bateman & Chakrabartty 2011).

At a very low temperature (4°C), both the aggregation process of $A\beta_{1-42}$ and the cell activities are slowed down, and the clathrin–mediated endocytosis is blocked (Harding et al. 1983). We observed that very small aggregates from early aggregation process, i.e. either a negative or positive ThT/ThS states, are capable bind rapidly on the plasma membrane under these conditions (**Figure 4–14** a, **Figure 4–16** a and b). Furthermore, when the concentration of added monomeric $A\beta_{1-42}$ is above a threshold concentration, membrane bound aggregates could be taken up directly after binding to the cell membrane (**Figure 4–16** c, **Figure 4–17** a, and **Figure 4–19**).

5.2.1.2 Uptake by the cells

We observed the uptake of monomeric $A\beta_{1-42}$ only occurred when their concentration above the threshold concentration at 200–300 nM (**Figure 4–12** a and b). However, the concentration of $A\beta_{1-42}$ monomer in the medium needed for $A\beta_{1-42}$–membrane binding is lower than the concentration needed for uptake. $A\beta_{1-42}$–membrane binding can already be detected at 150 nM $A\beta_{1-42}$ concentration (**Figure 4–14** a), at which concentration the uptake of monomer was not observed within 24 h (**Figure 4–6** c). **Figure 4–14** a shows that the labeled $A\beta_{1-42}$ peptide is located in form of isolated spots on the plasma membrane. At increased concentrations of $A\beta_{1-42}$ in the medium (500 nM and 1 µM), membrane–bound $A\beta_{1-42}$ formed aggregates. The aggregation process could be observed by the colocalization of $A\beta_{1-42}$ monomers labeled with two different fluorophores and by FRET between the fluorophores (**Figure 4–16**). These data indicate that $A\beta_{1-42}$ associates with the cell membrane in the form of small aggregates, when their concentrations are above a threshold

concentration (200–300 nM), the aggregated species can then be taken up (**Figure 4–16** c, and **Figure 4–17** a).

Our FRET data provide evidence that membrane associated $A\beta_{1-42}$ can be in aggregated form. The observations by Johnson et al. support our hypothesis, they observed that only early oligomers of Aβ bind to neurites (Johnson et al. 2011; Johnson et al. 2013). On the other hand, our data still could not completely exclude whether monomeric $A\beta_{1-42}$ is also able to bind to the plasma membrane or not.

Even though we cannot exclude that monomeric $A\beta_{1-42}$ forms small earlier aggregates in solution, our data show that i) when adding the monomer of $A\beta_{1-42}$ to the cell culture media at low concentrations (< 150 nM), $A\beta_{1-42}$ peptide cannot be taken up very efficiently; and ii) the aggregated form, which is a requisites for cellular uptake, can be formed directly on the plasma membrane.

This observation also suggests an explanation for the threshold concentration of the monomer uptake process. The process of nucleated polymerization is characterized by a threshold concentration, below which aggregation cannot occur, which is called the critical concentration for aggregation and is the same as the saturation concentration for monomeric Aβ peptide in equilibrium with aggregates (see introduction chapter 1.4). If $A\beta_{1-42}$ needs to form defined aggregate structure before its cellular uptake, the threshold concentration for uptake would correspond to the critical concentration for $A\beta_{1-42}$ aggregation on the plasma membrane or in solution. Once the $A\beta_{1-42}$ aggregates reached a certain size and/or form, they can be then taken up. The critical concentration of $A\beta_{1-42}$ was reported to be approximate at 160 nM in solution (Usui et al. 2009). It could be considerably lower for membrane–bound Aβ (Usui et al. 2009), but the aggregation of $A\beta_{1-42}$ in equilibrium with binding to a membrane surface has not been analyzed quantitatively in this study.

Friedrich et al. had speculated that, after association of soluble Aβ with the cells, the amyloid plaques would be formed intracellularly (**Figure 1–8** b). Our data provided a more detailed evidence of membrane associated $A\beta_{1-42}$ structures and the possible location of aggregate formation. Our resultes suggest that intracellular $A\beta_{1-42}$ aggregate can be formed in the plasma membrane from soluble $A\beta_{1-42}$, which can be the monomer and / or small aggregates in very early aggregation state. We observed FRET between labeled monomeric $A\beta_{1-42}$ species, indicating their aggregation, in endocytic vesicles under conditions that permitted endocytosis (**Figure 4–16** c). However, we also observed FRET between the same $A\beta_{1-42}$ species on the plasma membrane, when blocking their uptake. These observations may suggest that the formation of toxic $A\beta_{1-42}$ aggregates occurred membrane binding, rather than after entry into the endocytic vesicles.

Hu et al. showed that $A\beta_{1-42}$ (1 nM in cell culture medium) could be detected after 24 h incubation with SHSY5Y cells. The authors observed a monomer uptake at a much lower

concentration than our results (Hu et al. 2009). However, their study did not characterized the monomers they used, and did not clearly state the monomers that used were monomerized by specialized treatment, such as by using SEC or membrane filtration. Rather, the $A\beta_{1-42}$ peptide was simply diluted out of DMSO solution. Without a specific monomerization treatment, it is likely that the $A\beta_{1-42}$ was present aggregates/oligomers not monomers.

Moreover, we found that preexisting $A\beta_{1-42}$ aggregates could also be internalized directly.

Our observations therefore also raise the question, what structure or size the aggregates need to be for a successful cellular uptake. The uptake of aggregated $A\beta_{1-42}$ will be discussed in the next section.

5.2.2 Uptake of $A\beta_{1-42}$ aggregates

Compared to the uptake of monomers, the cellular uptake of preaggregated $A\beta_{1-42}$ species is more efficient (**Figure 4–12**). Bateman and Chakrabartty have reported similar observations. Aggregated species of $A\beta_{1-42}$, which was a mixture with hydrodynamic radius from 10 to 1000 nm as measured by DLS and that were ThT positive, were collected from aggregation assay. These aggregates (1.5 µM) were taken up more rapidly than $A\beta_{1-42}$ monomers by PC12 cells (Bateman & Chakrabartty 2011).

Small aggregates containing preexisting β–sheet–rich structures can be internalized at very low concentration. The lowest concentration that we used to treat the cells in our experiments is 15 nM (corresponding monomer concentration, **Figure 4–12** c). It must be noted, this is the concentration of $A\beta_{1-42}$ in the cell culture media, not on the plasma membrane or inside the cells.

A threshold concentrations similar to that required for monomer uptake, at approximately concentration range 200–300 nM, was not observed for the uptake of aggregates with β–sheet–rich structures, supporting the mode that $A\beta_{1-42}$ aggregation facilitates its cellular uptake.

We hypothesize that the β–sheet–rich structures might be the key factor for cellular uptake of Aβ peptides. Aggregates with β–sheet structure were internalized immediately after the $A\beta_{1-42}$–membrane binding, whereas monomers or small aggregates without β–sheet first had to convert into β–sheet structures on the plasma membrane before being taken up.

We will therefore then examine and discuss the secondary structures of membrane associated and internalized $A\beta_{1-42}$.

5.2.3 Secondary structure of internalized Aβ$_{1-42}$

To detect the β–sheet structure of internalized Aβ$_{1–42}$ in the cultured cells, a classic thioflavin dyes, ThS, was used (LeVine 1993).

ThS is widely used dye to identify amyloid structure in tissue or in the cultured cells. Similar to ThT, ThS binds specifically to β–sheet–rich structures and displays then an enhanced emission fluorescence (Sun et al. 2002; Cullen et al. 1996; Guntern et al. 1992). But unlike ThT, ThS is less sensitive to pH. Lowering pH (< pH 5) has no significant influence on its fluorescence (LeVine 1993). Thus, ThS is better suitable for staining inside the endocytic vesicles. Additionally, from my observations, ThS seems to better pass through the membranes, and binds then selectively to Aβ aggregated form with high affinity. Therefore, instead of ThT that was used for reporting formation of β–sheet in vitro, ThS was used for recognizing the secondary structure of Aβ$_{1–42}$ in cultured cells by microscopy. ThS is routinely used to stain deposited Amyloid–β in the visual cortex of the brains of AD patients (Grienberger et al. 2012).

Our experiments combining aggregation kinetic in vitro and ThS staining of cells show that: i) the amount of internalized Aβ$_{1–42}$ correlates with the formation of ThT positive aggregates in vitro, and ii) that internalized Aβ$_{1–42}$ is ThS positive.

Figure 4–20 a and c show that, the amount of β–sheet structures in the samples is correlated with the amount of internalized Aβ$_{1–42}$, suggesting ß–sheet structure may promote the cellular uptake. ThS staining supports our hypothesis (**Figure 4–19**). By treating the Sh–EP cells with two types of labeled Aβ$_{1–42}$, Aβ$_{1–42}^{488}$ monomer at a concentration under the uptake threshold concentration (at 150 nM), and Aβ$_{1–42}^{633}$ β–sheet aggregate (at 900 nM), respectively, internalization of Aβ1$_{–42}^{488}$ occurred only via coaggregation with Aβ$_{1–42}^{633}$ aggregate. ThS and calcein were added to live cells to visualize β–sheet structure and location of Aβ$_{1–42}$, i.e. on the plasma membrane or in endocytic vesicle. Our observations show that, ThS and calcein fluorescence signals were very closely linked. Only the aggregates that contained β–sheet structure (ThS positive) were internalized (calcein positive). In contrast, ThS negative species only associated with cell surface and could not to be observed in typical endocytic vesicles.

These data demonstrate that aggregates with β–sheet structures are internalized more rapidly and efficiently than monomers or small aggregates without β–sheet structures, and support our hypothesis, that conversion into β–sheet structures facilitates the efficient uptake of Aβ$_{1–42}$ by neuroblastoma cells via an endocytotic mechanism.

We hypothesis that, non–β–sheet species of Aβ$_{1–42}$ are capable of binding to plasma membrane, and converting into β–sheet–rich aggregates on the plasma membrane. To the best of my knowledge, the exact reason and mechanism, that the plasma membrane provides a platform for Aβ$_{1–42}$ aggregation, are still unclear. Aβ has been observed to adopt

β–sheet structure on model membranes systems, which may support our hypothesis that lipid membranes assist β–sheet formation, but no data exist for physiological plasma membranes. Alternatively, $A\beta_{1-42}$ could bind to a receptor or other membrane protein, Aβ–receptor binding may facilitate Aβ aggregation and uptake. However, our data from model membrane systems indicate that small aggregates from early aggregation state can interact directly with the membrane lipids.

The interaction of Aβ with model membrane system will be discussed in detail in section 5.3.

These observations raise also the question, whether the uptake of $A\beta_{1-42}$ correlates with cytotoxicity and whether the uptake of $A\beta_{1-42}$ into the cells could cause an inhibition of the cellular metabolism activities.

5.2.4 The causal link between $A\beta_{1-42}$ uptake and its cytotoxicity

Many studies have already shown that different aggregate species of Aβ from different aggregation states displayed fairly different levels of toxicity to cultured cells or in mouse models (Zhang et al. 2002; Glabe 2006; Barghorn et al. 2005; Stefani 2010; Ahmed et al. 2010). In those aggregates, the soluble $A\beta_{1-42}$ oligomer is commonly thought to be the most and primary toxic aggregate species associated with memory dysfunction in the early stage of AD (Ahmed et al. 2010; Klein 2006; Walsh et al. 2002). There are many hypotheses for the mechanism of cell / neuron death or damage, such as the interaction of Aβ with the plasma membrane that bind cholesterol which results in channel formation (Di Scala et al. 2014), or reuptake of extracellular $A\beta_{1-42}$ results in neurotoxicity (Hu et al. 2009; Friedrich et al. 2010).

We examined whether the internalization of $A\beta_{1-42}$ adversely affect the activity of cell metabolism. For this end, MTT assay, which is a frequently used method for testing the cell viability and metabolic activity in the studies cited above, was used.

Our results show that, inhibition of the cell metabolism activity and the detection of internalized $A\beta_{1-42}$ are correlated. By treating the cells with monomeric $A\beta_{1-42}$, the drop of the metabolism activity is proportional correlated to amount of the $A\beta_{1-42}$ being taken up, which is in turn a dependent on the monomer concentrations in the medium.

It should be mentioned that the threshold concentration of $A\beta_{1-42}$ monomer for inhibition of cell metabolic activity was between 75 – 150 nM (monomer concentration in the medium, **Figure 4–20** e), which is lower than threshold concentration observed for monomer uptake (200 – 300 nM). A possible explanation could be the different aggregation rate between labeled and unlabeled $A\beta_{1-42}$. The fluorescence label had no effect on the morphology of formed fibril (**Figure 4–3** b and c), but it slowed down slightly the aggregation kinetics (**Figure 4–3** a). For MTT assay, the cells were treated with 100% unlabeled $A\beta_{1-42}$, and fluoresce labeled $A\beta_{1-42}$ was used for uptake experiments. Alternatively, it is possible that

the membrane associated $A\beta_{1-42}$, may already be able to influence the cell metabolism before being taken up. The third possible reason could be a lack of sensitivity in the readout method for uptake by HCS microscopy. Intracellular aggregates need to have a certain size or brightness to be detected by the HCS algorithm. At the threshold concentrations, approximately between 100 – 200 nM, the fluorescent signal of $A\beta_{1-42}$ may be too weak to be detected by conventional microscopy.

Nevertheless, by treating with monomeric $A\beta_{1-42,}$ when their concentrations below 100 nM, no uptake of $A\beta_{1-42}$ is detected, and cell viability by MTT assay is not changed, suggesting the monomeric $A\beta_{1-42}$ neither convert into β–sheet aggregates, nor is the peptide cytotoxic below the threshold concentration for uptake. The observation that the threshold concentration for uptake and cytotoxicity is very close to the critical concentration for $A\beta_{1-42}$ monomer aggregation, supports the hypothesis that formation and uptake of β–sheet positive aggregates is the prerequisite for metabolic toxicity of $A\beta_{1-42}$, while the monomeric peptide itself is relatively harmless. The damage of the neurons and the neurototoxicity may be caused by the accumulation of monomer and its aggregation products.

However, there are data disputing that the β–sheet positive aggregates of Aβ are the toxic species. Ahmed et al reported that a β–sheet negative $A\beta_{1-42}$ oligomer was highly neurotoxic (Ahmed et al. 2010). A close look at their assay conditions reveals that those oligomers were incubated with the neurons at 37 °C for 48 h and at a final $A\beta_{1-42}$ concentration of 5 µM. Our data demonstrate that this concentration is more than sufficient for the formation of β–sheet aggregates. Thus, the β–sheet negative $A\beta_{1-42}$ oligomers, which were the authors consider form for internalization, may not be in the state as the beginning of the experiments. $A\beta_{1-42}$ oligomers probably already convert into a higher ordered structure during the toxicity assay.

Walsh et al. found that SDS–stable trimers were highly neurotoxic and that they inhibited long term potentiation in the synaptic transmission of hippocampal neurons (Walsh et al. 2002). The secondary structure of those oligomers has not been characterized rigorously and it is not clear if the toxic species formed a larger aggregate under native conditions. Two possible models would reconcile the data of Walsh et al. with our results: i) the toxic species could be a β–sheet positive aggregate that dissociates into trimers after SDS denaturation; ii) there are two distinct mechanisms of Aβ toxicity affecting different neuronal processes. The second hypothesis is supported by the observations that two different modes of Aβ cytotoxicity exist, the interference with synaptic transmission and the inhibition of cellular metabolism activities. In the present study, we probed the second mechanisms of Aβ toxicity, while the study by Walsh et al. probed the first.

5.2.5 Pathway of $A\beta_{1-42}$ uptake

The extracellular molecules can be internalized via different endocytotic pathways (Marsh & McMahon 1999), such as phagocytosis for solid particles; macropinocytosis for fluid; and the clathrin or caveolin mediated endocytosis for small molecules, such as peptide or proteins (Mayor & Pagano 2007).

Endocytosis of misfolded proteins, such as Aβ, tau protein, α–synuclein and huntingtin, have already been described in cell models (Frost et al. 2009; Brundin et al. 2010) via several possible endocytic pathways (Kanekiyo et al. 2013; Holmes et al. 2013; Lai & McLaurin 2010; Treusch et al. 2011; Yu et al. 2014). It would be plausible that the observed differences in cytoxicity between small disordered aggregates and aggregates containing β–sheet structure, the protofibril or twisted fibrils may be linked to differences in the internalization process.

We observed internalized $A\beta_{1-42}$ located in endocytic vesicles (**Figure 4–5** a and b). To shed light on the endocytotic pathway, we examined their endocytosis by using varying methods to block endocytic pathways and by using immunofluorescence (IF) staining with different endocytosis markers.

Clathrin–mediated endocytic pathway can be blocked via lowering the temperature to 4°C (Harding et al. 1983). The inhibition of the clathrin–mediated endocytosis was confirmed by the fact that transferrin located primarily on the plasma membrane under this condition and was not endocytosed (**Figure 4–14**). Transferrin binds to the transferrin receptor on the plasma membrane and can be internalized by CME via clathrin–coated pits. Fluorescent transferrin conjugates are therefore broadly used as marker for investigating the early phase of CME (Iacopetta et al. 1983; Harding et al. 1983; Jandl & Katz 1963; Laurell & Ingelman 1947). The uptake of transferrin depends on both temperature and energy, thus can be blocked at low temperature (Harding et al. 1983). At 4°C, transferrin only binds to its receptor on the plasma membrane, and will not be taken up (Harding et al. 1983). Inhibition of CME pathway could be reported by the location of transferrin. However, it should be noted that at 4°C the fluidity of membrane is limited, which may also influence other endocytotic mechanisms or the aggregation of $A\beta_{1-42}$ (Uzman et al. 2000; Lodish et al. 2008).

At 4°C, the uptake of preaggregated $A\beta_{1-42}$ is reduced but cannot be totally blocked. Compared with 37 °C, the amount of internalized $A\beta_{1-42}$ decreased by 90% at the same concentration (150 nM, **Figure 4–15**). These data suggest that a clathrin independent pathway of $A\beta_{1-42}$ uptake may exist. Our data do not necessarily imply that 90% of $A\beta_{1-42}$ is taken up by CME. Since other endocytic processes are also affected by the decreased temperature, the observed drop of uptake rate at 4°C may be caused by decreased activity of the cells under this non–physiological temperature.

In another control experiment, clathrin–mediated endocytosis was selectively blocked by potassium depletion (Larkin et al. 1983; Ivanov 2008). Uptake of $A\beta_{1-42}$ was not completely

blocked but rather increased by lacking of K^+ (**Figure 4–22**), supporting the hypothesis that the internalization of $A\beta_{1-42}$ may be achieved through a clathrin independent pathway.

Colocalization experiments further supported our hypothesis. Interacellular $A\beta_{1-42}$ colocalize rarely with typical markers, clathrin and LAMP2, for the clathrin–mediated endocytic pathway by IF staining (**Figure 4–21**). No colocalization between internalized $A\beta_{1-42}$ and transferrin was detected as well (**Figure 4–14**).

We therefore conclude that extracellular $A\beta_{1-42}$ can enter the cells via a non–clathrin–mediated pathway, and locate then in the endocytic vesicles. Costaining with caveolin suggests a possible uptake route via the caveolin endocytosis pathway (**Figure 4–21**). Several studies have reported other amyloid proteins such as tau can be endocytosed through micropinocytosis and proteoglycan–mediated processes (Kanekiyo et al. 2013; Holmes et al. 2013; Lai & McLaurin 2010; Treusch et al. 2011; Yu et al. 2014). A further study may be needed to precisely determine the endocytosis pathway of $A\beta_{1-42}$.

Internalized $A\beta_{1-42}$ was observed to colocalize with lysosome by using lysosome marker (Bateman & Chakrabartty 2011) and LysoTracker (Hu et al. 2009); Friedrich et al. have observed internalized Aβ located within multivesicular bodies (MVBs) by Transmission electron microscopy (TEM) (Friedrich et al. 2010). These observations suggest those internalized $A\beta_{1-42}$ located into endosome and/or lysosome via typical endocytic traffic pathway.

Moreover, our data suggest that, internalized $A\beta_{1-42}$ accumulates in endocytic vesicles instead of being degraded. It is possible that β–sheet rich structures of aggregated $A\beta_{1-42}$ difficult to degrade. Additionally, the increased concentration of $A\beta_{1-42}$ and low pH in lysosome, both may facilitate the further aggregation of Aβ and stabilize their secondary structure, that may lead to cell damage and deposit of $A\beta_{1-42}$.

The degradation pathway of toxic $A\beta_{1-42}$ if it existed and possible apoptosis mechanism leaded by $A\beta_{1-42}$ could be the next goal. Considering that the cell damage and cell death might be the results of by intracellular accumulation of $A\beta_{1-42}$ over the time, an animal model might be more suitable for a long–term observation than cultured cell.

From what has been discussed above, we may reasonably assume that the stable and hard to degradad β–sheet–rich structures of internalized $A\beta_{1-42}$ may be one of the possible causes, leading to the cytotoxicity and cell death, finally to an accumulation in the plaques on brain of AD patients.

5.3 Interaction of $A\beta_{1-42}$ with membranes

The interaction of misfolded proteins with liquid / surface interfaces plays a crucial role for many protein–misfolding diseases, such as Alzheimer's disease, Parkinson's disease and Huntington's disease (Burke et al. 2013).

We have discussed that interaction of with the plasma membrane of neuronal model cells benefits the conversion of non–toxic $A\beta_{1-42}$ species into cytotoxic aggregate. However, their binding partner on the plasma membrane could be either lipid bilayer itself or membrane proteins.

In the following part, we therefore addressed the interaction of $A\beta_{1-42}$ with lipids by using simplified model membrane systems, such as GUVs and GPMVs. We found that aggregated Aβ, which is in ThT negative state, binds to Ld phase of lipid bilayers, and induces then negative membrane curvature in lipid bilayers leading to invaginations that look similar to endocytic vesicles.

5.3.1 Aβ–membrane binding

Amyloid precursor protein (APP) is a transmembrane glycoprotein highly concentrated in the synapse of neurons. Aβ peptide is produced by APP cleavage, contains part of transmembrane region of APP (Olsson et al. 2014; Haass et al. 1993; LaFerla et al. 2007). The amphiphilic character of Aβ make it capable to interact with membrane, and may also be able to insert into the lipid bilayer (Williams & Serpell 2011; Lansbury & Lashuel 2006; Burke et al. 2013).

5.3.1.1 Accumulation of $A\beta_{1-42}$ on ld phase of GUVs

We observed that $A\beta_{1-42}$ rapidly accumulated on the plasma membrane, and then formed aggregates directly on the plasma membrane (**Figure 4–14**, **Figure 4–16** a and b, **Figure 4–19**). In addition, we observed preferential binding of $A\beta_{1-42}$ to ld phase of GUVs model membrane systems (**Figure 4–26**).

Model membranes have been used for the studies of interaction of Aβ with different lipid components, such as cholesterol (Burke et al. 2013; Yip et al. 2001; Reiss et al. 2004; Yu & Zheng 2012), sphingolipids (Burke et al. 2013; Van Echten–Deckert & Walter 2012), gangliosides (Burke et al. 2013; McLaurin & Chakrabartty 1996), and neutral or charged phospholipids (Burke et al. 2013; McLaurin & Chakrabartty 1997; Sabaté et al. 2005; Sabaté & Estelrich 2005; Sabaté et al. 2012). The accumulation of oligomeric $A\beta_{1-40}$ has been observed in the ld phase of ld/lo phase–separated lipid monolayers (Hamada et al. 2010). A

selective location of $A\beta_{1-42}$ oligomer and prefibrils (defined as “protofibrils” in our study) in the DOPC rich region, i.e. ld phase, of cell–sized ld/lo phase–separated liposomes had also been reported by Morita et al (Morita et al. 2012).

Our experiments data confirmed the accumulation of $A\beta_{1-42}$ in the ld phase of the membrane. $A\beta_{1-42}$ readily accumulated in membrane of GUV that were formed from DOPC in pure ld phase (**Figure 4–26** a). No accumulation of Aβ was observed in the GUVs containing 100% cholesterol, GUVS in a relative pure lo phase (**Figure 4–26** b) (Stöckl & Herrmann 2010). Correspondingly, in GUVs with coexisting ld/lo phases, $A\beta_{1-42}$ only induced membrane negative curvature in the ld phase but not in the lo phase (**Figure 4–31**). Remodeling of membrane curvature by $A\beta_{1-42}$ coincided with membrane binding. Its possible mechanism is discussed in more detail below.

Several studies have reported that $A\beta_{1-42}$ associates with either the lipids or protein complexes in raft domains and have suggested that production of $A\beta_{1-42}$ and cholesterol levels are closely related (Lai & McLaurin 2010).

Our observations suggest, while $A\beta_{1-42}$ may interact with protein complexes in the cholesterol–rich lo domain in vivo, $A\beta_{1-42}$ preferentially binds to the lipid in the ld phase of the lipid bilayer and that the invaginations are formed specifically in the Ld phase of GUVs membrane.

Our observations also agree with those results that find binding of small aggregated (oligomeric) Aβ to the lipid bilayer. After short time (15 min) incubation of $A\beta_{1-42}$ monomer (10 µM) with GUVs, $A\beta_{1-42}$ accumulated on the membrane of DOPC GUVs (**Figure 4–26** a). On the other hand, no $A\beta_{1-42}$ binding was observed when $A\beta_{1-42}$ was diluted out directly after addition to the GUV membrane (**Figure 4–36**), suggesting that aggregation was necessary for membrane binding.

In our experiments, the accumulation occurred faster than the aggregation of $A\beta_{1-42}$ into ThT positive aggregates (**Figure 4–25**). ThT binding is the hallmark of β–sheet–rich aggregates. Therefore, our results suggest that $A\beta_{1-42}$ species that have higher membrane affinity are likely small aggregates (oligomer) from very early aggregation state and not β–sheet rich aggregates. However, from these experiments, we could not determine whether those small aggregates (oligomers) formed in solution before membrane binding or whether they had formed on the membrane surface.

Also, our observations on GUV model membranes raise the question why β-sheet rich aggregates are internalized so much more efficiently than monomeric or early small aggregates of Aβ. One possibility is that binding of β-sheet aggregates to cell membranes is mediated by factors such as proteoglycans or membrane complexes that are not present in the GUV model system. Another possibility is that the concentration of Aβ used in our GUV membrane model (10 µM), which was much higher than the threshold concentration of monomer uptake into cells, facilitated the formation of membrane active Aβ species.

More details of Aβ aggregation state that bound to model membrane will be discussed in section 5.3.3.

5.3.1.2 Mode of $A\beta_{1-42}$–membrane interaction

We probed the $A\beta_{1-42}$–membrane interaction by FRET measurement between $A\beta_{1-42}$ peptide and lipids of GUVs membrane. C6–NBD–PC of DOPC GUVs to $A\beta_{1-42}^{633}$ FRET verified that $A\beta_{1-42}$ peptide is very close to GUVs membrane (**Figure 4–27**). Based on the fact that the Föster distance between the donor and the acceptor is typically smaller than 100 Å, the maximum distance between the $A\beta_{1-42}$ and C6–NBD–PC in our experiments should be smaller than 10 nm.

Base on these FRET data, we can attempt to draw conclusions about the position of the Aβ molecule, whether it attaches to the membrane surface or inserts into the membrane bilayer. Fluorophores were attached the N–terminus of the Aβ peptide. The amphiphilic character of the N–terminus of Aβ make it capable to interact with membrane, and may also enable Aβ to insert into the lipid bilayer (Williams & Serpell 2011; Lansbury & Lashuel 2006; Burke et al. 2013).

As the NBD dye sits at the C6 position in the hydrophobic tail of the lipid, the FRET signal would suggest that $A\beta_{1-42}$ had inserted into the membrane. However, the NBD label can adopt two possible conformations: inserted into the membrane, or looping back to head group of the lipid molecule or even possibly extend into solution (Huster et al. 2001). This prevents us from determining whether the $A\beta_{1-42}$ peptide is inserted into the membrane or whether it remains bound to the lipid-water interface.

A more comprehensively experiment would be helpful, in which complementary labels are attached to the head group and different positions of hydrophobic tail of the lipid and the N– and C–terminus of $A\beta_{1-42}$ peptide, respectively.

5.3.2 Induction of negative membrane curvature

Generation of dynamic membrane curvature is one of the basic activities for the life, and is needed for the exchange of the substrates between in and outside the cells. Transport vesicles, such as endocytic or exocytic vesicles, and viral buds are typical representatives. The formation of dynamic membrane curvature is achieved either by lipids and proteins via protein–membrane interaction or via the local concentration change of membrane lipids (Stachowiak et al. 2013; McMahon & Gallop 2005). However, the dynamics of membranes

do not always have positive consequences. The membrane bending could be reduced by many peptides or proteins, which are involved in neurodegenerative diseases.

Many studies have suggested that aggregation of Aβ in or near membrane might lead to disruption of membrane structure, change of the membrane curvature or creation of membrane pores (McLaurin & Chakrabartty 1997; McLaurin & Chakrabartty 1996; Mirzabekov et al. 1996; Gorbenko & Kinnunen 2006; Burke et al. 2013). Arispe et al and Di Scala et al have reported binding of Aβ to cholosterol results a channel formation of the plasma membrane (Di Scala et al. 2014; Arispe, Pollard, et al. 1993; Arispe, Rojas, et al. 1993); Vestergaard et al had observed $A\beta_{1-42}$ induced membrane fusion by giant unilamellar vesicles (GUVs) (Vestergaard et al. 2013).

In our study, we observed for the first time the induction of negative membrane curvature by Aβ peptide. $A\beta_{1-42}$ is able to accumulate on ld phase of GUVs membrane. It then induces local negative curvature, namely invaginations, on the membrane of DOPC GUVs (from 100% DOPC, **Figure 4–26** a & **Figure 4–28**a) and of PE/PC GUVs (from DOPC : DOPE in 1:1 molar ratio, **Figure 4–29**) as well. In the ld/lo phase–separated GUVs (form DOPC : SSM : Chol in 1:1:1 molar ratio), the $A\beta_{1-42}$ induced invaginations were observed exclusively in the Ld phase (**Figure 4–31**). Furthermore, $A\beta_{1-42}$ induced invaginations could also be observed in GPMVs that isolated from SH–EP cells (**Figure 4–32** b).

Combined with the previously results that $A\beta_{1-42}$ accumulate only in ld phase, not in Lo phase (**Figure 4–26** a and b), our results suggest that both $A\beta_{1-42}$ binding and $A\beta_{1-42}$ induced membrane remodeling are primarily located to ld phase.

Membrane remodelling by $A\beta_{1-40}$ in SUVs model membrane system has been hypothesized by Matsuzaki and Horikiri from Fourier transform infrared spectroscopy with polarized attenuated total reflection (FTIR–PATR) data (Matsuzaki & Horikiri 1999). They investigated the $A\beta_{1-40}$–lipid interaction by a shift in IR resonances, and the molecular orientations were evaluated by polarization. Their CD and FTIR–PATR spectroscopy data suggest $A\beta_{1-40}$ may induce negative curvature strain on the ganglioside–containing membrane of SUVs (PC : GM1 in 4:1 molar ratio). However, Morita et al have recently reported a contrary observation by $A\beta_{1-42}$ using GUVs, that the location of oligomeric $A\beta_{1-42}$ (5 μM) was observed in the ld phase of cell–sized lo/ld phase–separated liposome, which were formed from DPPC, DOPC, cholesterol (Chol), fluorescent lipid analogs rhodamine–DHPE (Rho–PE) for ld and NBD–DPPE (NBD–PE) for lo phases. They observed that $A\beta_{1-42}$ (5 μM) oligomers induced the exo– and endo–buds from lo domains and enhanced the fluctuation of the ld phase by microscopy. They speculated that $A\beta_{1-42}$ oligomers may induce a change in the motion of lo domains (chol) that float within the ld phase (PC), and caused the budding of lo domains (Morita et al. 2014). Their different observations may be due to different liposome models

(SUVs and GUVs), or the different aggregation states of Aβ peptide or different preparations of samples.

α–Synuclein, another protein tightly associated with neurodegenerative disorders which accumulates in Parkinson's disease, is also able to associate with membrane (Jao et al. 2008; Stöckl et al. 2010). Braun et al shown the interaction of α–Synuclein with membrane can result both positive and negative curvature by molecular dynamics (MD) simulation calculations that were based on NMR data (Braun et al. 2012). α–Synuclein was found to increase positive membrane curvature on pure DOPS GUVs (Shi & Baumgart 2015; Shi et al. 2015). The authors speculate that this process may play a role in neurotoxicity in Parkinson's disease. However, the mechanism of this process is not yet well understood.

We observed, the induction of invaginations is related to the binding of $A\beta_{1-42}$ to membrane. This indicates that the remodelling of membrane curvatures is the result of the $A\beta_{1-42}$ /membrane binding and interaction. Those observations raise then an important question, namely which aggregates species of Aβ peptide interact with then membrane and whether these are the same species that induce negative membrane curvature.

5.3.3 ThT negative $A\beta_{1-42}$ aggregates induced membrane remodeling

In our study, we noted that there is always a time interval between adding $A\beta_{1-42}$ monomer to GUVs and the detection of invaginations (fig. 4–28). This time interval can be omitted by incubating GUVs with preaggregated Aβ. However, the spectrum of aggregate populations that are capable to induce membrane inagination is not very broad, i.e. Aβ preaggregated for 45 min or more seems to lose its membrane remodelling activity. When comparing this time window to the time scale of the ThT aggregation kinetic (**Figure 4–25**), we found that membrane activity coincides with the lag phase of aggregation. Neither monomer nor big aggregates, but only small ThT negative aggregate from the end of the lag–phase of ThT kinetics bind to ld phase (DOPC) with high affinity, and are capable to induce invaginations. This interpretation is reinforced our data from $A\beta_{1-40}$ aggregation (**Figure 4–38**). Here, it was also species from the end of the lag phase at 16 h incubation, which had membrane activity.

Matsuzaki and Horikiri have observed that $A\beta_{1-40}$ would be in different conformations when binding to different lipids. $A\beta_{1-40}$ was in an unordered structure in solution examined by CD and ThT assay. After membrane associations, $A\beta_{1-40}$ bound to membrane of PC SUVs was measured in unstructured form by CD spectroscopy, whereas $A\beta_{1-40}$ formed α–helix upon association with membrane of negatively charged PG SUVs and formed β–sheet conformation in the membrane of PC/GM1 SUVs (in 4:1 molar ratio) (Matsuzaki & Horikiri 1999).

Different to the conclusions from Morita et al (Morita et al. 2014), our data support that membrane transformations are induced by aggregated species not by monomers.

5.3.4 Possible mechanism of $A\beta_{1-42}$ induced membrane remodeling

Our results show that, Aβ aggregates are able to induce negative membrane curvature leading to the formation of spherical invaginations in GUVs model systems. Since no other components are present in the system, negative membrane curvature has to result from the Aβ–membrane interaction, but the mechanism is not known yet. Possibly, membrane curvature is induced by inserting Aβ aggregates into the membrane.

A spontaneous incorporation of $A\beta_{1-40}$ into neural liposomes (soybean PC, in average diameter about 200 nm) was reported by Sabaté et al (Sabaté et al. 2005).

Braun et al have reported the membrane remodeling effects of other amyloid protein, α–synuclein, using combination of experimental data from X–ray scattering and fluorescence correlation spectroscopy, coarse–grained molecular dynamics (MD) simulations and potential of mean force calculations, found that α–synuclein could induce both positive and negative curvature in membranes. They have suggested that curvature–generating amphipathic α–helices of α–synuclein to induce the negative Gaussian curvature on POPS/POPC (at a 1:3 mole ratio) bilayers (Braun et al. 2012).

Additionally, in our experiments, the osmotic pressure of buffer inside GUVs is larger than the outside. Due to the osmotic pressure difference between the in– and outside, membranes should be in an expanded state, which suggests the force generated from Aβ–lipid interaction has to be relatively large in order to overcome the osmotic pressure.

5.3.4.1 General principles for generating the negative membrane curvature by peptide action

In the normal, i.e. the relaxed, state of bilayers, the sum of lateral pressure is close to zero (Iversen et al. 2015). Koller and Lohner have sketched how a inserted molecule induce membrane curvature (**Figure 5–1**) (Koller & Lohner 2014). The insertion of protein or peptide into one monolayer of the membrane exerts a lateral pressure. This force probably arises from peptide–lipid interactions as well as peptide–peptide interactions. Those interaction processes induce then membrane curvatures. A lateral pressure on the hydrophobic tail region of phospholipids results negative curvature, i.e. curvature < 0, the lipid tails are pushed outward more than headgroups. A positive curvature is resulted by lateral pressure on lipid headgroup.

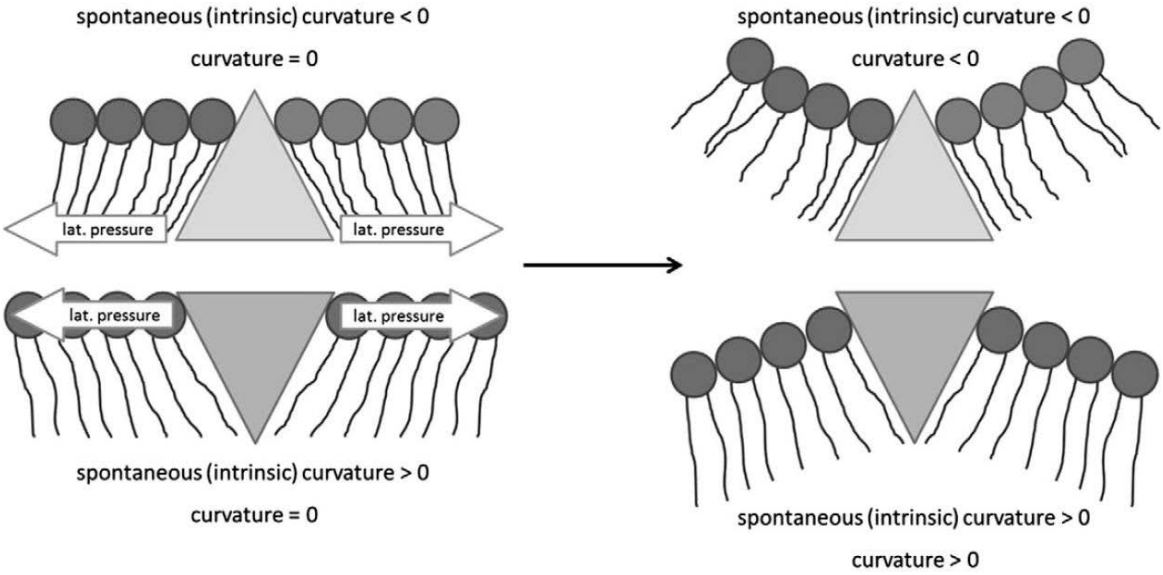

Figure 5–1: Definitions of negative and positive membrane curvature, which are driven by insertion of molecules (light grey) into monolayer that change the lateral pressure and induce the membrane curvatures. Figures adapted from Koller and Lohner (Koller & Lohner 2014).

By integration of a protein into the lipid bilayer (**Figure 5–2**), such as a transmembrane protein or transmembrane protein domain, the lateral pressure results deformation of membrane and protein oligomerization and conformation change (Iversen et al. 2015).

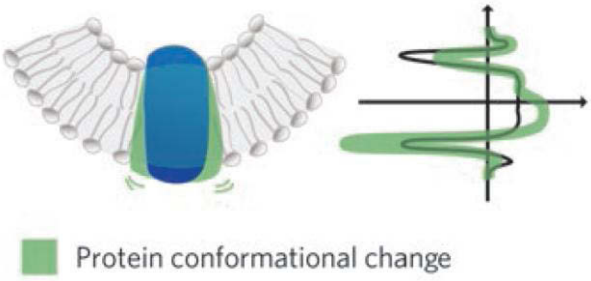

Figure 5–2: Membrane curvature is induced by lipid–protein interaction. Left: The conformation of transmembrane proteins is coupled to membranes via the lateral pressure profile. Right: the lateral pressure profile, which measured alone the bilayer, black, before and green, after the conformation changes of transmembrane protein. Figures adapted from Iversen et al (Iversen et al. 2015).

5.3.4.2 Possible structure of inserted $A\beta_{1-42}$

In the present study, we provide evidence that Aβ–membrane interactions can generate invaginations in the membrane of model membrane systems. Their interactions may have two effects on the membranes. On one hand, they may lead to a reorganization of membrane lipids to minimize their hydrophobic area. This may result a physical shape changes of membranes. On the other hand, the deformation of membrane, i.e. formation of

membrane negative curvature, may change the local physical properties of membrane and/ or lipids, which could then promote and modulate Aβ aggregation process. In other words, it can be thought that Aβ reorganizes its structure, especially the Aβ–lipid (in tail region of lipid) and Aβ–lipid–water (in lipid headgroup region) interface structures, to fit for surrounding ecology. This may also give Aβ a new biological activity. Additionally, our observations shown that Aβ aggregates in ThT negative state induced a negative membrane curvature in GUVs and GPMVs.

Following the model outlined above, in **Figure 5–3** we hypothesize that those Aβ aggregates embed into membranes, which induce and stabilize the negative membrane curvature, i.e. an invagination in the membrane (gray). Aβ peptides in an aggregated form embed into the lipid bilayer (green). Each Aβ peptide (orange) is in a hairpin structure, with the hydrophobic C–terminal part in the hydrophobic tail region of phospholipids, and N–terminal probably outside the membrane toward to the buffer. The hairpin structures of many single peptides may make the aggregate have a trapezoid shape. The longer base part of the trapezoid formed by the C–terminal part inserts into one monolayer of the membrane, while the shorter base part of the trapezoid formed by N-terminal part is toward to the buffer. By insertion of trapezoid shaped Aβ aggregate and Aβ–lipid interactions, the lateral pressure on the hydrophobic tail region of phospholipids may push the lipid tails outward more than headgroups, i.e. negative curvature is formed. The negative curvature may be enhanced through multiple insertion of Aβ aggregate and the reorganization of membrane lipids, i.e. an invagination is formed.

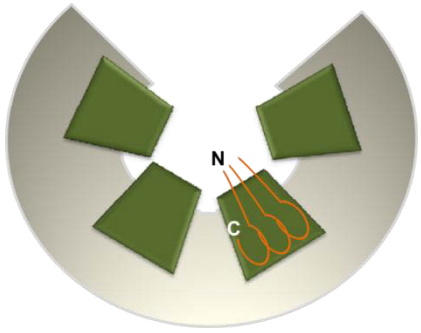

Figure 5–3: Schema of one invagination (grey) induced by embedded Aβ aggregate (green). Single Aβ aggregate embedded into the membranes, which induces and stabilizes the negative membrane curvature. Each Aβ peptide (orange) is in a hairpin structure, with hydrophobic C–terminal part in the hydrophobic tail region of phospholipids, and N–terminal probably outside the membrane toward to the buffer.

A similar model of $A\beta_{1-40}$, which insert C–terminal into the membrane, has been used by Lemkul et al to study the Aβ–membrane behavior by MD simulations (**Figure 5–4**), which found that the aggregates of $A\beta_{1-40}$ stably bind to membrane (Lemkul & Bevan 2013).

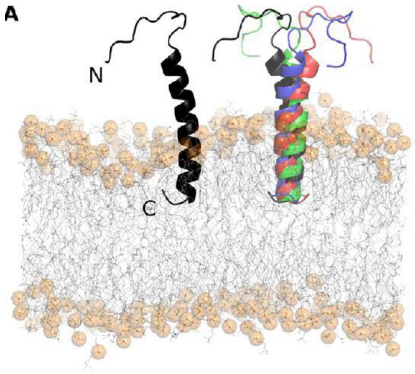

Figure 5–4: Configurations of $A\beta_{1-40}$ monomer (black) and aggregate (colored) with POPC membrane system by MD study. Figure adapted from Lemkul and Bevan (Lemkul & Bevan 2013).

Zhao et al. have investigated membrane interaction of $A\beta_{1-42}$ fragments using mix membrane from DPPC, chol., Cl^- and Na^+ by MD study (**Figure 5–5**). $A\beta_{1-42}$ fragment contains residues 1–27 (N–terminus) interact with the lipid-aqueous interface region, whereas residues 28–42 (C–terminus) embed into hydrophobic tail region (Zhao et al. 2011).

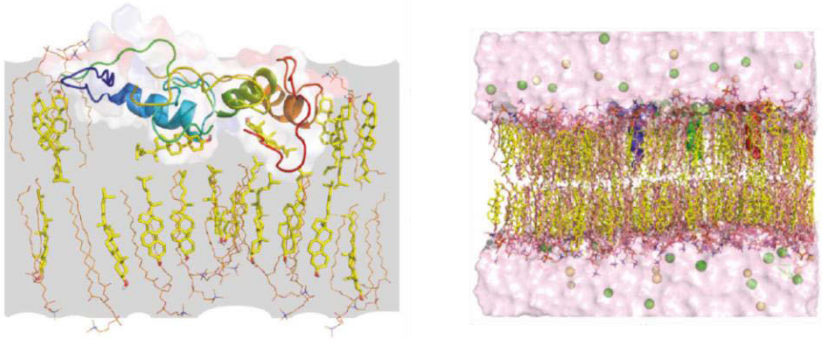

Figure 5–5: MD study of $A\beta_{1-42}$ fragments membrane interactions. Residues 1-27 (left) interact with the lipid-aqueous interface region. Residues 28-42 (right) inside the hydrophobic tail region. Membrane contained DPPC, chol., Cl^- and Na^+. Figure adapted from Zhao et al. (Zhao et al. 2011).

Based on those MD studies, we may imagine that part of Aβ aggregates insert into membrane, so that the embedded Aβ aggregates have their hydrophobic C–terminal part in the hydrophobic tail region, and, hydrophilic N–terminal probably remains contact with lipid headgroup. Within the bilayers, the $A\beta_{1-42}$ peptides might forms similar structures as were proposed for oligomeric $A\beta_{1-42}$ complexes in vitro (**Figure 5–6** a). Alternatively, the Aβ peptides could form a hairpin structure as in amyloid fibrils model (**Figure 5–6** b) (Ahmed et al. 2010).

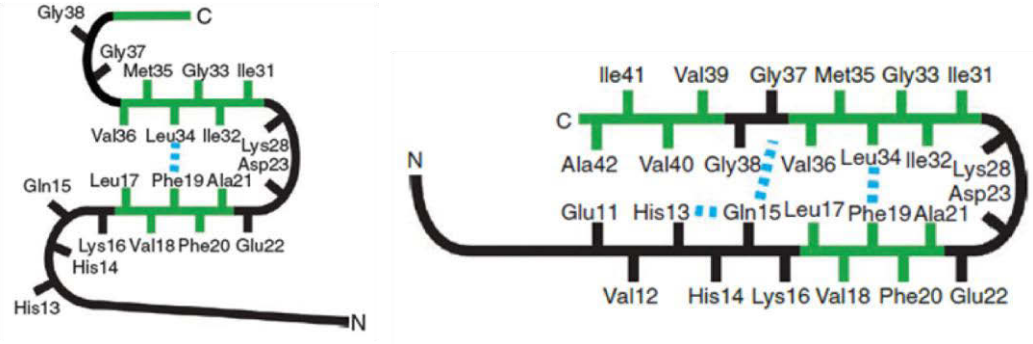

Figure 5–6: Schematic structure of $A\beta_{1-42}$ monomers, within the oligomer (left) and within fibrils (right). Figures adapted from Ahmed et al (Ahmed et al. 2010).

In our hypothetical membrane interaction model (**Figure 5–3**), Aβ aggregates embed into the membranes, and induce the negative membrane curvature. Each Aβ peptide is in a hairpin structure, with the hydrophobic C–terminal part embedded in the tail region of the lipids and N–terminal close to lipid headgroup (**Figure 5–3**). The localization of the hydrophobic hairpin structures makes the C–terminal part of $A\beta_{1-42}$ bulkier than the N–terminus, which leads to a wedge (trapezoid) shaped structure of the aggregates/oligomers in the membrane.

Several possible orientations of the C–terminus within $A\beta_{1-42}$ aggregate have been suggested by Ahmed et al for pentamers (**Figure 5–7**) and by Bernstein et al for haxamers (Figure not shown) (Bernstein et al. 2009; Ahmed et al. 2010).

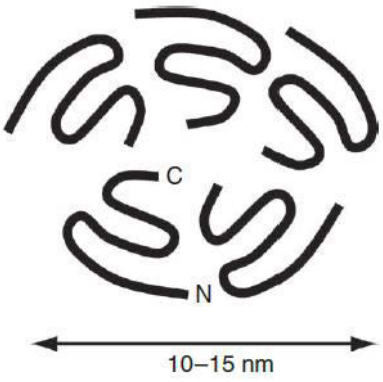

Figure 5–7: Schematic of the $A\beta_{1-42}$ pentamer based on SEC and AFM data. Figure adapted from Ahmed et al (Ahmed et al. 2010).

We measured an average diameter about 1 µm for a typical spherical invagination in GUVs that was induced by $A\beta_{1-42}$ (**Figure 4–28**). This is about 100–fold larger than the size of a single early Aβ oligomers (Ahmed et al. 2010). Based on the suggestion of possible size and structure of Aβ aggregates/oligomers by Ahmed et al (**Figure 5–7**) (Ahmed et al. 2010), we

assume that those invaginations, i.e. negative membrane curvatures, may be induced through embedding of multiple wedge shaped oligomers as shown in **Figure 5–3**.

Further mechanical details, such as the depth of Aβ insertion, the internal packing of insert Aβ aggregates complex contains only Aβ or it is an Aβ–lipid mixture, or the way of Aβ–membrane coupling, should be the goals in further studies.

6 Conclusion and outlook

One of the pathological hallmarks of Alzheimer's disease (AD) is deposits of the protein fragment β–amyloid in the form extracellular plaques (George G. Glenner & Wong 1984). Amyloid–beta peptides (Aβ) between 38–43 amino acids in length are formed by proteolytic cleavage of a membrane protein, the amyloid precursor protein (APP). Aβ is released as a monomer and tends to form aggregates spontaneously. The oligomeric species of $A\beta_{1-42}$ are tightly linked to AD pathogenesis and are presumed to be the cause of neuronal damage (Walsh et al. 2002). Many studies have suggested that the reuptake of extracellular $A\beta_{1-42}$ and subsequent formation of intracellular aggregates might be one pathway that leads to neuronal damage and neurotoxicity (Friedrich et al. 2010; Hu et al. 2009). However, questions remain as to where aggregates form, how the state of aggregation of $A\beta_{1-42}$ relates to its internalization, and why aggregated species (oligomer) are far more toxic than monomers and large fibrils. Clearly the aggregation and internalization of $A\beta_{1-42}$ and the connections between these processes may be vital in understanding the ultimate toxic effects of this peptide.

My thesis project aims to understand the structural and mechanistic details of $A\beta_{1-42}$ internalization. We used fluorescently labeled $A\beta_{1-42}$ to visualize the aggregation state of peptides and track their neuronal uptake in a human neuroblastoma (SH–EP) cell model. We examined the relationship between the aggregation state of extracellular $A\beta_{1-42}$ and the efficiency of its internalization to determine whether the formation of aggregates is a prerequisite to or the consequence of its neuronal uptake, and found that the cells very efficiently internalized β–sheet positive aggregates of $A\beta_{1-42}$ that form early in its aggregation kinetics. The cellular uptake was correlated with cytotoxicity. These results suggest that aggregate formation is the prerequisite rather than the consequence of $A\beta_{1-42}$ uptake and that interaction of the $A\beta_{1-42}$ oligomers with the membrane is the first step of the endocytotic process.

The second aim of my thesis is therefore to characterize Aβ membrane interaction in detail. By using two species of $A\beta_{1-42}$ monomers that were each labeled with a different fluorophore, we could track Aβ self–association by Förster resonance energy transfer (FRET). The FRET experiment showed that $A\beta_{1-42}$ aggregates form on the plasma membrane of the neuronal model cells, confirming that oligomer formation precedes cellular uptake of $A\beta_{1-42}$. This also suggests that the membrane serves as a platform for highly efficient aggregation.

A key reaction in these processes is the binding and aggregation of $A\beta_{1-42}$ on the plasma membrane. Therefore, next goal is to study the interactions of $A\beta_{1-42}$ with lipid bilayers in vitro by confocal microscopy using model membrane systems, such as various types of giant unilamellar vesicles (GUVs) and giant plasma membrane vesicles (GPMVs) isolated from the plasma membrane of neuroblastoma (SH–EP) cells. Surprisingly, we found that a population of Aβ species from the end of the lag phase of Thioflavin T aggregation kinetics has a very high affinity to the lipid of membranes and induces negative membrane curvature in both GUVs and GPMVs membranes. Both, the $A\beta_{1-40}$ and $A\beta_{1-42}$ induced membrane invaginations the liquid disordered (Ld) phase, whereas a control peptide, scrambled–$A\beta_{1-42}$, that was aggregation–incompetent did not.

Additionally, blocking the clathrin–mediated endocytosis pathway could not fully inhibit the uptake of $A\beta_{1-42}$. There was no colocalization of plasma membrane–bound $A\beta_{1-42}$ and transferrin, which implies that $A\beta_{1-42}$ did not localize into clathrin–coated pits. These observations suggest that there may be a route of $A\beta_{1-42}$ endocytosis that is independent of the clathrin–mediated process and that $A\beta_{1-42}$ may catalyze its own endocytosis.

While the steps that lead to the initial production of $A\beta_{1-40}$ and $A\beta_{1-42}$ from APP have been intensively studied, many questions remain about the roles the peptides play in healthy neurons and in the pathophysiology of AD. Here we hypothesized that cytotoxicity might be linked to an uptake of extracellular $A\beta_{1-42}$. Our experiments addressed two essential components of this hypothesis: i) that the β–sheet structure is possible a prerequisite for $A\beta_{1-42}$ internalization; and ii) that $A\beta_{1-42}$ oligomers can facilitate their own endocytosis resulting intracellular accumulation and cytotoxicity. We mapped out one of the mechanism by which $A\beta_{1-42}$ could be efficiently internalized: demonstrating the disordered aggregate species without β–sheet structure has a very high lipid affinity, bind rapidly to plasma membrane, where they aggregate, and are then taken up in endocytic vesicles. The cytotoxic effect is positively correlated with monomer uptake in a concentration–dependent manner, suggesting not only that the internalized $A\beta_{1-42}$ aggregates are more toxic, but also that the formation of higher aggregates species is the first step by which $A\beta_{1-42}$ leads to cytotoxicity. These experimental evidences may improve our understanding of Aβ toxicity and AD pathology, and suggest new approaches for potential therapies.

Moreover, our experimental evidence may permit us to recognize a possible physiological function of non–toxic $A\beta_{1-40}$. $A\beta_{1-40}$ has been observed in very close association with synaptic activity and neuron survival (Plant et al. 2003), but the understanding about mechanistic details is still limited. Very recently, a new ultrafast endocytosis of synaptic vesicles was characterized that is 200 times faster than clathrin–mediated endocytosis (Watanabe et al. 2013). APP is concentrated on the synaptic plasma membrane, where cleavage could occur and Aβ could be release at relatively high local concentrations. $A\beta_{1-40}$ might support the formation of invaginations in the presynaptic active zone. The

characterization of a possible role of $A\beta_{1-40}$ and $A\beta_{1-42}$ in synaptic vesicle endocytosis will be the next step in investigating for a possible physiological function of the Aβ peptides.

Bibliography

Ahmed, M. et al., 2010. Structural conversion of neurotoxic amyloid-beta(1-42) oligomers to fibrils. *Nature structural & molecular biology*, 17, pp.561–567.

Alberts, B., 2008. *Molecular Biology of the Cell*,

Allinson, T.M.J. et al., 2003. ADAMs family members as amyloid precursor protein alpha-secretases. *Journal of neuroscience research*, 74, pp.342–352.

de Almeida, R.F.M. et al., 2007. Complexity of lipid domains and rafts in giant unilamellar vesicles revealed by combining imaging and microscopic and macroscopic time-resolved fluorescence. *Biophysical journal*, 93, pp.539–553.

Altankov, G. & Grinnell, F., 1993. Depletion of intracellular potassium disrupts coated pits and reversibly inhibits cell polarization during fibroblast spreading. *Journal of Cell Biology*, 120, pp.1449–1459.

Alzheimer's Association, 2015. 2015 Alzheimer's disease facts and figures. *Alzheimer's & dementia : the journal of the Alzheimer's Association*, 11(3), pp.332–84.

Alzheimer, A., 1907. Uber eine eigenartige Erkrankung der Hirnrinde. *Allg Zeits Psychiatry PsychischYGerichtlich Med*, 64, pp.146–8.

Ambroggio, E.E. et al., 2005. Direct visualization of membrane leakage induced by the antibiotic peptides: maculatin, citropin, and aurein. *Biophysical journal*, 89, pp.1874–1881.

Anfinsen, C.B., 1973. Principles that govern the folding of protein chains. *Science (New York, N.Y.)*, 181(96), pp.223–230.

Anguiano, M., Nowak, R.J. & Lansbury, P.T., 2002. Protofibrillar islet amyloid polypeptide permeabilizes synthetic vesicles by a pore-like mechanism that may be relevant to type II diabetes. *Biochemistry*, 41(38), pp.11338–11343.

Arispe, N., Pollard, H.B. & Rojas, E., 1993. Giant multilevel cation channels formed by Alzheimer disease amyloid beta-protein [A beta P-(1-40)] in bilayer membranes. *Proceedings of the National Academy of Sciences of the United States of America*, 90(22), pp.10573–10577.

Arispe, N., Rojas, E. & Pollard, H.B., 1993. Alzheimer disease amyloid beta protein forms calcium channels in bilayer membranes: blockade by tromethamine and aluminum. *Proceedings of the National Academy of Sciences of the United States of America*, 90(2), pp.567–571.

Arvintes, T., Cudd, A. & Drake, A.F., 1993. The structure and mechanism of formation of human calcitonin fibrils. *The Journal of biological chemistry*, 268, pp.6415–22.

Asakura, S. & Oosawa, F., 1958. Interaction between particles suspended in solutions of macromolecules. *Journal of Polymer Science*, 33(126), pp.183–192.

Asakura, S. & Oosawa, F., 1954. On Interaction Between 2 Bodies Immersed In A Solution of Macromolecules. *Journal of Chemical Physics*, 22, pp.1255–1256.

Babusikova, E. et al., 2011. Alzheimer ' s Disease : Definition , Molecular and Genetic Factors. In Raymond Chuen-Chung Chang, ed. *Advanced Understanding of Neurodegenerative Diseases*. InTech, pp. 3–28.

Bacia, K., Scherfeld, D., et al., 2004. Fluorescence correlation spectroscopy relates rafts in model and native membranes. *Biophysical journal*, 87, pp.1034–1043.

Bacia, K., Schuette, C.G., et al., 2004. SNAREs prefer liquid-disordered over "raft" (liquid-ordered) domains when reconstituted into giant unilamellar vesicles. *Journal of Biological Chemistry*, 279, pp.37951–37955.

Bagatolli, L.A., 2006. To see or not to see: Lateral organization of biological membranes and fluorescence microscopy. *Biochimica et Biophysica Acta - Biomembranes*, 1758, pp.1541–1556.

Ball, K.A. et al., 2013. Differences in β-strand Populations of Monomeric Aβ40 and Aβ42. *Biophysical Journal*, 104, pp.2714–2724.

Barghorn, S. et al., 2005. Globular amyloid β-peptide1-42 oligomer - A homogenous and stable neuropathological protein in Alzheimer's disease. *Journal of Neurochemistry*, 95(3), pp.834–847.

Bateman, D. a & Chakrabartty, A., 2011. Cell surface binding and internalization of aβ modulated by degree of aggregation. *International journal of Alzheimer's disease*, 2011, p.962352.

Baumgart, T., Hunt, G., et al., 2007. Fluorescence probe partitioning between Lo/Ld phases in lipid membranes. *Biochimica et Biophysica Acta - Biomembranes*, 1768, pp.2182–2194.

Baumgart, T., Hammond, A.T., et al., 2007. Large-scale fluid/fluid phase separation of proteins and lipids in giant plasma membrane vesicles. *Proceedings of the National Academy of Sciences of the United States of America*, 104(9), pp.3165–70.

Baumgart, T., Hess, S.T. & Webb, W.W., 2003. Imaging coexisting fluid domains in biomembrane models coupling curvature and line tension. *Nature*, 425, pp.821–824.

Bernstein, S.L. et al., 2009. Amyloid-β protein oligomerization and the importance of tetramers and dodecamers in the aetiology of Alzheimer's disease. *Nature chemistry*, 1, pp.326–331.

Berridge, M. V & Tan, A.S., 1993. Characterization of the cellular reduction of 3-(4,5-dimethylthiazol-2-yl)-2,5-diphenyltetrazolium bromide (MTT): subcellular localization, substrate dependence, and involvement of mitochondrial electron transport in MTT reduction. *Archives of biochemistry and biophysics*, 303(2), pp.474–482.

Berridge, M. V., Herst, P.M. & Tan, A.S., 2005. Tetrazolium dyes as tools in cell biology: New insights into their cellular reduction. *Biotechnology Annual Review*, 11(SUPPL.), pp.127–152.

Bertram, L. & Tanzi, R.E., 2005. The genetic epidemiology of neurodegenerative disease. *The Journal of clinical investigation*, 115, pp.1449–1457.

Biancalana, M. & Koide, S., 2010. Molecular mechanism of Thioflavin-T binding to amyloid fibrils. *Biochimica et Biophysica Acta - Proteins and Proteomics*, 1804(7), pp.1405–1412.

Bieschke, J. et al., 2004. Autocatalytic self-propagation of misfolded prion protein. *Proceedings of the National Academy of Sciences of the United States of America*, 101(33), pp.12207–12211.

Bieschke, J. et al., 2005. Oxidative metabolites accelerate Alzheimer's amyloidogenesis by a two-step mechanism, eliminating the requirement for nucleation. *Biochemistry*, 44(13), pp.4977–4983.

Bieschke, J.A.N. et al., 2006. Small molecule oxidation products trigger disease-associated protein misfolding. *Accounts of Chemical Research*, 39, pp.611–619.

Bitan, G. et al., 2003. Amyloid beta -protein (Abeta) assembly: Abeta 40 and Abeta 42 oligomerize through distinct pathways. *Proceedings of the National Academy of Sciences of the United States of America*, 100(1), pp.330–335.

van Bockxmeer, F.M. & Morgan, E.H., 1979. Transferrin receptors during rabbit reticulocyte maturation. *Biochimica et biophysica acta*, 584, pp.76–83.

Braun, A.R. et al., 2012. α-synuclein induces both positive mean curvature and negative gaussian curvature in membranes. *Journal of the American Chemical Society*, 134(5), pp.2613–2620.

Brookmeyer, R., Gray, S. & Kawas, C., 1998. Projections of Alzheimer's disease in the United States and the public health impact of delaying disease onset. *Am J Public Health*, 88, pp.1337–1342.

Brundin, P., Melki, R. & Kopito, R., 2010. Prion-like transmission of protein aggregates in neurodegenerative diseases. *Nature reviews. Molecular cell biology*, 11(4), pp.301–307.

Bucciantini, M. et al., 2002. Inherent toxicity of aggregates implies a common mechanism for protein misfolding diseases. *Nature*, 416(6880), pp.507–511.

Burdick, D. et al., 1992. Assembly and aggregation properties of synthetic Alzheimer's A4/beta amyloid peptide analogs. *The Journal of biological chemistry*, 267(1), pp.546–554.

Burke, K.A., Yates, E.A. & Legleiter, J., 2013. Biophysical insights into how surfaces, including lipid membranes, modulate protein aggregation related to neurodegeneration. *Frontiers in Neurology*, 4 MAR.

De Camilli, P., 1995. Molecular mechanisms in synaptic vesicle recycling. *FEBS Letters*, 369, pp.3–12.

Campion, D. et al., 1995. Mutations of the presenilin I gene in families with early-onset Alzheimer's disease. *Human molecular genetics*, 4, pp.2373–2377.

Chan, Y.H.M. & Boxer, S.G., 2007. Model membrane systems and their applications. *Curr. Opin. Chem. Biol.*, 11, pp.581–587.

Chiti, F. & Dobson, C.M., 2006. Protein misfolding, functional amyloid, and human disease. *Annual review of biochemistry*, 75, pp.333–366.

Cohen, A.W. et al., 2004. Role of caveolae and caveolins in health and disease. *Physiological reviews*, 84, pp.1341–1379.

Cohen, S.I. a et al., 2013. Proliferation of amyloid-β42 aggregates occurs through a secondary nucleation mechanism. *Proceedings of the*

National Academy of Sciences of the United States of America, 110, pp.9758–63.

Couceiro, J.R. et al., 2015. Sequence-dependent internalization of aggregating peptides. *The Journal of biological chemistry*, 290(1), pp.242–58.

Cremona, O. et al., 1999. Essential role of phosphoinositide metabolism in synaptic vesicle recycling. *Cell*, 99, pp.179–188.

Cremona, O. & De Camilli, P., 1997. Synaptic vesicle endocytosis. *Current Opinion in Neurobiology*, 7, pp.323–330.

Crichton, R.R. & Charloteaux-Wauters, M., 1987. Iron transport and storage. *European Journal of Biochemistry*, 164(3), pp.485–506.

Cullen, K.M. et al., 1996. Improved selectivity and sensitivity in the visualization of neurofibrillary tangles, plaques and neuropil threads. *Neurodegeneration : a journal for neurodegenerative disorders, neuroprotection, and neuroregeneration*, 5(2), pp.177–187.

Curtain, C.C. et al., 2003. Metal ions, pH, and cholesterol regulate the interactions of Alzheimer's disease amyloid-beta peptide with membrane lipid. *The Journal of biological chemistry*, 278(5), pp.2977–2982.

Dahlgren, K.N. et al., 2002. Oligomeric and fibrillar species of amyloid-ß peptides differentially affect neuronal viability. *Journal of Biological Chemistry*, 277, pp.32046–32053.

Dickson, D.W., 2011. Introduction to Neurodegeneration: The Molecular Pathology of Dementia and Movement Disorders. In D. W. Dickson & R. O. Weller, eds. *Neurodegeneration: The Molecular Pathology of Dementia and Movement Disorders: Second Edition*. Wiley-Blackwell, pp. 1–5.

Dickson, D.W., 2010. Neuropathology of non-Alzheimer degenerative disorders. *International Journal of Clinical and Experimental Pathology*, 3, pp.1–23.

Dietrich, C. et al., 2001. Lipid rafts reconstituted in model membranes. *Biophysical journal*, 80, pp.1417–1428.

Ding, H. et al., 2012. β-amyloid (1-40) peptide interactions with supported phospholipid membranes: A single-molecule study. *Biophysical Journal*, 103, pp.1500–1509.

Dobson, C.M., 2004. Principles of protein folding, misfolding and aggregation. In *Seminars in Cell and Developmental Biology*. pp. 3–16.

Dobson, C.M., 2003. Protein folding and misfolding. *Nature*, 426(18 December), pp.884–890.

Dubavik, A. et al., 2012. Penetration of amphiphilic quantum dots through model and cellular plasma membranes. *ACS Nano*, 6, pp.2150–2156.

Van Echten-Deckert, G. & Walter, J., 2012. Sphingolipids: Critical players in Alzheimer's disease. *Progress in Lipid Research*, 51(4), pp.378–393.

Engelman, D.M., 2005. Membranes are more mosaic than fluid. *Nature*, 438, pp.578–580.

Farge, E. & Devaux, P.F., 1992. Shape changes of giant liposomes induced by an asymmetric transmembrane distribution of phospholipids. *Biophysical journal*, 61, pp.347–357.

Farsad, K. et al., 2001. Generation of high curvature membranes mediated by direct endophilin bilayer interactions. *Journal of Cell Biology*, 155, pp.193–200.

Feige, J.N. et al., 2005. PixFRET, an ImageJ plug-in for FRET calculation that can accommodate variations in spectral bleed-throughs. *Microscopy Research and Technique*, 68(1), pp.51–58.

Ford, M.G. et al., 2001. Simultaneous binding of PtdIns(4,5)P2 and clathrin by AP180 in the nucleation of clathrin lattices on membranes. *Science (New York, N.Y.)*, 291, pp.1051–1055.

Förster, T., 1948. Zwischenmolekulare Energiewanderung und Fluoreszenz (Intermolecular energy migration and fluorescence, Translated by Knox RS). *Ann. Phys.*, 437, pp.55–75.

Francis, R. et al., 2002. aph-1 and pen-2 are required for Notch pathway signaling, gamma-secretase cleavage of betaAPP, and presenilin protein accumulation. *Developmental cell*, 3, pp.85–97.

Frank Ferrone, 1999. Analysis of protein aggregation kinetics. *Methods in Enzymology*, 309(1), pp.256–274.

Frankenfield, K.N., Powers, E.T. & Kelly, J.W., 2005. Influence of the N-terminal domain on the aggregation properties of the prion protein. *Protein science : a publication of the Protein Society*, 14, pp.2154–2166.

Frazier, J.L. et al., 1982. Studies of the transferrin receptor on both human reticulocytes and nucleated human cells in culture. Comparison of factors regulating receptor density. *Journal of Clinical Investigation*, 69, pp.853–865.

Friedrich, R.P. et al., 2010. Mechanism of amyloid plaque formation suggests an intracellular basis of Abeta pathogenicity. *Proceedings of the National Academy of Sciences of the United States of America*, 107(5), pp.1942–1947.

Frost, B. et al., 2009. Conformational diversity of wild-type Tau fibrils specified by templated conformation change. *The Journal of biological chemistry*, 284(6), pp.3546–3551.

Frost, B. & Diamond, M.I., 2010. Prion-like mechanisms in neurodegenerative diseases. *Nature reviews. Neuroscience*, 11(3), pp.155–159.

Gaidarov, I. et al., 1999. Spatial control of coated-pit dynamics in living cells. *Nature cell biology*, 1, pp.1–7.

Garzon-Rodriguez, W. et al., 1997. Soluble amyloid Aβ-(1-40) exists as a stable dimer at low concentrations. *Journal of Biological Chemistry*, 272(34), pp.21037–21044.

George-hyslop, P.S. & Schmitt-ulms, G., 2010. Alzheimer's disease: Selectively tuning gamma-secretase. *Nature*, 467, pp.36–37.

Glabe, C.G., 2006. Common mechanisms of amyloid oligomer pathogenesis in degenerative disease. *Neurobiology of Aging*, 27(4), pp.570–575.

Glabe, C.G., 2008. Structural classification of toxic amyloid oligomers. *Journal of Biological Chemistry*, 283, pp.29639–29643.

Glenner, G.G., 1983. Alzheimer's disease. The commonest form of amyloidosis. *Archives of Pathology and Laboratory Medicine*, 107, pp.281–282.

Glenner, G.G. & Wong, C.W., 1984. Alzheimer's disease and Down's syndrome: sharing of a unique cerebrovascular amyloid fibril protein. *Biochemical and biophysical research communications*, 122, pp.1131–1135.

Glenner, G.G. & Wong, C.W., 1984. Alzheimer's disease: Initial report of the purification and characterization of a novel cerebrovascular amyloid protein. *Biochemical and Biophysical Research Communications*, 120(3), pp.885–890.

Goldstein, R.F. & Stryer, L., 1986. Cooperative polymerization reactions. Analytical approximations, numerical examples, and experimental strategy. *Biophysical journal*, 50, pp.583–599.

Gorbenko, G.P. & Kinnunen, P.K.J., 2006. The role of lipid-protein interactions in amyloid-type protein fibril formation. *Chemistry and Physics of Lipids*, 141(1-2), pp.72–82.

Gravina, S.A. et al., 1995. Amyloid beta protein (A beta) in Alzheimer's disease brain. Biochemical and immunocytochemical analysis with antibodies specific for forms ending at A beta 40 or A beta 42(43). *The Journal of biological chemistry*, 270, pp.7013–7016.

Greener, T. et al., 2001. Caenorhabditis elegans auxilin: a J-domain protein essential for clathrin-mediated endocytosis in vivo. *Nature cell biology*, 3, pp.215–219.

Grienberger, C. et al., 2012. Staged decline of neuronal function in vivo in an animal model of Alzheimer's disease. *Nature Communications*, 3, p.774.

Grundke-Iqbal, I. et al., 1986. Abnormal phosphorylation of the microtubule-associated protein tau (tau) in Alzheimer cytoskeletal pathology. *Proceedings of the National Academy of Sciences of the United States of America*, 83, pp.4913–4917.

Guntern, R. et al., 1992. An improved thioflavine S method for staining neurofibrillary tangles and senile plaques in Alzheimer's disease. *Experientia*, 48(1), pp.8–10.

Haass, C. et al., 2012. Trafficking and proteolytic processing of APP. *Cold Spring Harbor Perspectives in Medicine*, 2(5).

Haass, C. et al., 1993. β-Amyloid peptide and a 3-kDa fragment are derived by distinct cellular mechanisms. *Journal of Biological Chemistry*, 268, pp.3021–3024.

Haass, C. & Selkoe, D.J., 2007. Soluble protein oligomers in neurodegeneration: lessons from the Alzheimer's amyloid beta-peptide. *Nature reviews. Molecular cell biology*, 8(2), pp.101–112.

Hamada, T. et al., 2010. Biomimetic Microdroplet membrane interface: Detection of the lateral localization of amyloid beta peptides. *Journal of Physical Chemistry Letters*, 1(1), pp.170–173.

Harding, C., Heuser, J. & Stahl, P., 1983. Receptor-mediated endocytosis of transferrin and recycling of the transferrin receptor in rat reticulocytes. *Journal of Cell Biology*, 97, pp.329–339.

Harper, J.D. et al., 1997. Observation of metastable Abeta amyloid protofibrils by atomic force microscopy. *Chemistry & biology*, 4(2), pp.119–125.

Hartl, F.U. & Hayer-Hartl, M., 2009. Converging concepts of protein folding in vitro and in vivo. *Nature structural & molecular biology*, 16(6), pp.574–581.

Hasegawa, K. et al., 1999. Interaction between A beta(1-42) and A beta(1-40) in Alzheimer's beta-amyloid fibril formation in vitro. *Biochemistry*, 38, pp.15514–15521.

Higgins, M.K. & McMahon, H.T., 2002. Snap-shots of clathrin-mediated endocytosis. *Trends in Biochemical Sciences*, 27, pp.257–263.

Hilbich, C. et al., 1991. Aggregation and secondary

structure of synthetic amyloid beta A4 peptides of Alzheimer's disease. *Journal of molecular biology*, 218(1), pp.149–163.

Hinshaw, J.E., 2000. Dynamin and its role in membrane fission. *Annual review of cell and developmental biology*, 16, pp.483–519.

Holmes, B.B. et al., 2013. Heparan sulfate proteoglycans mediate internalization and propagation of specific proteopathic seeds. *Proceedings of the National Academy of Sciences of the United States of America*, 110(33), pp.E3138–47.

Holmes, B.B. et al., 2014. Proteopathic tau seeding predicts tauopathy in vivo. *Proceedings of the National Academy of Sciences*, 111(41), pp.E4376–E4385.

Hommelgaard, A.M. et al., 2005. Caveolae: Stable membrane domains with a potential for internalization. *Traffic*, 6, pp.720–724.

Hoshi, M. et al., 2003. Spherical aggregates of beta-amyloid (amylospheroid) show high neurotoxicity and activate tau protein kinase I/glycogen synthase kinase-3beta. *Proceedings of the National Academy of Sciences of the United States of America*, 100(11), pp.6370–6375.

Hsu, V.W., Bai, M. & Li, J., 2012. Getting active: protein sorting in endocytic recycling. *Nature reviews. Molecular cell biology*, 13(5), pp.323–328.

Hu, X. et al., 2009. Amyloid seeds formed by cellular uptake, concentration, and aggregation of the amyloid-beta peptide. *Proceedings of the National Academy of Sciences of the United States of America*, 106(48), pp.20324–20329.

Hurshman, A.R. et al., 2004. Transthyretin aggregation under partially denaturing conditions is a downhill polymerization. *Biochemistry*, 43, pp.7365–7381.

Hussain, I. et al., 1999. Identification of a novel aspartic protease (Asp 2) as beta-secretase. *Molecular and cellular neurosciences*, 14, pp.419–427.

Huster, D. et al., 2001. Dynamics of membrane penetration of the fluorescent 7-nitrobenz-2-oxa-1,3-diazol-4-yl (NBD) group attached to an acyl chain of phosphatidylcholine. *Biophysical journal*, 80(2), pp.822–831.

Iacopetta, B.J., Morgan, E.H. & Yeoh, G.C., 1983. Receptor-mediated endocytosis of transferrin by developing erythroid cells from the fetal rat liver. *J Histochem Cytochem*, 31(2), pp.336–344.

Ida, N., Masters, C.L. & Beyreuther, K., 1996. Rapid cellular uptake of Alzheimer amyloid betaA4 peptide by cultured human neuroblastoma cells. *FEBS letters*, 394(2), pp.174–178.

Israelachvili, J.N., Marcelja, S. & Horn, R.G., 1980. *Physical principles of membrane organization.*,

Ito, M. et al., 2000. *Human herpesvirus 6-meningoencephalitis in an HIV patient with progressive multifocal leukoencephalopathy.*,

Ivanov, A.I., 2008. Pharmacological inhibition of endocytic pathways: Is it specific enough to be useful? *Methods in Molecular Biology*, 440, pp.15–33.

Iversen, L. et al., 2015. Membrane curvature bends the laws of physics and chemistry. *Nature Chemical Biology*, 11(11), pp.822–825.

Iwatsubo, T. et al., 1996. Full-length amyloid-beta (1-42(43)) and amino-terminally modified and truncated amyloid-beta 42(43) deposit in diffuse plaques. *The American journal of pathology*, 149, pp.1823–1830.

Jandl, J.H. & Katz, J.H., 1963. The plasma-to-cell cycle of transferrin. *J Clin Invest*, 42(3), pp.314–326.

Jang, H. et al., 2009. Highly pathogenic H5N1 influenza virus can enter the central nervous system and induce neuroinflammation and neurodegeneration. *Proceedings of the National Academy of Sciences of the United States of America*, 106, pp.14063–14068.

Jao, C.C. et al., 2008. Structure of membrane-bound alpha-synuclein from site-directed spin labeling and computational refinement. *Proceedings of the National Academy of Sciences of the United States of America*, 105(50), pp.19666–19671.

Jarrett, J.T., Berger, E.P. & Lansbury, P.T., 1993. The carboxy terminus of the beta amyloid protein is critical for the seeding of amyloid formation: implications for the pathogenesis of Alzheimer's disease. *Biochemistry*, 32(18), pp.4693–4697.

Johnson, R.D. et al., 2011. Direct observation of single amyloid-β(1-40) oligomers on live cells: Binding and growth at physiological concentrations. *PLoS ONE*, 6(8).

Johnson, R.D. et al., 2013. Single-molecule imaging reveals Aß42:Aß40 ratio-dependent oligomer growth on neuronal processes. *Biophysical Journal*, 104(4), pp.894–903.

Kahya, N., Brown, D.A. & Schwille, P., 2005. Raft Partitioning and Dynamic Behavior of Human Placental Alkaline Phosphatase in Giant Unilamellar Vesicles. *Biochemistry*, 44, pp.7479–7489.

Kaiser, H.-J. et al., 2009. Order of lipid phases in model and plasma membranes. *Proceedings of the National Academy of Sciences of the*

United States of America, 106, pp.16645–16650.

Kanekiyo, T. et al., 2013. Neuronal clearance of amyloid-β by endocytic receptor LRP1. *The Journal of neuroscience : the official journal of the Society for Neuroscience*, 33(49), pp.19276–83.

Karin, M. & Mintz, B., 1981. Receptor-mediated Endocytosis of Transferrin in Developmentally. *The Journal of biological chemistry*, 256(7), pp.3245–3252.

Karnovsky, M.J. et al., 1982. The concept of lipid domains in membranes. *The Journal of cell biology*, 94(1), pp.1–6.

Kayed, R. et al., 2003. Common structure of soluble amyloid oligomers implies common mechanism of pathogenesis. *Science (New York, N.Y.)*, 300(5618), pp.486–489.

Kelényi, G., 1967. On the histochemistry of azo group-free thiazole dyes. *The journal of histochemistry and cytochemistry : official journal of the Histochemistry Society*, 15(3), pp.172–180.

Khurana, R. et al., 2005. Mechanism of thioflavin T binding to amyloid fibrils. *Journal of Structural Biology*, 151(3), pp.229–238.

Klein, W.L., 2006. Synaptic targeting by Aβ oligomers (ADDLS) as a basis for memory loss in early Alzheimer's disease. *Alzheimer's and Dementia*, 2, pp.43–55.

Knowles, T.P.J., Vendruscolo, M. & Dobson, C.M., 2014. The amyloid state and its association with protein misfolding diseases. *Nature reviews. Molecular cell biology*, 15(6), pp.384–96.

Kojro, E. & Fahrenholz, F., 2005. The non-amyloidogenic pathway: structure and function of alpha-secretases. *Sub-cellular biochemistry*, 38, pp.105–127.

Koller, D. & Lohner, K., 2014. The role of spontaneous lipid curvature in the interaction of interfacially active peptides with membranes. *Biochimica et biophysica acta*, 1838(9), pp.2250–9.

Korlach, J. et al., 1999. Characterization of lipid bilayer phases by confocal microscopy and fluorescence correlation spectroscopy. *Proceedings of the National Academy of Sciences of the United States of America*, 96, pp.8461–8466.

Krafft, G.A. & Klein, W.L., 2010. ADDLs and the signaling web that leads to Alzheimer's disease. *Neuropharmacology*, 59(4-5), pp.230–242.

Kumar, S. & Walter, J., 2011. Phosphorylation of amyloid beta (A??) peptides - A trigger for formation of toxic aggregates in Alzheimer's disease. *Aging*, 3(8), pp.803–812.

LaFerla, F.M., Green, K.N. & Oddo, S., 2007. Intracellular amyloid-beta in Alzheimer's disease. *Nature reviews. Neuroscience*, 8(7), pp.499–509.

Laganowsky, A. et al., 2012. Atomic View of a Toxic Amyloid Small Oligomer. *Science*, 335(6073), pp.1228–1231.

Lai, A.Y. & McLaurin, J., 2010. Mechanisms of amyloid-Beta Peptide uptake by neurons: the role of lipid rafts and lipid raft-associated proteins. *International journal of Alzheimer's disease*, 2011, p.548380.

Lakowicz, J.R., 2006. *Principles of fluorescence spectroscopy*,

Lambert, M.P. et al., 1998. Diffusible, nonfibrillar ligands derived from Abeta1-42 are potent central nervous system neurotoxins. *Proceedings of the National Academy of Sciences of the United States of America*, 95(11), pp.6448–6453.

Lansbury, P.T. & Lashuel, H.A., 2006. A century-old debate on protein aggregation and neurodegeneration enters the clinic. *Nature*, 443(7113), pp.347–72.

Larkin, J.M. et al., 1983. Depletion of intracellular potassium arrests coated pit formation and receptor-mediated endocytosis in fibroblasts. *Cell*, 33, pp.273–285.

Lashuel, H.A. et al., 2002. Neurodegenerative disease: amyloid pores from pathogenic mutations. *Nature*, 418(6895), p.291.

Laurell, C. & Ingelman, B., 1947. The Iron-Binding Protein of Swine Serum. *Acta Chemica Scandinavica*, 1, pp.770–776.

Lee, M.-T. et al., 2013. Process of inducing pores in membranes by melittin. *Proceedings of the National Academy of Sciences of the United States of America*, 110(35), pp.14243–8.

Lee, V.M. et al., 1991. A68: a major subunit of paired helical filaments and derivatized forms of normal Tau. *Science (New York, N.Y.)*, 251, pp.675–678.

Lemkul, J.A. & Bevan, D.R., 2013. Aggregation of alzheimer's amyloid ??-peptide in biological membranes: A molecular dynamics study. *Biochemistry*, 52, pp.4971–4980.

Lesné, S. et al., 2006. A specific amyloid-beta protein assembly in the brain impairs memory. *Nature*, 440, pp.352–357.

Levental, I. et al., 2009. Cholesterol-dependent phase separation in cell-derived giant plasma-membrane vesicles. *The Biochemical journal*, 424, pp.163–167.

Levental, I. et al., 2010. Palmitoylation regulates raft affinity for the majority of integral raft proteins. *Proceedings of the National Academy of Sciences of the United States of America*, 107, pp.22050–22054.

Levental, I., Grzybek, M. & Simons, K., 2011. Raft domains of variable properties and compositions in plasma membrane vesicles. *Proceedings of the National Academy of Sciences of the United States of America*, 108, pp.11411–11416.

LeVine, H., 1999. Quantification of β-sheet amyloid fibril structures with thioflavin T. *Methods in Enzymology*, 309, pp.274–284.

LeVine, H., 1993. Thioflavine T interaction with synthetic Alzheimer's disease beta-amyloid peptides: detection of amyloid aggregation in solution. *Protein science : a publication of the Protein Society*, 2(3), pp.404–410.

Levitan, D. et al., 2001. PS1 N- and C-terminal fragments form a complex that functions in APP processing and Notch signaling. *Proceedings of the National Academy of Sciences of the United States of America*, 98, pp.12186–12190.

Levy-Lahad, E. et al., 1995. Candidate gene for the chromosome 1 familial Alzheimer's disease locus. *Science (New York, N.Y.)*, 269, pp.973–977.

Lim, J.P. & Gleeson, P.A., 2011. Macropinocytosis: an endocytic pathway for internalising large gulps. *Immunology and Cell Biology*, 89(8), pp.836–843.

Liu, C. et al., 2012. Out-of-register β-sheets suggest a pathway to toxic amyloid aggregates. *Proceedings of the National Academy of Sciences of the United States of America*, 109(51), pp.20913–8.

Lodish, H.F. et al., 2008. *Molecular Cell Biology*,

Lomakin, A. et al., 1997. Kinetic theory of fibrillogenesis of amyloid beta-protein. *Proceedings of the National Academy of Sciences of the United States of America*, 94(15), pp.7942–7947.

Lomakin, A. et al., 1996. On the nucleation and growth of amyloid beta-protein fibrils: detection of nuclei and quantitation of rate constants. *Proceedings of the National Academy of Sciences of the United States of America*, 93(3), pp.1125–1129.

Lue, L.F. et al., 1999. Soluble amyloid beta peptide concentration as a predictor of synaptic change in Alzheimer's disease. *The American journal of pathology*, 155(3), pp.853–862.

Margineanu, A. et al., 2007. Visualization of membrane rafts using a perylene monoimide derivative and fluorescence lifetime imaging. *Biophysical journal*, 93, pp.2877–2891.

Marks, B. et al., 2001. GTPase activity of dynamin and resulting conformation change are essential for endocytosis. *Nature*, 410, pp.231–235.

Marks, B. & McMahon, H.T., 1998. Calcium triggers calcineurin-dependent synaptic vesicle recycling in mammalian nerve terminals. *Current biology : CB*, 8, pp.740–749.

Marsh, M. & Helenius, A., 1980. Adsorptive endocytosis of Semliki Forest virus. *Journal of molecular biology*, 142, pp.439–454.

Marsh, M. & McMahon, H.T., 1999. The structural era of endocytosis. *Science (New York, N.Y.)*, 285, pp.215–220.

Martin, J.B., 1999. Molecular basis of the neurodegenerative disorders. *The New England journal of medicine*, 340, p.1970.

Masters, C.L. et al., 1985. Amyloid plaque core protein in Alzheimer disease and Down syndrome. *Proc.Natl.Acad.Sci.U.S.A*, 82, pp.4245–4249. Available at: PM:3159021.

Matsuzaki, K. & Horikiri, C., 1999. Interactions of amyloid β-peptide (1-40) with ganglioside-containing membranes. *Biochemistry*, 38(13), pp.4137–4142.

Maxfield, F.R. & McGraw, T.E., 2004. Endocytic recycling. *Nature reviews. Molecular cell biology*, 5, pp.121–132.

Mayor, S. & Pagano, R.E., 2007. Pathways of clathrin-independent endocytosis. *Nature reviews. Molecular cell biology*, 8(8), pp.603–612.

McLaurin, J. & Chakrabartty, A., 1997. Characterization of the interactions of Alzheimer beta-amyloid peptides with phospholipid membranes. *European journal of biochemistry / FEBS*, 245(2), pp.355–363.

McLaurin, J. & Chakrabartty, A., 1996. Membrane disruption by Alzheimer ß-amyloid peptides mediated through specific binding to either phospholipids or gangliosides. Implications for neurotoxicity. *Journal of Biological Chemistry*, 271(43), pp.26482–26489.

McLean, C.A. et al., 1999. Soluble pool of Aβ amyloid as a determinant of severity of neurodegeneration in Alzheimer's disease. *Annals of Neurology*, 46(6), pp.860–866.

McMahon, H.T. & Gallop, J.L., 2005. Membrane curvature and mechanisms of dynamic cell membrane remodelling. *Nature*, 438(7068), pp.590–596.

van Meer, G., Voelker, D.R. & Feigenson, G.W., 2008. Membrane lipids: where they are and how they behave. *Nature reviews. Molecular cell biology*, 9, pp.112–124.

Mégret, F. et al., 2007. Modulation of HLA-G and HLA-E Expression in Human Neuronal Cells After Rabies Virus or Herpes Virus Simplex Type 1 Infections. *Human Immunology*, 68, pp.294–302.

Meinhardt, J. & Fändrich, M., 2009. Structure of amyloid fibrils. *Der Pathologe*, 30(3), pp.175–81.

Meisl, G. et al., 2014. Differences in nucleation behavior underlie the contrasting aggregation kinetics of the Aβ40 and Aβ42 peptides. *Proceedings of the National Academy of Sciences of the United States of America*, 111(26), pp.9384–9.

Mercer, J. & Helenius, A., 2009. Virus entry by macropinocytosis. *Nature cell biology*, 11(5), pp.510–520.

Mirsky, A.E. & Pauling, L., 1936. On the Structure of Native, Denatured, and Coagulated Proteins. *Proc Natl Acad Sci USA*, 22(1892), pp.439–447.

Mirzabekov, T.A., Lin, M.C. & Kagan, B.L., 1996. Pore formation by the cytotoxic islet amyloid peptide amylin. *Journal of Biological Chemistry*, 271(4), pp.1988–1992.

Morales-Penningston, N.F. et al., 2010. GUV preparation and imaging: Minimizing artifacts. *Biochimica et Biophysica Acta - Biomembranes*, 1798, pp.1324–1332.

Mori, I. & Kimura, Y., 2001. Neuropathogenesis of influenza virus infection in mice. *Microbes and infection / Institut Pasteur*, 3, pp.475–479.

Morita, M. et al., 2014. Endo- and exocytic budding transformation of slow-diffusing membrane domains induced by Alzheimer's amyloid beta. *Physical chemistry chemical physics : PCCP*, 16(19), pp.8773–7.

Morita, M. et al., 2010. Real-time observation of model membrane dynamics induced by Alzheimer's amyloid beta. *Biophysical chemistry*, 147(1-2), pp.81–86.

Morita, M. et al., 2012. Selective localization of Alzheimer's amyloid beta in membrane lateral compartments. *Soft Matter*, 8(10), p.2816.

Morris, S.A. et al., 2010. Alcohol inhibition of neurogenesis: A mechanism of hippocampal neurodegeneration in an adolescent alcohol abuse model. *Hippocampus*, 20, pp.596–607.

Mosmann, T., 1983. Rapid colorimetric assay for cellular growth and survival: application to proliferation and cytotoxicity assays. *Journal of immunological methods*, 65(1-2), pp.55–63.

Mouritsen, O.G., 2005. *Life–as a matter of fat: the emerging science of lipidomics*,

Mullan, M. et al., 1992. *A pathogenic mutation for probable Alzheimer's disease in the APP gene at the N-terminus of beta-amyloid.*,

Murphy, R.M., 2002. Peptide aggregation in neurodegenerative disease. *Annual review of biomedical engineering*, 4, pp.155–174.

Murray, I.V.J. et al., 2007. Membrane-mediated amyloidogenesis and the promotion of oxidative lipid damage by amyloid beta proteins. *The Journal of biological chemistry*, 282(13), pp.9335–9345.

National Center for Health Statistics, 2015. *National Center for Health Statistics. Deaths: Final Data for 2013. National Vital Statistics Report.*,

Neve, R.L., McPhie, D.L. & Chen, Y., 2000. Alzheimer's disease: a dysfunction of the amyloid precursor protein. *Brain Res*, 886, pp.54–66.

Nixon, K., 2006. Alcohol and adult neurogenesis: Roles in Neurodegeneration and recovery in chronic alcoholism. *Hippocampus*, 16, pp.287–295.

Nunez, M.T. et al., 1977. Transferrin receptors in developing murine erythroid cells. *British journal of haematology*, 36, pp.519–526.

O'Brien, R.J. & Wong, P.C., 2011. Amyloid precursor protein processing and Alzheimer's disease. *Annual review of neuroscience*, 34, pp.185–204.

Olsson, F. et al., 2014. Characterization of intermediate steps in amyloid beta (Aβ) production under near-native conditions. *Journal of Biological Chemistry*, 289(3), pp.1540–1550.

Omtri, R.S. et al., 2012. Differences in the cellular uptake and intracellular itineraries of amyloid beta proteins 40 and 42: Ramifications for the Alzheimer's drug discovery. *Molecular Pharmaceutics*, 9(7), pp.1887–1897.

Owen, D.M. et al., 2006. Fluorescence lifetime imaging provides enhanced contrast when imaging the phase-sensitive dye di-4-ANEPPDHQ in model membranes and live cells. *Biophysical journal*, 90, pp.L80–L82.

Papadopulos, A. et al., 2007. Flippase activity detected with unlabeled lipids by shape changes of giant unilamellar vesicles. *Journal of Biological Chemistry*, 282, pp.15559–15568.

Parasassi, T. et al., 1990. Phase fluctuation in phospholipid membranes revealed by Laurdan fluorescence. *Biophysical journal*, 57(6), pp.1179–1186.

Parton, R.G., 2003. Caveolae--from ultrastructure to molecular mechanisms. *Nature reviews. Molecular cell biology*, 4, pp.162–167.

Parton, R.G. & del Pozo, M. a, 2013. Caveolae as plasma membrane sensors, protectors and organizers. *Nature reviews. Molecular cell biology*, 14, pp.98–112.

Parton, R.G. & Simons, K., 2007. The multiple faces of caveolae. *Nature reviews. Molecular cell biology*, 8, pp.185–194.

Pelkmans, L., Kartenbeck, J. & Helenius, A., 2001. Caveolar endocytosis of simian virus 40 reveals a new two-step vesicular-transport pathway to the ER. *Nature cell biology*, 3, pp.473–483.

Perl, D.P., 2010. Neuropathology of Alzheimer's disease. *Mount Sinai Journal of Medicine*, 77, pp.32–42.

Plant, L.D. et al., 2003. The production of amyloid beta peptide is a critical requirement for the viability of central neurons. *The Journal of neuroscience : the official journal of the Society for Neuroscience*, 23(13), pp.5531–5.

Powers, E.T. et al., 1986. Mechanisms of protein fibril formation: nucleated polymerization with competing off-pathway aggregation. *Biophysical journal*, 50(1), pp.379–391.

Powers, E.T. & Powers, D.L., 2008. Mechanisms of protein fibril formation: nucleated polymerization with competing off-pathway aggregation. *Biophysical journal*, 94, pp.379–391.

Prindle, A. et al., 2015. Ion channels enable electrical communication in bacterial communities. *Nature*, 527(7576), pp.59–63.

Prusiner, S.B., 1998. Prions. *Proceedings of the National Academy of Sciences of the United States of America*, 95(23), pp.13363–13383.

Przedborski, S., Vila, M. & Jackson-lewis, V., 2003. Neurodegeneration: What is it and where are we? *The Journal of Clinical Investigation*, 111(1), pp.3–10.

Rajasekaran, S.A. et al., 2001. Na,K-ATPase activity is required for formation of tight junctions, desmosomes, and induction of polarity in epithelial cells. *Molecular biology of the cell*, 12, pp.3717–3732.

Reiss, A.B. et al., 2004. Cholesterol in neurologic disorders of the elderly: Stroke and Alzheimer's disease. *Neurobiology of Aging*, 25(8), pp.977–989.

Remedios, C.G., 2001. Fluorescence Resonance Energy Transfer. *ENCYCLOPEDIA OF LIFE SCIENCES*, pp.1–9.

Rice, A. et al., 2003. Overcoming the blood-brain barrier to taxane delivery for neurodegenerative diseases and brain tumors. *Journal of molecular neuroscience : MN*, 20, pp.339–343.

Rogaev, E. et al., 1995. Familial Alzheimer's disease in kindreds with missense mutations in a gene on chromosome 1 related to the Alzheimer's disease type 3 gene. *Nature*, 376, pp.775–778.

Roher, A.E. et al., 1993. beta-Amyloid-(1-42) is a major component of cerebrovascular amyloid deposits: implications for the pathology of Alzheimer disease. *Proceedings of the National Academy of Sciences of the United States of America*, 90, pp.10836–10840.

Säälik, P. et al., 2011. Penetration without cells: Membrane translocation of cell-penetrating peptides in the model giant plasma membrane vesicles. *Journal of Controlled Release*, 153, pp.117–125.

Sabaté, R. et al., 2012. Effect of the surface charge of artificial model membranes on the aggregation of amyloid β-peptide. *Biochimie*, 94(8), pp.1730–1738.

Sabaté, R. & Estelrich, J., 2005. Evidence of the existence of micelles in the fibrillogenesis of beta-amyloid peptide. *The journal of physical chemistry. B*, 109(21), pp.11027–11032.

Sabaté, R., Gallardo, M. & Estelrich, J., 2005. Spontaneous incorporation of β-amyloid peptide into neutral liposomes. *Colloids and Surfaces A: Physicochemical and Engineering Aspects*, 270-271(1-3), pp.13–17.

Sanders, D.W. et al., 2014. Distinct Tau Prion Strains Propagate in Cells and Mice and Define Different Tauopathies. *Neuron*, pp.1–18.

Di Scala, C. et al., 2014. Interaction of Alzheimer's β-amyloid peptides with cholesterol: Mechanistic insights into amyloid pore formation. *Biochemistry*, 53(28), pp.4489–4502.

Scott, R.E. et al., 1979. Plasma membrane vesiculation in 3T3 and SV3T3 cells. I. Morphological and biochemical characterization. *Journal of cell science*, 35, pp.229–243.

Sekar, R.B. & Periasamy, A., 2003. Fluorescence resonance energy transfer (FRET) microscopy imaging of live cell protein localizations. *The Journal of cell biology*, 160, pp.629–633.

Selkoe, D.J., 2002. Alzheimer's disease is a synaptic failure. *Science (New York, N.Y.)*, 298(5594), pp.789–791.

Sengupta, P. et al., 2008. Structural determinants for partitioning of lipids and proteins between coexisting fluid phases in giant

plasma membrane vesicles. *Biochimica et Biophysica Acta - Biomembranes*, 1778, pp.20–32.

Serio, T.R. et al., 2000. Nucleated conformational conversion and the replication of conformational information by a prion determinant. *Science (New York, N.Y.)*, 289, pp.1317–1321.

Sezgin, E., Kaiser, H.-J., et al., 2012. Elucidating membrane structure and protein behavior using giant plasma membrane vesicles. *Nature Protocols*, 7, pp.1042–1051.

Sezgin, E., Levental, I., et al., 2012. Partitioning, diffusion, and ligand binding of raft lipid analogs in model and cellular plasma membranes. *Biochimica et Biophysica Acta - Biomembranes*, 1818, pp.1777–1784.

Shaw, J.E. et al., 2006. Correlated fluorescence-atomic force microscopy of membrane domains: structure of fluorescence probes determines lipid localization. *Biophysical journal*, 90, pp.2170–2178.

Shi, Z. et al., 2015. Biophysics of α-synuclein induced membrane remodelling. *Physical chemistry chemical physics : PCCP*, 17(24), pp.15561–8.

Shi, Z. & Baumgart, T., 2015. Membrane tension and peripheral protein density mediate membrane shape transitions. *Nature communications*, 6(May 2014), p.5974.

Shogomori, H. et al., 2005. Palmitoylation and intracellular domain interactions both contribute to raft targeting of linker for activation of T cells. *Journal of Biological Chemistry*, 280, pp.18931–18942.

Shoji, M. et al., 1992. Production of the Alzheimer amyloid beta protein by normal proteolytic processing. *Science (New York, N.Y.)*, 258(5079), pp.126–129.

Siegel, S.J. et al., 2007. The oxidative stress metabolite 4-hydroxynonenal promotes Alzheimer protofibril formation. *Biochemistry*, 46(6), pp.1503–1510.

Simons, M. et al., 1998. Cholesterol depletion inhibits the generation of beta-amyloid in hippocampal neurons. *Proceedings of the National Academy of Sciences of the United States of America*, 95(11), pp.6460–6464.

Singer, S.J. & Nicolson, G.L., 1972. The fluid mosaic model of the structure of cell membranes. *Science (New York, N.Y.)*, 175, pp.720–731.

Sinha, S. et al., 1999. Purification and cloning of amyloid precursor protein b-secretase from human brain. *Nature*, 402, pp.537–540.

Sokolowski, F. et al., 2003. Formation of Critical Oligomers Is a Key Event during Conformational Transition of Recombinant Syrian Hamster Prion Protein. *Journal of Biological Chemistry*, 278, pp.40481–40492.

Soreghan, B., Kosmoski, J. & Glabe, C., 1994. Surfactant properties of Alzheimer's Aß peptides and the mechanism of amyloid aggregation. *Journal of Biological Chemistry*, 269(46), pp.28551–28554.

Stachowiak, J.C., Brodsky, F.M. & Miller, E. a, 2013. A cost-benefit analysis of the physical mechanisms of membrane curvature. *Nature cell biology*, 15(9), pp.1019–27.

Stan, R. V., 2005. Structure of caveolae. *Biochimica et Biophysica Acta - Molecular Cell Research*, 1746, pp.334–348.

Staneva, G., Angelova, M.I. & Koumanov, K., 2004. Phospholipase A2 promotes raft budding and fission from giant liposomes. *Chemistry and Physics of Lipids*, 129, pp.53–62.

Stefani, M., 2010. Biochemical and biophysical features of both oligomer/fibril and cell membrane in amyloid cytotoxicity. *FEBS Journal*, 277, pp.4602–4613.

Steiner, H. et al., 2002. PEN-2 is an integral component of the γ-secretase complex required for coordinated expression of presenilin and nicastrin. *Journal of Biological Chemistry*, 277, pp.39062–39065.

Stier, A. & Sackmann, E., 1973. Spin labels as enzyme substrates Heterogeneous lipid distribution in liver microsomal membranes. *BBA - Biomembranes*, 311(3), pp.400–408.

Stöckl, M., Plazzo, A.P., et al., 2008. Detection of lipid domains in model and cell membranes by fluorescence lifetime imaging microscopy of fluorescent lipid analogues. *Journal of Biological Chemistry*, 283, pp.30828–30837.

Stöckl, M., Fischer, P., et al., 2008. α-Synuclein Selectively Binds to Anionic Phospholipids Embedded in Liquid-Disordered Domains. *Journal of Molecular Biology*, 375, pp.1394–1404.

Stöckl, M., Nikolaus, J. & Herrmann, A., 2010. Visualization of lipid domain-specific protein sorting in giant unilamellar vesicles. *Methods in molecular biology (Clifton, N.J.)*, 606, pp.115–126.

Stöckl, M.T. & Herrmann, A., 2010. Detection of lipid domains in model and cell membranes by fluorescence lifetime imaging microscopy. *Biochimica et biophysica acta*, 1798(7), pp.1444–1456.

Stowell, M.H. et al., 1999. Nucleotide-dependent conformational changes in dynamin: evidence for a mechanochemical molecular spring. *Nature cell biology*, 1, pp.27–32.

Sulkava, R., Rissanen, A. & Pyhälä, R., 1981. Post-influenzal encephalitis during the influenza A outbreak in 1979/1980. *Journal of neurology, neurosurgery, and psychiatry*, 44, pp.161–163.

Sullivan, A.L., Grasso, J.A. & Weintraub, L.R., 1976. Micropinocytosis of transferrin by developing red cells: an electron-microscopic study utilizing ferritin-conjugated transferrin and ferritin-conjugated antibodies to transferrin. *Blood*, 47, pp.133–143.

Sun, A., Nguyen, X. V & Bing, G., 2002. Comparative analysis of an improved thioflavin-s stain, Gallyas silver stain, and immunohistochemistry for neurofibrillary tangle demonstration on the same sections. *The journal of histochemistry and cytochemistry : official journal of the Histochemistry Society*, 50(4), pp.463–472.

Suzuki, N. et al., 1994. An increased percentage of long amyloid beta protein secreted by familial amyloid beta protein precursor (beta APP717) mutants. *Science (New York, N.Y.)*, 264, pp.1336–1340.

Sweitzer, S.M. & Hinshaw, J.E., 1998. Dynamin undergoes a GTP-dependent conformational change causing vesiculation. *Cell*, 93, pp.1021–1029.

Swift, S.R. & Trinkle-Mulcahy, L., 2004. Basic principles of FRAP , FLIM and FRET. *Proceedings of the Royal Microscopical Society*, 39, pp.3–10.

Takei, K. et al., 1999. Functional partnership between amphiphysin and dynamin in clathrin-mediated endocytosis. *Nature cell biology*, 1, pp.33–39.

Terzi, E., Hölzemann, G. & Seelig, J., 1995. Self-association of beta-amyloid peptide (1-40) in solution and binding to lipid membranes. *Journal of molecular biology*, 252(5), pp.633–642.

Treusch, S. et al., 2011. Functional Links Between A Toxicity, Endocytic Trafficking, and Alzheimer's Disease Risk Factors in Yeast. *Science*, 334(6060), pp.1241–1245.

Usui, K. et al., 2009. Site-specific modification of Alzheimer's peptides by cholesterol oxidation products enhances aggregation energetics and neurotoxicity. *Proceedings of the National Academy of Sciences of the United States of America*, 106(44), pp.18563–18568.

Uzman, A. et al., 2000. Molecular Cell Biology (4th edition) New York, NY, 2000, ISBN 0-7167-3136-3. *Biochemistry and Molecular Biology Education*, 29, p.Section 5.3.

Vassar, P.S. & Culling, C.F., 1959. Fluorescent stains, with special reference to amyloid and connective tissues. *Archives of pathology*, 68, pp.487–498.

Vassar, R. et al., 1999. β-secretase cleavage of Alzheimer's amyloid precursor protein by the transmembrane aspartic protease BACE. *Science*, 286, pp.735–741.

Vassilieva, E. V. & Nusrat, A., 2008. Vesicular trafficking: Molecular tools and targets. *Methods in Molecular Biology*, 440, pp.3–14.

Veatch, S.L. & Keller, S.L., 2005. Seeing spots: Complex phase behavior in simple membranes. *Biochimica et Biophysica Acta - Molecular Cell Research*, 1746, pp.172–185.

Veatch, S.L. & Keller, S.L., 2003. Separation of liquid phases in giant vesicles of ternary mixtures of phospholipids and cholesterol. *Biophysical journal*, 85, pp.3074–3083.

Vestergaard, M.C. et al., 2013. Membrane fusion and vesicular transformation induced by Alzheimer's amyloid beta. *Biochimica et biophysica acta*, 1828(4), pp.1314–21.

Virchow, R., 1853. Ueber eine im Gehirn und Rückenmark des Menschen aufgefundene Substanz mit der chemischen Reaction der Cellulose. *Archiv für pathologische Anatomie und Physiologie und für klinische Medicin 1854*, 6(1), pp.135–138.

Walsh, D.M. et al., 1999. Amyloid b-protein fibrillogenesis - Structure and biological activity of protofibrillar intermediates. *Journal of Biological Chemistry*, 274(36), pp.25945–25952.

Walsh, D.M. et al., 1997. Amyloid ß-protein fibrillogenesis: Detection of a protofibrillar intermediate. *Journal of Biological Chemistry*, 272(35), pp.22364–22372.

Walsh, D.M. et al., 2002. Naturally secreted oligomers of amyloid beta protein potently inhibit hippocampal long-term potentiation in vivo. *Nature*, 416(6880), pp.535–539.

Wang, S. et al., 2013. Dysregulated mTOR-dependent signaling in neurodegeneration or carcinogenesis: Implication for alzheimer's disease and brain tumors. *Journal of Alzheimer's Disease*, 37, pp.495–505.

Ward, J.H., Kushner, J.P. & Kaplan, J., 1982. Regulation of HeLa cell transferrin receptors. *Journal of Biological Chemistry*, 257, pp.10317–10323.

Warren H. Lewis, 1936. Pinocytosis: drinking by cells. *The Johns Hopkins Medical Institutions*. Available at: https://youtu.be/7qUCTgJ8C8s.

Watanabe, S. et al., 2013. Ultrafast endocytosis at mouse hippocampal synapses. *Nature*, 504(7479), pp.242–7.

Wei, J. et al., 2005. Development of novel amyloid

imaging agents based upon thioflavin S. *Current Alzheimer research*, 2(2), pp.109–14.

White, M.R. et al., 2014. Alzheimer's associated β-Amyloid protein inhibits influenza a virus and modulates viral interactions with phagocytes. *PLoS ONE*, 9.

Williams, T.L. & Serpell, L.C., 2011. Membrane and surface interactions of Alzheimer's Aβ peptide - Insights into the mechanism of cytotoxicity. In *FEBS Journal*. pp. 3905–3917.

Winkelmann, A. et al., 2015. Identification of a new genomic hot spot of evolutionary diversification of protein function. *PloS one*, 10(5), p.e0125413.

Wolfe, M.S. et al., 1999. Two transmembrane aspartates in presenilin-1 required for presenilin endoproteolysis and gamma-secretase activity. *Nature*, 398, pp.513–517.

Wood, W.G. et al., 2003. Amyloid beta-protein interactions with membranes and cholesterol: Causes or casualties of Alzheimer's disease. *Biochimica et Biophysica Acta - Biomembranes*, 1610(2), pp.281–290.

Yamamoto, N. et al., 2007. A ganglioside-induced toxic soluble Aβ assembly: Its enhanced formation from Aβ bearing the arctic mutation. *Journal of Biological Chemistry*, 282(4), pp.2646–2655.

Yip, C.M. et al., 2001. Cholesterol, a modulator of membrane-associated A beta- fibrillogenesis and neurotoxicity. *Journal of Molecular Biology*, 311(4), pp.723–734.

Younkin, S.G., 1998. The role of Aβ42 in Alzheimer's disease. In *Journal of Physiology Paris*. pp. 289–292.

Yu, A. et al., 2014. Protein aggregation can inhibit clathrin-mediated endocytosis by chaperone competition. *Proceedings of the National Academy of Sciences of the United States of America*, 111(15), pp.E1481–90.

Yu, G. et al., 2000. Nicastrin modulates presenilin-mediated notch/glp-1 signal transduction and betaAPP processing. *Nature*, 407, pp.48–54.

Yu, X. & Zheng, J., 2012. Cholesterol promotes the interaction of alzheimer ß-amyloid monomer with lipid bilayer. *Journal of Molecular Biology*, 421(4-5), pp.561–571.

Zhang, Y. et al., 2002. Selective cytotoxicity of intracellular amyloid beta peptide1-42 through p53 and Bax in cultured primary human neurons. *The Journal of cell biology*, 156(3), pp.519–529.

Zhao, L.N. et al., 2011. Amyloid ß peptides aggregation in a mixed membrane bilayer: A molecular dynamics study. *Journal of Physical Chemistry B*, 115(42), pp.12247–12256.

Zhou, L., Miranda-Saksena, M. & Saksena, N.K., 2013. Viruses and neurodegeneration. *Virology journal*, 10, p.172.

Erklärung

Hiermit erkläre ich, die Dissertation selbstständig und nur unter Verwendung der angegebenen Hilfen und Hilfsmittel angefertigt zu haben. Ich habe mich anderwärts nicht um einen Doktorgrad beworben und besitze keinen entsprechenden Doktorgrad. Ich erkläre, dass ich die Dissertation oder Teile davon nicht bereits bei einer anderen wissenschaftlichen Einrichtung eingereicht habe und dass sie dort weder angenommen noch abgelehnt wurde.

Sha Jin

Berlin, Mai 2016